



Università degli Studi di Ferrara

DOTTORATO DI RICERCA IN
"Scienze dell'Ingegneria"

CICLO XXIX

COORDINATORE Prof. Stefano Trillo

**Instability Phenomena in Multistage Compressors:
Experimental Analysis and Dynamic Modeling**

Settore Scientifico Disciplinare ING-IND/08

Dottorando

Dott. Munari Enrico

Tutori

Prof. Venturini Mauro

Prof. Pinelli Michele

Anni 2014/2016

Dedicated to my wife Pilar

and my daughter Nicole

Abstract

Flow instability conditions, in particular during surge and stall phenomena, have always influenced the operational reliability of turbo-compressors and have attracted significant interest resulting in extensive literature. Nowadays, this subject is still one of the most investigated because of its high relevance on centrifugal and axial compressor operating flow range, performance and efficiency. However, there is another fundamental aspect to be considered; which is the magnitude of the unsteady forces generated in the compressor during these unstable operations. These forces can become highly dangerous for the mechanical and aerodynamic structure of the compressor.

Many researchers approach this important issue by developing numerical models, whereas others approach it through experimental studies specifically carried out in order to better comprehend this phenomenon. The aim of this work is: (i) to experimentally analyze the stable and unstable operating conditions of an aeronautic turbo-shaft gas turbine axial-centrifugal compressor installed on a brand new test-rig properly designed for this purpose; and (ii) to develop a nonlinear model for simulating the dynamic behavior of compression systems.

The test facility is set up in order to obtain (i) the compressor performance maps at rotational speeds up to 25,000 rpm and (ii) the compressor transient behavior during surge. By using two different test rig layouts, instabilities occurring in the compressor, beyond the peak of the characteristic curve, are identified and investigated. These two types of analysis are carried out thanks to pressure, temperature and mass flow sensors located in strategic positions along the circuit. These measurement sensors are part of a proper control and acquisition system, characterized by an adjustable sampling frequency. Thus, the desired operating conditions of the compressor, in terms of mass flow and rotational speed, and transient of these two parameters, are regulated by this dedicated control system.

Successively, a vibro-acoustic analysis, is carried out in order to demonstrate the efficaciousness of accelerometers and microphones in detecting rotating stall and surge and their inception.

The dynamic model is implemented in Matlab®/Simulink® environment and developed by means of a general bond graph approach which leads to a highly modular lumped parameter structure. The thermodynamics of the model was validated by using the experimental data provided by the test rig cited above, showing high reliability in simulating the dynamics of the compressor operating point in both the stable field of the characteristic curve and unstable field, reproducing with high fidelity the surge cycle generated.

The simulator, is also provided with a supplementary tool to estimate the axial force frequency and amplitude, taking into consideration all the contributions to the axial fluid-dynamic thrust generation, and to the resultant axial mechanical force which acts on the thrust bearing. The test case facility layout, which was simulated by the model, is located at SouthWest Research Institute laboratory in which a 522 kW industrial air centrifugal compressor was performed in surge conditions. The model was tuned and validated by using the test case axial force data showing a good agreement with the experimental results and demonstrating to well predict the amplitude and frequency of the net axial thrust.

From these results and analyses some final remarks and conclusions can be drawn, which are presented at the end of this Thesis.

Sommario

Le condizioni di instabilità fluidodinamica, in particolare durante fenomeni come stallo e pompaggio, hanno sempre influenzato l'affidabilità operativa dei compressori dinamici e hanno attirato un considerevole interesse che ha portato ad un notevole numero di lavori in letteratura. Oggi, questo argomento è ancora uno dei più studiati a causa della sua elevata rilevanza nell'ambito del campo di funzionamento dei compressori centrifughi ed assiali, e delle loro prestazioni anche in termini di efficienza. Tuttavia, vi è un altro aspetto fondamentale da considerare; che è la grandezza delle forze generate nel compressore durante questi fenomeni di instabilità. Queste forze possono diventare molto pericolose per la struttura meccanica ed aerodinamica del compressore.

Molti ricercatori affrontano questo importante problema attraverso lo sviluppo di modelli numerici, mentre altri, attraverso studi sperimentali, al fine di comprendere meglio le caratteristiche di questi fenomeni. Lo scopo di questo lavoro è: (i) analizzare sperimentalmente le condizioni operative di stabilità ed instabilità di un compressore assial-centrifugo, appartenente ad una turbina a gas di tipo turbo-albero di derivazione aeronautica, installato su un nuovo banco prova adeguatamente progettato per questo scopo; e (ii) sviluppare un modello non lineare per la simulazione del comportamento dinamico dei sistemi di compressione.

L'impianto di prova è costruito in modo da ottenere (i) le mappe di prestazione del compressore a velocità di rotazione fino a 25,000 rpm e (ii) il comportamento transitorio del compressore in stallo e pompaggio. Utilizzando due diverse configurazioni del banco, vengono individuate ed esaminate le instabilità che si verificano nel compressore una volta superato il picco della curva caratteristica. Questi due tipi di analisi sono effettuati grazie all'utilizzo di sensori di pressione, temperatura e portata in massa situati in posizioni strategiche lungo il circuito. Questi sensori di misura costituiscono parte di un adeguato sistema di controllo e acquisizione, caratterizzato da una frequenza di campionamento regolabile. Pertanto, le condizioni operative del compressore, in termini di portata in massa e velocità di rotazione, e i transitori di questi due parametri, sono regolati da questo sistema di controllo dedicato.

Un'analisi vibro-acustica, è stata effettuata successivamente, al fine di dimostrare l'efficacia di accelerometri e microfoni nel rilevare lo stallo rotante ed il pompaggio.

Un modello dinamico è implementato in ambiente Matlab® / Simulink® e sviluppato mediante l'uso dei bond-graph, che porta ad una struttura a parametri concentrati altamente modulare. La termodinamica implementata nel modello ed i risultati sono stati validati utilizzando i dati sperimentali forniti dal banco prova realizzato. Il modello mostra elevata affidabilità nel simulare la dinamica del punto di funzionamento del compressore, sia nel campo stabile della curva caratteristica, sia in campo instabile, riuscendo ad ottenere anche un'ottima corrispondenza con i dati sperimentali in pompaggio.

Il modello è inoltre dotato di uno strumento supplementare per stimare l'ampiezza e la frequenza delle forze assiali, prendendo in considerazione tutti i contributi che producono la spinta fluidodinamica assiale, e la conseguente forza meccanica assiale che si scarica sul cuscinetto reggispinta. Il *test case*, è il banco prova situato presso il laboratorio del Southwest Research Institute, nel quale è installato un compressore centrifugo industriale da 522 kW che è stato fatto operare in condizioni di pompaggio. Il modello è calibrato e validato utilizzando i dati di tale banco prova e mostra una buona correlazione con i risultati sperimentali riferiti ad ampiezza e frequenza della spinta assiale.

Da questi risultati e analisi, alcune importanti osservazioni e conclusioni finali possono essere tratte; queste sono presentate alla fine di questa Tesi.

Index

Abstract	i
Sommario	iii
Index	vii
List of Figures	xi
List of Tables.....	xix
I Rationale	I
II Aim, Originality and Limitations.....	V
III Contributions by Others	VII
IV List of Papers	IX
1 Compressors: Background	13
1.1 History of Centrifugal and Axial Flow Compressors.....	13
1.2 Compressor Operative Principles - The Basics	15
1.2.1 Axial Compressors	15
1.2.2 Centrifugal Compressors	16
1.3 Compressor Performance and Thermodynamics.....	17
1.3.1 First Law of Thermodynamics.....	18
1.3.2 Second Law of Thermodynamics	19
1.3.3 Gas constant and Specific Heats.....	21
1.3.4 Euler Work Equation	22
1.3.5 Efficiency	23
1.3.6 Polytropic Efficiency	24
1.3.7 Compressor Performance	27
1.4 Modern Applications of Compressors.....	30
1.5 Compressor Stability and Unstable Behavior.....	32
2 Rotating Stall and Surge	37
2.1 What is Known Today.....	38
2.1.1 Centrifugal Compressors Stability.....	48

2.1.2	Axial Compressors Stability	50
2.2	Background.....	52
2.2.1	Early Developments	52
2.2.2	Hysteresis Effect.....	55
2.2.3	The Rotating Stall Cells.....	58
2.2.4	Surge or Rotating Stall?.....	59
2.2.5	Stall Inception.....	63
2.3	Stall and Surge in Centrifugal Compressors.....	64
2.3.1	Steady Stall	65
2.3.2	Dynamic Stall (Rotating Stall).....	71
2.3.3	Stage Stall and Surge	79
2.4	Recent Developments	84
2.4.1	Current Methodology	84
2.4.2	Future Perspective of the Research: The High-Speed Compressors.....	89
3	Experimental Activity - Part I.....	91
3.1	Introduction	91
3.2	Literature Review	94
3.3	Test Facility	97
3.3.1	Gear Train System	99
3.3.2	Compression Piping System.....	104
3.3.3	Measurement Sensor System.....	108
3.3.4	Control and Acquisition System.....	109
3.4	Methodology.....	111
3.4.1	Compressor Steady State Performance Maps	111
3.4.2	Compressor Dynamic Test and Surge Inception	112
3.5	Test Results and Discussion	114
3.5.1	Cursory Analysis and Test Conditions	114
3.5.2	Steady-State Behavior	115
3.5.3	Dynamic Behavior.....	119
3.6	Conclusions	125
4	Experimental Activity - Part II	129
4.1	Introduction	130
4.2	Literature Review	131
4.3	Cyclostationary Analysis.....	134
4.4	Test rig.....	136
4.5	Methodology and Data Acquisition.....	140
4.6	Uncertainty	141

4.7	Test Results and Discussion	141
4.7.1	Frequency Analysis	141
4.7.2	Cyclostationary Analysis	144
4.8	Conclusions	150
5	Dynamic Modeling: Thermodynamics	153
5.1	Introduction	153
5.1.1	System Modeling	154
5.2	Bond Graph Approach	154
5.3	Literature Review	157
5.4	Physical Model and System Components	159
5.4.1	The Valve Element	161
5.4.2	The Duct Element	161
5.4.3	The Plenum Element	162
5.4.4	The Compression Stage Element	163
5.5	Test Case Application	167
5.6	Validation and Results	170
5.7	Conclusions	173
6	Dynamic Modeling: Thermodynamics and Axial Forces	175
6.1	Introduction	176
6.2	Literature Review	177
6.3	Improvement of the Thermodynamics of the Model	180
6.3.1	General Improvements	180
6.3.2	The Valve Element	180
6.3.3	The Duct and the Plenum Elements	181
6.3.4	The Compression Stage Element	181
6.3.4.1	Single stage maps predictions	185
6.4	Axial Force Calculation	188
6.4.1	Aerodynamic Thrust	188
6.4.2	Mechanical Thrust	196
6.5	Test Case Application: Two-stage Centrifugal Compressor (SwRI)	197
6.5.1	The Choice of the Test Case	198
6.5.2	The test Rig and the Layout of the Model	198
6.6	Validation and Results	202
6.6.1	Deep Surge	208
6.6.2	Sensitivity Analysis	209
6.7	Conclusions	213
7	Final Remarks and Recommendations	215

7.1	Summary of the Results.....	215
7.2	Future Directions	220
	List of Symbols.....	223
	Bibliography.....	229
	Acknowledgments.....	239

List of Figures

I Rationale

Fig. I.1 - Typical compressor maps I

1 Compressors: Background

Fig. 1.1 - Three-casing centrifugal compressor, built by the Brown Boveri & Cie in 1906 (Lüdtke, 2004) which operated for one of the newly developed first gas turbine 14

Fig. 1.2 - Axial compressors: (a) sketch of the pressure, velocity and temperature variation along the stages (Boyce, 2003); (b) axial rotor of a high pressure ratio gas turbine (Boyce, 2003)..... 16

Fig. 1.3 - Centrifugal compressors: a) sketch of the pressure, velocity and temperature variation along a single stage (Boyce, 2003); (b) impeller with inducer and backward leaning blades (Lüdtke, 2004) 17

Fig. 1.4 - Generic control volume representing a turbomachine (Dixon & Hall, 2013) 19

Fig. 1.5 - Adiabatic compression process in a enthalpy-entropy diagram (Dixon & Hall, 2013) 23

Fig. 1.6 - Compression process by small stages (Dixon & Hall, 2013) 25

Fig. 1.7 - Performance map of a multistage axial compressor (Dixon & Hall, 2013) 29

Fig. 1.8 - Continuous flow and displacement compressor operation ranges (Brown & Lewis, 1986) 30

Fig. 1.9 - Typical compressor maps of a high speed compressor (Farokhi, 2014). In low-pressure compressor the acceleration path and the deceleration path are inverted compared to high pressure compressor's 33

2 Rotating Stall and Surge

Fig. 2.1 - Typical unstalled and stalled curves (taken from (Day, 2016))..... 39

Fig. 2.2 - Types of rotating stall cells: part-span and full-span cells (taken from (Cumpsty, 1989))..... 40

Fig. 2.3 - Typical formation of rotating stall cells along the stalled and unstalled characteristic curve of a compressor (taken from (El-Sayed, 2008)) 40

Fig. 2.4 - Sequence of stall in a single blade passage (taken from (Lennemann & Howard, 1969))..... 42

Fig. 2.5 - Velocity distribution at the stall onset (taken from (Watanabe, et al., 1994))..... 43

Fig. 2.6 - Typical operating point path during classic surge (taken from (Cumpsty, 1989)) 45

Fig. 2.7 - Mild surge oscillations: adimensional axial velocity, Mach number and isentropic head coefficient (taken from (Fink, et al., 1992)) 46

Fig. 2.8 - Classic and deep surge oscillations at compressor inlet and inside the plenum (taken from (Greitzer, 1976b))..... 46

Fig. 2.9 - Development of deep surge reversal flow in an engine compressor (taken from (Mazzawy, 1980)) 47

Fig. 2.10 - The stability of a centrifugal compressor components, based on the stability parameter values SP_i .(source: (Dean, 1974); taken from (Cumpsty, 1989)) 49

Fig. 2.11 - Stage stall static pressure coefficient as a function of the ratio between the diffusion length and the exit passage width: (a) low-speed compressors; (b) high-speed compressors (source: (Koch, 1981), taken from (Farokhi, 2014)) 51

Fig. 2.12 - Lateral view draw of a part-span cell in an axial flow compressor (source: (Foley, 1951), taken from (Day, 2016))..... 53

Fig. 2.13 - Effect of speed acceleration on stall margin (Huppert & Benser, 1953)..... 54

Fig. 2.14 - Rotating stall: theoretical stall inception in a single blade (left); and in more blade channels (right) (Cumpsty, 1989) 55

Fig. 2.15 - Graphic scheme of stalled and unstalled sector performance (taken from (Day, 2016))..... 56

Fig. 2.16 - Effect of the design flow coefficient on the rotating stall hystereis (source: (Day, et al., 1978), taken from (Cumpsty, 1989)) 57

Fig. 2.17 - Skecth of the flow in a rotating stalled cell (source: (Day & Cumpsty, 1978), taken from (Day, 2016)) 58

Fig. 2.18 - Stalled flow velocity and flow angle measurements before and after the rotor. The data are referred to the mid-span location at a flow coefficient of 0.33 (the compressor designed flow coefficient was 0.55) (source: (Day & Cumpsty, 1978); taken from (Cumpsty, 1989))..... 59

Fig. 2.19 - Effct of greitzer parameter B on the unstable behavior of the compressor after the characteristic curve peak: (a) rotating stall; (b) surge; (source (Greitzer, 1976); taken from (Farokhi, 2014))..... 60

Fig. 2.20 - Typical compressor characteristic curve in the stable and the unstable field (taken from (Day, 2016)) 62

Fig. 2.21 - Effect of stage matching on the instability onset of a two-stage compressor: second stage mismatched with an extra stagger (left); second stage perfectly matched (right); (source: (Longley, 1988); taken from (Cumpsty, 1989))	62
Fig. 2.22 - Type of stall inception phenomena: modal oscillations (left); spikes (right); (taken from (Day, 1993))	64
Fig. 2.23 - Turbocharger compressor characteristic curves (pressure rise against reference mass flow rate): local inducer and diffuser stall (taken from (Japikse, 1981))	66
Fig. 2.24 - Maps (left) and velocity profiles at the impeller inlet of a centrifugal compressor (right) (source: (Kammer & Rautenberg, 1986); taken from (Japikse, 1996)).....	66
Fig. 2.25 - Experimental data centrifugal compressor: (a) compressor maps; (b) laser velocimeter data before and after splitter blade ($Mu=0.70$); (source: (Girsberger & Rohne, 1990); taken from (Japikse, 1996))	67
Fig. 2.26 - Experimental data of a centrifugal pump/compressor together with indicators which illustrate the orientation of the tufts, located at the inlet (left) and at the outlet (right) (Barrand, et al., 1984).....	68
Fig. 2.27 – Separation, or stalled zone, at the impeller exit, i.e. the jet/wake phenomenon: (a) a 3-D sketch (source: (Dean & Young, 1977)); taken from (Japikse, 1981); (b) Velocity measurements of a centrifugal impeller with no backsweep, at $N=14,000$ rpm (source: (Eckardt, 1976); taken from (Japikse, 1981))	69
Fig. 2.28 - The reverse flow at the impeller outlet: (a) velocities streamlines; (b) pressure and flow angle variation along the blade channel width (taken from (Japikse, 1981))	70
Fig. 2.29 - Performance characteristics and stability limit with different diffuser geometry (source: (Abdelhamid & Bertrand, 1980); taken from (Japikse, 1981)).....	72
Fig. 2.30 - Pressure field of two adjacent blade channels during a rotating stall disturbance (taken from (Chen, et al., 1994))	74
Fig. 2.31 - Pressure values along the middle stramline of the channel (left channel of Fig. 2.30) at time steps n.8 (nominal conditions, left diagram), n. 20 (rotating stall high-pressure zone, middel diagram) and n. 24 (rotating stall low-pressure zone, right diagram); (taken from (Chen, et al., 1994)).....	75
Fig. 2.32 - Experimental tests of a centrifugal compressor with different system configurations: (a) Configuration A; (b) rotating stall observations referred to Configuration A; (c) Configuration B and C; (d) rotating stall observations referred to Configuration B; (e) rotating stall observations referred to Configuration C (source: (Frigne & Van Den Braembussche, 1984); taken from (Japikse, 1996))	79
Fig. 2.33 - Deep surge oscillations: adimensional axial velocity, Mach number and isentropic head coefficient (taken from (Fink, et al., 1992))	81
Fig. 2.34 - Measurement of surge phenomenon in a centrifugal compressor: (a) location of the sensors (displacements are expressed in mm); (b) compressor static head coefficients during deep surge with $Mu\approx 0.92$ (taken from (Fink, et al., 1992))	81

Fig. 2.35 - Surge at different valve setting (Arnulfi, et al., 1999): (a) operating point; (b) flow coefficient (left) and pressure coefficient (right).....	82
Fig. 2.36 - Classic and deep surge. Comparison between experimental data and model results (Arnulfi, et al., 1999).....	83
Fig. 2.37 - (a) point A (Design point), B (near stall). In blu, low pressure area, in green high pressure area; (b) stall condition; (taken from (Zaki, 2009)).....	85
Fig. 2.38 - Formation of the Tramped Shaped Vortex: (a) leading edge separation circle; (b) vortex tube forms, uppers and moves circumferentially along casing; (c) lower end of tube moves downstream along suction surface; (taken from (Pullan, et al., 2015))	86
Fig. 2.39 - CFD Analysis of surge inception in a centrifugal compressor: (a) instantaneous Mach numbers at various time-steps before surge; (b) Absolute velocity vectors at time-step f (referred to Fig. 2.39 (a)); (taken from (Trébinjac, et al., 2015)).....	87
Fig. 2.40 - Radial velocity normalized with respect to impeller tip tangential speed: (a) before the flow destabilizes onset (radial), (b) in rotating stall conditions (taken from (Dazin, et al., 2008))	89

3 Experimental Activity - Part I

Fig. 3.1 - Tested multistage compressor: (a) the rotor with the six axial stages and the centrifugal impeller (without casing); (b) the compressor installed into the facility....	98
Fig. 3.2 - Designed aluminum frame: (a) 3D representation; (b) installation	98
Fig. 3.3 - Modification of the original epicyclic gearbox of the Allison 250-C18 turboshaft engine: the original component (on the left) was scanned and modified by welding it with a new flange (on the right).....	99
Fig. 3.4 - Assembly of the epicyclic gearbox into the test rig.....	100
Fig. 3.5 - Solar shaft axial blocker: 3D and 2D lateral view draws of the component (on the top); the realized component (on the bottom).....	101
Fig. 3.6 - 3D draw of the transmission line assembly with the new designed components	102
Fig. 3.7 - 3D sketch of the power transmission line components	102
Fig. 3.8 - Double-gear mini-shaft and its internal shaft (the threads are not shown): 3D sketch (left); and installation (right)	103
Fig. 3.9 - Schematic draw of the lubricating system	103
Fig. 3.10 - 3D sketch (colored) of the piping system: in violet the inlet duct, light brown the compressor, grey the outlet duct of Layout #1; in blue the added part belonging to Layout #2	104

Fig. 3.11 - Flow conveyor: 3D project (on the left); installation in the piping system (on the right).....	105
Fig. 3.12 - Orifice plate (according to the standards UNI 1570-1596 and UNI EN ISO 5167): 3D project (on the left) and installation in the piping system (on the right) ...	106
Fig. 3.13 - 2D sketch of the piping system: (a) Layout #1; (b) Layout #2.....	108
Fig. 3.14 - Diagram of the control and acquisition system	110
Fig. 3.15 - Steady state performance map: pressure ratio	116
Fig. 3.16 - Steady state performance maps: isentropic efficiency.....	117
Fig. 3.17 - Steady state performance maps: static pressure ratio at stage five (bleed valve position)	117
Fig. 3.18 - Dynamic Test @ $v = 10,000$ rpm.....	120
Fig. 3.19 - Dynamic test @ $v = 10,000$ rpm. Typical surge oscillations encountered on p_2 , m_1 , m_3 and $P_{mec,norm}$	120
Fig. 3.20 - Dynamic Test @ $v = 10,000$ rpm. Characteristic curve towards to surge and recover from surge	121
Fig. 3.21 - Dynamic Test @ $v = 15,000$ rpm. Surge pulsations of p_2 , m_1 , m_3 and $P_{mec,norm}$	122
Fig. 3.22 - Dynamic Test @ $v = 10,000$ rpm. Fast response transducers signals at compressor a few instants before surge	123
Fig. 3.23 - Dynamic Test @ $v = 10,000$ rpm. Stall analysis at compressor inlet. Frequency domain analysis.....	124
Fig. 3.24 - Dynamic Test @ $v = 10,000$ rpm. Stall analysis at compressor inlet. Complete development of rotating perturbations.....	125

4 Experimental Activity - Part II

Fig. 4.1 - The tested compressor	137
Fig. 4.2 - Piping system configuration. Layout #1 and Layout #2 with the (a) thermodynamic and (b) vibro-acoustic sensors	138
Fig. 4.3 - Installation of the accelerometer on the axial part (a) and the radial part (b) of the compressor	139
Fig. 4.4 - Layout #1 steady-state test microphone P_f spectrum: valve completely opened (a), valve completely closed (b).....	142
Fig. 4.5 - Layout #1 steady-state test; comparison of $g_{3a,x}$ accelerometer signal	143

Fig. 4.6 - Layout #1 steady-state test microphone P_f time signal (left) with its MIP (right):
 (a) valve completely opened, (b) valve completely closed..... 144

Fig. 4.7 - Layout #1 transient test: cyclic power of microphone P_f 145

Fig. 4.8 - Layout #1 steady-state test CMS of the $g_{3a,x}$ accelerometer: (a) valve completely open, (b) valve completely closed 147

Fig. 4.9 - Layout #1 transient test: cyclic power of accelerometer $g_{3a,x}$ 148

Fig. 4.10 - Layout #2 transient test: cyclic power of accelerometer $g_{3a,x}$ 150

5 Dynamic Modeling: Thermodynamics

Fig. 5.1 - Scheme and bond graph of the basic elements of the model..... 160

Fig. 5.2 - Steady-state measured and interpolated curve of performance maps: (a) pressure ratio; (b) isentropic efficiency..... 164

Fig. 5.3 - Parametric procedure: (a) the modelling of the performance curves; (b) the trend of characteristic parameters of the performance curves 165

Fig. 5.4 - Diagram of the system: (a) graphic representation; (b) bond graph..... 168

Fig. 5.5 - Steady-state interpolated curves of performance maps: (a) pressure ratio; (b) isentropic efficiency..... 169

Fig. 5.6 - Parametric procedure: the trend of the characteristic parameters of performance curves..... 170

Fig. 5.7 - The model representation in the Simulink main screen; from left to right: inlet valve, inlet duct, compressor, plenum, outlet duct and outlet valve (the terms and names used in Simulink for certain parameters, or elements, may not be the same as those used in this chapter)..... 170

Fig. 5.8 - Comparison between experimental and model results: (a) dynamic characteristic curve; (b) pressure fluctuation in the plenum. 171

Fig. 5.9 - Mass flow rate at the compressor inlet, m_1 , and at the plenum outlet, m_2 172

Fig. 5.10 - Simulation results: plenum temperature 173

6 Dynamic Modeling: Thermodynamics and Axial Forces

Fig. 6.1 - Sketch of the “single stage” module and nomenclature of the inlet and outlet sections; this nomenclature is also valid for reverse flow conditions (case 3)..... 182

Fig. 6.2 - Compressor curves in surge conditions: (a) Moore and Greitzer Cubic Law; (b) sudden pressure rise/drop..... 183

Fig. 6.3 - Sketch of the impellers of a multistage compressor and the physical quantities (pressure and temperature) in direct flow	185
Fig. 6.4 - Sketch of the impellers of a multistage compressor and the physical quantities (pressure and temperature) in reverse flow	187
Fig. 6.5 - Sketch of the impeller velocity at the suction and at the discharge in the meridian plane (direct flow).....	189
Fig. 6.6 - Sketch of the impeller velocity triangles at the inlet (section 1) and at the outlet (section 2) in the front plane (direct flow)	190
Fig. 6.7 - Sketch of the impeller velocity at the suction (left) and at the discharge (right) in the meridian plane (reverse flow)	192
Fig. 6.8 - Sketch of the impeller velocity triangles at the inlet (section 2) and at the outlet (section 1) in the front plane (direct flow)	193
Fig. 6.9 - Force contributions in a single impeller	194
Fig. 6.10 - Qualitative illustration of the discretization points used to calculate the pressure along the gaps	195
Fig. 6.11 - Example of calculation of the area at each discretization point (shroud cavity)	195
Fig. 6.12 - Bearing system: (a) diagram; (b) bond graph	197
Fig. 6.13 - P&ID of the test rig.....	199
Fig. 6.14 - Layout of the system: (a) graphic representation; (b) bond graph.....	200
Fig. 6.15 - Steady-state interpolated curve of performance maps: pressure ratio	200
Fig. 6.16 - Parametric procedure: the trend of characteristic parameters of the performance curves	201
Fig. 6.17 - Simulink diagram of the model applied to the SwRI test case	201
Fig. 6.18 - Model results: (a) operating point path (comparison with steady state experimental curve); (b) discharge pressure of the impellers.....	204
Fig. 6.19 - Model results of the net axial force acting on the bearing at 13,000 rpm	205
Fig. 6.20 - Validation of the model: comparison of the axial force results at 13,000 rpm in surge and non surge conditions.....	206
Fig. 6.21 - Validation of the model: peak-to-peak forces (a); surge frequency (b).....	208
Fig. 6.22 - Deep surge simulation @13,000 rpm: compressor characteristic curve (a) and net axial force $F_{ax,B}$ (b)	210
Fig. 6.23 - Influence of the compressor downstream volume on the axial force	211

Fig. 6.24 - Influence of the bearing stiffness on the axial force.....	212
Fig. 6.25 - Influence of the rotor mass on the axial forces.....	212

List of Tables

3 Experimental Activity - Part I

Tab. 3.1 - Results of the CFD simulation: the final geometry of the conveyor.....	105
Tab. 3.2 - Values of non-dimensional parameter B referred to Layout #2.....	107
Tab. 3.3 - Pipeline dimensions and volumes	107
Tab. 3.4 - Instrumentation characteristics.....	109
Tab. 3.5 - Ambient conditions during tests.....	115

4 Experimental Activity - Part II

Tab. 4.1 - Number of stator and rotor blades of each stage.....	139
Tab. 4.2 - Type of tests carried out.....	141

5 Dynamic Modeling: Thermodynamics

Tab. 5.1 - Bond graph basic elements.....	156
Tab. 5.2 - Causality of energy storage elements.....	157

6 Dynamic Modeling: Thermodynamics and Axial Forces

Tab. 6.1 - Comparison between experimental and model results: pressure ratio at surge conditions.....	204
Tab. 6.2 - Simulation results at surge condition	205
Tab. 6.3 - Comparison between simulations results and test data	205

I Rationale

Nowadays, axial and centrifugal compressors are the main components of many systems adopted in industry processes, military and civil aeronautical sector, but also in naval aviation. Unfortunately, despite the numerous advantage that they offer, the performance of compressors is affected by several parameters which can also affect their stability.

The compressor operating range is limited for lower flow rates by the inception of instability. For this reason, the stability range of this type of turbomachinery is one of the main concerns in (i) the design of the systems which they are part of and (ii) the selection of compressors in specific applications. The instability usually occurs when the operating point of the compressor achieves the surge line: which is the line that separates the stable from the unstable performance field as defined by the designers (see Fig. I.1) - in this figure also an ideal working line with a typical operating point is also illustrated). Beyond the surge line, the orderly flow can break down and settle into rotating stall or into surge, consequently affecting the compression system operation.

Despite the great advancements made since the 1950s, the understanding of these types of disturbances is not yet fully complete, and thus the research today aims to achieve a better comprehension of their inception process and development.

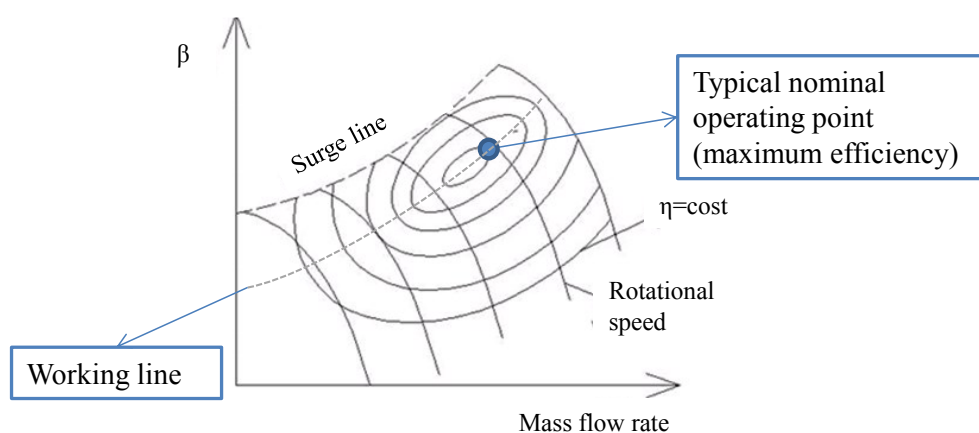


Fig. I.1 - Typical compressor maps

Over the past 75 years, many researchers have put a great deal of effort and dedication into improving the methods of predicting the fluid-dynamic phenomena accompanying these instabilities; by means of bettering their understanding of rotating stall and surge.

As described in depth by Day in his recent paper on this topic (Day, 2016), the research has led to an impressive list of achievements since the World War II. This has resulted in learning about the generation, propagation and structure of the stall cells, the identification of the stalled curve of the compressors, the discovery of the hysteresis effect related to the stalled-to-unstalled transitions, and the explanation of the difference between stall and surge and their potential precursors.

This activity was accompanied by the development of many models for the prediction of a compressor's behavior during stall and surge. Thanks to this progress, different types of systems for detection, avoidance and control of surge were developed for several types of compressor applications. Other powerful modern tools supporting the research, such as the computational fluid dynamics (CFD), are now becoming popular for trying to explain the influence of the flow field, approaching and leaving the blades, on inception of rotating stall and then surge. However, any theoretical or numerical analysis needs sufficient experimental data to be evaluated, otherwise the numerical results cannot be considered reliable. For such purpose, new state-of-the-art test rigs and advanced instrumentation will be fundamental.

As outlined above, it clearly appears that the unstable behavior of compressors is, still, an attractive topic in the field of turbomachines. Many researchers, aerodynamicists, and authorized personnel involved in various industries are de facto trying to overcome this problem.

Unfortunately, great part of the existing literature has a strongly descriptive nature and fails to deliver a contribution significant enough to improve the stability of new compressors, or better yet avoid rotating stall and surge altogether. Modern knowledge and instrumentation have made it easier to interpret and explain a stall/surge event after its occurrence; however, it is still difficult to exactly predict, in a rigorous way, how a new designed compressor will stall or surge (and their inception mechanisms). Thus, the currently existing research only partially fulfill the true objective.

There are other important consequences, beyond the fluid-dynamics, that instabilities cause on the compressor system. The structure of the compressor unit and its components, as well as the piping system, can be subject to unexpected stresses during rotating stall and surge, which requires frequent inspections and maintenance, that sometimes reveals to be worthless.

As suggested by Day, all these topics need to be further investigated, starting from the advancements achieved over the years, with different approaches, which focus on real compressors, with real problems, such as stage matching, large tip clearance, eccentricity and service life degradation (also taking into account the mechanical system's components, not only the aerodynamic ones). In particular, provided that the fluid-dynamic models are highly efficient in evaluating the compressor's dynamic behavior, they need to count on a great amount of reliable experimental data to be consistent: thus the future direction of the research will have to be centered on the experiments, especially on high speed compressors.

Following this indication, this Ph.D. project is perfectly centered in the current context of the research on these topics. In fact, it aims to give a functional contribution to the knowledge of rotating stall and surge, by means of an extensive experimental activity, also using non-intrusive sensors, and modeling (only the surge phenomenon) of the thermodynamic, and mechanical effects of such instabilities.

The justification of the themes and methodology approach is given by will of the Author to give an original support to the researchers and the industry sector involved in this subject matter.

II Aim, Originality and Limitations

This work consists of the combination of experimental analyses and modeling of compressors installed in a given piping systems and operating at different working conditions, obviously focusing on the two main instabilities occurring in such turbomachines, i.e. stall and surge.

A great part of the Thesis is concentrated on the experimental activity and its results. Some of them were obtained at the Engineering Department of the University of Ferrara, whereas others were taken from the test case facility of the Southwest Research Institute laboratories.

The modeling activity plays another fundamental role in the project. It is strongly focused on surge - which is recognized as the most catastrophic event during the compressor operation - and its thermodynamics, together with the mechanical consequences on the thrust bearing.

The aim is to contribute to the existing literature with interesting data regarding stall and surge, presenting results of wide interest to investigators attracted by complex phenomena involved in compressor instability and its consequence on the mechanical components of the compressor system. The present study is thus carried out in order to give a better understanding of what occurs during these disturbances and how they can be detected. Moreover, it aims to offer a significant and reliable preliminary method for determining if a generic transient event generates the compressor surge, and thus a risk of damage to mechanical structures such as the close clearance components.

In detail, the targets of the research are:

- The set-up of a reliable experimental test rig, suitable for studying the transient behavior of the compressor;
- The detection of stall and surge characteristics through the use of specific sensors and the design of an embedded measurement system;
- The measurement of the force fluctuations on the thrust bearing during surge;

- The development of a model for the simulation of the pressure, temperature and mass flow rate oscillations during surge and the evaluation of the net axial thrust acting on the bearing.

The originality of the project is mainly due to:

- the novel methodology and type of experimental data acquired;
- the innovative data analysis method adopted for non-intrusive measurements;
- the original surge modeling approach and its validation;
- the enhanced analysis on the mechanical parameter characteristics for evaluating the axial force on the thrust bearing during surge.

The limitations of this work are given by the following issues:

- The low maximum rotational speed achievable by the test rig of the Engineering Department, lower than the nominal speed of the tested compressor - mainly due to the maximum power limit of the electric motor;
- The assumptions used in the model, in particular the adiabatic features of the system;
- The incapability of the model to simulate stall, as this implementation would require much effort in order to maintain a reasonable computational cost;
- The lack of experimental data regarding force amplitudes and frequency during deep surge. Therefore, the deep surge results given by the model, despite being qualitatively reliable, are not quantitatively validated.

III Contributions by Others

This work is the result of a partnership between the University of Ferrara, the University of Parma, the Southwest Research Institute and the Solar Turbine Inc. Therefore, other persons were involved in this study and their contribution is outlined below.

My advisor, Prof. Michele Pinelli, Ph.D., explained to me the relevance of the research and the potential final aim. Since the beginning of the Ph.D. program, he has given me many precious suggestions and general guidelines by actively proposing strategies to overcome the problems faced in the experimental activity and the modeling.

Prof. Pier Ruggero Spina, Ph.D., supported the research by verifying and revising the methodologies adopted, especially in regard to the test rig performance.

The main contribution was given by Prof. Mirko Morini, Ph.D., (University of Parma, Italy), who has supported my work during all its development stages. He has inspired the methodology of the experimental dynamic tests and shared the basic code, successively improved, for the steady-state thermodynamic data analysis. Moreover, he provided me the impetus to use the bond graph modeling approach to simulate the compressor surge. He also put much effort into helping me on the revision and interpretation of the experimental and model results.

Dr. Rainer Kurz (Manager, System analysis, at Solar Turbines Incorporated, San Diego, CA, USA) and Dr. Klaus Brun (Program Director of Machinery Program at Southwest Research Intitute, Houston, TX, USA), inspired the use of the developed surge model to evaluate the axial net thrust acting on the bearings, also providing precious hints and useful experimental data to validate the additional simulator tool.

Dr. Gianluca D'Elia, (assistant professor of the Mechanics of Machine and Vibration Research Group of the University of Ferrara), analyzed the vibro-acoustic measurements by developing the code to use the cyclostationary analysis.

Regarding the experimental activity developed at the Engineering Department, a consistent contribution, during the first stages of the project, was given by Mr. Tommaso Mazzini, M.Sc., who gave significant assistance in the setting up of the test rig.

The contribution of these persons was fundamental in order to begin, develop and conclude my Ph.D. program.

IV List of Papers

- 1) Munari, E., Morini, M., Pinelli, M., Spina, P.R., Suman, A. Experimental Investigation of Stall and Surge in a Multistage Compressor. *Journal of Engineering for Gas Turbines and Power*, (2017) Vol. 139(2): 022605
 - Presented at *ASME TurboExpo 2016*, Turbine Technical conference and Exposition, GT2016-57168, June 13-17, Seoul, South Korea.
- 2) Munari, E., Morini, M., Pinelli, M., Spina, P.R. Experimental Investigation and Modeling of Surge in a Multistage Compressor. In press, *Energy Procedia*
 - Presented at the *8th International Conference on Applied Energy, ICAE 2016*, October 8-11, Beijing, China
- 3) D’Elia, G., Morini, M., Mucchi, E., Munari, E., Pinelli, M., Spina, P.R. Experimental Investigation of Vibrational and Acoustic Phenomena for Detecting Stall and Surge of a Multistage Compressor. Submitted (accepted) to *ASME TurboExpo 2017*, GT2017-64894.
- 4) Brun, K., Simons, S., Kurz, R., Pinelli, M., Morini, M., Munari, E. Measurement and Prediction of Centrifugal Compressor Axial Forces During Surge – Part 1: Test and Force Measurement Results. Submitted (accepted with Journal quality) to *ASME TurboExpo 2017*, GT2017-63070.
- 5) Munari, E., Morini, M., Pinelli, M., Brun, K., Simons, S., Kurz, R. Measurement and Prediction of Centrifugal Compressor Axial Forces During Surge – Part 2: Dynamic Surge Model. Submitted (accepted with Journal quality) to *ASME TurboExpo 2017*, GT2017-63070.
- 6) Brun, K., Simons, S., Kurz, R., Morini, M., Pinelli, M., Munari, E., Broerman, E. Shaft Forces During Centrifugal Compressor Surge. Submitted to *46th Turbomachinery and 33th Pump Symposia*, Houston, TX.

Other papers:

- 7) Barbieri, E., Morini, M., Munari, E., Pinelli, M., Spina, P.R., Vecci, R. Concurrent Optimization of Size and Switch-on Priority of a Multi-Source Energy System for a Commercial Building Application. *Energy Procedia*, (2015) Vol 81, pp 45-54.
 - Presented at the 69th Conference of the Italian Thermal Machines Engineering Association, ATI 2014, September 10-12, Milano, Italy.

1 Compressors: Background

This introduction offers the basics of axial and centrifugal compressors principles of operations and typical applications in order to highlight the importance of these machines (and their performance), which are frequently used in the modern industry. Subsequently, an overview of the instability and related consequences in specific applications is given: this preliminary part aims to make the reader aware of the relevance of compressors and their stability when operating.

1.1 History of Centrifugal and Axial Flow Compressors

A compressor is a mechanical device which has the function of raising the pressure of a certain mass flow of gas. There are different type of compressors: reciprocating, rotary centrifugal, and axial. The first two types, increment the gas pressure by decreasing the volume which contains it, but they will not be treated in this work. Here, only the continuous flow types of compressors will be treated, i.e. axial and centrifugal (or radial) compressors.

As reported in (Lüdtke, 2004) the first prototype of a single stage centrifugal compressor was invented around the end of the 19th century by Professor Auguste Rateau, and successively set up and employed as industrial unit in 1903. Two years after, he had assembled the first five stage single-shaft centrifugal compressor for his company. In the same period, a Swiss company, the “Brown Boveri & Cie” (commonly called BBC) used a Rateau three-casing experimental centrifugal compressor, which was driven by the World’s first operable gas turbine, located in France and built by Armengaud and Lemale. A few years later, BBC obtained the Rateau patents and developed its first multi stage compressor, similar to the Rateau three-casing centrifugal compressor, for gas turbine applications (See Fig. 1.1)

Later, the development of centrifugal compressors continued, especially during and after the “Second World War”, and the use of these machines branched out, not only in all

fluid processing industries, but also the aviation, even if their disadvantageous characteristics had become clear (Campbell & Talbert, 1945) and would lead to favor the use of axial compressors in the next age of aircraft engine propulsion. As reported in (Dixon & Hall, 2013), in the mid-1960s, technological advances were made in order to satisfy the requirement of innovative military helicopters driven by small gas turbines.

These advances also showed and encouraged the potential expansion of the field of applications of centrifugal compressors, that started to be designed also for diesel engine turbochargers, chemical plant processes, factory workshop air supplies, large-scale air conditioning and plant, and refrigerating plants with compression-type heat pumps.

The progress of axial flow compressors underwent more difficulties than centrifugal compressors, especially during the first steps of its development. As described by Stoney (Stoney, s.d.), in 1884 Sir Charles Parson obtained a patent for the use of a reversed turbine as an axial compressor and built almost two thousand of these machines, which were then successfully used, at that time, for blast furnace work (in low pressure applications).

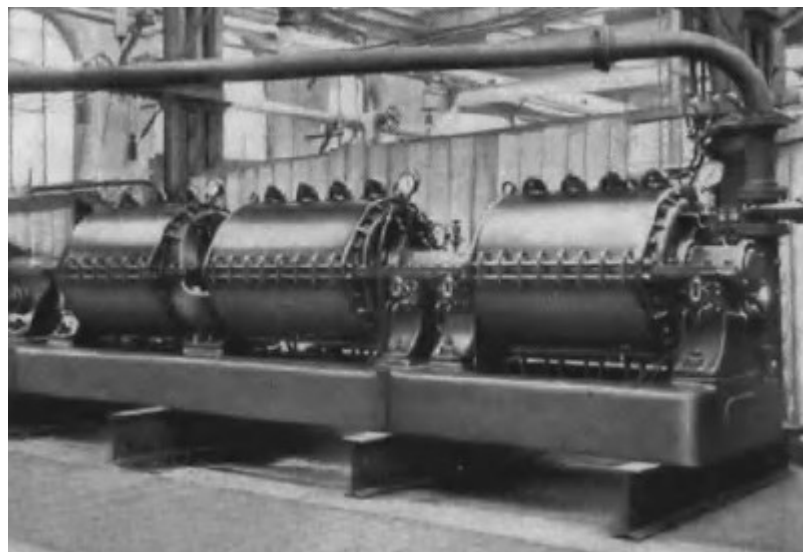


Fig. 1.1 - Three-casing centrifugal compressor, built by the Brown Boveri & Cie in 1906 (Lüdtke, 2004) which operated for one of the newly developed first gas turbine

However, these compressors were characterized by an efficiency of 55%, which is nowadays attributable to rotating stall phenomena. Later, he undertook the building of a two-stage high pressure axial flow compressor, but he encountered many difficulties, possibly due to compressor surge, and abandoned the project early. Rateau also, built a

multistage axial compressor a few years later. These first trial machines did not offer great performance due to their low efficiency; and thus the use and development of axial compressors was abandoned, until advanced investigations, started by A.A. Griffith on the airfoil aerodynamics, revealed the potential advantages of these turbomachines in the 1920s

These studies were exploited in the 1930s by Brown Boveri & Cie, who were pioneers in using axial compressor technology for typical modern applications. The subsequent history of the axial compressor was substantially characterized by its application and development in aircraft gas turbines.

1.2 Compressor Operative Principles - The Basics

In this section the operating principles of axial and centrifugal compressors will be briefly summarized without examining the thermodynamic laws which govern their operation in detail.

A continuous flow compressor consists of one or more stages, and each stage is made of a rotor and a stator. The rotor is a row of rotating airfoils (or blades), whereas a stator is a row of stationary blades. Of course, in axial compressors the flow enters and exits axially from each stage, whereas in centrifugal compressors it enters axially and exits radially.

1.2.1 Axial Compressors

An axial compressor operates by compressing the working fluid by accelerating the fluid and then decelerating it through diffusing channels to increase the potential energy, i.e. the pressure of the fluid. This process happens at each stage of the compressor: specifically, the acceleration occurs in the rotor while the diffusion in the stator.

Typically, these compressors are provided with a stationary row at the inlet, which allows the flow to approach the first stage rotor with the correct incidence angle. Moreover, they are often equipped with an additional diffuser at the compressor exit; which allows to further increase the pressure and regulate the flow. Compared to centrifugal compressors, the aerodynamic characteristics of an axial compressor stage

allow a smaller pressure ratio (11:1 – 1.4:1, (Boyce, 2003)) and operating region (surge to choke margin), but with very higher efficiency.

For this reason, the use of multistage axial compressors is usually desired, as they can provide high pressure ratios, depending on the stage number. A general indication followed by designers is that each stage should supply the same energy rise (Boyce, 2003).

Fig. 1.2 (a) shows the qualitative trend of the pressure, velocity, and temperature of the working fluid through a multistage axial compressor. Noticeably, the energy is inputted only by the rotor stages; which is in turn testified by the increase of the total pressure, total temperature, and velocity. Fig. 1.2 (b) shows a multistage axial gas turbine rotor (produced by Alstom). A low-pressure and a high pressure axial compressor precede a high-pressure and a low-pressure turbine - which is a typical configuration for high pressure applications.

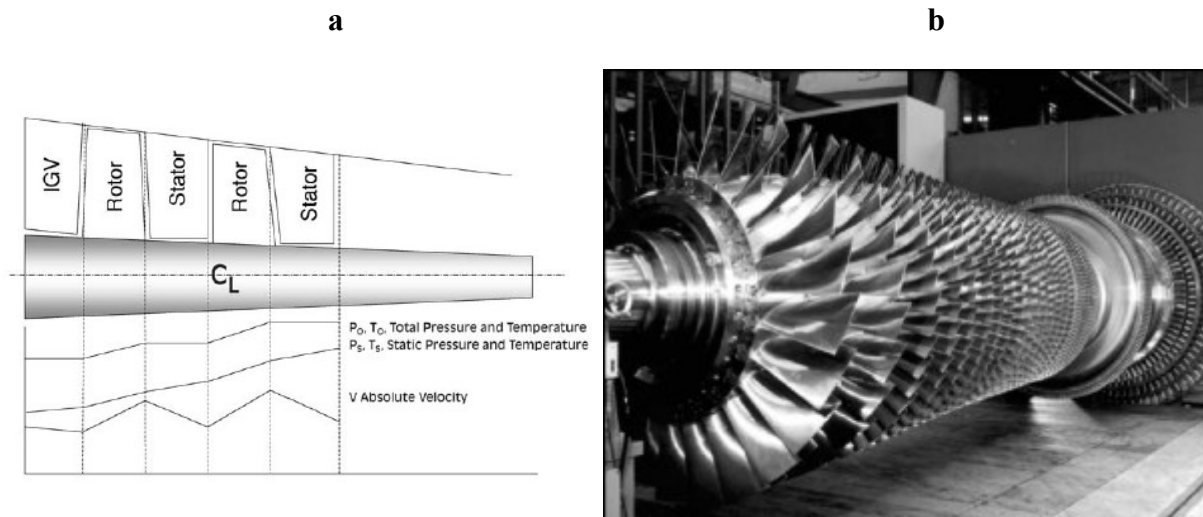


Fig. 1.2 - Axial compressors: (a) sketch of the pressure, velocity and temperature variation along the stages (Boyce, 2003); (b) axial rotor of a high pressure ratio gas turbine (Boyce, 2003).

1.2.2 Centrifugal Compressors

A centrifugal compressor stage consists of an impeller (the rotor) and a diffuser (the stator). Usually, centrifugal impellers are also equipped with an inducer - which is an integral part of the impeller, but with an aerodynamics similar to an axial flow rotor. Different type of impeller designs exists, designed and chosen depending on the application. But this classification will not be treated here: only one example of this is given in Fig. 1.3 (b) - which shows a backward leaning blades impeller.

By exiting the impeller, the flow enters into the diffuser which is usually characterized by a vaneless space and a vaned diffuser (used in high-pressure ratio compressors), before passing through a scroll, or collector. On the other hand, in the case of low-to-medium pressure ratios, the compressor stator consists of a vaneless diffuser. Similarly to axial compressors, centrifugal compressor are also usually preceded by inlet guide vanes to give a pre-whirl to the flow and to reduce the relative velocity at the inducer tip.

As shown in Fig. 1.3 (a), the fluid pressure and velocity are increased by the rotor as the fluid passes through the impeller while compressing. The diffuser then has the function of converting the kinetic energy of the flow into static pressure. The overall pressure ratio of the stage is usually equally supplied by the impeller and the diffuser.

In general, centrifugal compressors have a higher stability range than axial compressors, but they are less efficient. Their performance are more efficient at middle flow rates and high-pressure ratios.

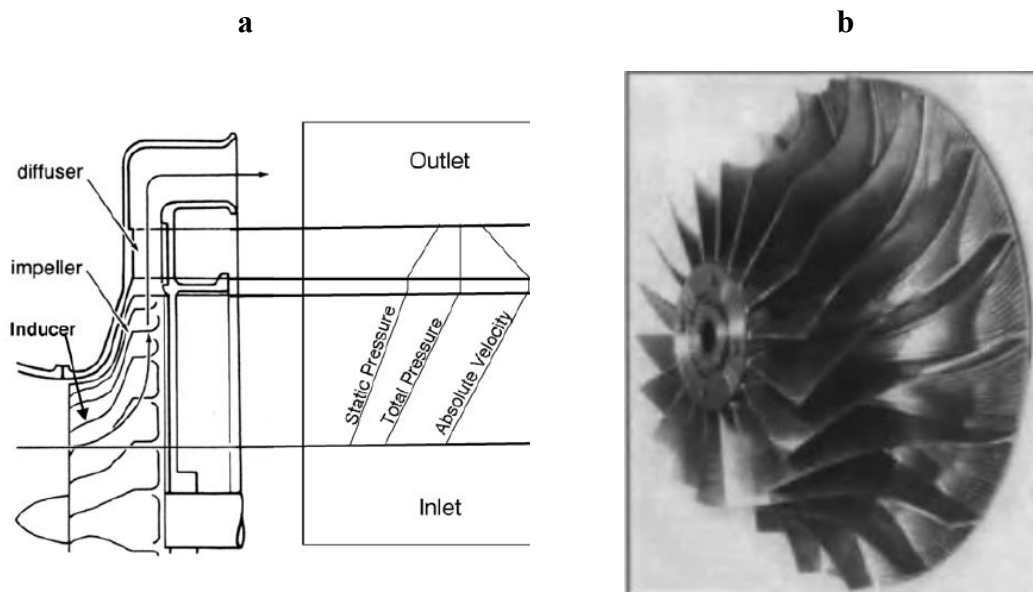


Fig. 1.3 - Centrifugal compressors: a) sketch of the pressure, velocity and temperature variation along a single stage (Boyce, 2003); (b) impeller with inducer and backward leaning blades (Lüdtke, 2004)

1.3 Compressor Performance and Thermodynamics

In this section of the Thesis, only the main thermodynamic laws of turbomachines will be reported. The aim of this paragraph is thus to only introduce basilar notions of these, to be mentioned as a reference throughout the work. Therefore, not all

thermodynamic formulations will be reported (for this purpose, many text books offer exhaustive dissertations), but only the basic ones.

1.3.1 First Law of Thermodynamics

The differential form of the first law of thermodynamics implies that, when a generic system accomplishes a determined process, in which the heat is supply and work is done (Greitzer, 2007)

$$d E_0 = d Q - d W \quad (1.1)$$

The total energy E_0 is a property (i.e. a state variable), thus its change do not depend on the path taken to achieve the change. Work, W , and heat, Q , are not properties and their quantity can vary depending on the path used to complete the change. Therefore, if a change from condition 1 to condition 2 occurs, the equation can be expressed as:

$$E_{02} - E_{01} = \int_1^2 (d Q - d W) \quad (1.2)$$

Or more in general

$$\Delta E_0 = Q - W \quad (1.3)$$

Where ΔE_0 is the change of the system total energy, Q is the heat supplied to the system, and W is the work done.

In steady-state conditions, considering a control volume (see Fig. 1.4) through which a fluid flows, with a stationary mass flow rate \dot{m} , from the control section 1 to the control section 2, it is possible to say that a transfer of energy occurs (in a compressor, this happens thanks to the rotor blade action).

By using the standard convention of sign (positive work done by the system and positive heat supply to the system), the steady flow energy equation is:

$$\dot{Q} - \dot{W}_x = \dot{m} \left[(h_2 - h_1) + \frac{1}{2} (c_2^2 - c_1^2) + g(z_2 - z_1) \right] \quad (1.4)$$

h being the specific enthalpy, $\frac{1}{2}c^2$ the specific kinetic energy, gz the specific potential energy, \dot{Q} the heat exchange rate, and \dot{W}_x the work rate. By assuming a negligible difference between z_2 and z_1 and introducing the stagnation enthalpy as:

$$h_0 = h + \frac{1}{2}c^2 \quad (1.5)$$

the steady flow equation becomes:

$$\dot{Q} - \dot{W}_x = \dot{m} (h_{02} - h_{01}) \quad (1.6)$$

In the case of a turbomachine, it is usually assumed that the transformation is adiabatic, so the heat exchange rate is zero. If the generic control volume represents a compressor (it absorbs work), the equation becomes:

$$W_C = -\dot{W}_x = \dot{m} (h_{02} - h_{01}) \quad (1.7)$$

On the other hand, if the control volume represents a turbine (which produces work), the following equation can be obtained:

$$W_T = \dot{W}_x = \dot{m} (h_{01} - h_{02}) \quad (1.8)$$

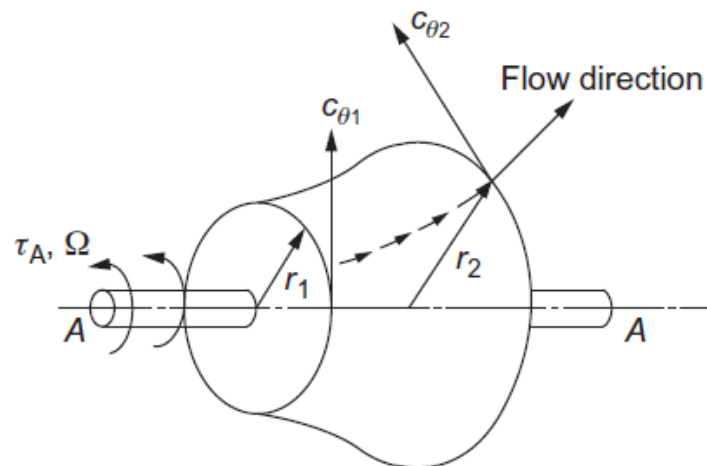


Fig. 1.4 - Generic control volume representing a turbomachine (Dixon & Hall, 2013)

1.3.2 Second Law of Thermodynamics

The second law of thermodynamics is based on the concept of entropy, which basically determines the degree of irreversibility of a process. The thermodynamic quantity

“entropy” can be defined by considering an ideal process during which the heat is transferred to the system by means of a reversible transformation. If T is the temperature of the system, it can be said that:

$$d S = \frac{d Q_{\text{reversible}}}{T} \quad (1.9)$$

If a finite change from state 1 to state 2 is considered:

$$S_2 - S_1 = \int_1^2 \frac{d Q_{\text{reversible}}}{T} \quad (1.10)$$

In a generic transformation the variation of entropy of the system can be expressed as:

$$d S \geq \frac{d Q_{\text{reversible}}}{T} \quad (1.11)$$

This inequality is not valid for a reversible process during which the entropy does not change. Therefore, equation (1.11) implies that, if an adiabatic process is considered, then:

$$d S \geq 0 \quad (1.12)$$

$$S_2 \geq S_1 \quad (1.13)$$

Now, considering that for incremental reversible process in a simple compressible substance, the heat addition to the fluid is

$$d Q = T d S \quad (1.14)$$

by neglecting the kinetic energy change, for the reverse process the work done can be written as

$$d W = p d V \quad (1.15)$$

By exploiting the first law of thermodynamics (equation (1.1)), and using specific quantities, the Gibbs equation can be derived:

$$d e = T d s - p d v \quad (1.16)$$

e , s and v being the total energy, entropy, and volume per unit mass.

This equation is not limited to reversible transformation. Now introducing the thermodynamic property enthalpy, h , as:

$$h = e + \frac{p}{\rho} \quad (1.17)$$

From equation (1.17), a formulation (which is often used in the turbomachines and energy system field) can be derived:

$$d h = T d s - p d v + d \left(\frac{p}{\rho} \right) = T d s - p d v + d (p v) = T d s + v d p \quad (1.18)$$

If an isentropic process is considered, equation (1.18) becomes:

$$d h = \frac{1}{\rho} d p \quad (1.19)$$

1.3.3 Gas constant and Specific Heats

Two important thermodynamic properties are the specific heat at constant volume, C_v , and the specific heat at constant pressure, C_p , which can be defined as derivatives of the internal energy, e , and enthalpy, h , which, for a perfect gas, only depends on temperature. Therefore :

$$d e = C_v (T) d T \quad (1.20)$$

$$d h = C_p (T) d T$$

where C_p and C_v varies with the temperature. Moreover, given that

$$d h = d e + d (p v) = C_v d T + R_g d T \quad (1.21)$$

where R_g is the gas constant of the gas, which is equal to the universal gas constant divided by the molecular weight of the gas.

For a perfect gas, the following relation is valid:

$$C_v = C_p - R_g \quad (1.22)$$

In addition, it must be said that in many applications it is possible to neglect the variation of the specific heat with temperature, by using an appropriate mean value of C_p and C_v so that:

$$e_2 - e_1 = C_v (T_2 - T_1) \quad (1.23)$$

$$h_2 - h_1 = C_p (T_2 - T_1) \quad (1.24)$$

The relations obtained in equation (1.23) are valid only for a perfect gas with constant specific heat.

1.3.4 Euler Work Equation

A compressor rotor with an angular velocity ω , the rate at which the rotor transfers work to the fluid is (Dixon & Hall, 2013):

$$M \omega = \dot{m} (U_2 c_{\theta 2} - U_1 c_{\theta 1}) \quad (1.25)$$

Where M is the torque, $c_{\theta 1}$ and $c_{\theta 2}$ are the tangential velocity of the fluid at the rotor inlet and rotor exit respectively, \dot{m} is the mass flow rate of the fluid, and the generic terms U_1 and U_2 indicate the blade speed at rotor inlet and exit respectively. This implies that, for a compressor, the specific work done on the fluid is:

$$gH_C = U_2 c_{\theta 2} - U_1 c_{\theta 1} > 0 \quad (1.26)$$

For a turbine, the work is done by the fluid on the rotor and can be calculated as:

$$gH_T = U_1 c_{\theta 1} - U_2 c_{\theta 2} > 0 \quad (1.27)$$

Equation (1.26) and (1.27) are known as the “Euler’s pump equation” and the “Euler’s turbine equation” respectively. In a compressor, the work done by the rotor can be equalized to the rise of stagnation enthalpy (considering the first law of thermodynamics required assumptions and the hypothesis of steady, adiabatic and reversible flow):

$$gH_C = U_2 c_{\theta 2} - U_1 c_{\theta 1} = h_{02} - h_{01} \quad (1.28)$$

An analogous deduction can be applied for a turbine.

1.3.5 Efficiency

The compressor isentropic efficiency can be defined as (Dixon & Hall, 2013)

$$\eta_{is,C} = \frac{\text{useful energy input to the fluid in unit time}}{\text{power input to the rotor}} \quad (1.29)$$

By considering a transformation from state 1 to state 2, and assuming an adiabatic system, the specific work done by the compressor is:

$$W_C = (h_{02} - h_{01}) + g(z_2 - z_1) \quad (1.30)$$

where the second term, which is the potential energy variation is usually neglected.

By looking at Fig. 1.5, which represents a Mollier diagram of the compression process, it is possible to identify the actual transformation (from state 1 to state 2) and the ideal transformation (from state 1 to state 2s) which stands on an isentropic line. Therefore, considering an adiabatic transformation, it is possible to define the isentropic efficiency as:

$$\eta_{is,C} = \frac{\text{ideal process work input}}{\text{actual process work input}} = \frac{h_{02s} - h_{01}}{h_{02} - h_{01}} \quad (1.31)$$

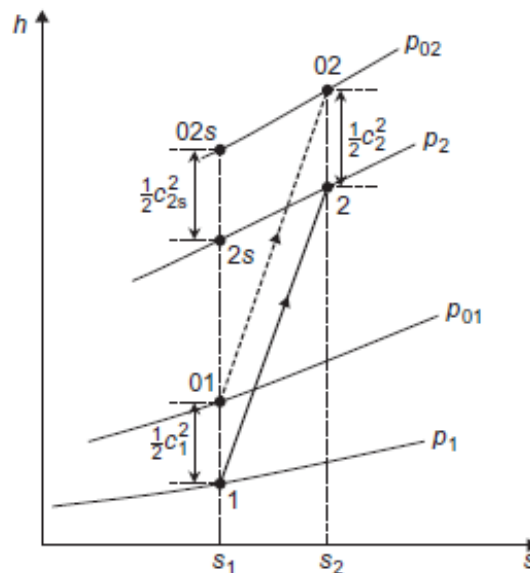


Fig. 1.5 - Adiabatic compression process in a enthalpy-entropy diagram (Dixon & Hall, 2013)

As can be seen, stagnation quantities are used for the calculation of the isentropic efficiency. However, it is common practice to assume that the dynamic component of the

stagnation enthalpies are comparable, so that $\frac{1}{2}c_1^2 \cong \frac{1}{2}c_2^2$ - which implies that the isentropic efficiency can be defined by using the static enthalpies:

$$\eta_{is,C} = \frac{h_{2s} - h_1}{h_2 - h_1} \quad (1.32)$$

1.3.6 Polytropic Efficiency

When analyzing different compressors with diverse pressure ratios, the isentropic efficiency is not a comprehensive parameter. A compression process, or rather a generic compressor, can be divided into several “small stages” (regardless of the actual number of compressor stages). Considering these small stages to have the same efficiency, the overall compressor isentropic efficiency will not coincide with the stage efficiency. This dissimilarity depends on the pressure ratio of the compressor.

In Fig. 1.6, a compression process between p_1 and p_2 (by small stages) is depicted in an enthalpy-entropy diagram. This plot represents an adiabatic compression from state 1 to state 2. As previously explained, assuming that (i) the compression transformation can be thought as the sum of many small stages processes, and (ii) these small stages have the same efficiency $\eta_{pol,C}$, the actual work input can be written as

$$W_{actual,C} = (h_x - h_1) + (h_y - h_x) + (h_2 - h_y) = (h_2 - h_1) \quad (1.33)$$

while the work corresponding to the ideal process is

$$W_{is,C} = (h_{xs} - h_1) + (h_{ys} - h_{xs}) + (h_{2s} - h_{ys}) \quad (1.34)$$

And as each stage has the same stage efficiency, it is possible to define this efficiency as:

$$\eta_{p,C} = \frac{W_{is,C}}{W_{actual,C}} = \frac{(h_{xs} - h_1) + (h_{ys} - h_{xs}) + (h_{2s} - h_{ys})}{(h_2 - h_1)} \quad (1.35)$$

Therefore it is possible to say:

$$\eta_{p,C} = \frac{W_{is,C}}{W_{actual,C}} = \frac{W_{is, stage}}{W_{actual, stage}} \quad (1.36)$$

where $W_{is,stage}$ and $W_{actual,stage}$ are the ideal and the actual work of the stage, respectively.

By evaluating this type of efficiency, it is possible to make some further considerations. From equation (1.18), assuming a constant pressure transformation, it results:

$$\left(\frac{\partial h}{\partial s}\right)_{p=const} = T \tag{1.37}$$

(Note that in equation (1.37) the differential symbol ∂ is used to indicate that it is a partial derivative). This result shows how the slope of an isobaric curve of an enthalpy-entropy diagram changes with temperature. In Fig. 1.6, this is not represented, since it is based on the assumption of constant temperature; and thus the slopes of the isobaric curve p_1 and p_2 are the same.

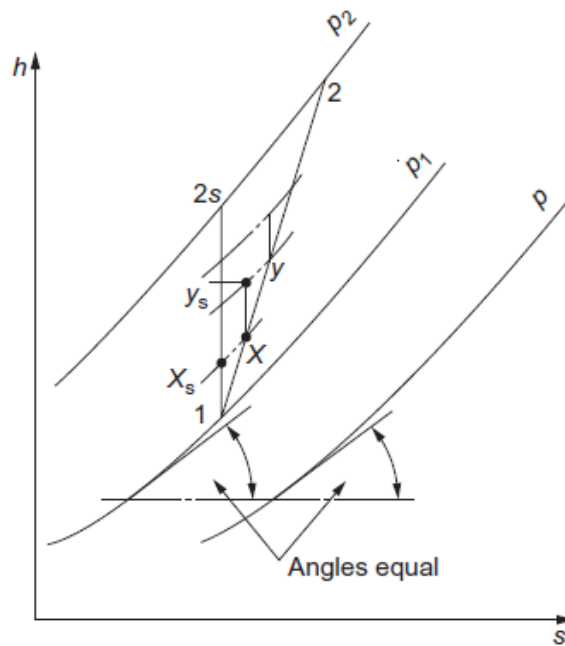


Fig. 1.6 - Compression process by small stages (Dixon & Hall, 2013)

However, in a Mollier diagram of a gas (the enthalpy of which usually depends on the temperature) which considers the effect of the temperature, these two isobaric curves would diverge. For instance, for a perfect gas, considering a constant specific heat C_p , equation (1.37) can be written as:

$$C_p \left(\frac{dT}{ds} \right) = T \quad (1.38)$$

which, if integrated results as:

$$s = C_p \log(T) + \text{constant} \quad (1.39)$$

Due to the divergence of the isobaric curves (when considering the small stage concept, and thus the isobaric curve slopes affected by the temperature), it is clear that the isentropic efficiency is lower than the small stage efficiency (note that the considerations above were made by using static quantities by they are valid for stagnation quantities as well):

$$\eta_{p,C} > \eta_{is,C} \quad (1.40)$$

Continuing the example of a perfect gas, it becomes clear that, for a differential increment dp due to the stage, the actual enthalpy rise is dh and the corresponding isentropic process enthalpy rise in dh_{is} . Therefore, by exploiting equation (1.18), the polytropic efficiency for a small stage is :

$$\eta_{p,C} = \frac{dh_{is}}{dh} = \frac{v dp}{C_p dT} \quad (1.41)$$

By then using the perfect gas law (equation of state):

$$p = \rho R_g T \quad (1.42)$$

and :

$$C_p = \frac{\gamma R_g}{(\gamma-1)} \quad (1.43)$$

where γ is the ratio of the specific heat.

Thus equation (1.41) becomes:

$$\frac{dT}{T} = \frac{(\gamma - 1)}{\eta_{p,C} \gamma} \frac{dp}{p} \quad (1.44)$$

Keeping the assumption of equality among the efficiency of each small stage, and integrating along the whole transformation:

$$\frac{T_2}{T_1} = \left(\frac{p_2}{p_1} \right)^{(\gamma-1)/\eta_{p,c} \gamma} \quad (1.45)$$

If we consider the isentropic transformation, the relation becomes:

$$\frac{T_{2s}}{T_1} = \left(\frac{p_2}{p_1} \right)^{(\gamma-1)/\gamma} \quad (1.46)$$

1.3.7 Compressor Performance

The performance of a compressor is identified by evaluating the property changes, from inlet to outlet, of the fluid which goes through it. It is common practice to assume the processed gas flowing through the compressor to be a perfect gas (i.e. an ideal gas with constant value of C_p , C_v and γ), but this obviously depends on the application. Therefore, all the properties seen in the previous sub-sections, as well as the stagnation speed of sound at the compressor inlet, a_0 , are involved in this evaluation.

The first observation is that, as there usually are significant changes of density during the process, the mass flow rate, \dot{m} , is preferred to the volume flow rate, Q ; and the isentropic stagnation enthalpy change, Δh_{0s} , which can be consider equal to the work done by the compressor (in an ideal and adiabatic process), is used instead of the head, H .

The performance parameters of a compressor (where the inlet section can be called state 1) are Δh_{0s} , η , and the power supplied, P ; their functional dependence is:

$$\Delta h_{0s}, \eta, P = \alpha(\varrho, \Omega, D, \dot{m}, \rho_{01}, a_{01}, \gamma) \quad (1.47)$$

By means of some passages, reported in many text books ((Dixon & Hall, 2013), for instance), we can obtain three non-dimensional groups which have the following functional relationship:

$$\frac{p_{02}}{p_{01}}, \eta, \frac{\Delta T_0}{T_{01}} = \alpha \left(\frac{\dot{m} \sqrt{R_g T_{01}}}{p_{01} \sqrt{\gamma} D^2}, \frac{\omega D}{\sqrt{\gamma} R_g T_{01}}, Re, \gamma \right) \quad (1.48)$$

For a machine of a specific size, handling a single gas, and operating at high Reynolds numbers, the terms D , γ , R , and Re are usually dropped in industry, obtaining:

$$\frac{p_{02}}{p_{01}}, \eta, \frac{\Delta T_0}{T_{01}} = \propto \left(\frac{\dot{m} \sqrt{T_{01}}}{p_{01}}, \frac{\omega}{\sqrt{T_{01}}} \right) \quad (1.49)$$

Note that in this case the groups are no longer dimensionless. Another type of groups utilized for the performance is expressed by the so called “corrected mass flow” and “corrected rotational speed” (the name is due to the units of the first being kg/s while the units of the second are rad/s) :

$$\frac{p_{02}}{p_{01}}, \eta, \frac{\Delta T_0}{T_{01}} = \propto \left(\frac{\dot{m} \sqrt{\theta}}{\delta}, \frac{\omega}{\sqrt{\theta}} \right) \quad (1.50)$$

$$\text{Where } \theta = \frac{T_{01}}{T_{\text{amb}}} \text{ and } \delta = \frac{p_{01}}{p_{\text{amb}}}$$

Other two useful parameters used for compressor design and analysis are the “flow coefficient” and the “stage loading”, which are usually employed for the characterization of single stages.

$$\phi = \frac{c_m}{U} = \frac{\dot{m}}{p_{01} A_1 U} = \frac{\dot{m} R_g T_{01}}{p_{01} A_1 U} = \propto \left(\frac{\dot{m} \sqrt{C_p T_{01}}}{p_{01} D^2}, \frac{\omega D}{\sqrt{\gamma R_g T_{01}}} \right) \quad (1.51)$$

$$\psi = \frac{\Delta h_0}{U^2} = \frac{\Delta T_0}{T_{01}} / \left(\frac{U}{\sqrt{C_p T_{01}}} \right)^2 = \propto \left(\frac{\dot{m} \sqrt{C_p T_{01}}}{p_{01} D^2}, \frac{\omega D}{\sqrt{\gamma R_g T_{01}}} \right) \quad (1.52)$$

An alternative formulation of the stage loading is:

$$\Psi = \frac{\Delta p}{\rho U^2} \quad (1.53)$$

Another parameter which can be used is the static pressure rise coefficient (particularly used for analyzing a diffuser performance):

$$\psi = \frac{p_2 - p_1}{p_{01} - p_1} \quad (1.54)$$

Which for incompressible flow can be written as:

$$\psi = \frac{p_2 - p_1}{\frac{\rho}{2} U^2} \quad (1.55)$$

The isentropic efficiency can be expressed as:

$$\eta_{is,C} = \frac{h_{02s} - h_{01}}{h_{02} - h_{01}} = \frac{\left((p_{02}/p_{01})^{\gamma/(\gamma-1)} - 1 \right)}{\Delta T_0/T_{01}} \quad (1.56)$$

An example of the performance maps of a compressor is presented in Fig. 1.7, which is referred to a 10-stage high speed axial compressor. The total-to-total pressure ratio, and the contours of the isentropic efficiency are depicted as a function of the corrected mass flow rate and the corrected rotational speed. It can be noted that each curve referred to the rotational speed finishes, at its left side, on the stall/surge line, (which separates the stable from the unstable behavior).

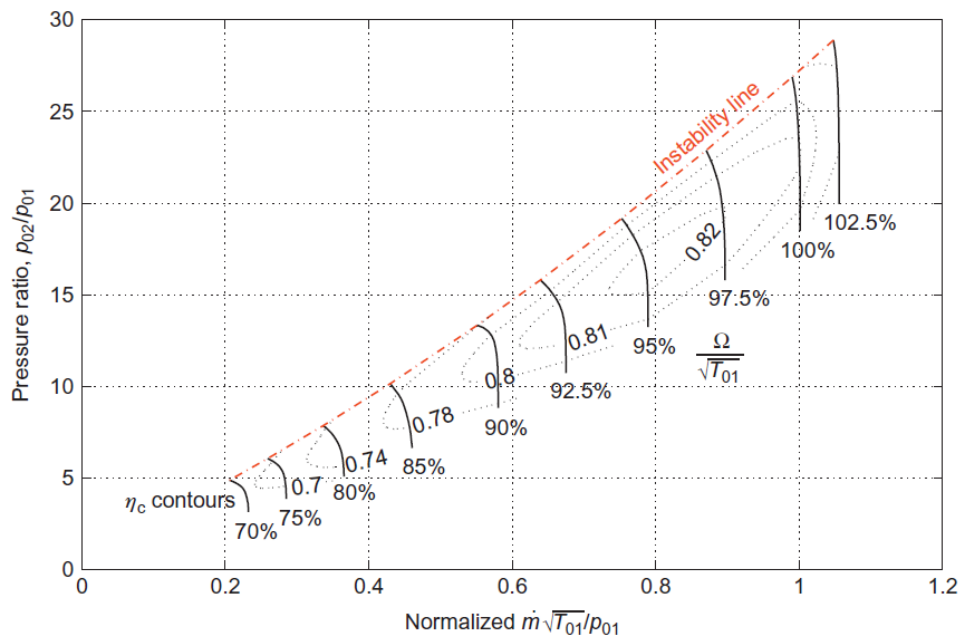


Fig. 1.7 - Performance map of a multistage axial compressor (Dixon & Hall, 2013)

A stall/surge margin (SM) is often adopted to prevent the compressor to operate unstably by monitoring the operating point position relatively to the surge line. The surge margin is usually defined as:

$$SM = \frac{(pr)_s - (pr)_o}{(pr)_o} \quad (1.57)$$

where $(pr)_o$ and $(pr)_s$ are the operating pressure ratio and the surge line pressure ratio respectively, at the operating rotational speed. On the other hand, at its right side, each curve assumes a vertical trend, which means that the corrected mass flow rate cannot be further increased since the compressor is in choke conditions (Mach number equal to one, $Ma=1$).

1.4 Modern Applications of Compressors

As already stated above, the compressors can be used in a wide range of applications, but depending on the typical requirements and usage, there are some applications where axial flow compressors are preferred and others where radials are more desirable. In Fig. 1.8 the typical ranges of various types of compressors are shown, as a function of pressure ratio (in the figure the displacement compressors are also present, even if they are not the focus of this study).

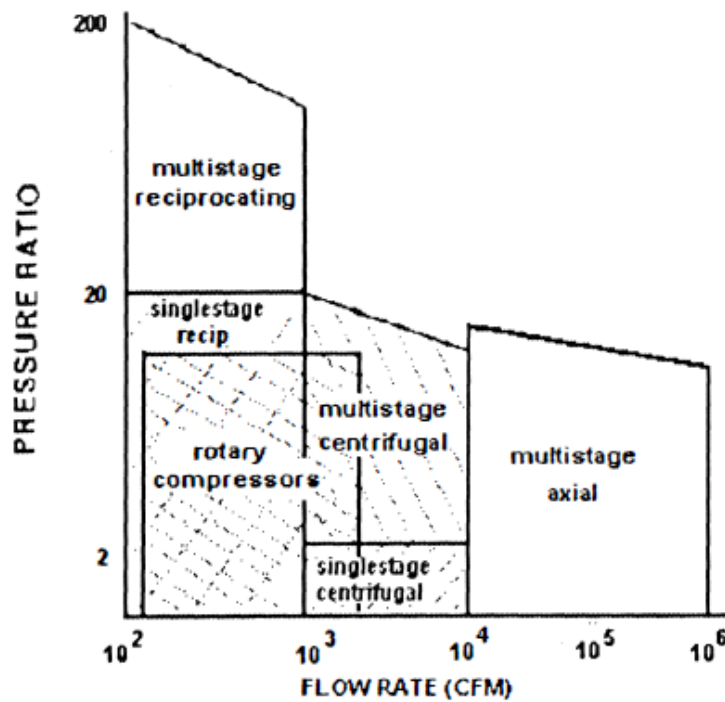


Fig. 1.8 - Continuous flow and displacement compressor operation ranges (Brown & Lewis, 1986)

Nowadays, when thinking about compressors, the first thing that comes to mind is their use in gas turbines. The gas turbines are energy systems which are made of: a compressor, which generates the pressure rise, a combustion chamber, where the fuel and the compressed gas are mixed and burned causing an increase of temperature, and a

turbine, which is used to drive the compressor and generate a net positive power output by means of the gas-fuel mixture expansion. These systems are usually employed in aeronautics, in marine propulsion, and for electric power generation.

In aeronautics, gas turbines are configured as turbojet, turbofan, turboprop, or turboshaft engines (Mattingly, 1996). The turbojet exploits the thrust given by the exhaust flow exiting the nozzle located at the turbine downstream. Similarly, the turbofan engine - which is equipped with a ducted fan installed ahead of the compressor - exploits the thrust produced by the jet exiting the nozzle, but it offers a reduced specific fuel consumption compared to the turbojet engine. On the other hand, the turboprop exploits the thrust generated by the propeller and by the exhaust flow through the nozzle. Finally, the turboshaft engine uses the mechanical power output from the turbine to drive the helicopter rotors.

According to (Gravdahl & Egeland, 2012), aero-derivative gas turbine are also used for marine propulsion of commercial vessels (yachts, fast ferries, fast cargo ships and cruise liners) and military vessels, due to their low weight and environmental emissions. Despite the low specific fuel consumption at part load (which can be overcome by using combined power plants), gas turbines are considered a convenient technology.

In modern power generation market, gas turbines are considered one of the major alternatives. Both aeroderivatives and heavy-duty gas turbines are used to produce electricity in many power plants all over the world for base-load duty, offshore oil and gas production platforms, and cogeneration plants. This is mainly due to the presence of great reserves of natural gas, which implies cheap fuel, as well as a low production of carbon dioxide (since natural gas contains a high quantity of hydrogen); but it is also due to the capability of these systems to satisfy a wide range of power applications - up to 300 MW in simple cycle, and 500 MW in combined cycle (in combination with steam turbines or diesel engines) (Wlash & Fletcher, 2004). Moreover, gas turbines are also used as standby generators (for local emergency use when there may be a loss of the main supply, as in hospitals and public buildings), APU (auxiliary power unit, in aircraft), and as topping cycle in cogeneration plants.

Also, the process industry represents a great segment of compressor applications. Here compressors are usually driven by an engine, in order to accomplish a determined process, and can manage with different fluids (air, natural gas, hydrogen-rich gas, etc).

Some example of industry processes include the refrigeration systems, where the most common refrigerants involved are ammonia, propane, propylene and ethylene (Lüdtke, 2004). In addition, other compressor employments on this sector are for low-temperature distillation, and nitric acid production (Balchen & Mummé, 1988). All these types of processes can require different types of compressors, but the most used is the centrifugal compressor.

Another important operation for which compressors are fundamental is the transferring of fluids along pipelines. The transportation of gases requires the use of compressors to provide the pressure difference which allows the gas movement. The compressor characteristics required for these types of operations are the low pressure ratios (typically 1.1-1.4) and the high mass flow rates. In this sector, the compressor is usually driven by an electrical motor or a gas turbine, but the second is the most employed in oil and gas applications for natural gas transportation, since it can employ the processed gas as fuel.

The last, but no less important, application which deserves to be mentioned is the supercharging of internal combustion engines (*IC*). This is a practice mostly used in the automotive sector, but it is also employed for stationary applications. The principle of supercharging is to supply additional air, with density higher than ambient, to an *IC* in order to increase its maximum power. This is usually accomplished by turbochargers, that consist of a turbine, driven by the exhaust gas of the engine, which in turn operates a compressor for supplying supplementary air to the engine.

1.5 Compressor Stability and Unstable Behavior

The instability of compressors is well-known as a problem and has been ever since the birth of this type of turbomachinery (as mentioned above regarding the Parson axial compressors).

In order to preserve compressors from a loss of performance and damage, the working range cannot be totally exploited at low mass flow rates. This is a limitation which, despite many years of research, still exists. For this reason, when a compressor is designed or selected for a specific application, beside the best efficiency point, the surge

and choke points are also relevant references to be taken into account, since they confine the compressor operation within a restricted range.

A typical compressor map is represented in Fig. 1.9: in this case, the machine is a high-pressure compressor. The x-axis represents the mass flow rates through the compressor (usually in industrial practice the corrected mass flow rate is adopted), while the y-axis represents the pressure ratio from the discharge to the suction sections of the compressor (as alternatives, the differential pressure or the head are often used). Fig. 1.9 clearly shows the steady-state operating points of the compressor at the different rotational speeds. In the figure, the stall/surge line, which in practice is usually called surge line, can also be seen. As mentioned in the “Rationale” section, the surge line indicates the compressor working condition limit before manifesting its instability (i.e. the compressor unstable behavior). Moreover, the maps show the compressor behavior at different throttle settings. The throttle is the fuel flow control to the combustor of a gas turbine, but it can also be seen as a compressor downstream valve of a piping system (this similitude is important in surge models). By looking at the diagram, it is evident that, depending on the type of compressor (high pressure or low-pressure), one of the possible causes of stall and surge can be a transient acceleration, but also a sudden deceleration is highly dangerous if developed when the operating point is close to the surge line.

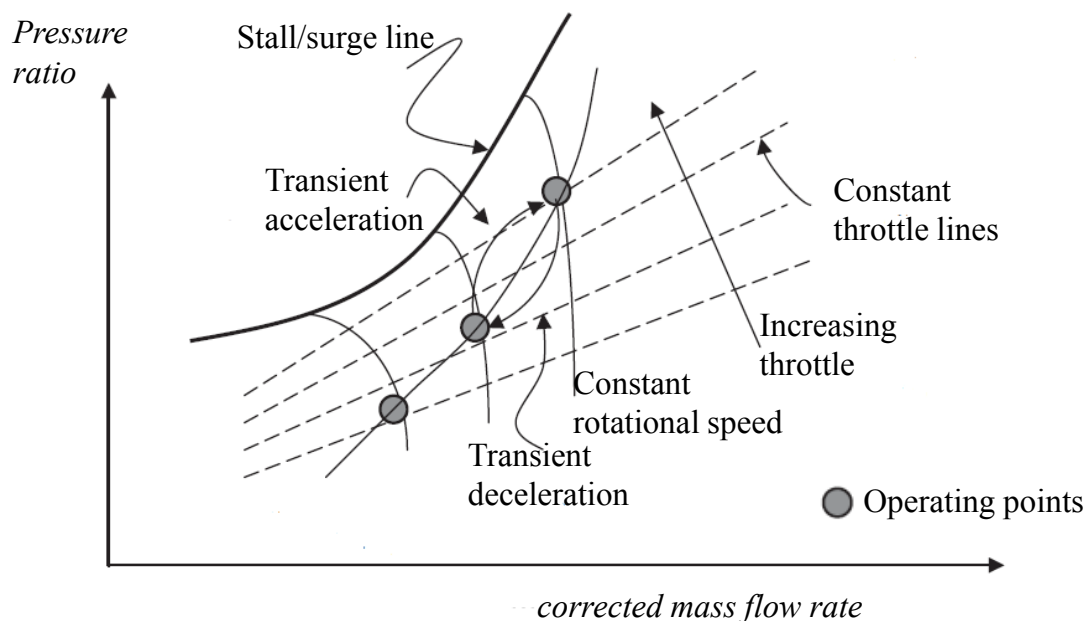


Fig. 1.9 - Typical compressor maps of a high speed compressor (Farokhi, 2014). In low-pressure compressor the acceleration path and the deceleration path are inverted compared to high pressure compressor's.

Since the use of compressors has become essential for many types of industries (see paragraph “Modern Applications of Compressors”) great attention needs to be put on the stability of these turbomachines. It is not difficult imagine how a compressor failure could affect certain applications.

For instance, if rotating stall takes place in an aircraft engine (stall and surge happen more often than what travelers might think), it would influence flight operating conditions, causing significant loss in performance together with anomalous vibrations and the subsequent risk of resonances. Pilots usually need to increase the compressor velocity or to decrease the throttle to recover from this instability. However, sometimes it is very hard to take rotating stall out: this is the case of the so called “lock in stall” condition (a phenomenon which typically occurs in jet engines), which forces to shut down the engine. If rotating stall, which is generally less dangerous of surge, can lead to such a risk, the consequences of surge are even worse. Besides a complete aerodynamic failure of the compressor aerodynamics (likely shutting down the engine and causing a flameout), it is accompanied by potential structural damage - which implies the activation of emergency procedures, inspections, and components repairing.

In the power plants, but also more in general in the industry sector, these issues implicate a great loss of power, production, unsuccessful gas transportation, or failure of important processes, which can lead to high unpredictable costs.

The unstable behavior of compressors has been the subject of many studies, and it is known that even if the compressor working point comes in proximity of the surge line, even without surpassing it, rotating stall or surge can occur nevertheless. This depends on many factors, but especially on the piping system configuration. Today, some well-reputable industrial solutions exist to avoid the surge inception by simply keeping the operating point into the stable performance field of the compressor maps, i.e. at the right of the surge line. This can be done by adopting a safety margin that prevents the working point of the compressor from moving too close to the surge line.

A person who is not an expert on this topic could think that electronic based control systems represent the definitive solution to the problem; however, engineers of this sector know that this is only partially true. In fact, the closer the operating point is to the surge line, the higher the risk of stall and/or surge, but also the greater the benefit of increased pressure ratio and efficiency. Moreover, the control systems are not always flawless, so the

instability can occur in some particular circumstances, such as a rapid variation of the compressor's working conditions, or an emergency shutdown (ESD) of the process system.

Hence, though it is undeniable that the accurate prediction of the surge line and margin plays an essential role in the design of a compressor, the evaluation of the unstable behavior of the compressor and its inception process, and consequences are fundamental, and need to be further investigated.

The next chapter will explain in detail the rotating stall and surge phenomena.

2 Rotating Stall and Surge

Stall and surge are the two main instabilities which limit the operating range of a compressor. A first clarification needs to be made regarding the terminology, which still generate confusion today. Rotating stall and surge are two distinct phenomena since they produce different effects on the aerodynamic performance of the compressor, even though they are often strictly correlated to one another.

Despite the fact that this has been explained and demonstrated in numerous studies over the past years, there is still a tendency to confuse these two topics. This is a particularly common mistake in aeronautics, in which the word “stall” is frequently used (some textbooks even talk about positive and negative stall of a blade, which only makes greater confusion). A first distinction must be made between the stall of the aircraft (which refers to the stall of the wings) and the stall of the engine (which is an incorrect word, since the term stall is typically used when referring to a compressor).

The stall of the aircraft only depends on the attack angle of the air during the flight; if this angle is out of the limits, the aircraft wings cannot offer the suitable lift to the airplane, which then goes into stall. The same phenomenon happens on a smaller scale with the compressor blades. If the inlet flow approaches the blades with a too high incidence angle, the blade will stall and tend to propagate the stall the closest blades. This generates the so called “rotating stall”. This work will only be treating the rotating stall, i.e. the stall of the compressor.

While rotating stall is sometimes difficult to detect, or its effects are not immediately easily visible, the surge is surely more perceptible, since it produces strong fluctuations of pressure and mass flow through the compressor. The reason these two phenomena can be associated to one another, as stated above, is that the rotating stall often precedes the surge.

In the following paragraphs, a highly detailed description of rotating stall and surge is reported, taking also into account their effects on performance.

2.1 What is Known Today

As already shown in the previous chapter, a compressor's characteristic curve indicates that the compressor increases its pressure rise while decreasing the mass flow rate to a maximum achievable peak (of pressure ratio), which depends on the design of the compressor. When the operating point goes beyond the surge line which can be thought (as a first approximation) as the curve that links all the peaks of the characteristic curves at the different rotational speeds, the compressor enters either into stall or surge. Therefore, at this point, the regular and organized flow somehow collapses highly affecting the overall performance.

Rotating stall is a local phenomenon which generates in a single blade (or more than one) and develops around the annulus of the compressor. It leads to local mass flow variations and can usually manifest in two different ways: namely, "progressive stall" and "abrupt stall" (Cumpsty, 1989). In Fig. 2.1 these different behaviors of the stalled regimes are highlighted. Progressive stall generates a slight drop in performance, and typically manifests in centrifugal compressors and low pressure rise axial machines (Day, 2016). In this case, stall is hard to detect with classic instrumentation (low sampling frequency), but it is accompanied by a notable change of the compressor noise. Abrupt stall instead causes a relevant drop in pressure and mass flow rate, and typically occurs in axial compressors with high pressure rise. In this case the operating point quickly moves through the throttle line (only with high frequency sampling this motion is detectable) and achieves a curve, called "stalled curve", with can also have a pressure rise 50 % lower.

Both progressive and abrupt stall indicate that the compressor is not working with an organized axisymmetric flow, which is instead disturbed by rotating perturbations around the annulus, named "stall cells"; from which derive the name "rotating stall".

These cells, represent the physical consequence of such instability and are to be considered as a response of the compressor to a mass flow rate which is too low with respect to the nominal values. When the mass flow is very low, the compressor reacts by generating one or more stalled cells, which correspond to the areas of the annulus with very small, or zero, flow; these allow the remaining part of the annulus to have a higher flow, closer to the nominal values. Therefore, in order to withstand very low mass flow rates, the compressor originates a non-axisymmetric flow characterized by rotating cells which occupy one or more blade passages and clearly distinguish the stalled flow from the

unstalled flow. The number of cells is not always the same, it depends on the aerodynamic of the compressor blades and on the operating condition. Moreover, the cells can extend over a part of the annulus (part-span cells) or over the whole annulus (full-span cells). For example, short blades with a high load usually manifest a single full span cell (Day, 2016). This type of stalled cells can cover the whole axial length of the compressor, whereas part-span cells usually occupy a partial length thereof. Fig. 2.2 illustrates the multiple part-span cells (left) and full-span cell (right) producing stalled and unstalled flow, as explained above.

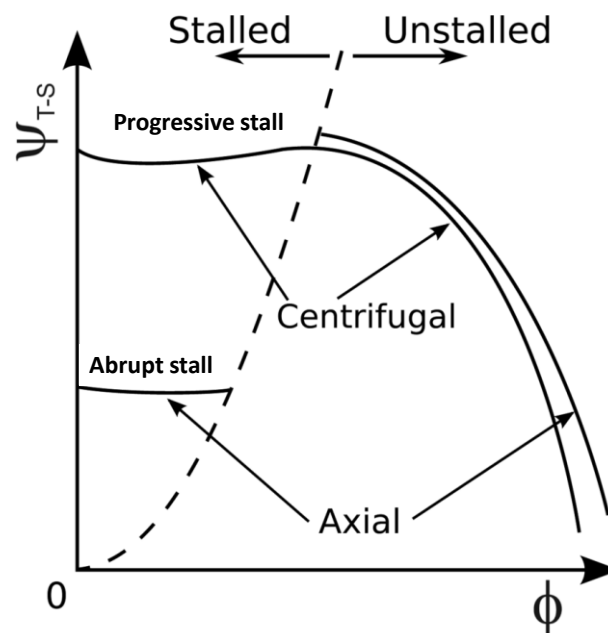


Fig. 2.1 - Typical unstalled and stalled curves (taken from (Day, 2016))

In addition to what is stated above, some cell features have been noticed during the past years of investigations, but these features are uncertain:

- Depending on the size, the stall cells rotate with a higher or lower velocity, thus a bigger cell rotates more slowly than a smaller one. They rotate in the reverse direction of the rotor, but since they are usually slower than the rotor velocity, for a fixed observer they seem to move in the rotor's direction.
- A correlation between the type of stall and the type of stall cells could be deduced by the experience of the research. The progressive stall usually goes together with part-span cells whereas the abrupt stall is usually linked to full-span cells. Moreover, if during a progressive stall a further throttling occurs, the part span cells can generate a full-span cell with a consequence

abrupt drop in performance, typical of abrupt stall. This phenomenon is highlighted in Fig. 2.3.

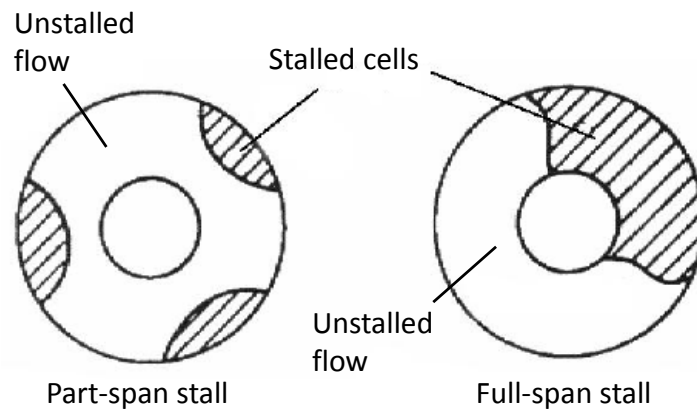


Fig. 2.2 - Types of rotating stall cells: part-span and full-span cells (taken from (Cumpsty, 1989))

On the other hand, what it is certain is that these cells, in particular full-span cells, are dangerous, not only because they affect the thermodynamics and aerodynamics of a blade row or the entire compressor, but also because they generate vibrations, an unsteady mechanical loading of the compressor blades, and an increment of temperature: which represent a risk for the integrity of the compressor. Part-span cells are generally less serious especially when generated at the front stages due to the stage mismatching at low rotational speeds (for example, during startup); however, this is a situation to avoid.

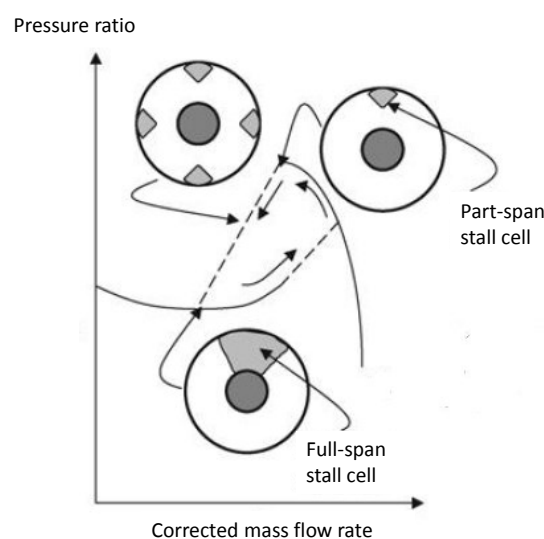


Fig. 2.3 - Typical formation of rotating stall cells along the stalled and unstalled characteristic curve of a compressor (taken from (El-Sayed, 2008))

The considerations on rotating stall in axial compressors cannot be considered completely valid for centrifugal compressors. In the case of radial machines, the mechanisms are different. Despite the many investigations carried out it is difficult to completely describe the rotating stall of a centrifugal compressor, but it can be stated that this instability can arise in the impeller or in the diffuser with different characteristics.

Impeller rotating stall can be of three types: mild, abrupt, or progressive. The characteristics of these types of stall (rotating velocity and number of the perturbations) are strongly correlated to the inviscid flow feature.

Abrupt rotating stall has been theoretically explained over the years, but it is still hard to predict. It is characterized by large amplitude velocity and pressure variations both upstream and downstream in the impeller, but also in the diffuser (usually vaneless diffuser); and this can result in a discontinuity of the overall characteristic curve (abrupt stall usually occurs in the positive slope side of the curve, but can sometimes manifest in the negative slope side as well). In this case, the rotational speed of the perturbations is 20-30 % of the rotor speed, and is practically independent from the diffuser inlet flow angle. The onset of an abrupt stall in the impeller is strictly related to the interaction among downstream (but also upstream) perturbations. An example of these perturbations could be: (i) the distortions generated by the diffuser vanes or by a downstream volute working off-design. Often, this type of stall occurs together with the vaneless diffuser rotating stall (another cause of inception can be the boundary layer), which usually trigger such instability. When analyzing the data spectrum in the abrupt stall period, it is likely to find higher harmonics of rotating stall frequency.

Mild rotating stall of the impeller is instead a phenomenon discernible for the several number of stall cells (generally four or five) and low relative rotational speed (about 14 %). This type of stall was noted only by few authors over the years, and in each case arose beyond the peak of the compressor performance curve, presenting mild relative pressure oscillations. It is likely that mild rotating stall of the impeller is a precursor of a successive abrupt rotating stall (in case the mass flow is further reduced). Since no significant evidence of this type of impeller stall has yet been found, mild stall is not completely well defined.

Progressive stall of the impeller is instead an instability which also occurs to the left of the peak but is characterized by a rotating disturbance with a typical velocity of 50-

80 % which produce oscillation amplitudes inferior to those of the abrupt stall. Progressive stall of the impeller can usually be referred to the rotating stall of axial compressors, since more often the stall cells are generated in the inducer (which is practically an axial compressor) by separated zones of the impeller. In progressive stall, the compressor can be operated quite satisfactorily. The explanation of this phenomenon can be seen by looking at Fig. 2.4 . It can be noticed that the separation along the suction side of the blade (channel 1) is the inception of the phenomena, causing a blockage and a local recirculation, i.e. local reverse flow. Successively (channel 2), the fluid tends to go backwards towards the inducer, producing a separation on the pressure side of the blade. The passage vortex generated (channel 3) and the more regular inlet conditions allow the flow to be more ordered, and finally, a uniform flow is achieved again (channel 4). The rotation of the disturbance strongly depends on the existence of the backflow. If the backflow does not generate the instability, it is maintained within the channel. Progressive rotating stall is characterized by a rotational speed of the disturbances, which increases by reducing the mass flow rate; this happens because the stall cells progressively increase their dimension.

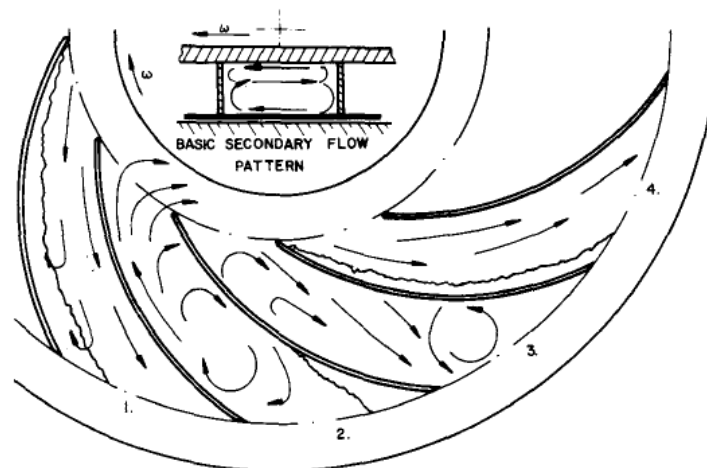


Fig. 2.4 - Sequence of stall in a single blade passage (taken from (Lennemann & Howard, 1969))

Despite the qualitative knowledge of this phenomenon, it is still hard to accurately predict the progressive stall characteristics due to the complex three-dimensional geometry of the impeller channel flow.

Low-solidity vaned diffusers usually allow more , since the inception of the diffuser rotating stall and surge is postponed (especially at higher rotational speeds (Japikse, 1996)), but they are characterized by limited operating ranges. High-solidity vane diffusers are much more prone to stall inception, which is why they are usually avoided in process

compressors. Vaneless diffuser stall is quite commonly observed in centrifugal compressor performing in the unstable field, or in the vicinity. It is triggered by local return flow in the diffuser and it can exist even with a stable flow at the compressor inlet and outlet sections. This instability, which is nowadays predictable with acceptable accuracy, develops in the negative slope curve near the peak, producing rotating stalled cells (usually two or three), which rotate at 15-20 % of the compressor rotational speed, and generate fluctuation amplitudes of the same magnitude of those of the impeller progressive stall. The inception of this instability depends on the boundary layer (local recirculation and increased blockage), whereas the characteristics of the instability depend on the inviscid part of the flow. By reducing the flow rate, these cells can diminish in number, often decreasing their velocity and increasing the amplitudes. A typical variation of velocity pattern during vaneless diffuser rotating stall is shown in Fig. 2.5. In this figure, the stall onset occurs and the average velocity distribution shows a low velocity region, which is a stalled zone.

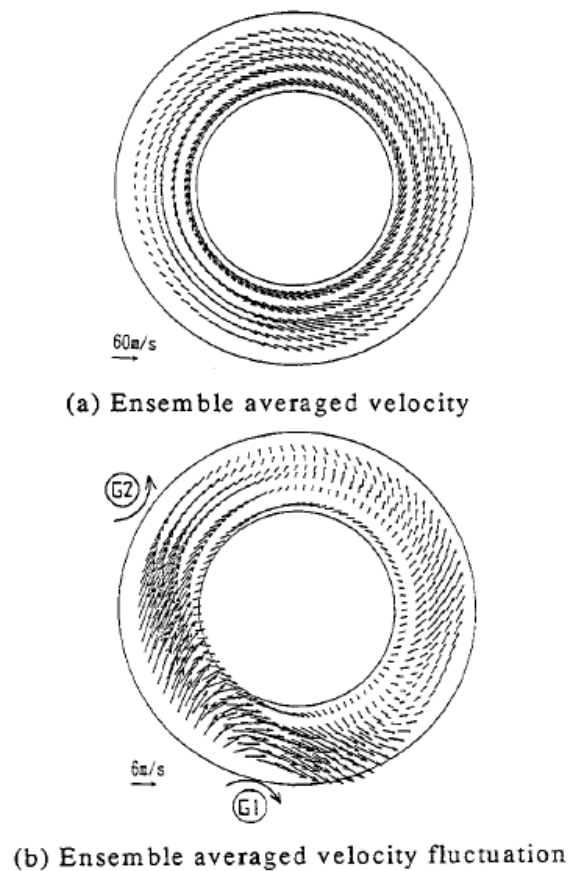


Fig. 2.5 - Velocity distribution at the stall onset (taken from (Watanabe, et al., 1994))

This region is preceded by a reversed flow from the outer surface of the diffuser to the inside thereof (Watanabe, et al., 1994). After flowing inward, the flow moves back toward the diffuser outlet. The bottom image, which shows the average velocity fluctuations, depicts two eddies rotating in opposite directions (Watanabe, et al., 1994), which are in accordance with what stated above.

Surge is instead a macro phenomenon and involves the whole annulus of the compressor and the whole longitudinal length thereof. It is characterized by a fluctuating annulus averaged mass flow rate which leads the compressor operating point to a continuous repositioning from the unstalled to the stalled region, and viceversa. The typical behavior of a compressor in surge is depicted in Fig. 2.6. Different degrees of surge can be identified depending on the generated oscillations of pressure and mass flow rate: mild surge, classic surge and deep surge (see Fig. 2.8, where only typical classic and deep surge fluctuations are shown).

The mild surge is the minor degree of surge and it usually takes place in small turbochargers (in general is more likely to occur in centrifugal compressors) as an anticipation of a stronger level of surge. This degree of surge can be detected only by sensitive instrumentation or by an experienced ear for the typical sound made by compressors (though not always easy to recognize). If mild surge occurs, the operating point circles around the characteristic curve peak and the compressor usually manifests a typical bubbling sound. This behavior is the result of mild back and forth fluctuations of the entire annulus flow, without any net backflow over time. An example is given in Fig. 2.7.

The strongest level of surge is called “deep surge” which is the maximum aerodynamic instability of the compressor. The deep surge is such a severe and dangerous condition that the operating point executes very large oscillations during the instability process; these fluctuations are so large that reverse flow occurs. If the fluctuations are large but do not produce reversal flow, the surge is usually called “classic surge”.

The occurrence of rotating stall and surge is not casual, but it is ruled by several parameters: the compressor downstream volume, the type of compressor (the typology and the design of its components, which alter the characteristic curve), the throttle setting, the presence of inlet or outlet distortion, the rapid transients (if they occur during the process).

In general, the larger the downstream volume, the higher the probability of surge. Moreover, as stated above, axial compressors are more prone to surge deeply (though this is a general consideration given by their typical characteristic curve); whereas radial machines tend to stall - maintaining nevertheless satisfying performance - or to surge with only mild oscillations. Obviously, the more the throttle is closed, the more the mass flow is reduced increasing the tendency towards instability. For example, if a piping system compressor goes into stall, this does not mean that it will remain in stalled conditions by reducing the mass flow rate; if a further closing of the downstream valve is applied, there could be a point (on the compressor curve) beyond which the compressor surge may occur. Distortions play a fundamental role, since due to their presence, the surge line could be lowered significantly, so that stall or surge may manifest even if the instability was not expected. Finally, rapid accelerations or, for example, sudden shutting down of the system, can lead to surge, especially if the compressor is working near the surge line (where the maximum efficiency point is usually located).

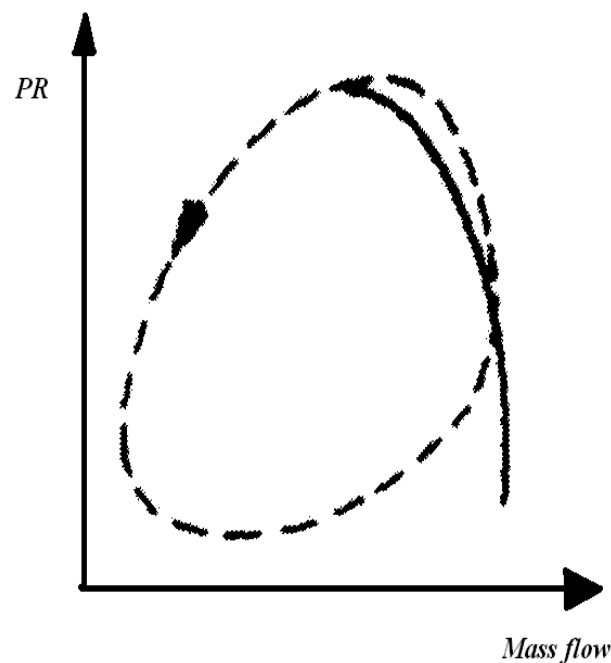


Fig. 2.6 - Typical operating point path during classic surge (taken from (Cumpsty, 1989))

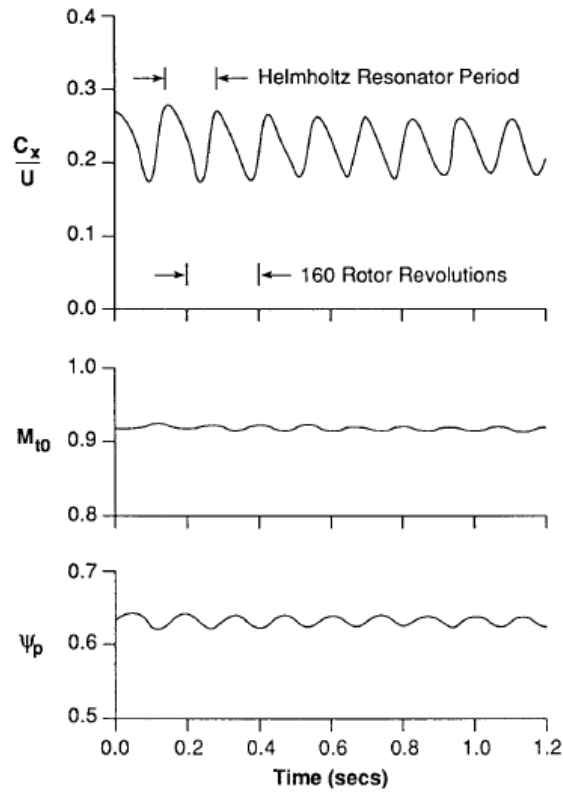


Fig. 2.7 - Mild surge oscillations: adimensional axial velocity, Mach number and isentropic head coefficient (taken from (Fink, et al., 1992))

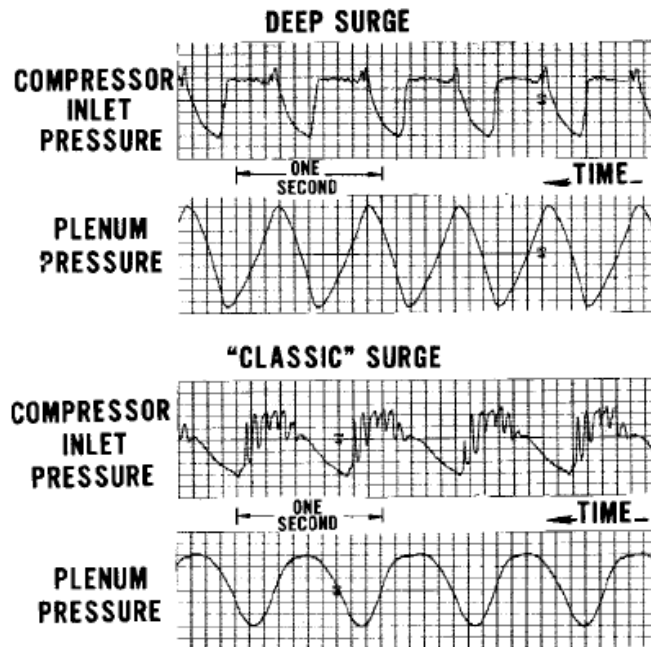


Fig. 2.8 - Classic and deep surge oscillations at compressor inlet and inside the plenum (taken from (Greitzer, 1976b))

To summarize it is possible to define the rotating stall as a bi-dimensional asymmetric phenomenon (even if it could be thought three-dimensionally, especially in centrifugal compressors), and the surge as a one-dimensional axisymmetric phenomenon, even if this is not true at the inception of the surge. This is clearly shown in Fig. 2.9, which illustrates the ejecting of the flame from an engine compressor inlet due to backflow. This phenomenon is very rapid, and at the beginning the flame is visible only in a minor part of the annulus. Then it grows more rapidly (in only one revolution, in the case of that high-speed compressor), developing in all the annulus area.

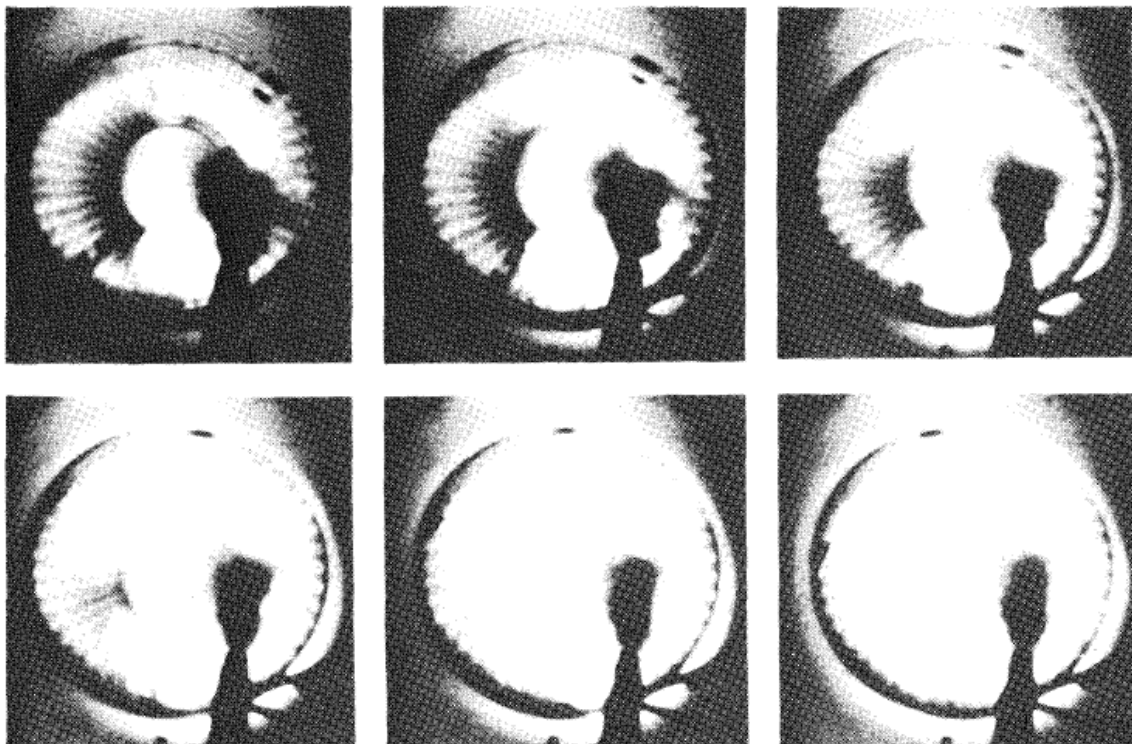


Fig. 2.9 - Development of deep surge reversal flow in an engine compressor (taken from (Mazzawy, 1980))

Now that rotating stall and surge have been described, an important thing to mention is that rotating stall usually precedes the compressor surge, but it can also momentarily manifest in the middle of a surge process.

Due to their different features, these two phenomena have different time scales; surge has a typical frequency of 0-10 Hz, although this depends on the compressor downstream volume's filling and emptying time; rotating stall has a higher frequency, which is a variable percentage of the compressor's rotational speed (usually from 20% to 60 %, but this range is purely approximated), its size, and number of the stalled cells.

2.1.1 Centrifugal Compressors Stability

The stall and surge in centrifugal compressors have led to many debates over the years. Despite the great number of works on radial machines, it seems that an investigation of the instability giving a general explanation for the mechanisms governing stall and surge is still missing (or it has not been highlighted yet). It is known that in centrifugal compressors, the rotating stall does not always significantly influence their performance. This generates confusion around this topic. In fact, centrifugal compressors often operate with separated regions (i.e. stalled regions - and many times they generate even far from stall/surge conditions), arising at the inducer tip, at the impeller outlet, at the diffuser, or at the volute (in the latter case this is likely due to the geometrical asymmetry produced by the volute). However, it has been proven over the years that radial machines can sometimes reasonably tolerate the rotating stall without showing a considerable drop in performance. The induced vibration and overheating which rotating stall produces needs to be further discussed.

The capability of centrifugal compressors to better withstand rotating stall is because a great part of the pressure rise is generated by the centrifugal effects, which are not much affected by the presence of stalled cells. Hence, it can be said that the most concerning issue of centrifugal compressors is surge, which occurs at very low flow rate and with characteristics similar to that of axial machines, even if radial ones can show less severe surge cycles.

De facto, the effects of rotating stall on the inception of surge in centrifugal compressors is less understood than in axial compressors. For this reason, it is not yet clear if and when rotating stall is a precursor of surge, nor if and when it precedes backflow during surge process, especially in high-speed machines. Experimental evidence supports both of these theses.

Therefore, it seems that one of the best ways to analyze the instability in radial compressors is to study the effect of its components coupling and matching. This idea was developed by Dean (Dean, 1974), who defined a stability parameter SP_i to evaluate the behavior of each component of a centrifugal compressor. The stability of a single component is given by $SP_i \leq 0$.

In Fig. 2.10, the trend of this parameter is shown as a function of the mass flow. In which case the impeller was neutrally stable (even if this fact cannot be generalized since impellers, if well designed, usually have a stabilizing effect), the vane diffuser passage was highly unstable whereas the inlet region of the diffuser had a greatly stabilizing effect.

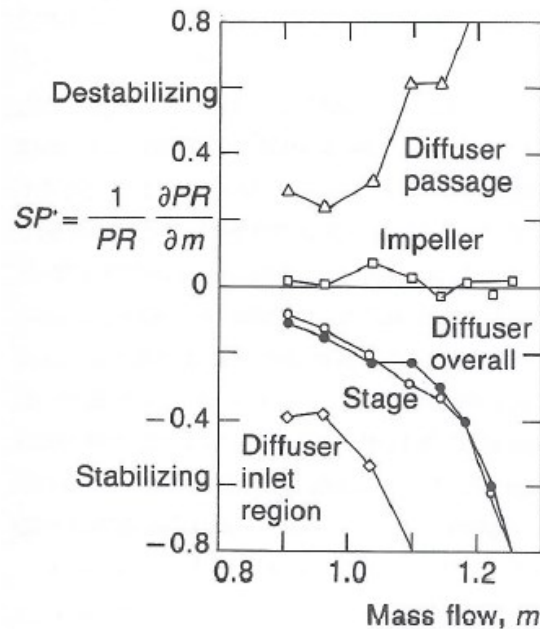


Fig. 2.10 - The stability of a centrifugal compressor components, based on the stability parameter values SP_i ; (source: (Dean, 1974); taken from (Cumpsty, 1989))

This image shows that despite the instability of some components, the important factor, which maintains the overall stage stable, is the matching between the components.

Some other points can be underlined regarding the stability of centrifugal compressors:

- The correct design of the impeller is vital for the stability of the stage.
- The backswept impellers are more stable because they generate a natural increment of pressure ratio with the diminishing of flow rate; for this reason, are used often, especially in industrial applications.
- Vaneless diffusers are often used (typically for low rotational speeds) when the process requires a large operating range. This can be confusing, since vaneless diffusers are innately unstable, while it has been proven that low solidity vane diffusers prevent rotating stall (in the diffuser thereof) and

delay the surge. The reason for the use of vaneless diffusers is probably that, although the SP is positive, it is very small in absolute value and continues to be small at various regimes of flow rate. This implies that the impeller, has to be at least slightly stable (differently from the example in Fig. 2.10). In practical terms, vaneless diffusers rotating stall manifests before than that of vaned diffusers, but the two instabilities have a different impact on the overall performance of the stage.

2.1.2 Axial Compressors Stability

Different methodologies can be adopted to evaluate the probability of stall on axial compressors. One of the most common was to maintain the diffusion factor $DF < 0.6$ (the DF is a parameter to assess the loading of cascades). By considering this parameter, it is possible to predict if a blade will suffer a separation on the suction side. It must be said that this parameter may not deliver a completely reliable evaluation of the stall vicinity of the compressor since a compressor can operate in stable conditions even with several areas of separation in blade rows (but obviously the presence of many rows with relevant stalled flows augment the probability of unstable behavior). Moreover, the DF did not consider the geometry of the blades - which has shown to be a relevant factor in evaluating the instability. It has been proven that with long blade chords the flow separation can be attenuated.

A good method of evaluating the stalling pressure rise of an axial flow compressor stage is that developed by Koch (Koch, 1981). He found a correlation for calculating the compressor pressure rise at stall by comparing the performance of a blade row with a straight diffuser, by exploiting a great amount of measurements on compressors from General Electric and classical diffusers (from (Reneau, et al., 1967)). He averaged the methodology in the whole stage without separating rotor and stator blading. The contribution of Reynolds number, tip clearance, and the rotor/stator axial spacing were isolated and then incorporated by normalizing the results for these parameters. Koch's stalling effective pressure rise final correlation for low and high-speed axial flow compressor stages is shown in Fig. 2.11 as a function of the camber line L divided by the staggered gap at outlet g_2 , and compared to the 2D diffuser correlation of Sovran and Klomp (Sovran & Klomp, 1967), with a blockage at the inlet of 9 %.

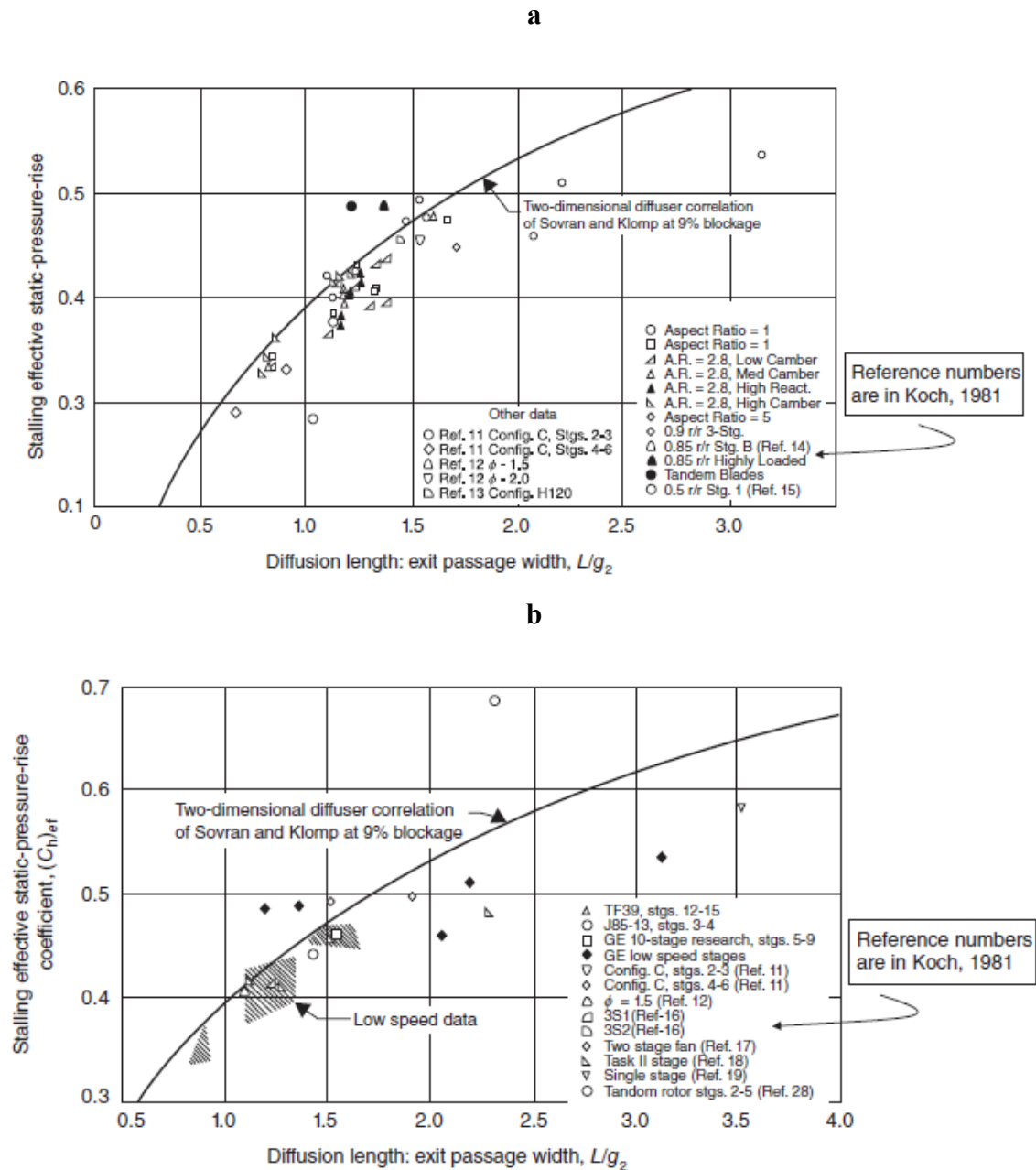


Fig. 2.11 - Stage stall static pressure coefficient as a function of the ratio between the diffusion length and the exit passage width: (a) low-speed compressors; (b) high-speed compressors (source: (Koch, 1981), taken from (Farokhi, 2014))

These plots are often used for designing the compressor’s blading, since they give a reliable indication of the maximum pressure rise obtainable before an the stall of an axial stage. These correlations also explain the greater stability demonstrated by high-staggered stages - which implies a low design flow coefficient. This type of compressors is usually more stable, even with values of diffusion factor higher than 0.6.

2.2 Background

When reporting the historical advancements in the knowledge of rotating stall and surge, Emmons et al. (Emmons, et al., 1955) is usually cited as the pioneer of the explanation of the rotating stall nature; but this is only partially true, as their theory had already been in circulation since a few years earlier. Therefore, it would be unfair to give their work all the credit without at least citing other earlier works.

2.2.1 *Early Developments*

As reported by Day (Day, 2016), the first observation of unstable flows was done in a water pump by Prandtl, et al (not referenced). After their work, the attention was focused on surge - which was probably due to the unawareness, at that time, of another complex phenomena such as the rotating stall. The first tangible investigation of surge was carried out in 1932 by Brooke (Brooke, 1932), and concentrated on a supercharger. After that, for about 20 years no other papers was found in literature, until a first patent of a surge preventing device for centrifugal compressors (Loss, 1949) appeared in 1949, together with another work regarding surge on axial compressors (Pearson & Bowmer, 1949). In 1950, one of the earliest patents of surge control system of a supercharged aircraft engine was taken from Bates: which underlines the increasing research activity on this topic.

Successively, a stronger effort was focused on the performances of compressor, and this led to rapid progress in the knowledge of their instability. In 1951, an investigation of surge in a turbojet engine was done by McAulay (McAulay, 1951), analyzing the effect of the altitude, the velocity approach to surge, and the acceleration regime on the surge line location. According to Day (Day, 2016), that same year Bullock and Finger (Bullock & Finger, 1951) studied the surge characteristics of a multistage compressor. In that paper, for the first time, a relation between the instability inception and the shape of the characteristic curve was reported, together with the observation of an hysteresis effect leading the compressor from the stalled region to the unstalled region. Moreover, they discovered the possibility to recover from surge by using a recirculating system, anticipating what would be later stated by Greitzer, in 1976, regarding the impact of the compressor downstream ducting volume on the surge frequency (bigger volumes produced surge with lower frequency, but higher amplitudes than smaller volumes).

Until then, a distinction between rotating stall and surge had not yet been recognized. The first step towards this distinction was probably made by Foley (Foley, 1951) only just in 1951, in the report of a discussion on surge held by many Engineers of the main companies involved in the aeronautical sector, but not only (the power production by means of gas turbine was also quickly progressing). Foley drew an important sketch of the disturbed flow due to instability in an axial flow compressor stage (see Fig. 2.12). This can be considered a fundamental contribution to understanding the rotating stall and surge, which were investigated even further during the following years. In 1952, Finger et al. (Finger, et al., 1952) investigated the effects of the blade angles on the surge limits of a 11-stage axial flow compressor. They discovered that, at high speed regimes, surge was probably caused by the stall of the exit stages, which was due to the high angle of attack. By adjusting the stator blade angles of the last stages, with the aim of reducing the loading of the hub section, they found an improvement of the general shape of the surge line at high speeds, but as a consequence they registered a drop of the thrust at low speed (possible cause of problems during take-off).

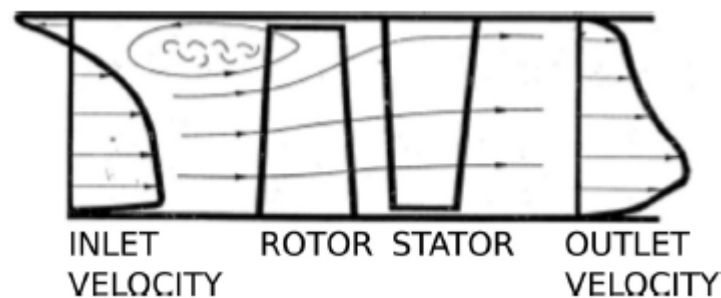


Fig. 2.12 - Lateral view draw of a part-span cell in an axial flow compressor (source: (Foley, 1951), taken from (Day, 2016))

A significant acceleration of the research was made in 1953. In that year, Iura and Rannie (Iura & Rannie, 1953) suggested the necessity of fast-response sensors to analyze stall. Moreover, they observed the tendency of the compressor to re-distribute the flow, with high incidence angle on the blades, in stalled and unstalled blade channels, and noted that the rotating stall was characterized by a constant average flow rate, contrary to the surge. In addition, they distinguished part-span and full-span cells, highlighting the tendency of the former to rotate faster than the latter.

A contemporary work was carried out by Benser (Benser, 1953) which studied the part-speed operation problem of high-speed multistage axial compressors. He stated that

low part-speed efficiency was to be attributable to the deterioration of stage performance due to rotating stall or the maldistribution of flow imposed by the inlet stages (severe stall characteristics of inlet stages) or stage interactions, or both - pointing out that the magnitude of the interaction effects and the number of stages affected, determined the decrement of performance at low and medium speeds. He also reported that the surge limit obtained during accelerations might be different from that obtained during decelerations, and confirmed the existence of an unstalling hysteresis effect. In addition, he confirmed the existence of a part-span stall which originated at one end of the blade and gradually extended in severity as the flow coefficient was decreased. Benser wrote a technical paper (Huppert & Benser, 1953) with Huppert confirming the results found in the other report and focusing on the effect of the speed acceleration on the stall margin (see Fig. 2.13). In their work, they highlighted the importance of a controlled acceleration, particularly at low speeds, to avoid compressor stall (at that time the actual difference between stall and surge was not clear yet).

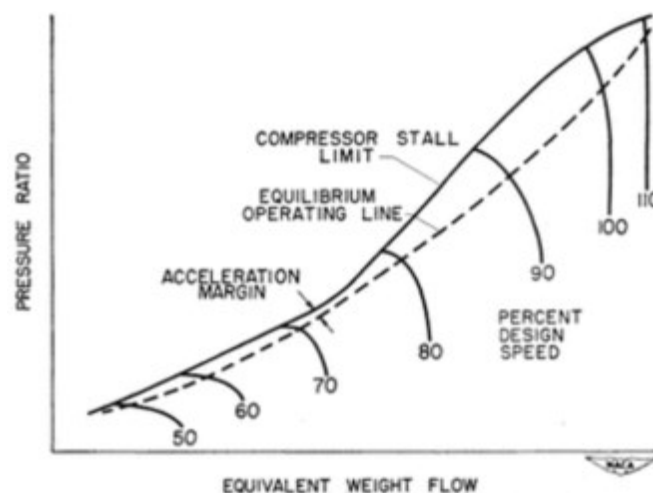


Fig. 2.13 - Effect of speed acceleration on stall margin (Huppert & Benser, 1953)

A few years later, when an answer for the frequent blade failure due to stall fatigue and induced vibration resonances started to be necessary, the work of Emmons et al. (Emmons, et al., 1955) appeared. They theorized through a model what had already been in thought around those years, i.e. the dependence of stall cell generation on the incoming flow approaching the blade, and thus on the incidence angle. They explained how the stall inception, induced by the high incidence of the flow on the blade, would generate a stall cell which caused a blockage, and thus an increased incidence on one side of the blade, and a decreasing incidence in the other side. This theory, supported by the famous sketch

provided in their paper (see Fig. 2.14), also suggested that the stalled cell would rotate backwards relative to the rotor. Their work helped to understand how a large stalled cell would generate a relevant blockage, leading to the deflection of the incoming flow (increase of the incidence on one side, and decrease on the other) and to the rotation of this disturbance.

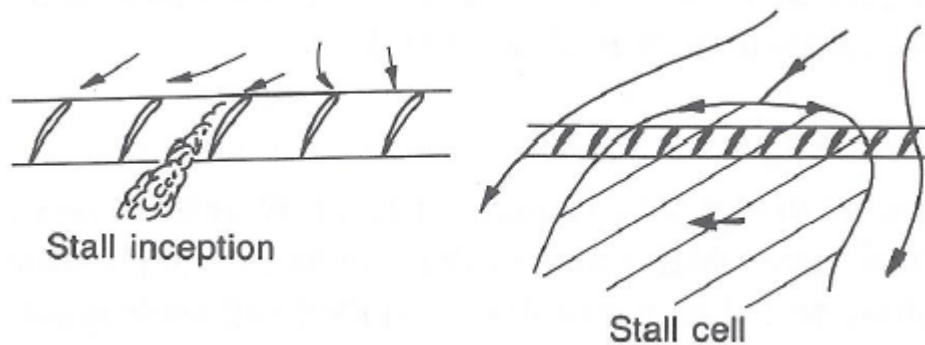


Fig. 2.14 - Rotating stall: theoretical stall inception in a single blade (left); and in more blade channels (right) (Cumpsty, 1989)

Another important discovery given from their work was that the instability inception had to be related to the peak of the characteristic curve. This was successively confirmed by Dunham (Dunham, 1965), who was one of the many authors who work hard to investigate this topic in the years after Emmons et al's, especially by adopting nonlinear models for the prediction of the cells characteristics. Unfortunately, despite all these important advancements, the real aim of the research, which at that time was to identify a method for estimating the number and the velocity of stall cells, was not successfully achieved. Only in the early 1980s it was suggested that the use of nonlinear small perturbation methods was probably not suitable to simulate rotating stall cells.

2.2.2 Hysteresis Effect

In the early second half of the century, the demand for further studying the stall cells characteristics slightly decreased due to a more important issue, hung stall, or lock-in stall or stagnation stall, or non-recoverable stall (these different definitions are reported to highlight once again the difficulty in finding a standard terminology). This type of instability implies the stall of the compressor is hard to clear with classic control methodologies. It was a relevant problem, especially for aircraft engines, and since its first episodes, it was attributable to the hysteresis loop. Obviously, to overcome this issue, the overall compressor install performance needed to be better understood and clarified. This

was first attempted by Smith and Fletcher, who were the forerunners of the parallel compressor theory initially formulated by Pearson and McKenzie (Pearson & McKenzie, 1959) in 1959, but formally theorized by McKenzie only in 1973. However, Smith and Fletcher were not supported by suitable amount of experimental data, and thus wrongly concluded that the dimension of the stall cells was always of a permanent value, i.e. half of the annulus. Obviously, this theory was refuted by contemporary authors.

As mentioned above, years later McKenzie came up with the parallel compressor model, which basically assumed that the installed performance of the compressor can be modeled by thinking of the compressor annulus as made of two parts, each part representing a compressor in parallel with the other: one operating with stalled flow, and another operating with uniform flow (unstalled flow). Both of these parts discharge the same static pressure. By looking at Fig. 2.15 (taken from (Day, 2016)), once in stall, the compressor operates along the line C-D. In particular, according to McKenzie theory, the stalled compressor operates at point C, whereas the unstalled compressor operates at point D. The level of pressure rise in stall regime was empirically found by McKenzie's at $\psi_{TS, stall} = 0.15 N$ (where N is the number of stages). These values were apparently independent from the type of compressors and their characteristics, while only dependent on the number of stages; unfortunately the reason for this was not explained the reason.

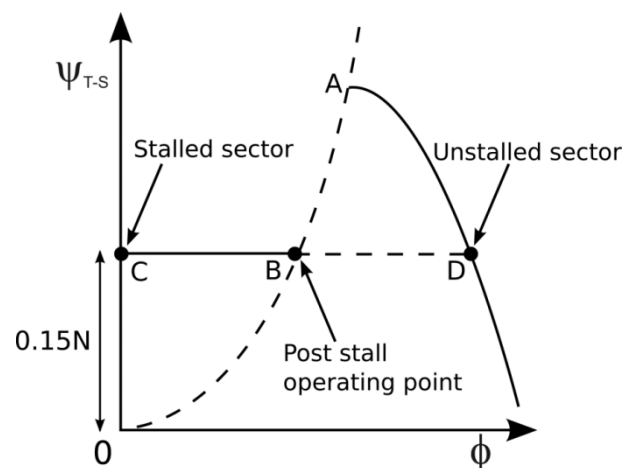


Fig. 2.15 - Graphic scheme of stalled and unstalled sector performance (taken from (Day, 2016))

This revolutionary theory was further developed by Day et al. (Day, et al., 1978), who improved the model and finally offered a theory to predict the type and approximated size of stall cells generated when the compressor goes into stall. They corrected, based on empirical data the shut-off level of pressure rise found by McKenzie, and also added the

corresponding non-dimensional total-to-static pressure rise referred to part-span stall: the new shut-off level was found to be $\psi_{TS, stall} = 0.11 N$, while the level related to part-span stall was $\psi_{TS, stall} = 0.17 N$ (obviously this modeling did not deal with part-span stall due to a compressor speed far below the design speed). Unfortunately, a reliable explanation of these two values and their strict dependence on the sole number of stages could not be given even by Day et al. (actually, this still represent a question mark today, and would need an answer).

In addition to this, they found an valid methodology to estimate the hysteresis loop size. They stated that the hysteresis loop largely depends on the compressor design flow coefficient ϕ^* . In Fig. 2.16, the graphic explanation (given in (Day, et al., 1978)) can be seen. The figure depicts the stalled characteristic curves in terms of total-to-static pressure rise coefficient, ψ_{TS} , flow coefficient, ϕ , for four different three stage compressors. It can be seen from the plots that, by increasing ϕ^* (which can be associated to higher pressure ratios), the hysteresis loop increments due to the different pressure drop occurring when the compressor stalls.

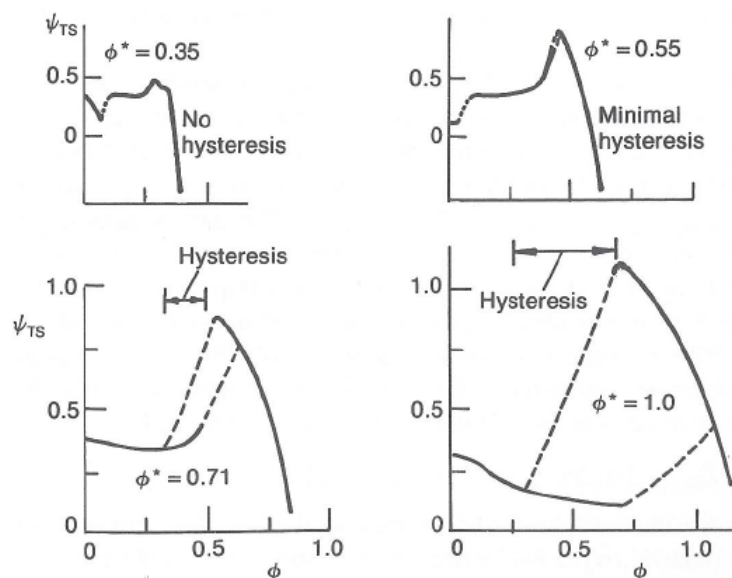


Fig. 2.16 - Effect of the design flow coefficient on the rotating stall hysteresis (source: (Day, et al., 1978), taken from (Cumpsty, 1989))

The hysteresis has an important implication for multistage compressors since the compressor characteristic is no longer one. For instance, if the compressor is operating at low speed and rotating stall is generated in one of the front stages, rotating stall can continue up to the nominal speed if the compressor is accelerated with a marked throttling.

Conversely, rotating stall can disappear if an increase of speed takes place with a minimum throttling.

2.2.3 The Rotating Stall Cells

The limitations of the instrumentation have delayed the measurements inside the cells until the last part of the 20th century. This was an important achievement, since it clarified that a stall cell was neither exactly a wake nor a vortex, as it was thought of at that time. In 1978, Day and Cumpsty (Day & Cumpsty, 1978) published the first set of measurements which could give reliable indications about the stall cells. They performed tests on multistage compressors characterized by different design points, and they discover that the stall cells are essentially axial and of constant width through the axial direction. Therefore, due to the aerodynamics of the blades, the fluid flow enters the cell from one side and exits them from the other. The sketch of the flow through a stall cell is depicted in Fig. 2.17.

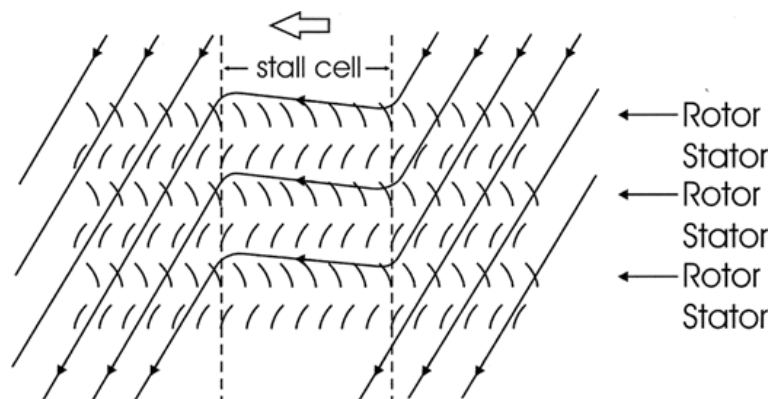


Fig. 2.17 - Sketch of the flow in a rotating stalled cell (source: (Day & Cumpsty, 1978), taken from (Day, 2016))

As can be seen, the average axial velocity is basically zero (near to zero) and the flow is mainly carried by the rotor blade passage. Based on the measurements on 50 % reaction compressors, the cells remained axially through the length of the compressor and the velocity pattern in the first stage was very similar to that of the last stage. They compared the velocity and the flow angle ahead and downstream the first stage rotor at the blade mid-span. The main results were that, before the rotor, the velocity inside the cell was very high - close to the rotor speed - and its direction was close to 90 ° of the axial, i.e. in the circumferential direction. After the rotor, the circumferential velocity inside the cell

was very low, and with an angle still close to 90° , over part of the cell, and 270° over the remaining part (see Fig. 2.18)

Day and Cumpsty also made a set of measurements at different radii of those compressors, and they noted a high radial gradient of both stagnation and static pressure just ahead the rotor due to the high circumferential velocity. The flow in the stalled cell resulted thus highly three-dimensional.

These conclusions were confirmed some years later by Das and Jiang (Das & Jiang, 1984), who collect a great amount of experimental data by means of fast response transducer and a digital acquisition system, and studied the flow field and distribution of flow parameters during rotating stall of a three-stage axial compressor.

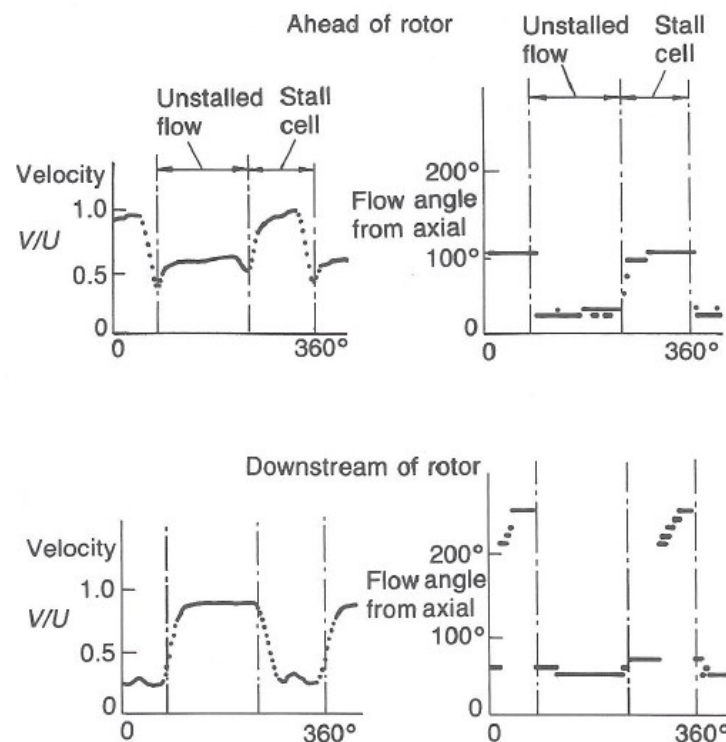


Fig. 2.18 - Stalled flow velocity and flow angle measurements before and after the rotor. The data are referred to the mid-span location at a flow coefficient of 0.33 (the compressor designed flow coefficient was 0.55) (source: (Day & Cumpsty, 1978); taken from (Cumpsty, 1989))

2.2.4 Surge or Rotating Stall?

At the beginning of the second half of the 19th century, the mechanisms of rotating stall, and the difference between stall and surge were not fully recognized; this is reported

in the brief historical review of this chapter. However, the increasing of the study activity regarding the generic “stall” of the compressor led to a gradual distinction of these two phenomena. The limitation which retarded the knowledge at that time was probably due to the not-yet advanced instrumentation but also to the tendency to interpret the compressor instability based on the acoustic sounds released by the compressor. Therefore, the different instability behavior (which would have been explained years later with part-span stall, full-span stall, and surge), but in particular the differences with the surge process, had not already been fully recognized.

Years later, when the difference between rotating stall and surge had become clear, the main issue regarded the prediction of which instability could arise. In 1976, a complete work on surge was done by Greitzer (Greitzer, 1976; Greitzer, 1976b), who developed a lumped parameter model to predict the dynamic behavior of a compression system (compressor duct, plenum, and throttle) and definitively established the circumstances for the occurrence of stall or surge. He came up with a nondimensional parameter, B , to define whether a specific system layout induced stall or surge of the compressor. The Greitzer B parameter basically compares the pressure rise capability of the compressor with the pressure rise required to generate mass flow oscillations of the system, and suggests that surge occurs when the pressure rise capability of the compressor is highest – otherwise, stall is induced. He stated that, in that case, the critic value, B_{critic} , which separating the occurrence of rotating stall from that of surge, was $B_{critic}=0.8$. An example of the effect of B on the unstable behavior of the compressor is given in Fig. 2.19. Unfortunately, this was not an universal value valid for any compression system with any compressor.

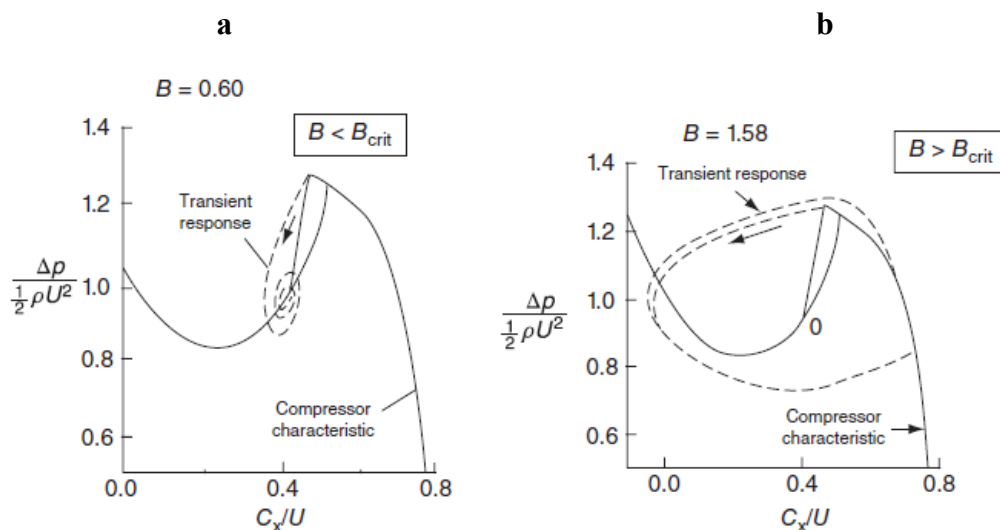


Fig. 2.19 - Effect of greitzer parameter B on the unstable behavior of the compressor after the characteristic curve peak: (a) rotating stall; (b) surge; (source (Greitzer, 1976); taken from (Farokhi, 2014))

Day (Day, 1994) stated that there was a gap in the literature concerning the flow during surge. He presented experimental data to give an explanation of what happens in the compressor during surge, and attempted to improve the stability prediction formulated by Greitzer. He observed that rotating stall was present at the beginning of each surge cycle in the low-speed axial compressors tested, and that the Helmholtz oscillations are not related to the surge fluctuations.

After Greitzer's work, many other models were developed in the following years, many of them were important, since they offered further explanations and a better comprehension of the instability. Moore was one of the authors who gave a great contribution with his works regarding the analysis of the flow perturbations (Moore, 1984; Moore, 1984b; Moore, 1984c). He was the first to present the idea of an axisymmetric characteristic curve beyond the peak of the stable compressor curve, i.e. beyond the surge point. This curve basically has the aim to represent the ideal compressor performance in the absence of the unsteadiness, i.e. with uniform flow. Moreover, he formulated valid calculations on the propagation of stall (defining the circumstances for the existence of modal disturbances preceding rotating stall), by predicting the stall cell velocity and explaining which parameters affect the most the hysteresis of stall.

The idea of extending of the stable characteristic curve even beyond the surge line attracted other authors to investigate with a similar perspective. Koff and Greitzer (Koff & Greitzer, 1986) found that the underlying curve could be expressed with a cubic relation (see Fig. 2.20). Successively, Moore and Greitzer produced some fundamental publications developing this idea. They made the unification of the one-dimensional and bi-dimensional theories linked to surge and stall possible, by developing a model which considered both these phenomena and provided an optimum agreement with the test data. The use of this stabilized curve allowed the prediction of the performance in surge condition to be highly improved. An extension of this model was published by Moore in (1986) (not, refereced), taking into consideration the development of rotating stall or surge under the influence of harmonic inlet distortion. A similar aim was reached by the model of Hynes and Greitzer (Hynes & Greitzer, 1987), trying to evaluate the drop of the stability margin due to inlet distortions. The definitive confirmation (if any was needed) of the existence of an underlying axisymmetric flow characteristic, was given by analyzing another aspect, considered in the following years, regarding multistage compressors and the matching of their stages.

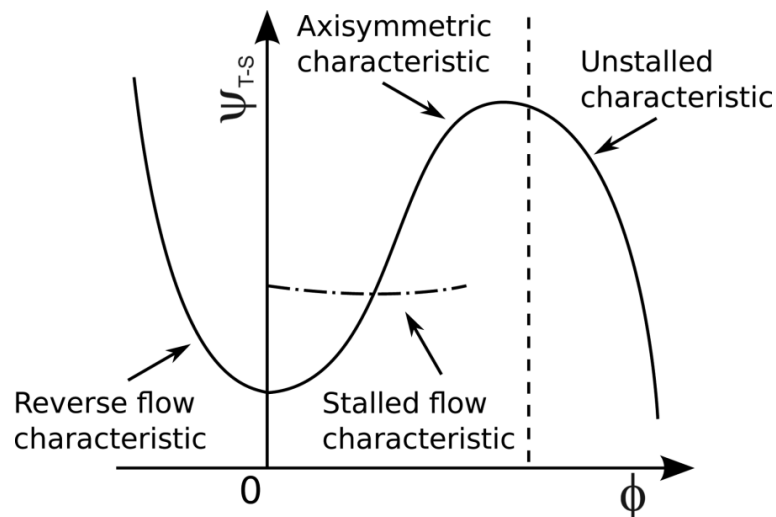


Fig. 2.20 - Typical compressor characteristic curve in the stable and the unstable field (taken from (Day, 2016))

Longley (Longley, 1988), and Longley and Hynes (Longley & Hynes, 1990) worked on this topic, demonstrating the influence of the matching/mismatching between the stages on the stability range. They demonstrated how the performance of a single row can be different on its own from that in a multistage compressor, depending on the matching/mismatching between the stages. In Fig. 2.21, the main concept of his work can be summarized.

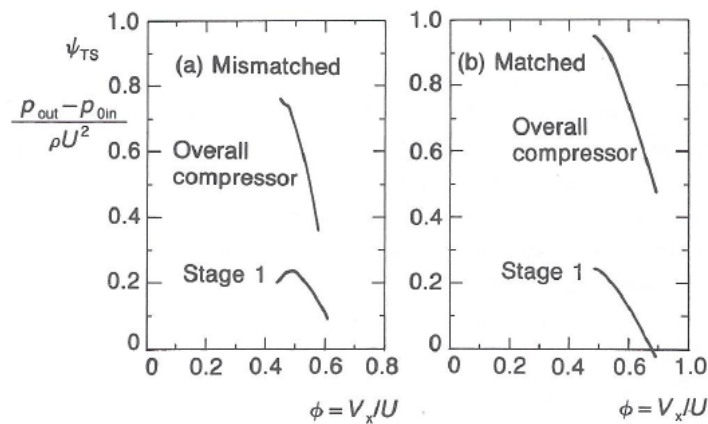


Fig. 2.21 - Effect of stage matching on the instability onset of a two-stage compressor: second stage mismatched with an extra stagger (left); second stage perfectly matched (right); (source: (Longley, 1988); taken from (Cumpsty, 1989))

The tested machine was a low-speed three stage compressor. As can be seen, the mismatched coupling of stage #1, designed for a certain flow rate, with the other two stages (stage #2 and stage #3), designed for a lower mass flow, postponed the onset of the

instability. In Fig. 2.21 (left), it can be noticed that stage #1 achieved operating points even beyond the characteristic peak, which demonstrates the stabilizing effect of stage #2 and stage #3. On the other hand, in Fig. 2.21 (right) the results related to a coupling with perfectly matched stages are shown (stage #1, stage #2 and stage #3 were designed for the same flow rate). The stages became simultaneously unstable, and a sudden drop of performance was registered near the peak.

In the 1990s, many other analytical works were carried out, almost all of them were based on the extension of the Moore and Greitzer model. For instance, the effects of viscous, dissipative forces in the instability of the compressor was investigated by Adomaitis and Abed (Adomaitis & Abed, 1993) and by Wang et al. (Wang, et al., 1994) Another work to be mentioned is the one by Wang et al. (Wang, et al., 1997), which analyzed the effect of the steepness of the right and left side of the of the characteristic curve maximum. They stated that, the steeper the left side of the peak, the deeper hysteresis generated, and thus the more difficult to clear rotating stall.

2.2.5 *Stall Inception*

The last decade of the 19th century was also important because of the definitive identification of the stall cells formation process. As already observed by Moore, the existence of modal perturbation preceding the formation of stall cells was confirmed by Mc Dougall et al (McDougall, 1990). For some years, these modes were considered to be the unique inception process of instability, and thus the stall and surge active control techniques were developed on this assumption. Surprisingly, after some years, Day (Day, 1993) discovered a different inception process by means of an array of hot-wire sensors, characterized by the so called “spike”. The feature of this spike was its sudden generation (without any type of warning); this came as a great disappointment to those thought that the control of the instability had achieved a high reliability (it must be said that control systems were then made able to manage spikes as well). Fig. 2.22 shows the results obtained by Day; specifically, Fig. 2.22 (left) depicts modal perturbation stall inception, whereas Fig. 2.22 (right) shows spike inception.

After this important discovery, Camp and Day (Camp & Day, 1998) continued the study on instability inception, producing a significant publication. They tried to theorize the reason why some compressors manifest instability at the characteristic curve peak (as theoretically demonstrated over the years), while others became instable before the peak.

They concluded that spikes are disturbances localized in a blade row, and frequently appear when the compressor has stalled before the peak. On the other hand, modes appear at the characteristic peak, but only if spikes do not manifest before.

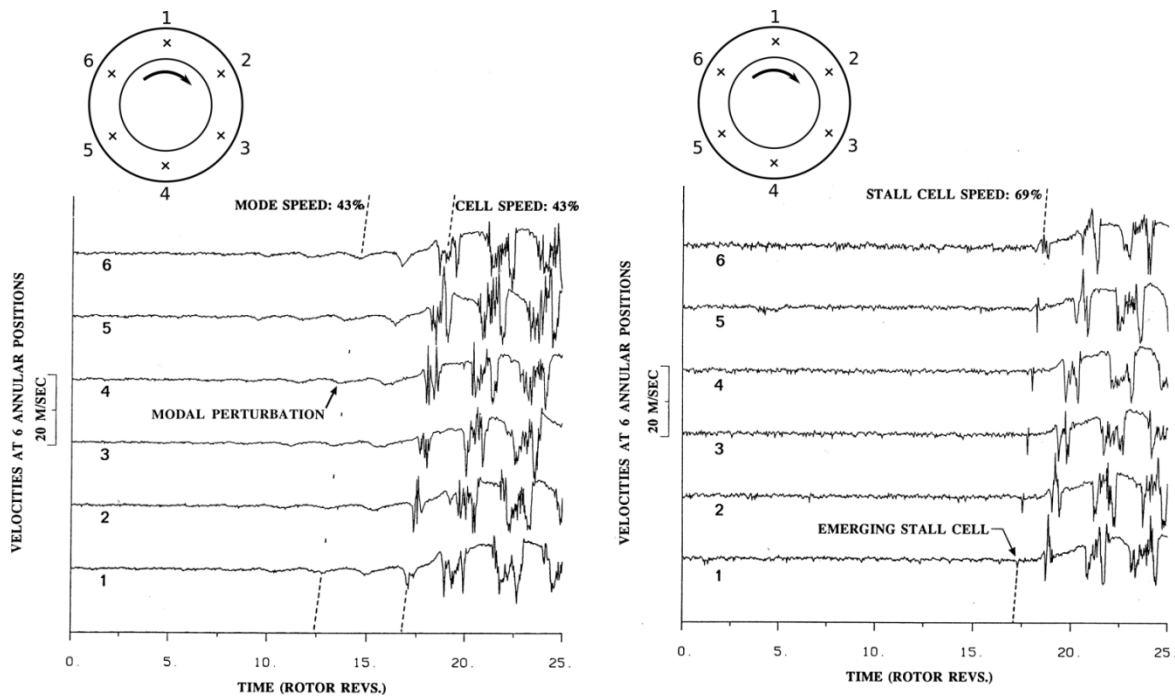


Fig. 2.22 - Type of stall inception phenomena: modal oscillations (left); spikes (right); (taken from (Day, 1993))

2.3 Stall and Surge in Centrifugal Compressors

Most of the considerations stated above can be easily referred to the axial compressor behavior, and not all of them instead can be useful for evaluating centrifugal compressors instability - whose instability process is less known than that of axial machines. For this reason, the main historical studies on centrifugal compressors deserve a separate section.

Despite the first episode of rotating stall was recognized in centrifugal compressor in 1945, (the progress of the axial compressor had temporarily died out due to early development difficulties). Successively, with the increase in interest for axial machines, much of the effort was then re-oriented towards the study of axial compressor instability.

One of the most active authors on the instability of centrifugal compressor was undoubtedly Japikse. In (Japikse, 1981), Japikse reported a definition of “stationary stall” and “dynamic stall”. The difference, as the name may suggest, was that stationary stall was

characterized by a fixed position of the disturbances (or separated flow regions, see (Japikse, 1996)) within the machine, whereas the dynamic stall was characterized by the rotation of the disturbances within the compressor (now commonly known as rotating stall). It must be said that the presence of pure steady-stall was not always well documented by the investigators.

2.3.1 *Steady Stall*

There are various phenomena which can be associated with steady-stall. The possible features of steady-stall are well documented in (Japikse, 1996) – here, for the sake of brevity, only the main ones are listed (they are usually related to boundary layer phenomena, saddle points, or bubbles separation):

- Flow separation in a blade channel due to high aerodynamic load (the phenomenon is limited to a specific channel and do not propagate as in the case of rotating stall). It consists of a secondary flow (with low momentum) which manifests in a primary flow;
- Leading edge separation caused by a high incidence of the flow;
- Local recirculation flow (usually rotor inlet and exit).
- Passage vortices and horseshoe vortices

In the 1970s and 1980s, it was discovered that radial compressors can encounter stationary stall at the inducer, which happens by reducing the mass flow (thus increasing the incidence), causing the separation of the flow. Japikse explained that the stall of the inducer does not necessarily imply the inception of surge - which also depends on the characteristics of the other stage components. He demonstrated that in high-pressure ratio machines, the inducer stall can lead to surge whereas at very low pressure ratio it is possible to observe a stall of the inducer, while the entire stage still operates stably (Japikse, 1981). An example of this is given in Fig. 2.23.

Successively more complete maps were published by Kämmer and Rautenberg (Kammer & Rautenberg, 1986), who also presented very interesting compressor inlet measurements (see Fig. 2.24). Fig. 2.24 (left) shows that it is generally possible to operate the compressor at low speed, even beyond the surge line (in accordance with Fig. 2.23),

whereas the compressor's behavior is different at higher pressure ratios (which means higher rotational speeds) - when the surge line occurs much earlier, making it impossible to operate with inlet recirculation. In Fig. 2.24 (right), the axial velocity values at compressor inlet are reported. These plots clearly show the evidence of recirculation at the inlet of the compressor.

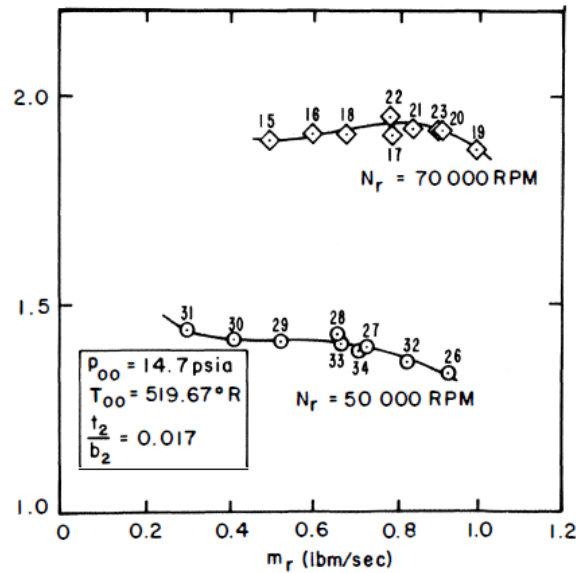


Fig. 2.23 - Turbocharger compressor characteristic curves (pressure rise against reference mass flow rate): local inducer and diffuser stall (taken from (Japikse, 1981))

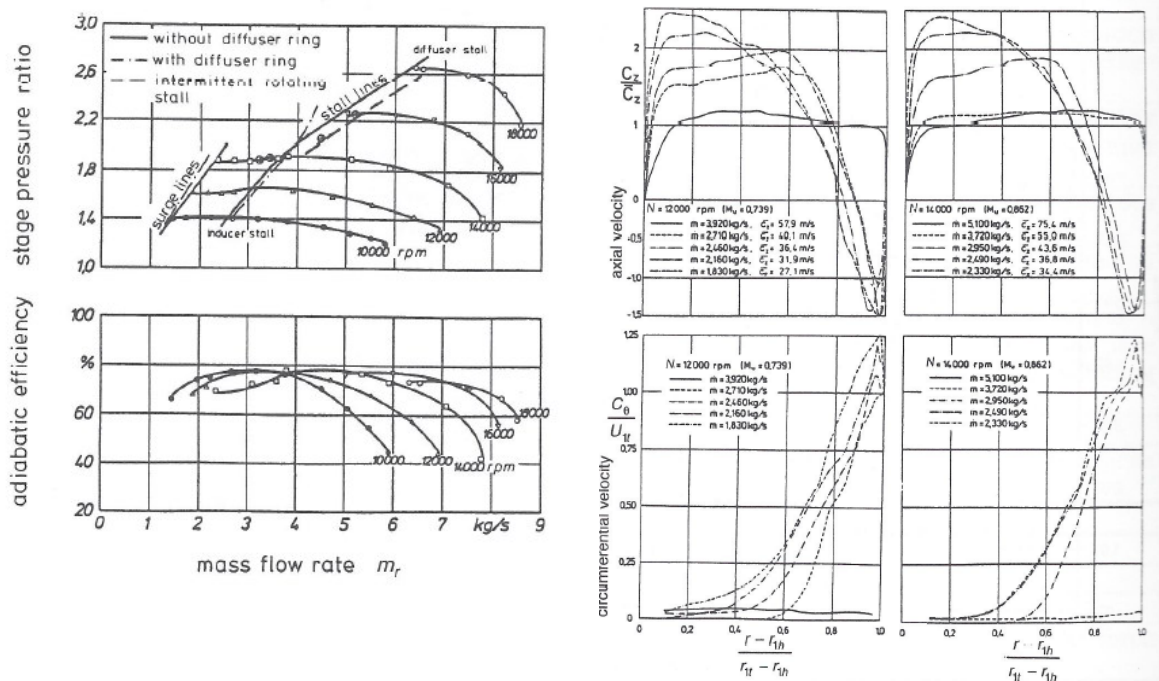


Fig. 2.24 - Maps (left) and velocity profiles at the impeller inlet of a centrifugal compressor (right) (source: (Kammer & Rautenberg, 1986); taken from (Japikse, 1996))

More recent studies regarding stationary stall were conducted by other authors. Girsberger and Rohne (Girsberger & Rohne, 1990) studied the performance of compressors with inlet recirculation phenomena: in particular, what they called the “mild surge region” (see Fig. 2.25 (a), in which they used static pressure tappings to analyze the stationary stall at the impeller inlet.) By also using laser velocimeter data (see Fig. 2.25 (b)), they found the recirculation region arises first in the passage and then moves towards the inlet by reducing the flow rate. Their measurements did not reveal any dynamic instability.

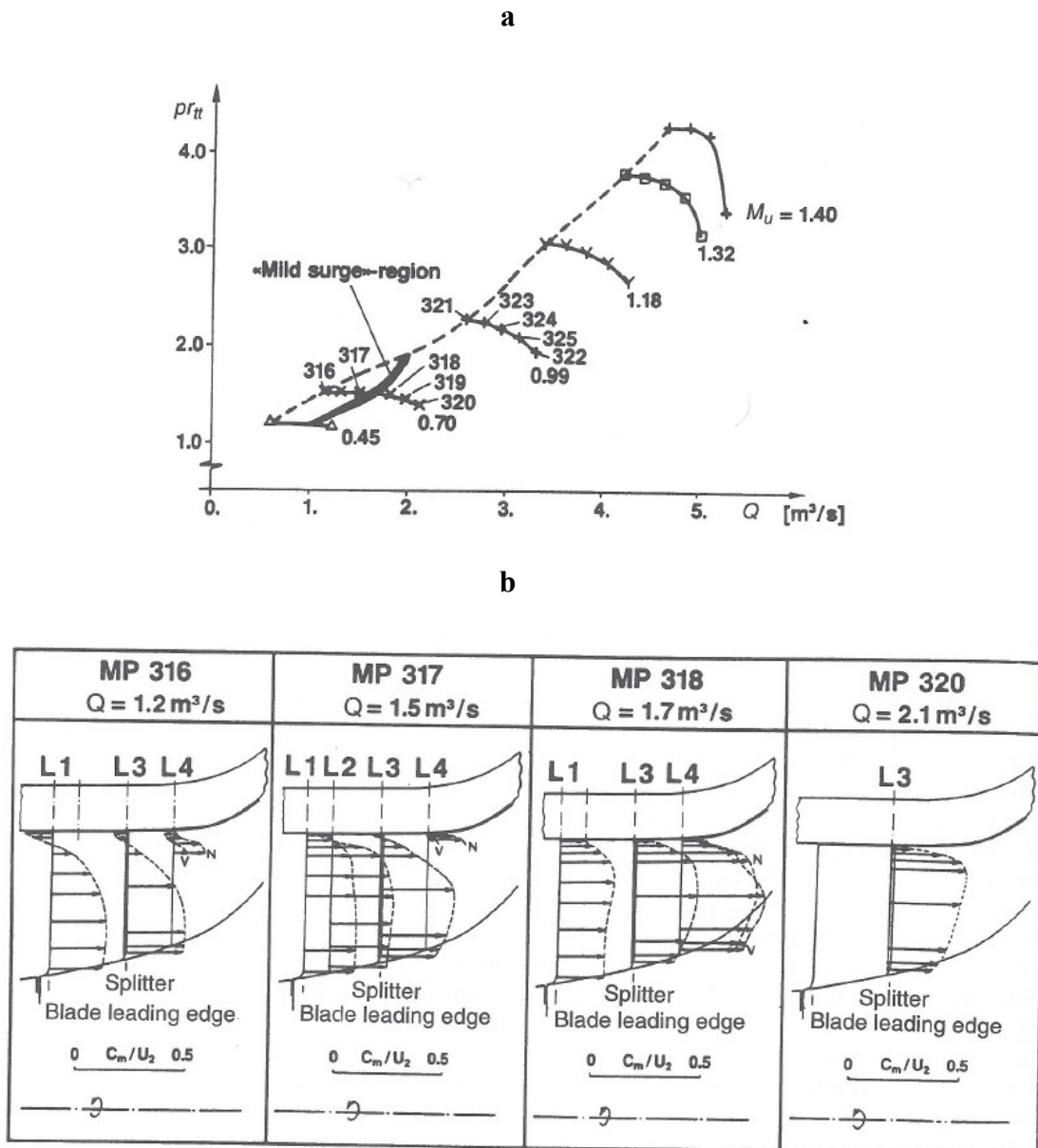


Fig. 2.25 - Experimental data centrifugal compressor: (a) compressor maps; (b) laser velocimeter data before and after splitter blade ($M_u=0.70$); (source: (Girsberger & Rohne, 1990); taken from (Japikse, 1996))

Barrand et al. (Barrand, et al., 1984) actually showed that impeller exit recirculation could be triggered before the inlet recirculation. They positioned three tufts at the impeller inlet and three at the impeller outlet; their results are showed in Fig. 2.26. It is possible to see that the swirl effect increases by reducing the flow rate; however, it is clear that before the inception of a new flow regime (see the last marker of (a) and (b)), backflow took place at the impeller exit first. Unfortunately, it is not possible to know if the phenomena at the impeller exit and inlet were related. Also, in that case, no evidence of dynamic stall was detected.

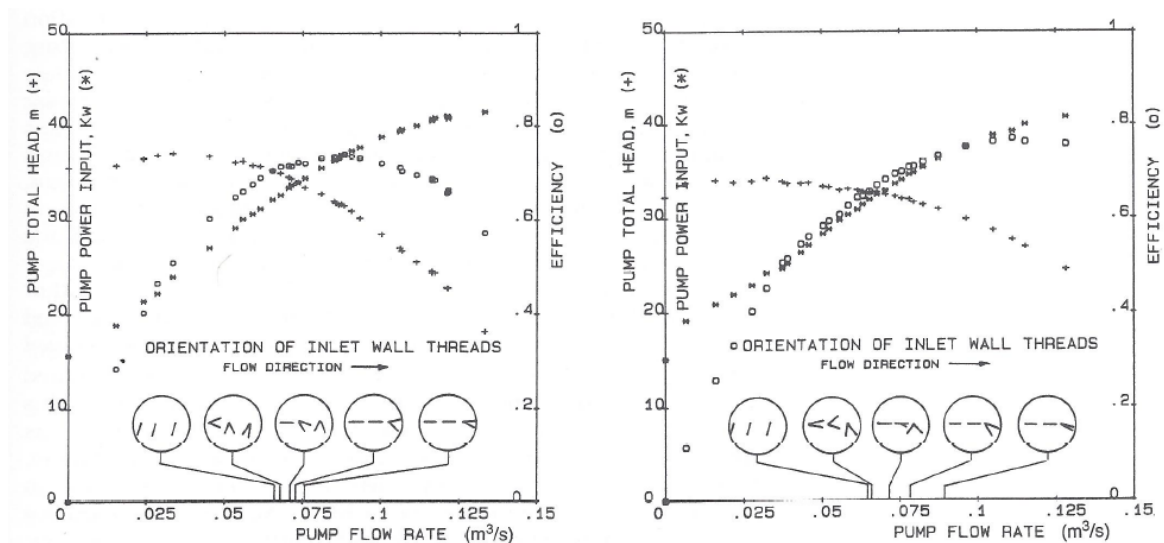


Fig. 2.26 - Experimental data of a centrifugal pump/compressor together with indicators which illustrate the orientation of the tufts, located at the inlet (left) and at the outlet (right) (Barrand, et al., 1984)

Assuming that the inducers does not stall, or that the flow restored and continued with a regular pattern, the flow passing through the impeller (the axial flow gradually becoming radial) receives strong Coriolis forces, which tend to separate the higher from the lower speed streamlines. This generates the so called jet/wake effect (firstly theorized in a two-dimensional model by Dean and Senoo (Dean & Senoo, 1960)), but the first reliable measurements were carried out by Eckardt (Eckardt, 1976), as shown in Fig. 2.27. This separation, or stationary stalled region of the impeller, had already been commonly observed at that time in most centrifugal compressors and can be partially reduced by high blade backsweep. The jet flow has the proper stagnation pressure while the wake has a small velocity with a considerable lower relative stagnation pressure. The wake can occupy considerable parts of the passage area.

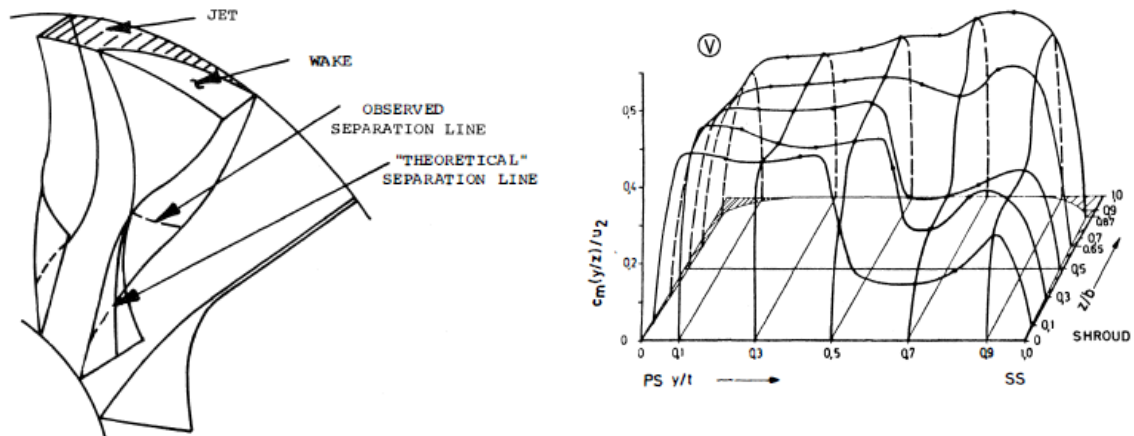


Fig. 2.27 – Separation, or stalled zone, at the impeller exit, i.e. the jet/wake phenomenon: (a) a 3-D sketch (source: (Dean & Young, 1977)); taken from (Japikse, 1981); (b) Velocity measurements of a centrifugal impeller with no backsweep, at $N=14,000$ rpm (source: (Eckardt, 1976)); taken from (Japikse, 1981)

The separation, or stationary stall region, was already observed in some diffusers as well. Japikse reported that in the case of vaneless diffusers, these phenomena were very common - since the streamlines close to the wall have less kinetic energy - but are subjected to the same radial pressure gradient, and thus the flow in these parts is swept back towards the impeller (see Fig. 2.28 (a)). This breakdown of the regular flow due to steady stall, decreases the diffuser performance and increase the possibility for the so called “stage stall”. However, it is very common that these separations, or stationary stall areas of the vaneless diffuser, do not cause an unstable behavior of the stage (stage stall), but only to a formation of some separation bubbles in the diffuser - i.e., small flow recirculating area, which can be seen as local inward flow phenomena at the impeller tip. In Fig. 2.28 (b), the consequent trend of total pressure and flow angle along the diffuser channel width are illustrated.

In case of a channel diffuser, or vaned diffuser, the situation changes. The channel diffuser is usually preceded by a so called “vaneless space” (or semivaneless space), which is important because it rules the fluid-dynamic of the diffuser inlet region and is useful to increase the pressure recovery by reducing the mass flow at constant speed (Japikse, 1981). Dean and Young stated, based on their work (Dean & Young, 1977), that a critical value of the pressure rise recovery exists before the stage instability occurs; they found this value to be 0.4 under subsonic working conditions.

If compared to vaneless diffusers, the channel diffuser and vaned diffuser (which typically have a reduced choke margin), can manifest steady stall as well - usually due to single separation phenomena.

This type of stall, can be avoided by carefully exploiting the diagram of the pressure recovery map when designing the diffuser - obviously depending on the application. A rule of thumb is to design channel diffusers with a high value of diffuser length-to-width ratio in order to avoid the transitory stall (a type of stall which arises in channel diffusers) (Japikse, 1981).

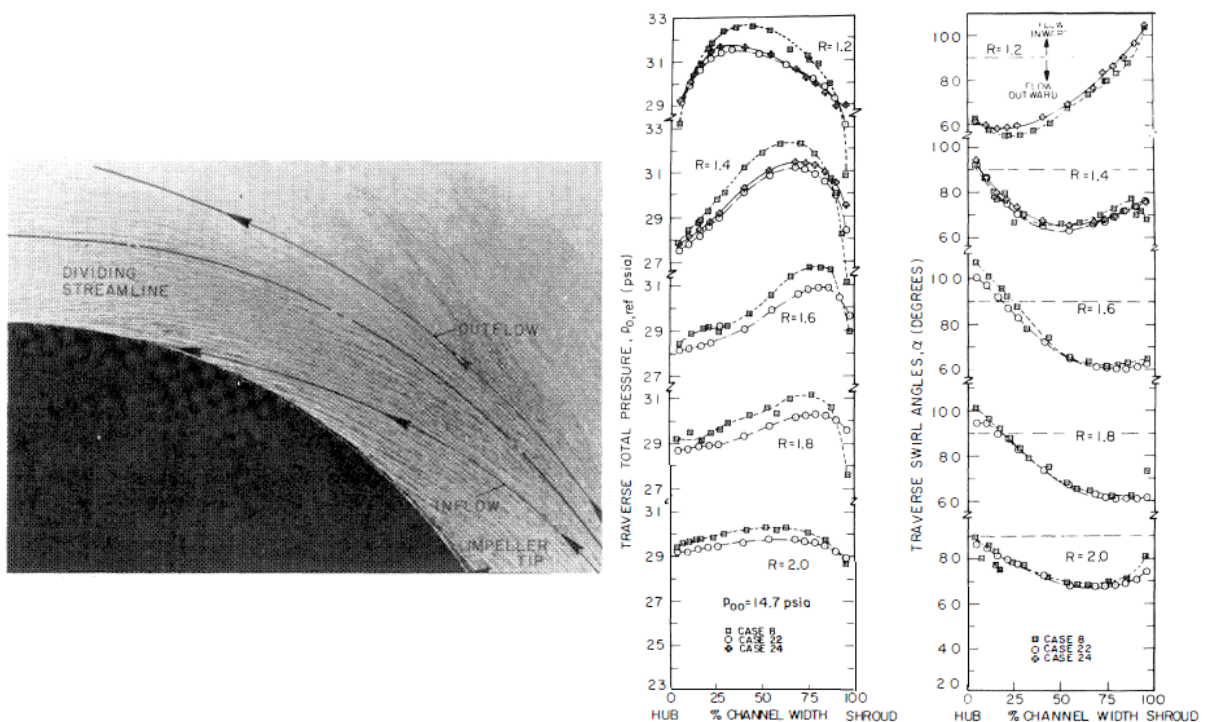


Fig. 2.28 - The reverse flow at the impeller outlet: (a) velocities streamlines; (b) pressure and flow angle variation along the blade channel width (taken from (Japikse, 1981))

The volute of a centrifugal stage was demonstrated to manifest stall due to the changes of its operativeness as the flow rate is reduced (Japikse, 1981; Japikse, 1982). However, the strong swirling flow of the volute has been proven to delay stall and thus the surge inception. Some notes regarding the aforementioned works need to be made, as reported in (Japikse, 1996). Most of the studies on stationary stall are not always complete, due to the lack of much information, especially on the blade design. Thus, it is not possible to generalize the results found in those works to apply to broader applications: also because, due to the new advancements and design methodologies, centrifugal compressors today have very different characteristics and performances. It is possible that, in some

cases, what those authors identified as steady-stall, could actually be characterized by some time-dependent features (nowadays a stall with weak periodicity is called quasi-steady stall).

2.3.2 *Dynamic Stall (Rotating Stall)*

In (Japikse, 1981), Japikse also describes the dynamic stall conditions as disturbances which rotate in the machine instead of in a fixed location. He observed that dynamic stall can exist in the inducer, in the impeller and in the diffuser as well, but he admitted to have a poor knowledge at that time of the dynamic stall condition: *"Many studies have reported the probable existence of dynamic stall conditions. Only a few have studied them in sufficient depth to provide an initial understanding of their basic characteristics. By contrast, far more is known of dynamic stall conditions in axial compressors"*.

Amann and Nordenson (Amann & Nordenson, 1961) were the first to distinguish between two types of dynamic stall: first stall, which consists of mild disturbances; and second stall, which leads directly to surge. Another significant work was produced by Abdelhamid and Bertrand (Abdelhamid & Bertrand, 1980), who reported dynamic stall in the impeller of a centrifugal compressor - although in that case, it was probably referred to the instability generated by dynamic stall in the vaneless diffuser.

Many other authors investigated the dynamic stall in vaneless diffusers. Some of them linked the onset of rotating stall with reverse flow. Jansen was one of them: stating that stationary stall must be generated before dynamic stall (rotating stall). He also derived the linear form of the governing wave equation by using the continuity and momentum equations in the radial and tangential directions, for unsteady, inviscid, and incompressible flow. His work was continued and extended by Senoo, Kinoshita, and Ishida (Senoo, et al., 1977), who arrived to the conclusion that a reverse flow in the vaneless diffuser would cause a surge or dynamic stall, depending on its severity and extension to the subsequent components (return channel and volute).

On the other hand, other researchers of the time were not completely convinced of this theory. Abdelhamid et al. (Abdelhamid, et al., 1979) reported that dynamic stall developed gradually in the vaneless diffuser space with the decreasing of the flow rate, and with a slight increasing in rotation velocity and amplitudes of the disturbances after the

critical operating point. Abdelhamid went on to further develop his theory with other authors. In 1980, his definitive work, carried out together with Bertrand, was published (Abdelhamid & Bertrand, 1980). They discovered that the inception of rotating stall strongly depended on the diffuser's diameter and width, as these dimension could make the instability occur earlier or later. They also found a correlation between the speed of the disturbances and the diffuser's diameter. In Fig. 2.29, the characteristic curves of the compressors tested is plotted; and it is evident that (i) the onset of the rotating disturbances occurred far before the inception of surge, and as is (ii) the change of mass flow coefficient at which the disturbances arise. This work was important because it finally confirmed the existence of two different rotating disturbances in the vaneless diffuser: a slowly rotating pattern was first identified as the flow rate decreased - these oscillations were successively replaced by others with higher speed and different pattern.

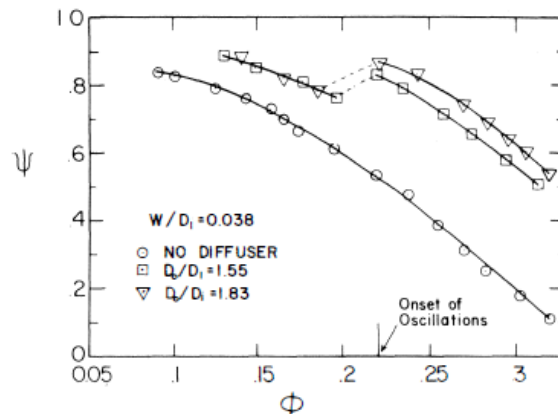


Fig. 2.29 - Performance characteristics and stability limit with different diffuser geometry (source: (Abdelhamid & Bertrand, 1980); taken from (Japikse, 1981))

Such pressure oscillations extend into the whole diffuser and are not only due to the rotating zones of boundary layer. The work thus remarks that dynamic stall can also arise in absence of reverse flow regions, and that stable flow conditions can coexist with reverse flow zones in the diffuser.

Many of the results of Abdelhamid and Bertrand's results were confirmed later by the studies conducted by Nishida et al 1988 (not referenced), who in their first report observed that by increasing the width of the diffuser channel, the onset of stall occurred earlier. In the second part of the study, Kobayashi et al. 1990 (Kobayashi, et al., 1990) also discovered the importance of the diffuser's inlet shape on the compressor stability. In the last part of the work, Nishida et al 1991 (not referenced) focused on rotating stall

suppression methods. Again, they observed the positive effect of reducing channel width, though leading to a consequent decrease of head. Similar results were found by eliminating the vaneless diffuser. In addition to this, they tested many low-solidity airfoil diffusers with different channel widths and different inlet radius ratios. They observed that these types of diffusers were able to delay stall inception; moreover, they found that the smaller the inlet radius ratio, the higher the stabilizing effect.

In the 1980s, the studies on dynamic stall (or rotating stall) led to conclude that the two main compressor components where rotating stall can take place are the impeller and the diffuser. Unfortunately, a universal process was never identified but many authors produced papers showing the different characteristics of rotating stall depending on the inception location and cause. It must be said that, today, the inception process of stall and the origin of surge is not yet fully understood in centrifugal compressors. In 1980, Abdelhamid (Abdelhamid, 1980) theorized a method of analyzing the stability of diffusers, and identified the possible conditions for abrupt stall of impellers. He found that forward leaning blade impellers are much more prone to manifest abrupt stall, generating flow oscillations at low rotational speed independently on the diffuser's layout. In this case, instability occurs at the right side of the peak. However, he concluded that even with backward leaning blades, abrupt rotating stall can manifest if the non-uniformity or perturbation of the flow exiting from the impeller (or entering in the vaneless or vaned diffuser) are such that the fluid cannot track back the designed streamline of the blade channel sufficiently. He deduced that when very strong perturbations occur at the rotor exit, the abrupt stall can occur well away from the characteristic peak. This phenomenon was linked to a relevant decay of flow, and resulted in a discontinuity of the compressor's rise curve.

Progressive rotating stall has been observed in many studies over the years. Lennmann and Howard (Lennemann & Howard, 1969) gave a qualitative description of the fluid phenomena occurring during this instability - thanks to an experimental analysis done by using hydrogen bubbles (see section 2.3.2). Their theory was confirmed by Mizuki et al (Mizuki, et al., 1978), who used an experimental approach and verified that the stall cells increased their dimension and velocity by reducing the mass flow rate. One of the most interesting works cited in this section is surely that of Y. N. Chen et al. (Chen, et al., 1994). They published a paper in which they sketched out the measured pressure field inside the blade channel, during rotating stall (see Fig. 2.30). The figure depicts the eight

most representative instants of the phenomenon (instants are numbered as a function of time). The cross-hatched areas are low pressure regions encircled by high pressure zones, whereas the dark areas are high pressure regions encircled by low pressure zones. Fig. 2.30 can be better interpreted and clarified by looking at Fig. 2.31, which reports the trend of the pressure variation along the blade channel streamline (Fig. 2.31 illustrates a reference line named “21” in each of the three plots to increase the assessment of the results). In instant 8 (Fig. 2.30), normal operating conditions are present, and the pressure increase along the channel is almost continuous, although some variations which should not be present at design conditions can be seen in the plot on the left of Fig. 2.31. In instant 20, a stalled region characterized by high pressure is present. This peak of pressure in the middle region of the blade channel is represented by the central plot of Fig. 2.31. Finally, at instant 24 (and 26), a low pressure stalled region manifests, which mirrors the trend shown in the right plot of Fig. 2.31 - in which it is possible to identify strong oscillations just upstream of this low pressure region

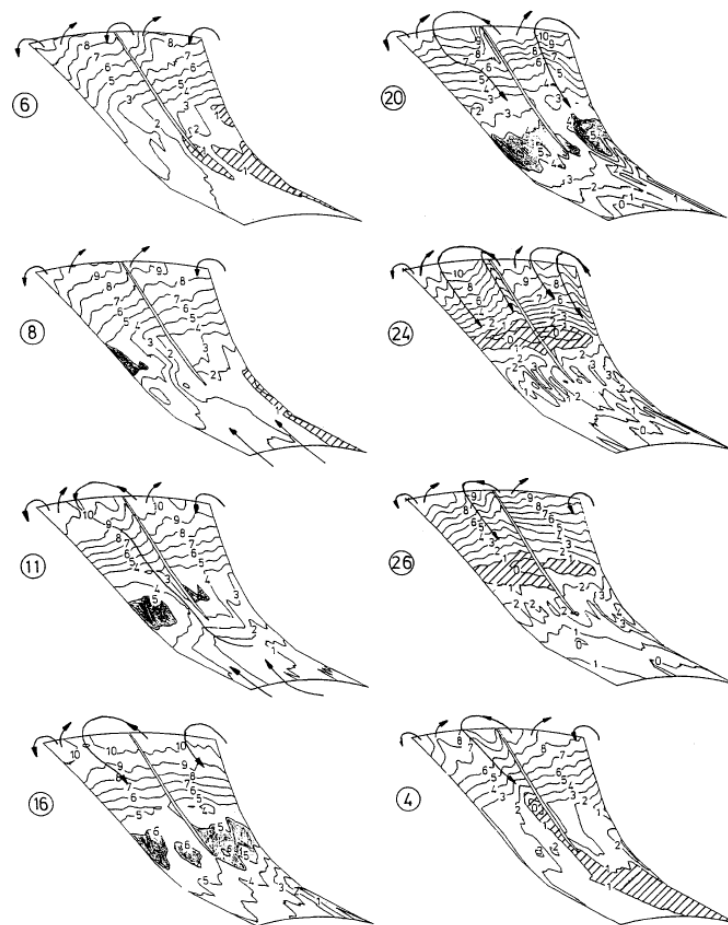


Fig. 2.30 - Pressure field of two adjacent blade channels during a rotating stall disturbance (taken from (Chen, et al., 1994))

Many attempts were made to predict the progressive stall of the impeller theoretically. The most reliable method was probably the one formulated by Kosuge et al. (Kosuge, et al., 1982), who found a consistent relation between the inducer tip incidence and the inducer-to-throat velocity ratio - however some experimental data partially contradict this type of prediction.

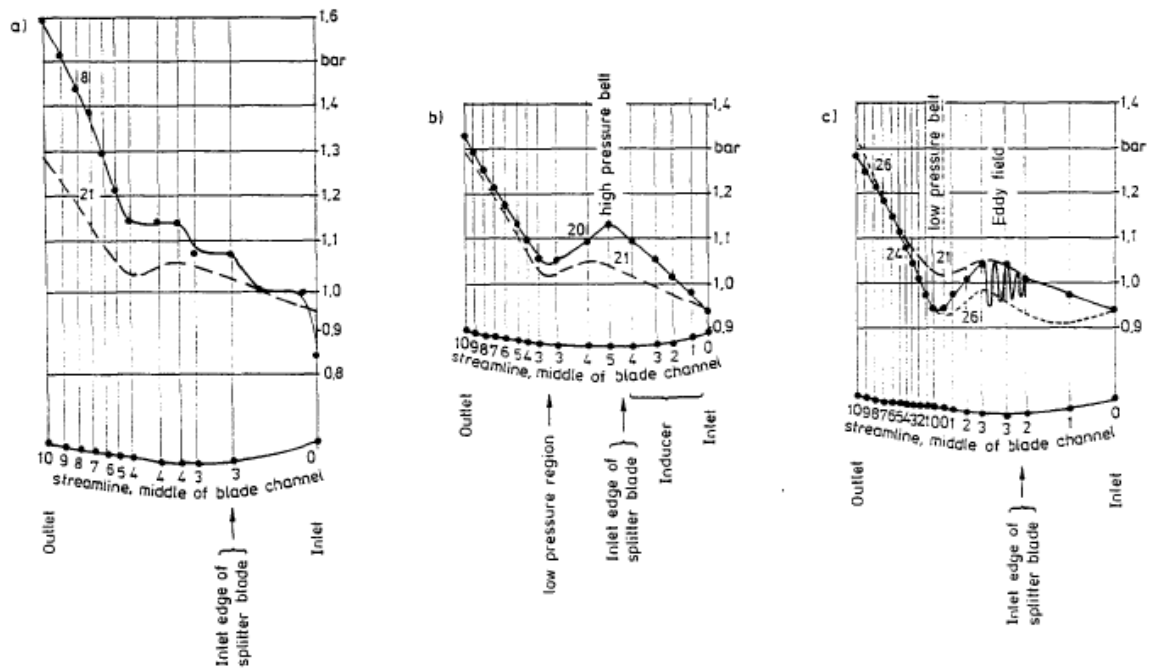


Fig. 2.31 - Pressure values along the middle streamline of the channel (left channel of Fig. 2.30) at time steps n.8 (nominal conditions, left diagram), n. 20 (rotating stall high-pressure zone, middle diagram) and n. 24 (rotating stall low-pressure zone, right diagram); (taken from (Chen, et al., 1994))

This was also later confirmed in a study of the effects of inlet distortions by Ariga et al. (Ariga, et al., 1987)) on the inception and characteristics of the impeller progressive rotating stall. Moreover, Fink et al (Fink, et al., 1992) successively demonstrated how the induced volute distortion, which can propagate up to the impeller inlet, has a notable effect on the inception of stall and surge. Based on what reported in this section, it is once again clear that a universal method for predicting this type of rotating stall is very hard to find.

A concise description of all the types of rotating stall observed in centrifugal compressors can be found in a single work, which was able to detect them all. This work was carried out by Frigne and Van den Braembussche (Frigne & Van Den Braembussche, 1984), who studied an impeller working with many different stator configurations, and the results are shown in Fig. 2.32. Three different system configurations, A (presented in Fig. 2.32 (a)), B, and C (both presented in Fig. 2.32 (c)), were performed. In Fig. 2.32, the static

pressure rise coefficient of the impeller, diffuser, and overall compressor, are shown for three values of rotational speed, as a function of the impeller exit flow angle, α_2 , for each configuration, respectively in Fig. 2.32 (b), Fig. 2.32 (d), and Fig. 2.32 (e). In configuration A, a throttle valve is very close to the compressor, thus the compressor operating range is extended to low values of flow rate. From the figure, it can be seen that a first rotating stall in the impeller inlet and diffuser exit occurred, generating 4 stall cells rotating at 14 % of the impeller rotational speed. This type of stall, arose at $\alpha_2=78^\circ$ was called “mild impeller rotating stall”. This phenomenon had not been observed before nor after, in fact; and thus, it is not possible to describe it in detail. The only thing that can be said is that this type of stall could be a precursor of vaneless diffuser rotating stall. By further reducing the flow rate, at $\alpha_2=81^\circ$, a different type of rotating stall manifested. The number of cells ranged between 1 and 3, with a rotational speed in the range of 20-30 % of the compressor velocity. This was called “abrupt impeller rotating stall” due to its rapid arrival at both entrance and exit of the impeller, and to its characteristic high amplitude. This type of instability was also described by Abdelhamid (Abdelhamid, 1980) and in (Abdelhamid & Bertrand, 1980) . Configuration B was then tested to exclude the effect of the volute; moreover, the valve was positioned upstream the compressor, together with a settling chamber - the related results are showed in Fig. 2.32 (d). It is clear that the curves are similar to that of configuration A, but the effect of the chamber led to surge at a certain value of the flow rate. At the maximum value of the rotational speed, surge manifested when the peak of overall static pressure rise coefficient was achieved. On the other hand, at the lowest rotational speed, Surge was preceded by rotating stall, which arose in the impeller - in this case, also around the peak of the overall compressor $C_{p,s}$, with one-to-three stall cells with a normalized rotational speed of 70-80 %. As the flow rate decreased, the amplitude of the disturbance progressively increased, due to the recirculating region propagation: and for this reason, it was defined as “progressive impeller rotating stall”.

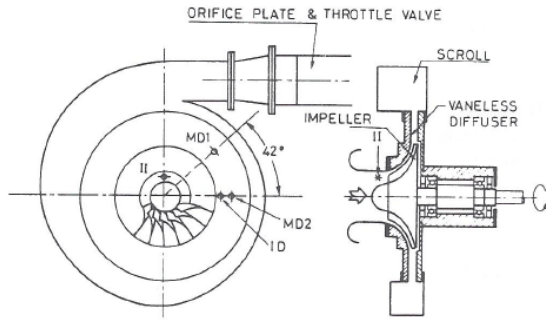
Configuration C - which basically consisted of configuration B with the addition of an inlet guide vane positioned before the impeller – was performed in a similar manner. In this case, as the impeller was unloaded, thanks to the stationary raw positioned upstream thereof, another type of rotating stall was identified; this was called “vaneless diffuser rotating stall”. This instability manifested at $\alpha_2=76^\circ$ (i.e., before the other two cases), with 3 cells rotating at a relative rotational speed of 20%. An important thing to mention is that, in this case, rotating stall occurred well before the overall characteristic curve peak. By

further reducing the mass flow rate, this rotating stall evolved into another form, with only two stalled cells rotating at a relative speed of about 15 %. This phenomenon happened immediately after the overall characteristic peak - after the origin of the progressive impeller rotating stall (with the same characteristics as described above). Frigne and Van den Braembussche's experiments (Frigne & Van Den Braembussche, 1984) proved fundamental as they supported the thesis of other previous authors such as (Abdelhamid, et al., 1979), Jansen (Jansen, 1964), Senoo and Kinoshita (Senoo & Kinoshita, 1978); and was also later confirmed by new measurements successively taken by other investigators (Kobayashi, et al., 1990). The different type of rotating stall identified by these authors are the types that still are known today.

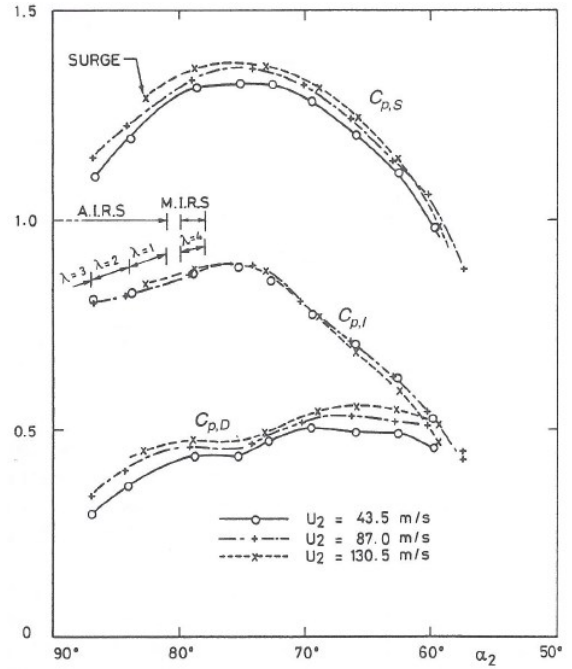
The stability of vaneless diffusers, which, based on the Senoo's work (Senoo & Kinoshita, 1978), is valid only if the inlet flow angle is lower than a critical value α_{2c} : which depends on the diffuser width and length, flow perturbations, and inlet velocity, Stability has proven to be increased, as cited above, by reducing the diffuser width – which can obviously lead to lower static pressure rise and high velocity at the volute inlet, which causes losses and low efficiency (Ludtke, 1983). Other techniques to increase the stability have been investigated. Abdelhamid (Abdelhamid, 1987) demonstrated an increase of stability in vaneless diffusers by adding small vanes at the diffuser exit. Obviously, a critical value of blade angle would exist (depending on the flow angle): if such value were to be exceeded, stall of the vanes would take place. Abdelhamid's work, gave another evidence of the benefits that compressors gain in stability thanks to vaned diffuser. Regarding this type of diffusers, an investigation on the effects of vaneless space dimensions on stability was carried out in (Yoshida, et al., 1990). That work proved that by reducing the impeller to vaned diffuser radial gap, rotating stall of the diffuser occurred at lower flow rates. However, despite this benefit, an excessive decrease of this gap can cause impeller rotating stall, especially for high loaded impeller exit geometries.

Another study, led by Japikse (Japikse, 1980), proved that the number of vanes in a vaned diffuser plays an relevant role on the stability of the compressor. He found that the reduction of the number of vanes led to a notable increment of the stability field (maintaining the overall performance of the compressor almost unchanged). This effect was more evident at high rotational speeds: which means that the number of the vanes can have a sensible effect on the stability of both the impeller and the diffuser - probably by stabilizing the interaction between these two adjacent components.

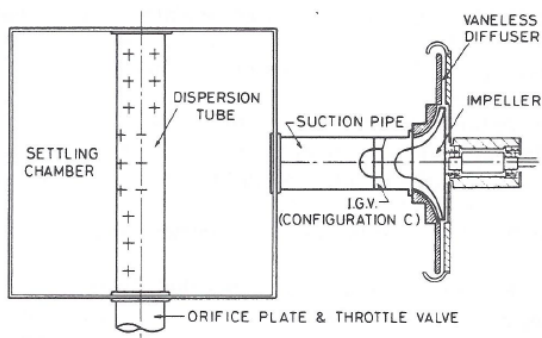
a



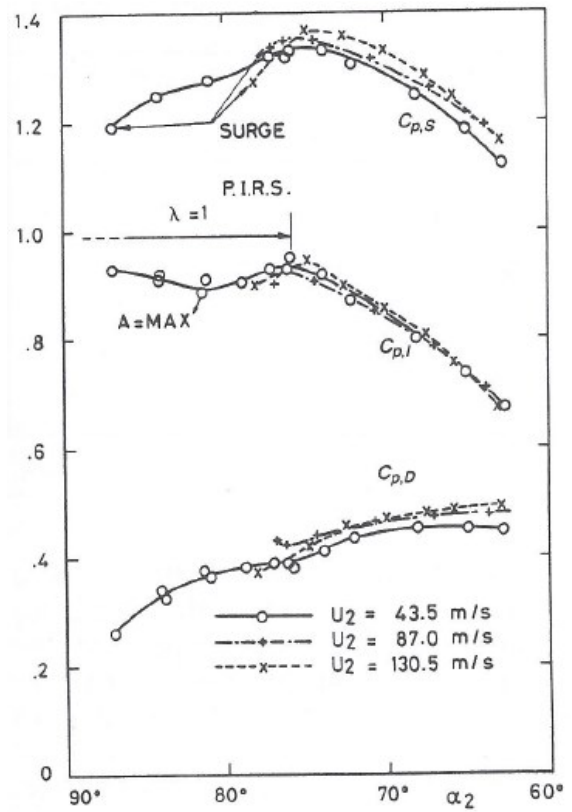
b



c



d



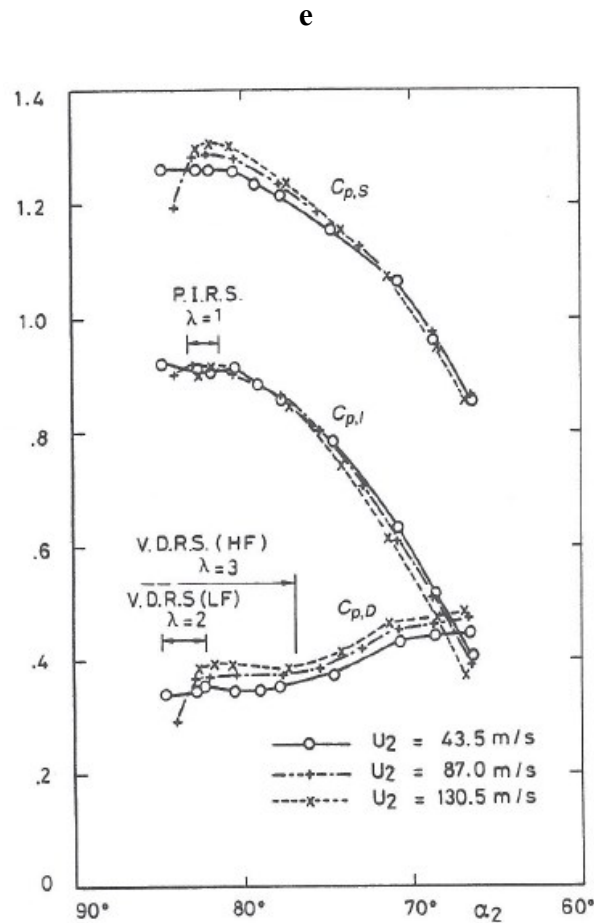


Fig. 2.32 - Experimental tests of a centrifugal compressor with different system configurations: (a) Configuration A; (b) rotating stall observations referred to Configuration A; (c) Configuration B and C; (d) rotating stall observations referred to Configuration B; (e) rotating stall observations referred to Configuration C (source: (Frigne & Van Den Braembussche, 1984); taken from (Japikse, 1996))

2.3.3 Stage Stall and Surge

In (Japikse, 1981), another concept of stall was also described. In fact, Japikse also treated the topic of “stage stall” and surge. Stage stall is the point at which the entire stage behavior becomes unstable (which can be usually associated to the left hand part of the characteristic curve). As mentioned above, a centrifugal stage can be subject to different types of stall, but it has proven to be less prone to these instabilities. In fact, it was observed that the overall stage can perform stably even with several areas of instability (rotating stall). However, as the flow rate continues to be decreased (with constant compressor rotational speed), a critical stable operating point (usually the peak of the stage curve) is achieved, at which point the overall stage performance is no longer stable. Over the years, it was proven that this does not directly imply surge condition, and that a centrifugal stage can operate for a reasonable range of time in these conditions (though surely vibrations and

overheating cannot be underestimated). However, depending on the unsteadiness level of the operating point, if an important flow perturbation arises (such as a rapid transient), the stage stall can degenerate into a temporary surge (an isolated event of backflow) or into a well-developed surge (also depending on the system layout). At that time (1980s), the mechanism of surge had been already introduced by Greitzer, as also reported by Japikse (Japikse, 1981). In (Japikse, 1981), he once again underlined the characteristics of surge as a noisy periodic phenomenon which can often result in a violent flow process also generating backflow. He said *“In some cases, the surge is mild with modest noise levels. In other cases, the surge is so violent that a single surge cycle can destroy a very complex and expensive machine”*. He also described the surge as *“a self-excitation of a dynamic system for which stalling of the stage is the driver and the entire network is driven, providing a feedback loop through the piping to which the compressor is installed”*. This leads to the conclusion that, even then, the stall stage was considered as the precursor of surge, even in centrifugal compressor

More recently, even though Greitzer's theory was proposed for axial compressors, it was demonstrated to be applicable to centrifugal compressors as well. In fact, many authors used his nonlinear model and extended it for further analyses and predictions of surge behavior of centrifugal compressor. An important example is given by the work of Hansen et al. (Hansen, et al., 1981), who experimentally tested the stable and unstable conditions of a centrifugal compressor by using high frequency pressure transducers and hot wires. They were unable to determine the positive slope side of the compressor curve, but they acquired precious data during surge. They used the Greitzer model, and achieved a satisfying agreement of surge data.

Another useful work was that of Fink et al. (Fink, et al., 1992), (already cited in a previous section of this chapter). Firstly, they experimentally obtained the turbocharger compressor maps - even the positive slope side (only at low rotational speed with a close coupled valve). The compressor was then tested with 2 layouts: one with small and another with larger compressor downstream volumes. In the latter configuration, they recorded data in mild surge and deep surge conditions (by further closing the throttle, see Fig. 2.33), observing that: (i) mild surge was accompanied by a chugging noise, and (ii) the deep surge process consisted of three main portions (see a quiescent stage, a mild surge characterized by the Helmholtz frequency of the system, and the backflow accompanied with a loud blowdown). In the same work, a deep analysis of the data from steady-state and

high response probes installed in different locations along the compressor was done (see Fig. 2.34 (a)). The investigations led to the conclusion that inducer tip recirculation, present at each deep surge cycle well before the overall backflow occurrence, was caused by the recirculation at the tongue of the volute (see Fig. 2.34 (b)).

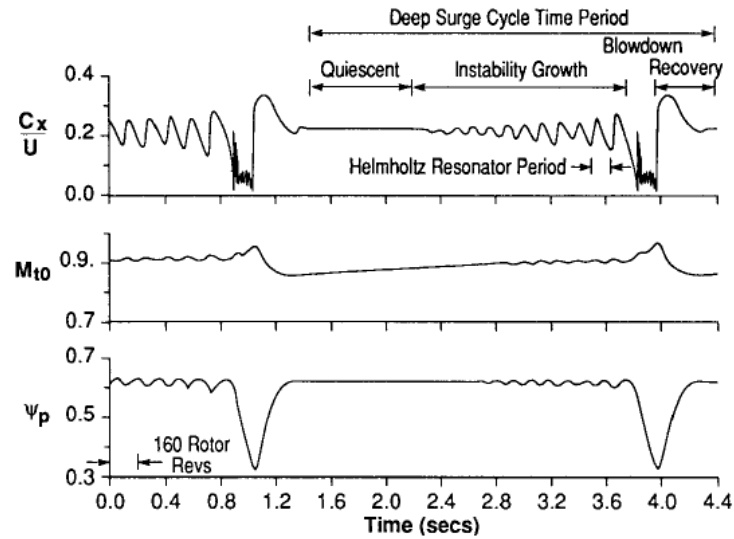


Fig. 2.33 - Deep surge oscillations: adimensional axial velocity, Mach number and isentropic head coefficient (taken from (Fink, et al., 1992))

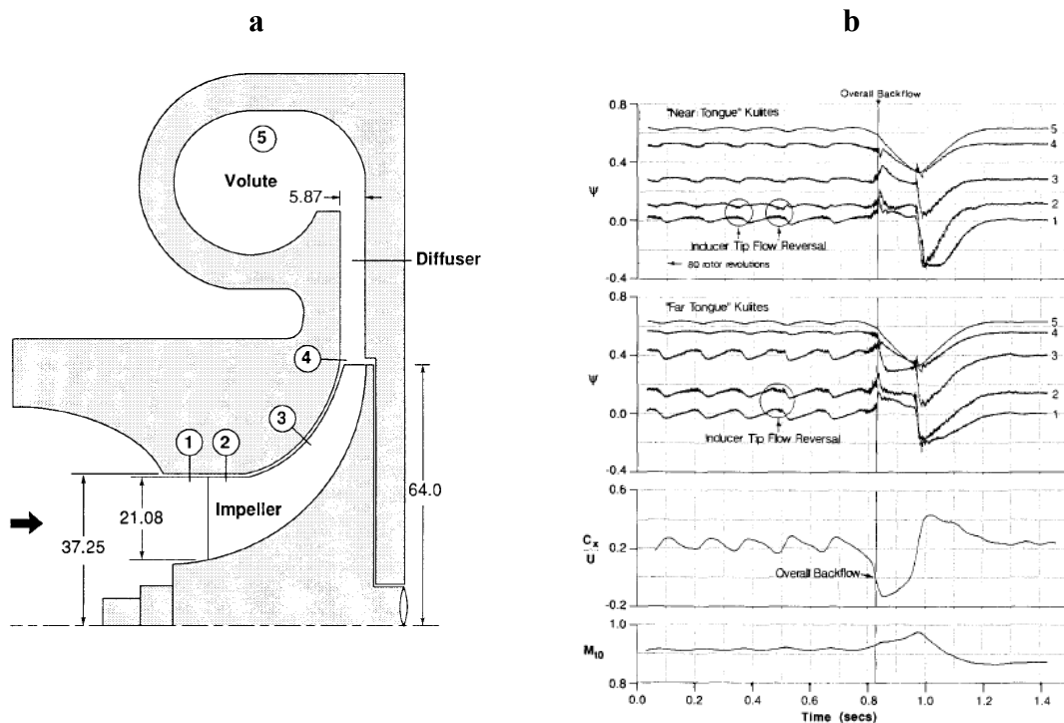


Fig. 2.34 - Measurement of surge phenomenon in a centrifugal compressor: (a) location of the sensors (displacements are expressed in mm); (b) compressor static head coefficients during deep surge with $Mu \approx 0.92$ (taken from (Fink, et al., 1992))

Moreover, Fink et al. connected the asymmetric inducer stall, caused by the scroll distortions, to the inception of surge. The influence of inducer rotating stall on the surge onset was thus reputed not relevant. A study on the dynamic response of centrifugal compressors was conducted by Wachter and Lohle (Wachter & Lohle, 1984), who experimentally tested a compressor by imposing dynamic closure of the control valve. The results showed that, by imposing cyclic variations of flow through the compressor, the operating point demonstrated to significantly diverge from the steady-state characteristic curve (even with reduced imposed oscillations); it was noted in every experiment that the dynamic curve obtained became flatter. More recently, the Greitzer model concept was successively used to simulate surge in modern multistage compressors. This also helped to develop control systems dedicated to this phenomenon. An example is the investigation conducted by Arnulfi et al. (Arnulfi, et al., 1999; Arnulfi, et al., 1999), see Fig. 2.35.

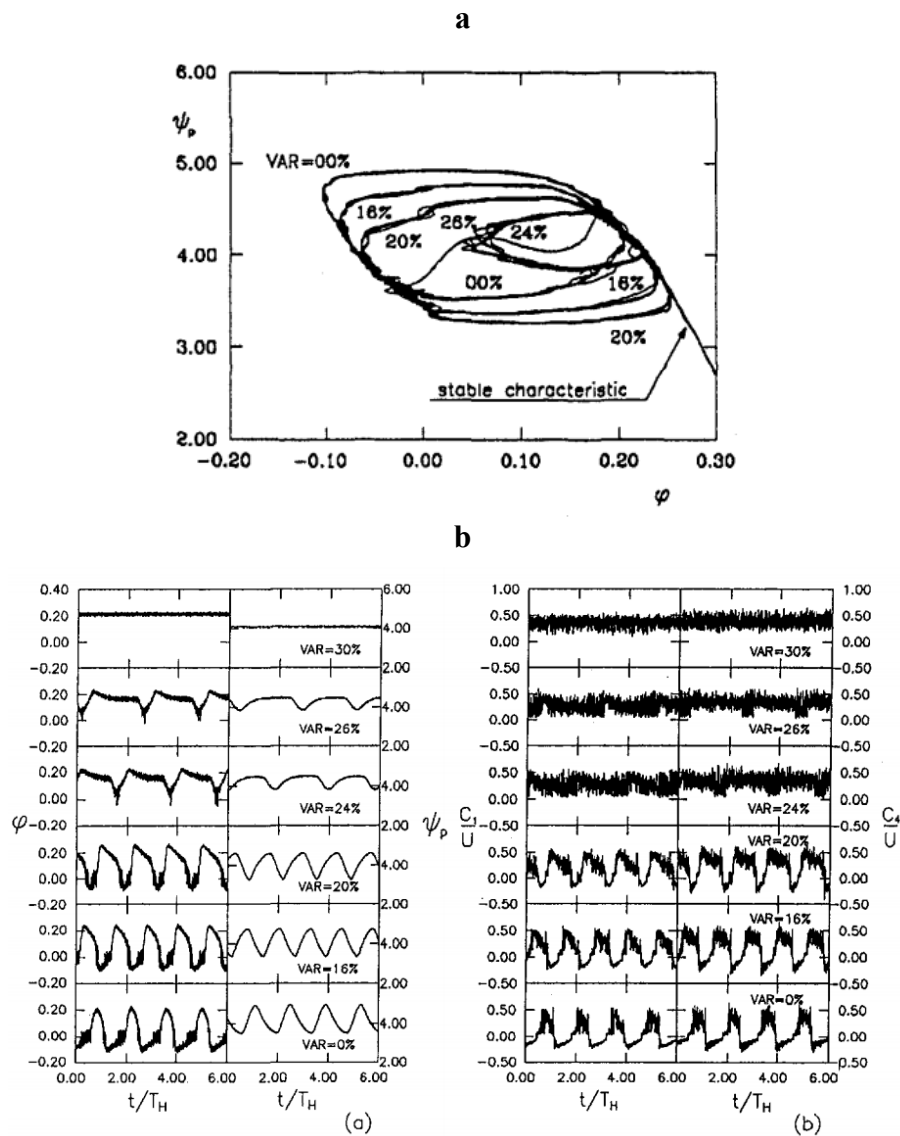


Fig. 2.35 - Surge at different valve setting (Arnulfi, et al., 1999): (a) operating point; (b) flow coefficient (left) and pressure coefficient (right)

They carried out an experimental and theoretical analysis on a low-pressure multistage centrifugal compressor, detecting different degrees of surge - depending on the valve setting (see Fig. 2.35). Fig. 2.35 (a) depicts the operating point of the compressor during a surge cycle, whereas in Fig. 2.35 (b) the pressure coefficient (right) and flow coefficient (left) measurements are plotted as a function of time. They also developed a non-linear lumped parameter model to simulate the various degrees of surge experimentally performed. In Fig. 2.36, the validation of their model is presented, demonstrating a high accuracy of the model in simulating both classic surge and deep surge; this is evident by looking at the compressor operating point, flow, and pressure coefficient in classic surge (respectively in the top-left corner and bottom-left corner), and deep surge (respectively in the top-right corner and bottom-right corner).

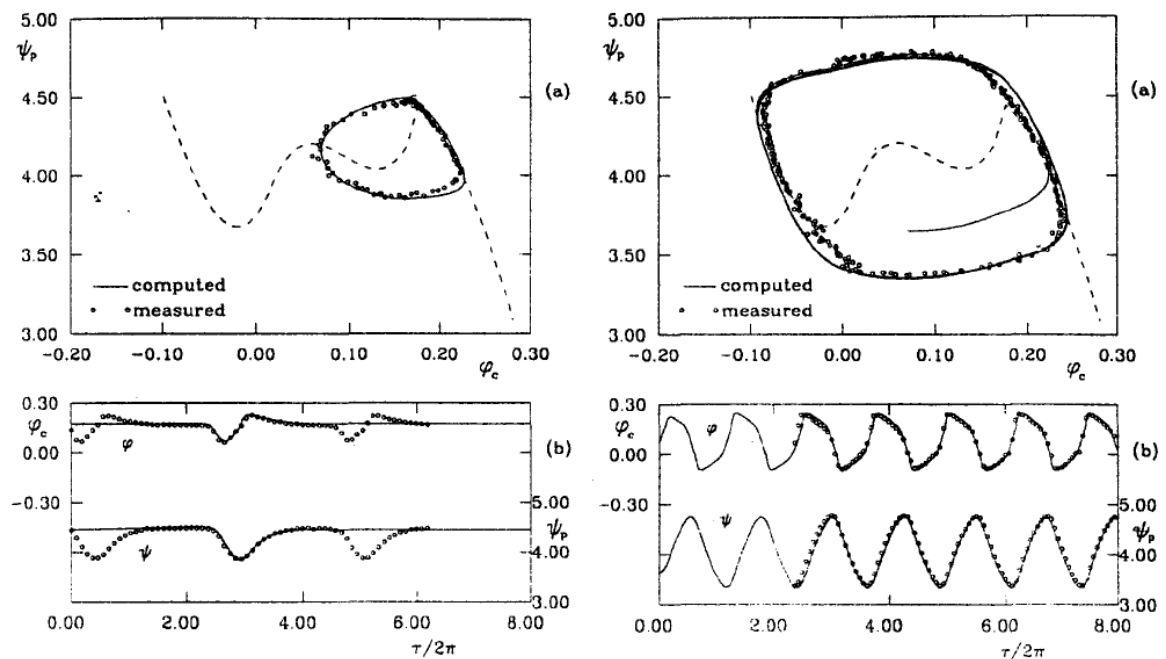


Fig. 2.36 - Classic and deep surge. Comparison between experimental data and model results (Arnulfi, et al., 1999)

Their experiments proved, together with newer experiments, that stall and surge are complex phenomena and it is difficult to predict which of these two events will exactly occur without a correct modeling. Many years of research were highly useful in that sense since now we now that generally, as also reported in (Japikse, 1996), and previously showed in this chapter, rotating stall is more often detected at low rotational speeds (i.e. at low pressure ratios), whereas surge is easier to be found at higher-pressure ratios - but obviously the type of instability strongly depends on the entire system characteristics.

2.4 Recent Developments

2.4.1 *Current Methodology*

Obviously, current methods of studying stall and surge are different from when the research started.

One of the most advanced methods currently in used is the CFD (Computational Fluid-Dynamic). This instrument started to be employed by the end of the 1990s, and thereafter it became increasingly popular and reliable. The CFD analysis proved to be effective in simulating:

- modal activity before stall (Hendricks et al. (Hendricks, et al., 1997))
- Rotating stall (Hendricks et al. (Hendricks, et al., 1997) and (Niazi, 2000)), the flow characteristics in full-span cells (Saxer-Felici, et al., 1998) multi-lobed rotating disturbances in a multistage high-speed compressor (Dodds and Vahdati (Dodds & Vahdati, 2015)))
- Stall/unstall Hysteresis (Choi et al. (Choi, et al., 2013))
- Surge behavior (Hendricks et al. (Hendricks, et al., 1997))

Other works later focused on vorticity and its influence on the inception mechanism of instability. Some authors identified the leakage vortex of a blade which moved towards the leading edge of the following blade as the beginning of the spike-type inception (Hoying, et al., 1988). This hypothesis was not completely supported by Inoue et al. (Inoue, et al., 2001), who suggested that what was noted in (Hoying, et al., 1988) was a radial vortex attached on the casing. A recent investigation on an axial compressor was presented in (Zaki, 2009): the first stage of a multistage axial compressor of a space shuttle engine was analyzed by using an advanced turbulence model in order to identify the stall onset (see Fig. 2.37 (a)). A shock wave arose (caused by the flow Mach number becoming greater than one) and moved in upstream direction from the leading edge of the blade. This phenomenon demonstrated to be stronger near stall (Operating point B). Moreover, the stage loading in the vicinity of the stall condition made the tip blade vortex grow stronger than in nominal operating conditions (operating point A). This also implies that the interaction between these two phenomena became more unsteady, and produced a low

momentum region close to the adjacent blade tip leading edge - causing flow spillage over it.

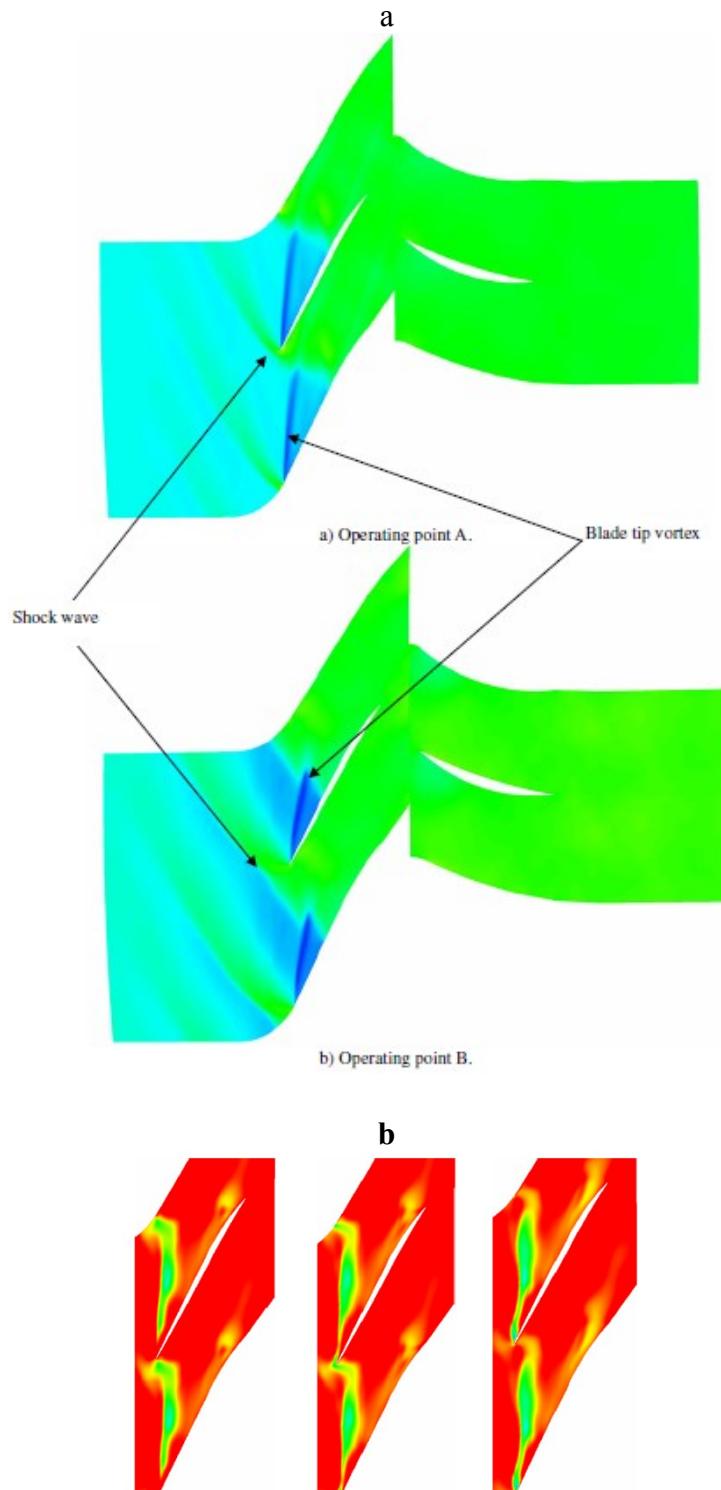


Fig. 2.37 - (a) point A (Design point), B (near stall). In blu, low pressure area, in green high pressure area; (b) stall condition; (taken from (Zaki, 2009))

This behavior obviously led to stall inception and agrees with the stall inception criterion of Vo et al. (Vo, et al., 2005). This is confirmed by Fig. 2.37 (b), which shows

how the tip clearance vortex flow influenced the flow field by generating negative axial velocities. A successive work, carried out by Pullan et al. (Pullan, et al., 2015), described the formation of tramped-shaped vortex (highly similar to the vortex proposed by Inoue et al.), explaining what was seen more than 50 year earlier by Stenning and Kriebel (1957) (not referenced) (see Fig. 2.38 (a), (b) and (c)). Moreover, Pullan et al. also proved that these vortices were not generated by tip-clearance flow.



Fig. 2.38 - Formation of the Tramped Shaped Vortex: (a) leading edge separation circle; (b) vortex tube forms, uppers and moves circumferentially along casing; (c) lower end of tube moves downstream along suction surface; (taken from (Pullan, et al., 2015))

A last example of CFD analysis is given by a recent work carried out by Trébinjac et al. (Trébinjac, et al., 2015). In this paper, a full-annulus simulation of a transonic centrifugal compressor was done to identify the surge inception mechanism. They found that 6 stall cells, Fig. 2.39 (a), rotating at 7 % of the compressor rotational speed, developed over the entire span between the last stable flow field condition (time step a) and instability (time step f). These stall cells induced the surge of the compressors. From the velocity field showed in Fig. 2.39 (b), which represents the flow field at time step (f) it is possible to see the absolute velocity vectors (in black) and the scheme of the flow trend (in white). The fluid is forced to flow from vane channel 2 (which is blocked) to channel 3, whereas channel 1 operated in nominal conditions. This structure of the flow, developed in three adjacent channels, led to the generation of the 6 stall cells - showed in Fig. 2.39 (b).

It is clear that CFD represents key technology to increasing the knowledge of the phenomena occurring in compressors during unstable behavior (Biliotti, 2013). On the other hand, one drawback is the great amount of data which needs to be stored in the fully unsteady simulations of an entire machine; which is the reason why many authors apply numerical models to specific parts of the compressors.

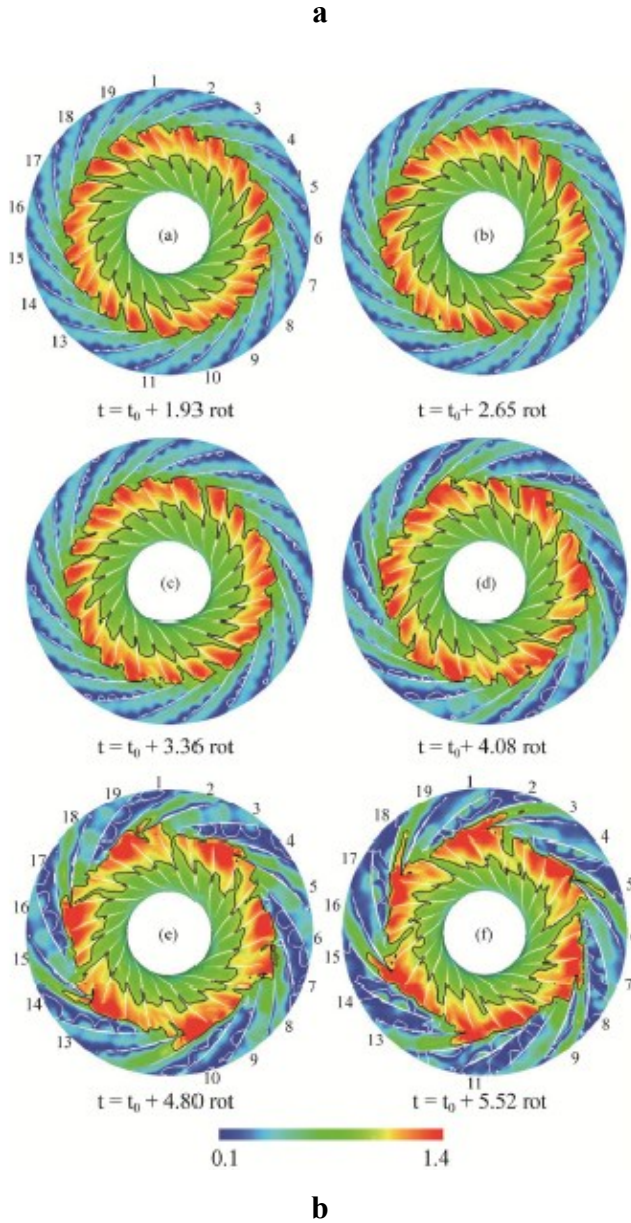


Fig. 2.39 - CFD Analysis of surge inception in a centrifugal compressor: (a) instantaneous Mach numbers at various time-steps before surge; (b) Absolute velocity vectors at time-step f (referred to Fig. 2.39 (a)); (taken from (Trébinjac, et al., 2015))

However, this procedure may not give reliable results in unsteady conditions, since it neglects to consider every interaction among the nearest components of the machines. In this context, the need for reliable experimental data becomes fundamental to validate such models - an example is given by the works of Everitt and Spakovszky (Everitt & Spakovszky, 2013), and Spakovszky and Roudnerr (Spakovszky & Roduner, 2009). In (Cameron, 2007), an experimental investigation was conducted by Cameron in order to identify the instability inception mechanism in a high-speed axial compressor. In that work, a new methodology based on a windowed two-point correlation between close sensors was used. This allowed the spatial and temporal resolution of the compressor precursor behavior of stall and stall inception. They created a non-uniform tip clearance by means of magnetic bearings in order to levitate the compressor rotor. The results highlighted the relation between length-scale stall inception phenomena and specific features of the tip clearance flow.

(Other recent works regarding stall and surge will be cited in the next chapter, in which an experimental activity literature review is carried out).

Many studies over the last years have been experimentally developed, especially for centrifugal compressors (since despite the use of CFD represents a significant modern advancement, its results can be affected by a certain level of uncertainty, (Cornelius, et al., 2013)). The tendency is to locate dynamic pressure probes at different positions - especially in diffusers which, based on the past works, are the element in which instability usually occurs. Spakovszky and Roudnerr (Spakovszky & Roduner, 2009) carried out an experimental investigation of a turbocharger centrifugal compressor, finding that without bleed air, the inception of stall is governed by spikes in the vaneless space (i.e. before the vaned diffuser). Moreover, it was found that (i) the bleed air (used for secondary flow systems) reduced the stable operating range of 50 %, and (ii) a four-lobed backward traveling rotating stall wave was identified. The authors could not explain in details which factor governs the type of instabilities inception: if spikes or modes; they only hypothesized that it must depend on the stability of the semi-vaneless space characteristics. Other experimental work was conducted by Ferrara et al (not referenced), who carried out dynamic tests in compressors with different geometrical configurations by closing the throttle until the instability inception occurred. The authors estimated that, the pressure oscillation amplitudes of sub-synchronous frequencies was comparable to that of synchronous ones. Finally, it is worth to cite one of the most attractive pieces of

technology for evaluating the three-dimensional flow characteristics in detail; the PIV. Dazin et al. (Dazin, et al., 2008) used the PIV for analyzing the flow field characteristics of a vaneless diffuser, and to identify three rotating stall cells. Fig. 2.40 illustrates the graphic CFD results in terms of radial velocity normalized to the impeller velocity, showing that before the flow destabilized, periodical wakes referred to any impeller blade were present (Fig. 2.39 (a)). On the other hand, once the rotating stall arose, it was possible to see the three stalled cells (Fig. 2.39 (b)). Their analysis demonstrated the possible formation of a blockage in the vicinity of the hub side diffuser entry.

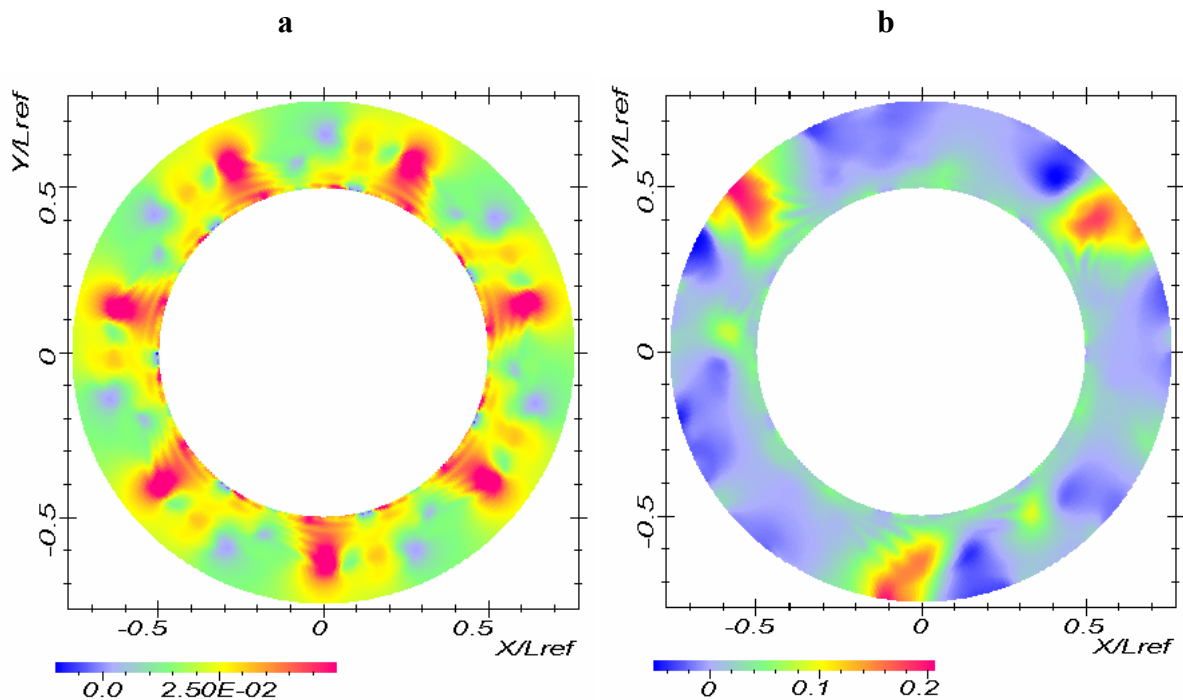


Fig. 2.40 - Radial velocity normalized with respect to impeller tip tangential speed: (a) before the flow destabilizes onset (radial), (b) in rotating stall conditions (taken from (Dazin, et al., 2008))

2.4.2 Future Perspective of the Research: The High-Speed Compressors

The work presented above, and in general much of the work of the time, were assumed the hypothesis of 2D incompressible flow. The effect of compressibility needs to be further investigated since the results obtained suggest that the phenomena which occur at low speeds are different from those which occur at high speeds. Based on the theories developed between then and now some general deductions can be made:

- High-speed compressors do not manifest the same stall inception phenomena of low-speed compressors. This is testified by the discovery of new modal disturbances with circumferential and axial structure (Hendricks,

et al., 1993; Bonnaure, 1991). Therefore, there is yet no universal theory to explain all types of stall cell inception (spike-type, modes type, vortex and rotating instability), but it will probably be impossible to identify anyway since this phenomenon could be characterized by randomness.

- High speed compressors often exhibit spike disturbances preceding full-span stalled cells. Classic modal perturbations were noted only in a narrow range of speeds, due to the perfect stage matching in those ranges, which does not allow the spikes to arise (Day, et al., 1999)
- Surge phenomena is very often preceded by rotating stall, especially at high-speed tests (Tryfonidis, et al., 1995). However, the rotating stall features are very hard to be captured, due to the quick transition to surge (Day & Freeman, 1994) (this deduction has to be linked to the work of Emmons, who was referring to a sort of shock wave caused by stall, and reported an asymmetric feature of the surge at its beginning)

3 Experimental Activity -

Part I

This chapter describes the experimental investigation on the axial-centrifugal compressor installed at the Industrial Laboratory of the Engineering Department of the University of Ferrara, implemented with thermodynamic sensors (pressure, temperature, mass flow rate sensors). The development and description of the test rig, the methodology of the tests and the results are presented.

3.1 Introduction

The experimental analysis of compressor performance is one of the essential factors in the turbomachinery sector, not only because it ensures the reliability of a machine but also because it shows the limits of its operating range and its critical working conditions. It is also undeniable that these data are helpful for giving guidance for improving the designs of actual dynamic compressors and gas turbines.

One of the crucial test field analyses is the evaluation of off-design conditions and flow instability phenomena. The experimental activity allows the turbomachine dynamic behavior to be examined and predicted, which is, nowadays, one of the main issues investigated by researchers. The two main instabilities which can occur on compressors, due to an excessive reduction of mass flow rate, are rotating stall and surge. Both of them cause a rapid change in the flow pattern in the compressor.

Rotating stall is a flow instability which develops circumferentially through rotating “stalled” cells around the annulus which sometimes can extend along the entire longitudinal dimension of the machine. These cells rotate, from a fixed observer point of view, in the same direction as the rotor but with a lower rotational speed, although in literature there is experimental evidence of backwards traveling rotating waves (Spakovszky, 2004).

Rotating stall can be classified in two categories: progressive stall and abrupt stall (Cumpsty, 1989). The first is distinguished by a change in noise of the compressor and by a

slight decrease in the pressure rise and the flow rate while the second is characterized by a drastic drop in performance, especially for axial compressors. During rotating stall the average mass flow rate through the compressor is constant, but the flow velocity varies locally.

Surge is instead an axisymmetric phenomenon and leads to a variable time averaged mass flow rate. The frequency of this variation depends on the storage volume, thus on its filling and emptying time. This phenomenon can occur as mild surge, when the operating point orbits around the peak of the characteristic curve; as classic surge, when the pressure ratio and mass flow oscillations become highly unstable; or as deep surge when it generates a back flow (Cumpsty, 1989) (Cousins, Ph.D. thesis, 1996) (Gravdahl & Egeland, 2012). The occurrence of surge depends on the characteristics of the compression system as explained below.

These two types of instabilities must obviously be avoided, in particular surge, because during its transients it can also lead to structural damage of rotor blades caused by stresses, fluttering and/or vibrations which are critical for their integrity.

Since the study of Emmons et al. (Emmons, et al., 1955) who first give a description of the local mechanism of rotating stall, the significance of this topic has led to many interesting studies such as that of Greitzer (Greitzer, 1976). He developed a non-linear model to predict the transient behavior of an axial compressor subjected to an initial perturbation. In (Greitzer, 1976), the non-dimensional system parameter

$$B = \frac{U}{2a} \sqrt{\frac{V_p}{A_c L_c}} \quad (3.1)$$

was also identified in order to establish the occurrence of surge. This parameter shows dependency not only on the rotational velocity of the compressor but also on the geometric characteristics and size of the compression system. Greitzer demonstrated that transitory behavior of a compressor, installed in a given compression system, depends on the value of B , in addition to the profile of the characteristic curve. He stated that there is a critical value of B (in that case equal to 0.8) which defines the type of instability which the compressor would experience beyond the peak of its characteristic curve. For higher values, the compressor would experience surge whereas for lower ones it would go into stall (the operating point moves to the stalled curve).

Later, another very successful model was presented by Moore and Greitzer (Greitzer & Moore, 1986). This model, and its approach, have been successively used and implemented by many authors such as in (Gravdahl & Egeland, 1997) for studying post-stall behavior in compressors.

Despite many attempts to theoretically describe the transitory behavior in detail, experimental tests are still necessary in order to better comprehend the dynamic correlations between the critical performance parameters, especially during stall and surge. These data are crucially important because they can be used for the comparison and validation of numerical models (Morini, et al., 2006). Moreover, they can also assist in the creation of reliable and robust surge and stall avoidance or control systems. Different techniques to avoid and control these flow instabilities are reported in literature (Gravdahl, et al., 2002; Strazisar, et al., 2004; Morini, et al., 2007; Kurz & White, 2004)

This work aims to contribute to the understanding of the surge phenomenon and its inception mechanism by acquiring experimental data from a test rig built at the University of Ferrara. This chapter presents reliable data regarding stall and surge in a high speed multistage axial-centrifugal compressor. The compressor performance was analyzed during stable and transient operating conditions.

The new facility replaces the previous ones described in (Morini, et al., 2007; Bettocchi, et al., 2005; Bettocchi, et al., 2011) and it is dedicated to the study of unstable working conditions, in particular surge and stall phenomena. The test rig is located inside an acoustic/soundproofed chamber and is characterized by (i) a new support frame for the compressor which allows a safe environment for off-design tests, (ii) a new gear train, installed to achieve higher rotational speeds and consuming less power, (iii) new instrumented sensors, some of them specifically chosen for studying flow instabilities, and (iv) a new upstream and downstream compressor piping system with solenoid throttling valves. Moreover, a new dedicated data acquisition and processing system is integrated on the facility by simultaneously using the NI cDAQ 9174 and NI SCXI 1000 together with the software LabVIEW.

This chapter shows the results of two different types of tests. Basically, the experiments were carried out with two different compression systems. A first series of tests was performed with a throttle valve immediately downstream of the compressor in order to obtain the steady state performance maps at different rotational speeds (up to 25,000 rpm). The second series of tests was carried out with a plenum volume placed between the

compressor and the throttle valve in order to allow the onset of surge while the mass flow rate is reduced.

The test field data are analyzed showing the performance of the turbomachinery and its transient behavior towards and during surge.

3.2 Literature Review

The difficulty of experimentally approaching stall and surge comes from different aspects: i) the need of reliable and accurate dynamic measurement sensors, ii) the problematic positioning of these sensors at the most significant locations in the system, and iii) the requirement of a suitable control and acquisition system because of the necessity of reliable time dependent information.

As stated in (Bulot, et al., 2010), pressure measurements are generally used to analyze unsteady phenomena. However, only a few works with a very high sampling frequency, or high temporal resolution such as greater or above 100 kHz, were presented. The sampling frequency is fundamental not only to detect disturbances which produce and lead to instability when approaching surge, but also to prevent aliasing errors and better define the amplitudes of these perturbations.

To recap, when an experimental study on stall and surge is carried out, the first main requirement is the appropriate design of a test rig dedicated to the investigation of critical working conditions. All the considerations stated above are a direct cause of the high cost for these types of experimental campaigns. Therefore, the tendency is to obtain the dynamic operational information by testing small scale compressors, leading to a smaller and less complex test bench.

Although stall and surge, and their inception, are clearly two distinct phenomena, and their consequences have a considerably different impact on the compressor, it is not always easy to study one without taking into consideration the other and vice versa. This literature review tries to keep separate, as much as possible, the works carried out for stall analysis from those dedicated to surge but, in some parts, the cited works inevitably connect these two themes.

Experimental investigations have been conducted by many authors in order to evaluate compressor behavior under transient conditions while also trying to identify the

stall and surge onset. The first significant representation of the dynamic behavior of a compressor during surge and stall was given by Greitzer (Greitzer, 1976; Greitzer, 1976b). In (Greitzer, 1976b) he studied a three stage axial flow compressor recognizing and describing, through the analysis of data, the compressor response to stall, classic surge and deep surge.

Successively, the work of Camp and Day (Camp & Day, 1998) gave a description of which type of disturbance can occur before stall on high and low speed compressors, formulating a simple descriptive model to define when modal oscillations occur rather than spike instability. Spakovszky and Roduner (Spakovszky & Roduner, 2009) found this theory consistent, analyzing the performance curves of centrifugal compressor vaned diffuser subcomponents. They confirmed the influence of the loading and matching of the subcomponents on the disturbance type of stall inception. Day and Freeman (Day & Freeman, 1994) discovered that spike, which causes stall inception, increases rapidly until it generates a rotating stall cell caused by the abrupt transition of flow. Another type of approach which proved to be effective in the detection of stall is vibro-acoustic analysis.

Morini et al. (Morini, et al., 2007) conducted a vibro-acoustic analysis in order to detect the inception of stall and validate the effectiveness of this process for identifying the precursor of unstable compressor behavior.

An in-depth literature review of the past 75 years of research on stall and surge was recently written by Day (Day, 2016). In (Day, 2016) he gave evidence of another important approach, also adopted by Gallus and Hoenen (Gallus & Hoenen, 1986), in order to detect stall inception disturbances. The authors of that work analyzed the blade passing signal noticing that, as the compressor draws near to the stall limit, this signal repeatability declined. A similar study with similar results was then carried out by Inoue et al. (Inoue, et al., 1991) who confirmed this phenomenon. Further, a correlation, developed by Dhingra et al. (Dhingra, et al., 2003), between degradation of blade passing signature and closeness to stall, was successfully adjusted and applied by Christensen et al. (Christensen, et al., 2008) to a real engine control system.

Because of the importance and the consequences that stall causes to turbomachines, this topic is still attractive to many authors. Dodds and Vahdati (Dodds & Vahdati, 2015) performed an investigation of an 8 stage high speed compressor along a fixed working line. They induced stable rotating stall by mismatching the front stages through the variable stator vanes in order to establish the length-scale and propagation speed of stall

disturbance; then they analyzed the data spectral content. They found that stall can occur at different frequencies and with diverse length scales depending on the stage in which it is generated.

During recent decades many authors have investigated various procedures for establishing the limit flow range of compressors before surge onset. Galindo et al. (Galindo, et al., 2013) used the air injection technique to measure the surge line of a turbocharger compressor, proving the advantages of this method in order to evaluate the influence of the inlet geometry and engine intake line acoustics.

Other works also focused on the surge phenomenon characteristics. In (Galindo, et al., 2006) a study on the frequency and amplitude of surge phenomena in different turbocharger compressors was performed confirming, as stated in (Fink, et al., 1992), that the surge frequency was in the range 5-15 Hz and varied with the compressor velocity and downstream volume. Liu and Theng (Liu & Zheng, 2013) proposed a reliable technique for finding surge points by using the standard deviation (*SD*) of the measurement data. The authors stated that the *SD* of fast-response thermocouple measurements is an effective surge diagnosis quantitative index.

Other recent specific experimental works on surge and surge limit analysis were developed in (Kabalyk, et al., 2016; Courtiade & Ottavy, 2013; Marelli, et al., 2014; Zheng & Liu, 2015). Kabalik et al. (Kabalyk, et al., 2016) investigated the influence, in a centrifugal blower, of the inlet duct configuration and its interaction with amplitudes and frequency of surge pulsations. They did not find a significant qualitative influence of the inlet duct volume on the spectra of pressure fluctuation at deep surge. The only parameter which was significantly subject to change was the amplitudes of the highest peaks. In (Courtiade & Ottavy, 2013) a study of surge precursor instabilities was carried out identifying rotating instabilities. The authors found that, when throttling the compressor toward surge, the rotating instabilities detected grew in amplitude and finally created a full-span stalled cell which induced surge to occur. The experimental campaign reported by Marelli et al. (Marelli, et al., 2014) aimed to study the characteristic performance map of a turbocharger compressor, even in the unstable operating region. They firstly defined an experimental method based on the surge occurrence pulsation at the compressor outlet in order to identify the surge line. Successively, they explored the left side of the surge line without causing surge thanks to the particular setting of their apparatus. In (Zheng & Liu, 2015) instead, the unstable behavior of a high speed centrifugal compressor was analyzed

and a description of a two-regime surge was presented by examining the different inception mechanisms of deep surge at different rotational speeds.

To conclude this section, it is worth highlighting that some modern works are trying to give a complete definition of the physical nature of stall and surge, and what exactly triggers it, from a different point of view. The work of Huang and Yin (Huang & Yin, 2014) can be classified in this context. They tried to demonstrate the independence of surge, at its initial stage, from the compression system characteristics. Using the experimental results obtained by (Mazzawy, 1980), Freeman and Day (Day & Freeman, 1994) and following the path marked by the paper of Cargill (Cargill & Freeman, 1991) they hypothesize that an analogy exists between the transient dynamics of stall and surge and the shock tube theory.

This reveals the interest on this fundamental issue and confirms that research is continuing in order to provide an answer to the most significant remaining doubts.

3.3 Test Facility

The experimental facility is located at the laboratory of the Engineering Department of the University of Ferrara. Fig. 3.10 shows a simplified 3D sketch of the entire test rig (only the piping system) where the different colors highlight the main parts of the circuit. A more detailed description is given in the compression piping system paragraph.

The compressor tested was manufactured by Allison and is part of the turbo-shaft engine 250-C18. This compressor has already been investigated in (Bettocchi, et al., 2005; Bettocchi, et al., 2011). It is characterized by a suction diameter of 0.104 m where an IGV row is present. Then, six axial stages and one centrifugal stage precede two semi-volutes, which conduct the flow out of the compressor through two circular exit sections with a diameter of 0.056 m each. The compressor, without the casing, is shown in Fig. 3.1 (a) shows the compressor (without its casing) so that the rotor axial blades and the centrifugal impeller geometry is clearly distinguishable. Fig. 3.1 (b) depicts instead the compressor installation in the piping system is illustrated.

At its nominal flight condition, the compressor achieves a pressure ratio of 6.2, with a rotational speed of 51,600 rpm and a mass flow rate of 1.36 kg/s. The compressor is installed on the test bench with a new aluminum frame, specifically designed for this

purpose, which is adaptable to various displacement adjustments. Fig. 3.2 (a) and Fig. 3.2 (b) show the 3D representation of the designed aluminum frame and the picture of the compressor fixed to the frame, respectively.

The description of the test rig is presented here in four main sub-paragraphs.

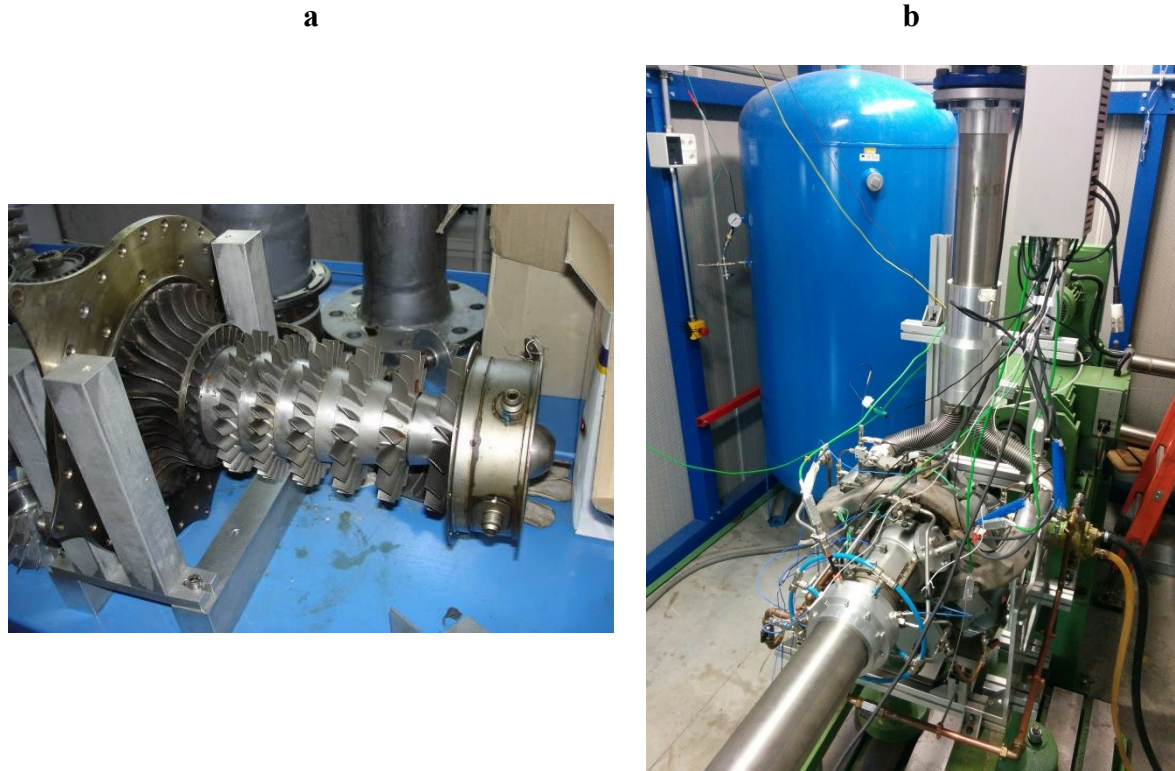


Fig. 3.1 - Tested multistage compressor: (a) the rotor with the six axial stages and the centrifugal impeller (without casing); (b) the compressor installed into the facility

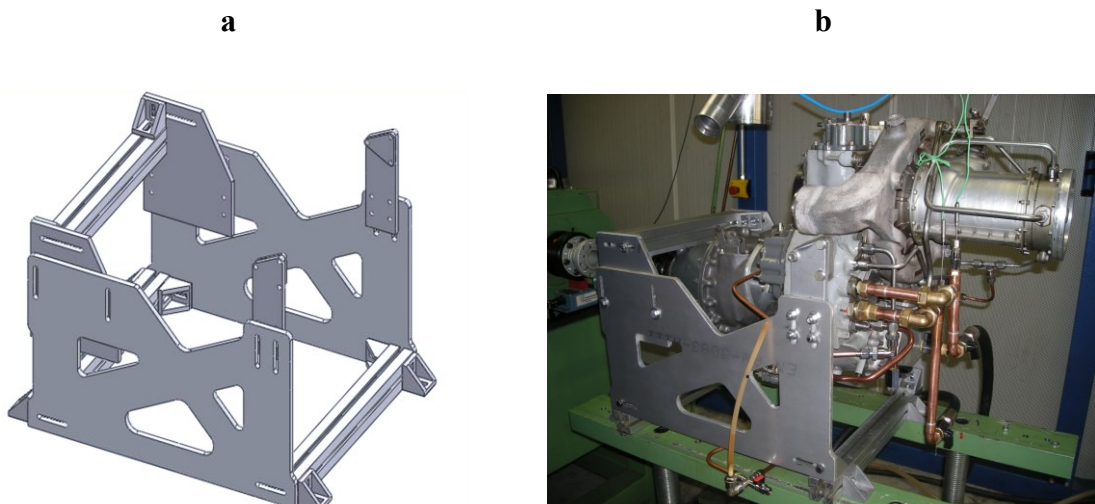


Fig. 3.2 - Designed aluminum frame: (a) 3D representation; (b) installation

3.3.1 Gear Train System

An asynchronous electric brake/motor, typically devoted for automotive engine testing, with a maximum power $P_{\text{mot,max}}$ of 87 kW and a maximum rotational speed $N_{\text{mot,max}}$ of 5,000 rpm, was used here as a drive motor and remotely controlled by an inverter (i.e. variable frequency drive). The power transmission from the AC motor to the compressor block (gear boxes and compressor) was made through a constant-velocity joint which reduced and tolerated vibrations due to misalignment between the shafts of the electric motor and the main gear train. The Allison engine original gear box was kept connected to the compressor but with the auxiliary utilities removed. Moreover, in order to achieve higher rotational speeds, the planetary reduction gear connected to the original engine power shaft (to transmit power to the propellers), was adapted to be installed in the test rig as a multiplier. The resulting total gear ratio was thus equal to 17.26:1. This adjustment was achieved after careful geometric measurements, carried out by means of a laser scanner, of each component to be adapted/connected (the actual geometry of the engine gearboxes were not available). As a result, an accurate graphic reproduction of the planetary gearbox encumbrance was obtained, and thus a correct design of new mechanical parts planned. Subsequently, the modification of the epicyclic gearbox was realized by cutting part of it, and welding the remaining part to a proper flange (see Fig. 3.3).

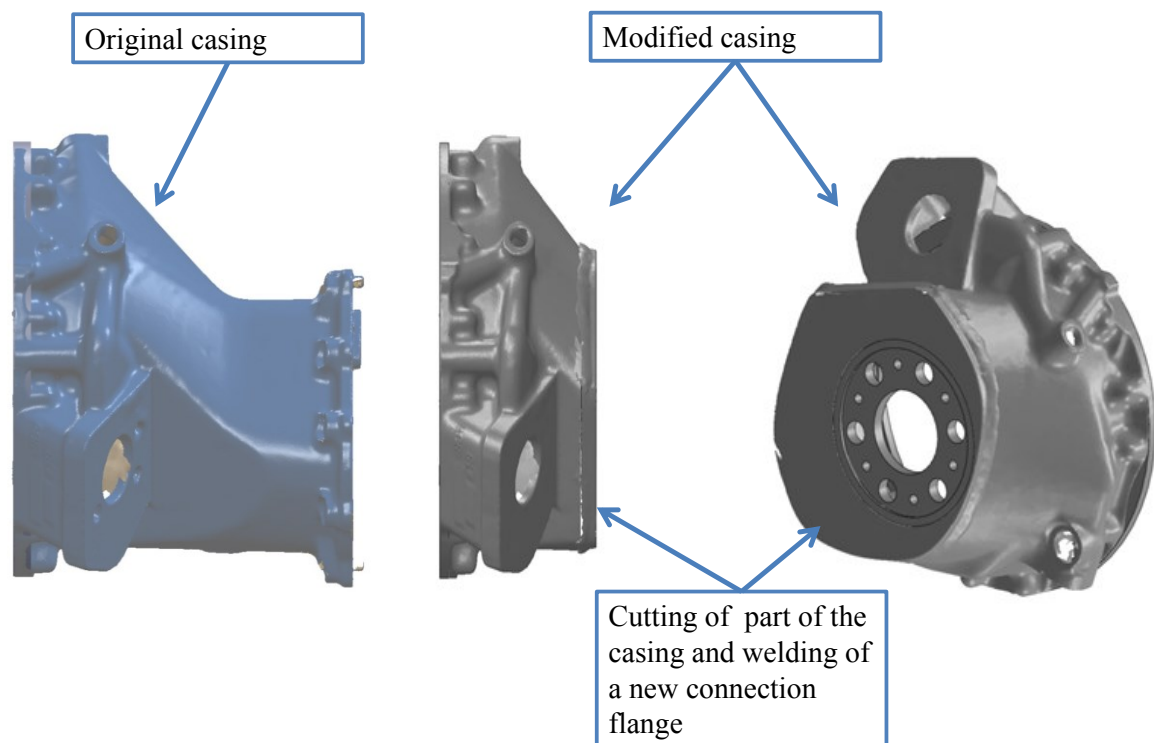


Fig. 3.3 - Modification of the original epicyclic gearbox of the Allison 250-C18 turboshaft engine: the original component (on the left) was scanned and modified by welding it with a new flange (on the right)

The assembly of the modified epicyclic gearbox into the facility is depicted in Fig. 3.4 as well as the new connection flange, which hosts the solar shaft of the planetary gearbox and allows the engagement to the compressor gearbox.

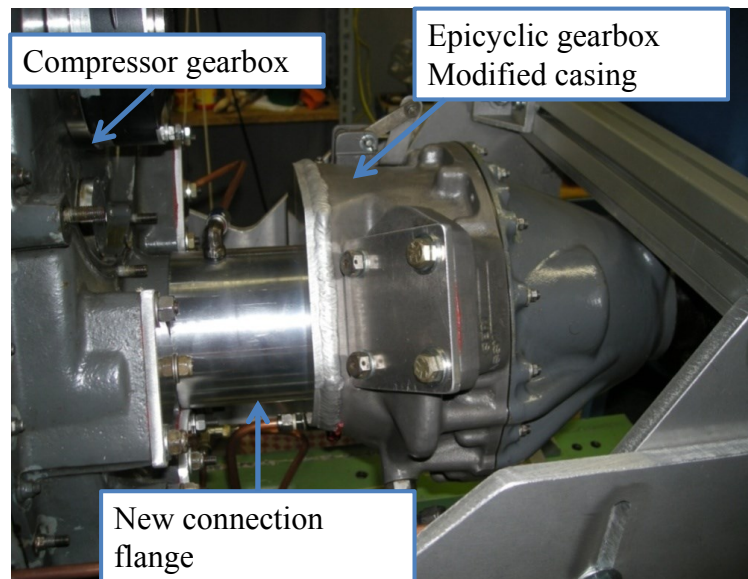


Fig. 3.4 - Assembly of the epicyclic gearbox into the test rig

Thence, this assembly allows the connection to the original compressor gear box (the solar shaft transmits the power). However, in order to achieve a proper power transmission, some issues, due to the numerous adjustments done, were fixed. The axial movement of the solar shaft during operation was one of the most important concerns. This movement was originally constrained by a specific component, which was installed in the removed part of the epicyclic gearbox. Thereafter, with a view to replicate this function, a new component called the “solar shaft axial blocker” was designed, and successively installed inside the gearbox so that to cover part of the solar shaft and limit the shaft axial oscillations. This implementation was possible thanks to the use of a small half-moon shaped bronze piece, which scrapes on the stop ring of the solar shaft. In addition, a lubrication system (a drilled mini-duct inside the solar shaft axial blocker) was also realized to ensure the correct functionality of this component. The design and realization of the solar shaft blocker are shown in Fig. 3.5. The entire transmission line and the new designed components are illustrated in Fig. 3.6, where the 3D draw of part of the assembly is depicted. As can be seen, the realization of other two connection flanges was necessary to connect the CV joint to the electric motor torquemeter and the epicyclic gearbox. In Fig. 3.7, a schematic 3D draw and the assembly of the gear transmission line are depicted (from compressor gearbox to the electric motor flange). The image shows the epicyclic gear box

“virtually opened” in order to put in evidence the presence of the solar shaft and ring gear inside.

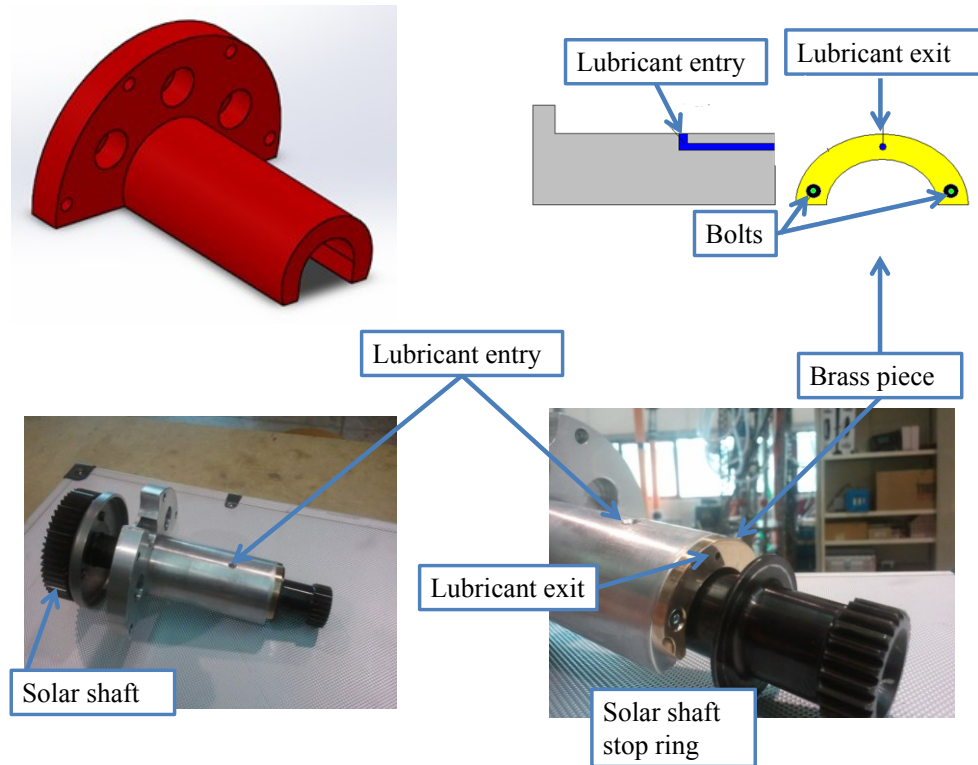


Fig. 3.5 - Solar shaft axial blocker: 3D and 2D lateral view draws of the component (on the top); the realized component (on the bottom)

Consequently, the power transmission from the electric motor to the compressor was finally completed by connecting two separated gear trains of the compressor gear box (the gearbox was configured with two gear trains because of the double spool characteristic layout of the turboshaft engine). To connect the two gear trains one each other, a new double geared mini-shaft was realized and installed in the compressor gearbox. An additional issue was the tendency of this mini-shaft to be ejected when high speeds, or strong regime variations were imposed/achieved. To solve this problem an internal mini-shaft was realized, which allowed the double-gearred mini-shaft to remain in a fixed position. The internal shaft was internally threaded on one side, in order to be coupled to the compressor shaft (the compressor shaft ends with a thread to remain axially constrained by means of a nut) and externally threaded on the other side, to be fixed by a proper nut. Such a solution revealed to be optimum since avoided the use of lubricant systems or bearings. The 3D sketch of these two shafts (the mini-shaft is transparent whereas the internal shaft is in red) and their installation into the compressor box are shown in Fig. 3.8.

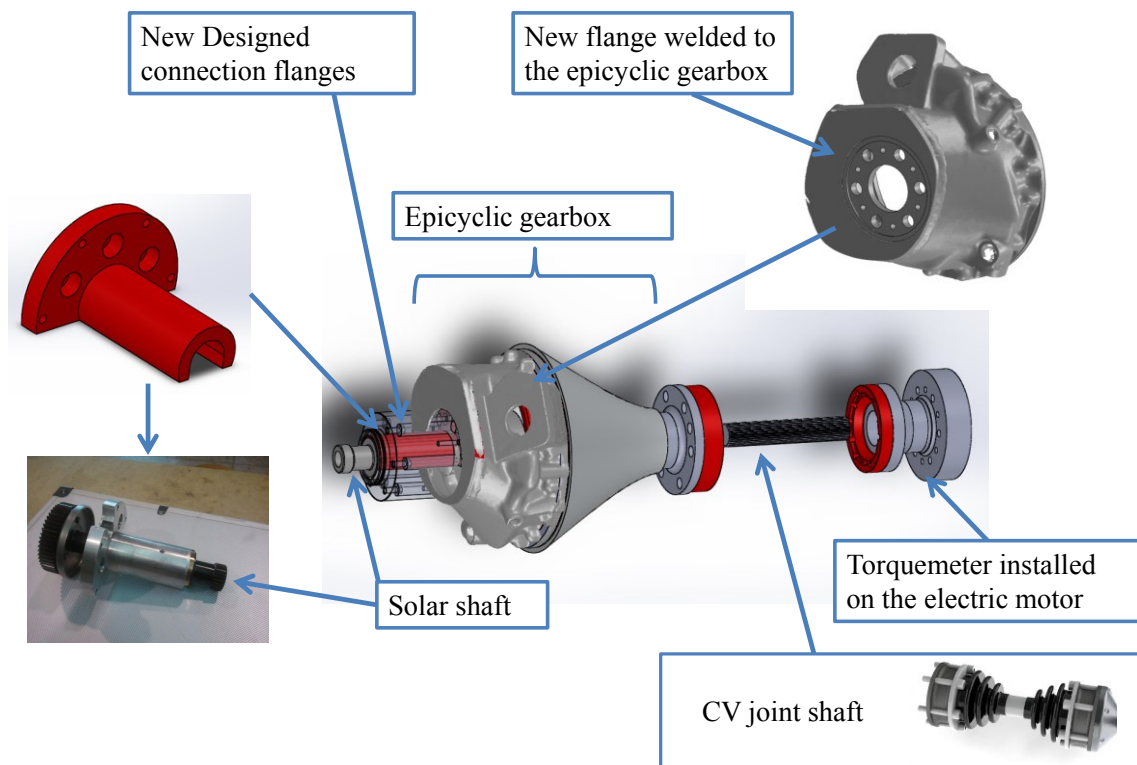


Fig. 3.6 - 3D draw of the transmission line assembly with the new designed components



Fig. 3.7 - 3D sketch of the power transmission line components

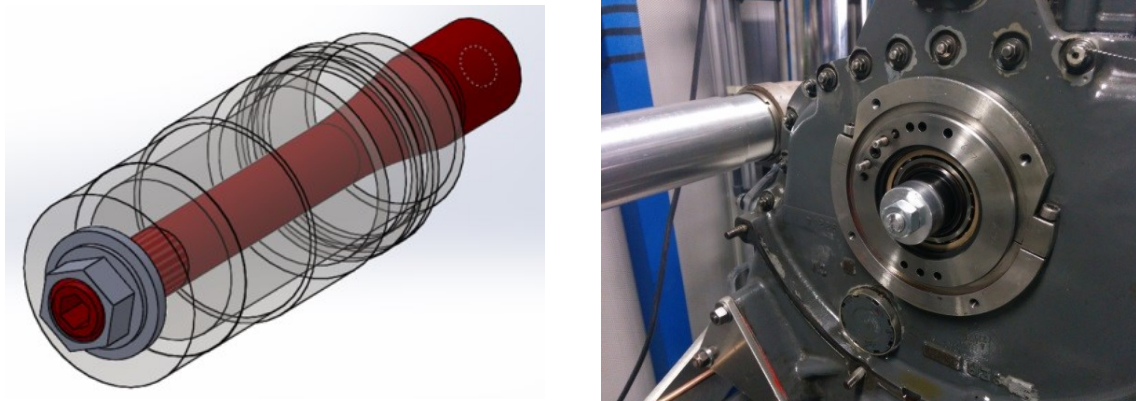


Fig. 3.8 - Double-geared mini-shaft and its internal shaft (the threads are not shown): 3D sketch (left); and installation (right)

The entire mechanism (compressor gearbox, epicyclic gearbox and solar shaft blocker) was lubricated by an ad hoc oil circuit, composed of a heat exchanger fed with cool water. This lubricating system was realized by using small-diameter copper ducts which were realized and fixed by following the Allison engine system principle. In Fig. 3.9 the 2D scheme of the lubricating system of the test rig is depicted.

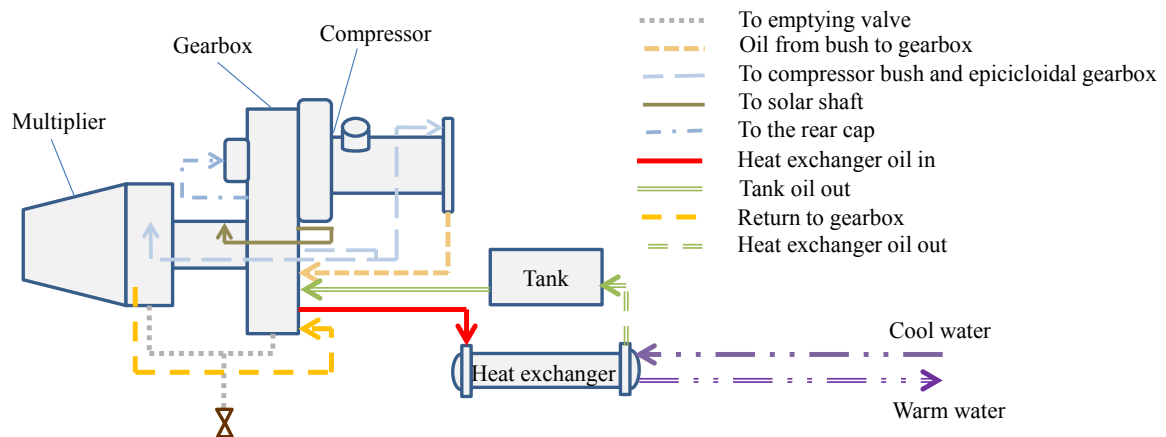


Fig. 3.9 - Schematic draw of the lubricating system

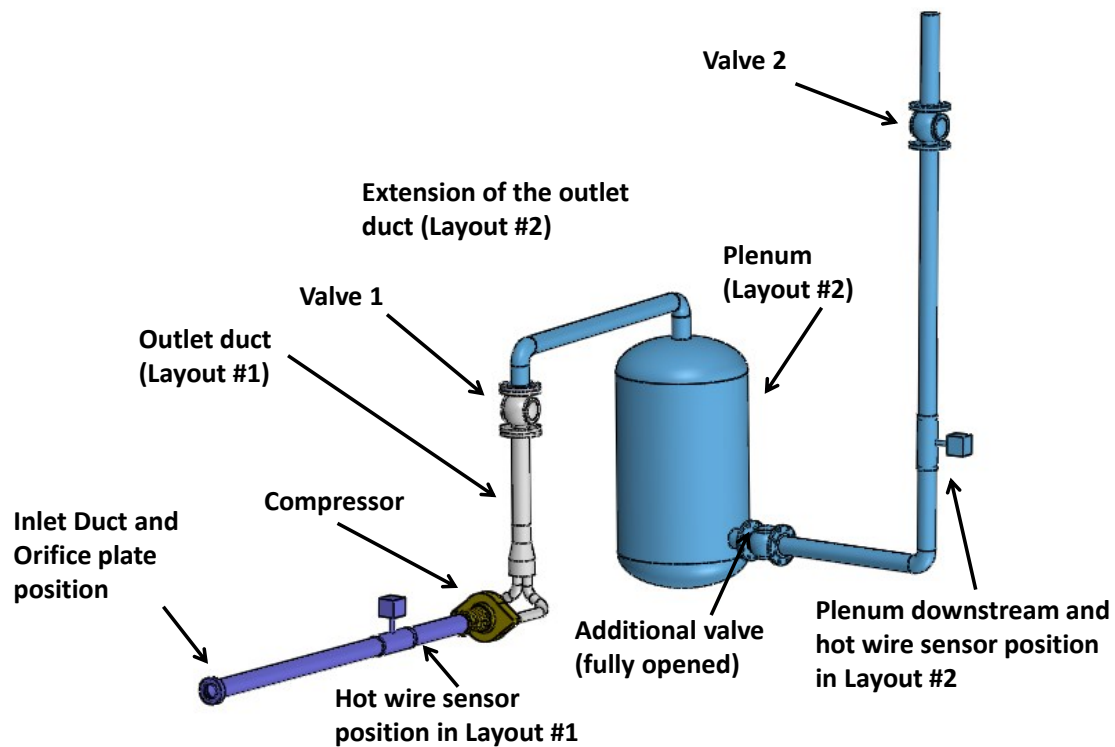


Fig. 3.10 - 3D sketch (colored) of the piping system: in violet the inlet duct, light brown the compressor, grey the outlet duct of Layout #1; in blue the added part belonging to Layout #2

3.3.2 Compression Piping System

As shown in Fig. 3.10 the compressor was preceded by an inlet duct with a length of about 3 m. This length was established as a compromise between the available space and the space required upstream and downstream of the installed orifice plate and mass flow rate sensor.

A new flow conveyor was then installed just downstream of the compressor. Its function is to guide the two centrifugal compressor outflows into a single duct. It was designed through CFD simulations, in order to find an optimal compromise between space limitations, the need to minimize pressure losses, and cost. In Fig. 3.11 the 3D project of the conveyor (on the left of the figure) and the installation on the piping system (on the right of the figure) are depicted. As can be noted, the final design of the conveyor consists of two threaded holes on the bottom (these holes are used to connect the conveyor to the two bend ducts, fixed to the compressor outlet) and a convergent shaped part which convey the flow towards the outlet duct. Internally, a separation wall is also installed in order to reduce the mixing losses from the two entering flows. In Tab. 3.1 the main results of the

CFD simulation are presented - the choice of the final conveyor geometry was based on the best compromise between costs and characteristic pressure drop.

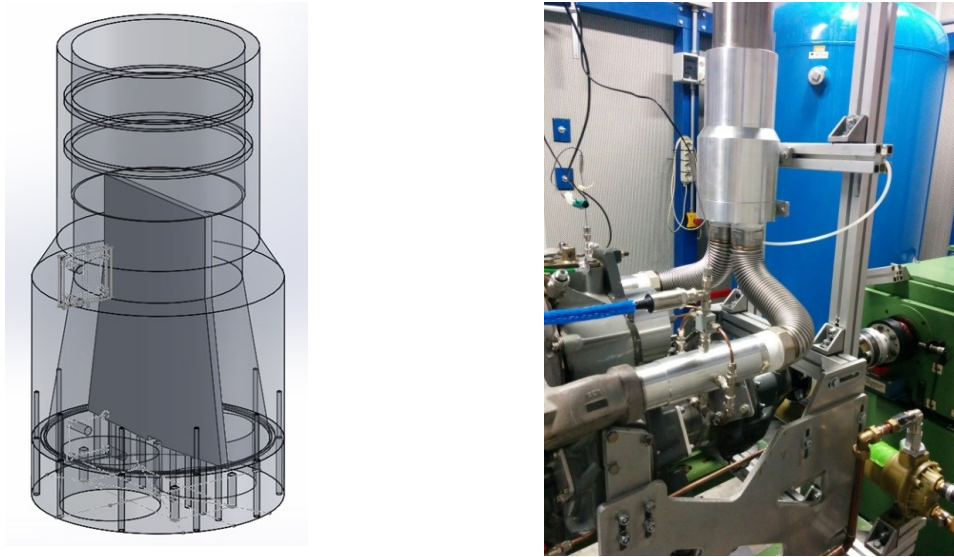


Fig. 3.11 - Flow conveyor: 3D project (on the left); installation in the piping system (on the right)

Tab. 3.1 - Results of the CFD simulation: the final geometry of the conveyor

Number of cells	1,824,697
Iterations	380
Total inlet pressure	141325 Pa
Total outlet pressure	139625.9 Pa
Delta P	1699.15 Pa
Uniformity index @1.60 m	0.98

Another component which was necessary in the piping system was a throttling device to measure the mass flow rate at the inlet of the compressor. The choice fell into an orifice plate, installed at the edge of the intake duct - the so called “extremity orifice plate”. The design of this component was carried out by following an old Italian standard (UNI 1570-1596, year: 1945); which allowed the installation of extremity orifice plates, and the actual European Standard (UNI EN ISO 5167, year: 2012); which does no longer allows the design and installation of extremity orifice plates. The final design was obtained so that

the chosen geometry was valid for both the standards. The orifice plate final geometry was selected by considering the potential future changes of the test rig (the orifice plate might be positioned along a duct, as recommended by the actual standard). In Fig. 3.12 the design (on the left) and the installation (on the right) of the orifice plate are illustrated.

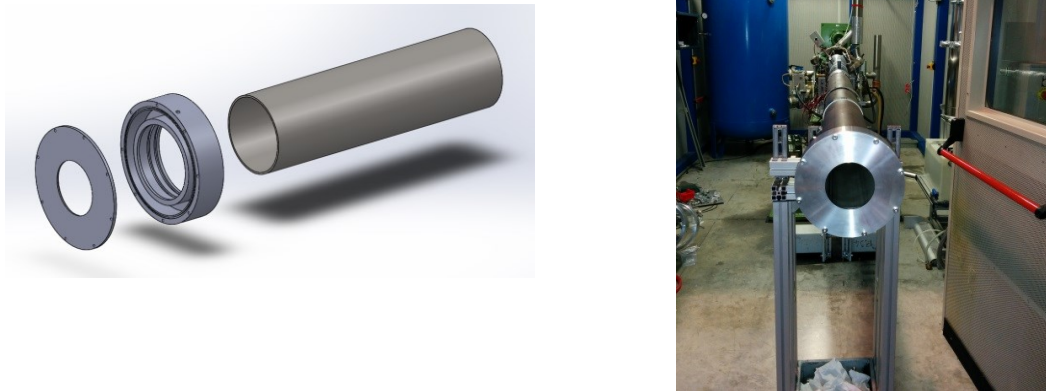


Fig. 3.12 - Orifice plate (according to the standards UNI 1570-1596 and UNI EN ISO 5167): 3D project (on the left) and installation in the piping system (on the right)

The piping system was intended to be modular in order to allow two different configurations at the compressor outlet. In the first configuration, Layout #1 in Fig. 3.13 (a), after leaving the compressor, the flow path consisted of the conveyor, a short duct (the minimum length required to achieve a uniform sectional flow) and a solenoid throttling valve. In Layout #1, the orifice plate and the hot wire sensor were both placed along the inlet duct to measure the mass flow and, at the same time, to determine an alignment or correlation between the two measurements. On the other hand, in the second arrangement, Layout #2 in Fig. 3.13 (b), the flow path was modified by adding a plenum and, after another duct, a second solenoid downstream. In Layout #2 the hot wire sensor was placed downstream of the plenum.

Layout #2 was used to lead the compressor to surge so, according to Greitzer (Greitzer, 1976), the value of the non-dimensional parameter B had to be greater than 0.8 during the dynamic tests. Based on Tab. 3.2, which reports the values of B at each rotational speed tested in dynamic tests, surge was expected to occur already at 5,000 rpm.

Tab. 3.2 - Values of non-dimensional parameter B referred to Layout #2

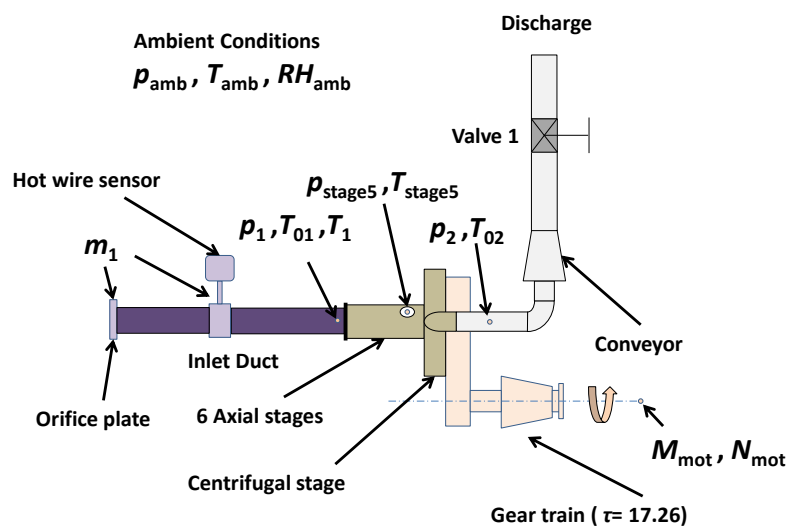
Rotational speed	B
5,000 rpm	1.04
10,000 rpm	2.08
15,000 rpm	3.12

Tab. 3.3 shows the dimensions of the different pipes belonging to the entire system so that the size of the whole facility is clearer.

Tab. 3.3 - Pipeline dimensions and volumes

Duct	Equivalent pipe length [m]	Equivalent pipe diameter [m]	Volume [m ³]
Inlet-first segment	1.500	0.109	0.014
Inlet-second segment	1.390	0.099	0.011
Centrifugal compressor outlets	0.900	0.050	0.002
Conveyor	0.130	0.11	0.001
From conveyor to Valve #1	0.480	0.099	0.004
From Valve #1 to plenum	3.220	0.099	0.025
Plenum	--	--	1.5
From Plenum to Valve #2	5.420	0.099	0.042

a



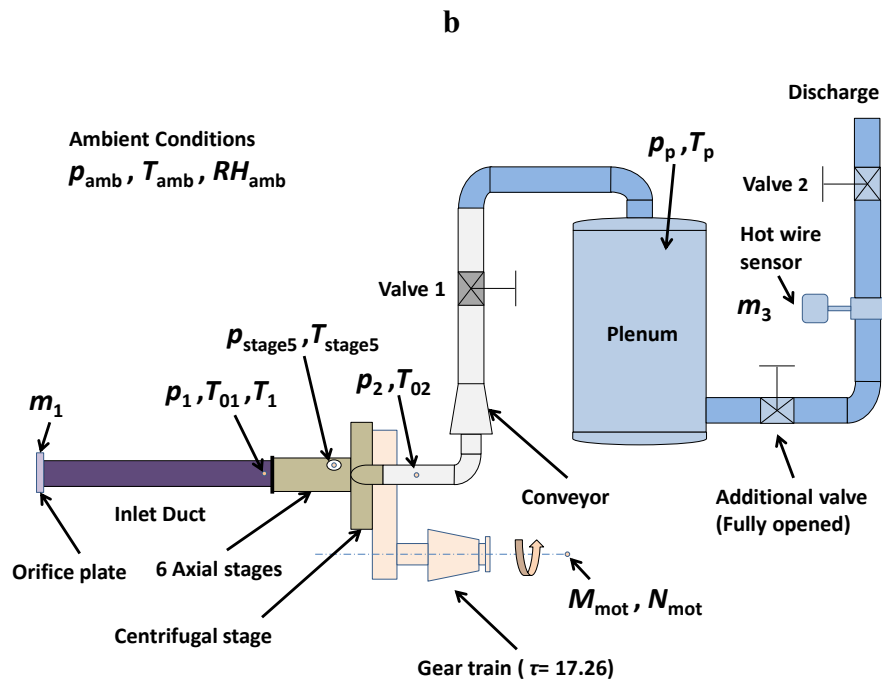


Fig. 3.13 - 2D sketch of the piping system: (a) Layout #1; (b) Layout #2

3.3.3 Measurement Sensor System

Fig. 3.13 shows in detail the type of measurement and the location of the sensors along the circuit. As stated in the previous paragraph, the mass flow rate was measured by an orifice plate (at the compressor inlet) and by a hot wire mass flow sensor placed at the inlet duct (Layout #1) or at the plenum outlet duct (Layout #2).

The electric motor rotational speed was obtained by a magnetic pick-up sensor fixed in the proximity of the motor wheel equipped with 60 teeth, while the torque is measured through a torquemeter (0-250 Nm) at low regimes and through a load cell (not used in this work) at high regimes.

Pressure transducers were located along the circuit to measure the absolute static pressure through annular chambers or rings, whereas thermocouples measured the stagnation temperatures at the compressor inlet, and outlet. All measurements are considered to be averaged annulus quantities.

The calculation of stagnation pressure and static temperature was performed considering the operating fluid as a perfect mixture of dry air and water vapor, through the same procedure explained in (Bettocchi, et al., 2005). Static temperature and static pressure values were also acquired at the bleed valve position and inside the plenum. All the sensors

on the test rig were used to evaluate, (i) the compressor steady-state characteristic curves, and (ii) the dynamic response of the compressor during surge (the expected phenomenon frequency range was 0-15 Hz). Finally, two Kulite fast response miniature piezoresistive transducers (XQ-093 series) were located circumferentially (spaced 180 ° from each other) at the compressor inlet in order to detect local instabilities (stall onset and development of rotating stall cells).

Tab. 3.4 shows the main characteristics of the instrumentation installed on the test rig. All the sensors were adequately calibrated before proceeding with the performance tests.

Tab. 3.4 - Instrumentation characteristics

Instrument	Type	Range/Capacity	Characteristics
Valve 1 and Valve 2	Ball	DN 100-PN 16	Cast Iron, PTFE seals
Actuator	Electric	300 Nm	Positioner 0-10 V, Position Transmitter 0-10 V
Orifice plate	Extremity throttling device	----	Diameters ratio=0.7
Mass flow rate sensor	Hot wire	0.95 kg/s	4" flow body
Pressure transducers	Membrane	0-3.5 bar a	Infinitesimal resolution, amplified output
Thermocouples	J and K	Typical	Sheathed
Fast response pressure transducers	Piezoresistive	0-3.5 bar a	Infinitesimal resolution. Distance from compressor inlet equal to 0.005 m
Torquemeter	Double-flange, dynamic	0-250 Nm	Resolution of 0.1 Nm
Pick-up	Magnetic	0-9999 rpm	Resolution of 1 rpm

3.3.4 Control and Acquisition System

The electric motor was operated by an inverter which was linked to a control unit. This unit is required by the operator to set the electric motor driving mode (constant rotational speed or constant torque) and the inverter controlling mode: manual (through the installed potentiometer) or automatic (through external hardware).

The tests were carried out by setting the constant rotational speed mode and through remotely controlling the inverter by using a specific cDAQ signal output module, also used for controlling solenoids, and another solid state relay module needed to remotely activate the inverter.

The ambient conditions were recorded by a specific environmental monitoring station. Due to the short duration of each test, the ambient conditions were constant throughout the experiments.

In Fig. 3.14 a schematic diagram of the data control and acquisition system is illustrated.

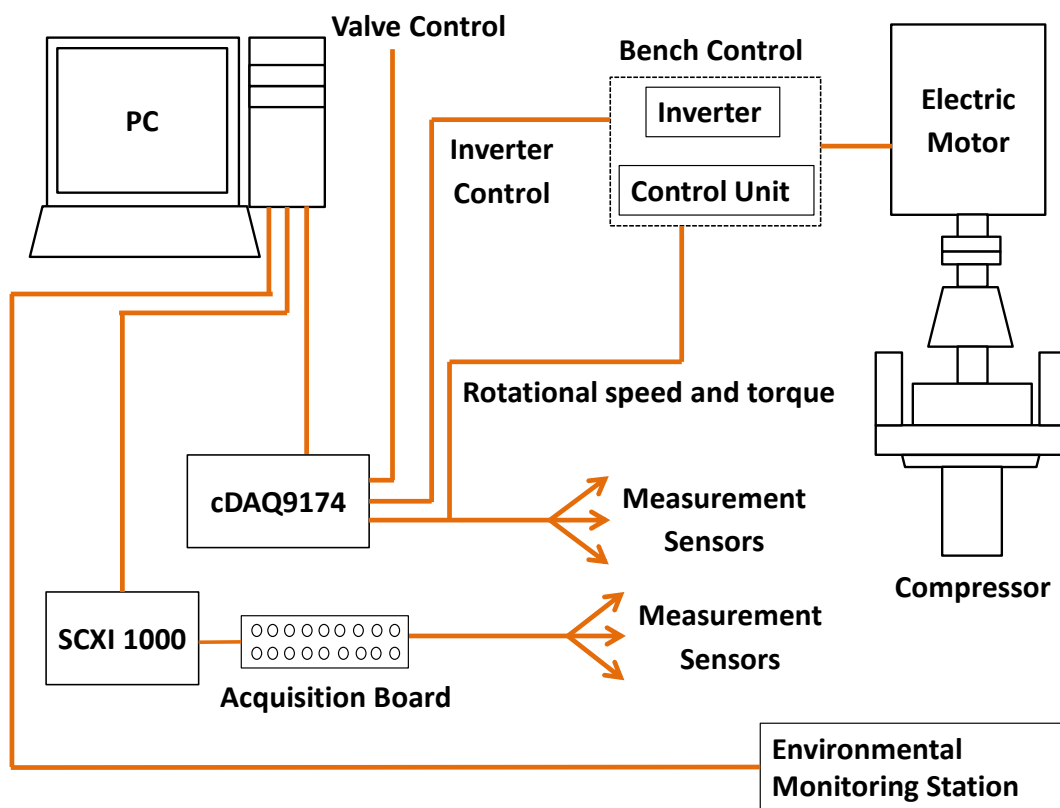


Fig. 3.14 - Diagram of the control and acquisition system

According to the maximum frequency response of the sensors and the characteristics of the acquisition modules, a distinction between the low frequency part and the high frequency part was made.

The low frequency analog signals were acquired by an NI compact DAQ-9174 chassis, and then converted into digital through two different modules installed: a 16-channel module (module 1, non-simultaneous maximum frequency of 70 Hz) was

dedicated to thermocouples and another 16-channel module (module 2, 8 voltage/8 current channels, non-simultaneous maximum frequency of 500 Hz) was used for pressure and mass flow sensor analog inputs. The high frequency measurements were performed by the NI SCXI-1000 chassis, with only one module installed: a 32-channel amplifier module (simultaneous maximum sample rate of 333 kHz) devoted to the orifice plate differential pressure transducer, the electric actuator positioner transmitter and the electric motor rotational speed and torque.

These hardware components were integrated into the data acquisition system by a software program developed in LabVIEW. This program was created with a conceptual design which allows the processes load on the CPU of the PC desktop dedicated to this test-rig to be minimized. This was done to avoid computer crashes during the tests, thus increasing the operational safety of the system.

The program allows a variable sampling frequency (see details in the Methodology paragraph), depending on the type of tests, and two different modes of data logging: dynamic and instantaneous.

3.4 Methodology

As already explained in the previous paragraph, the test bench was driven by the constant speed mode control in order to set the desired rotational speed at any time during the test. Therefore, once the rotational speed was set, the system ensures an optimum control of the AC motor rotational speed. The maximum rotational speed percentage variation recorded under test conditions at the compressor corrected rotational speed of 10,000 rpm, even during transient, was around 0.4 %. Only during surge peak values of 0.8 % were recorded.

3.4.1 Compressor Steady State Performance Maps

The compressor characteristic maps were obtained by testing the machine with the plant Layout #1 presented in Fig. 3.13 (a) in order to minimize the circuit pressure losses and extend the mass flow operating range. Moreover, this configuration allowed the achievement of reliable results even at the left of the characteristic curve peak because the compressor could not surge due to the absence of mass storage and flow inertia (considering the inlet duct flow inertia to be negligible). Therefore, even operating points

on the positive slope of the characteristic curve were identified because the compressor reached stable working conditions and did not show average mass flow or pressure oscillations. This situation was maintained until the point of static instability which caused rotating stall as explained in (Cumpsty, 1989).

The tests aimed to describe the stable behavior and characteristic maps of the compressor at different shaft corrected rotational speeds v : 5,000, 10,000, 15,000, 20,000, 25,000 rpm. Each curve was obtained by throttling via software the solenoid valve (Valve 1) from $\alpha = 90^\circ$ (valve completely opened) to a specific closing angle, established by the authors' experience and knowledge of the test-rig before any unsafe situation could arise on the compressor system and sensors (change of sound and vibrations was an appropriate precursor for dangerous conditions).

The closing of Valve 1 occurred with steps of 5° . For each step the measurement signals were acquired after setting the compressor corrected rotational speed (by software) and waiting long enough for the measurement values to stabilize. This methodology, coupled with the reliable control and data acquisition system, was useful in obtaining experimental data at conditions closely corresponding to the desired compressor rotational speed, v , despite the slight inevitable electrical/mechanical instability of the motor speed (N_{mot} variation was 1-5 rpm) at a very low regime (below 5,000 rpm).

The performance parameters used to determine the compressor operating points were the total-to-total pressure ratio β_0 and the isentropic efficiency η_{is} as function of the corrected speed v and of the corrected mass flow rate μ .

3.4.2 Compressor Dynamic Test and Surge Inception

This series of tests was executed by running the compressor at 10,000 and 15,000 rpm with Layout #2 (as described in the Test Facility paragraph and shown in Fig. 3.13 (b) in order to create the necessary conditions for surge onset and development. The first step of this experiment was to linearly accelerate the compressor up to the desired corrected rotational speed.

The valve located immediately after the compressor (Valve 1) was kept fully open. The experiment was then carried out by closing at a specified angle the valve located downstream of the plenum (Valve 2). The closing/opening velocity of the valve was $1.5^\circ/\text{s}$. In the vicinity of the characteristic curve peak, when the valve was closed further,

dynamic instability was achieved and compressor surge occurred (see (Cumpsty, 1989)). Valve 2 was then stopped for a time range suitable to permit the complete development of surge. After that, Valve 2 was progressively re-opened to restore stable conditions and evaluate the hysteresis which characterized stall and surge phenomena in this system.

The dynamic data were acquired throughout this process and evaluated by plotting the oscillating values of mass flow sensors, pressure transducers and thermocouples measured at the compressor inlet and outlet as functions of time. Other significant parameters analyzed for detecting surge conditions were the plenum pressure, p_p and normalized power, $P_{\text{mec,norm}}$, (through the measurement of the torque, M_{mot} , at the motor shaft) required by the electric motor,

$$P_{\text{mec,norm}} = \frac{P_{\text{mec,mot}}}{P_{\text{mot,max}}} \quad (3.2)$$

where

$$P_{\text{mec,mot}} = \frac{2 \pi N_{\text{mot}} M_{\text{mot}}}{60} \quad (3.3)$$

For both types of tests presented in this work, the LabVIEW program recorded data at a frequency of 10 Hz but cDAQ and SCXI were set to a sampling frequency of 10 kHz. Obviously, only the data acquired by the SCXI had effectively that desired frequency thanks to its great velocity feature; on the other hand cDAQ modules had a sampling frequency equal to

$$f_{\text{cDAQ,mod1}} = \frac{500}{c_{\text{mod1}}} = \frac{500}{10} = 50 \text{ Hz} \quad (3.4)$$

where c_{mod1} is the number of channels activated in module 1, and

$$f_{\text{cDAQ,mod2}} = \frac{70}{c_{\text{mod2}}} = \frac{70}{10} = 7 \text{ Hz} \quad (3.5)$$

where c_{mod2} is the number of channels activated in module 2.

The results and discussion of this experimental investigation are presented in the next paragraph.

3.5 Test Results and Discussion

The obtained results are presented by distinguishing the steady-state tests, which were carried out first, from the dynamic tests, which were successively done.

3.5.1 *Cursory Analysis and Test Conditions*

The uncertainty analysis of the old version of the test rig (different system layout, limited acquisition and data analysis, and older sensors) was investigated in (Bettocchi, et al., 2005) and it was found a quite large uncertainty of isentropic efficiency ($\pm 2.7\%$) and corrected mass flow rate ($\pm 2.3\%$) and a lower value for compressor corrected rotational speed (± 80 rpm). However, these values were only referred to preliminary tests done at that time. Today, the test methodology is certainly improved, more accurate and advanced instrumentation is used, and many components and important measurement sections were designed in order to minimize the measurement errors. Therefore, the results of (Bettocchi, et al., 2005) can only represent an upper limit for the current uncertainty of this new test rig data. In order to establish the current actual level of accuracy, a future work will be surely carried out.

Before presenting the test series results it is important to highlight, once more, that all the sensors, pressure transducers, and thermocouples, were calibrated using a proper calibrator provided with a valid certificate of calibration issued by an authorized institution. Another important factor to point out is that the signal noise was significantly reduced thanks to the use of shielded cables and positioning the acquisition systems outside the shielded box so that the electro-magnetic disturbances coming from the inverter and the motor were minimized, although still present. The typical network electric noise was then further reduced by supplying the power to the sensor by means of 12 V batteries.

Based on these considerations, it should be underlined that the measurement errors are rather insignificant compared to the variation in the actual physical magnitudes themselves. Therefore, the results and the consideration reported in the next paragraphs can be considered reliable and repeatable as much for steady state as for dynamic tests. Tab. 3.5 illustrates the ambient conditions of each test conducted at specific corrected rotational speeds.

Tab. 3.5 - Ambient conditions during tests

Corrected Rotational Speed	Type of test	p_{amb} [mbar]	RH_{amb} %	T_{amb} [°C]
5,000 rpm	Steady-state	1021	43.2	22.6
	Dynamic	1026	37.5	20.8
10,000 rpm	Steady-state	1020	44.5	22.7
	Dynamic	1026	32.8	20.9
15,000 rpm	Steady-state	1020	44.7	22.7
	Dynamic	1026	37.5	20.8
20,000 rpm	Steady-state	1020	44.7	22.7
	Dynamic	-	-	-
25,000 rpm	Steady-state	1019	46.2	21.9
	Dynamic	-	-	-

3.5.2 *Steady-State Behavior*

The characterization of the steady state points was carried out using the circuit in Layout #1. Fig. 3.15, Fig. 3.16, and Fig. 3.17 illustrate the compressor characteristics at the different rotational speeds. It is clear that the piping system configuration also allowed a description of the positive slope part of these curves. Each point was obtained through 3-5 different measurements executed arbitrarily in a maximum time of 3 s. For each of these three measurements, 1,000 data values were acquired in a time of 0.1 s and an average of each parameter was calculated.

It is important to note that, at low rotational speeds (5,000, 10,000 and 15,000 rpm), data acquisition was done for all the valve opening positions whereas at high velocity (20,000 and 25,000 rpm) the maximum achieved closure was 10° and 25° respectively, due to burble sounds and increasing vibration which could cause some damage to the instrumentation.

At 5,000 rpm most of the overall pressure rise (see Fig. 3.15) seemed to be given by the centrifugal stage (the trend was similar to that of the theory of centrifugal compressors) while the axial compressor did not contribute significantly. This appeared evident by observing the static pressure ratio at stage five (where the bleed valve was originally placed) shown in Fig. 3.17.

It is clear that at low rotational speeds the axial stages worked off-design, destabilizing the overall performance. This was probably due to the stall regions of the first stages, and the choking phenomenon of the latter stages which both affect their

performances (the bleed valve was not present whereas under these operating conditions it should be opened to prevent this behavior). As the velocity was increased, this phenomenon progressively diminished, as expected by theory, and the part of the curve with negative slope increased.

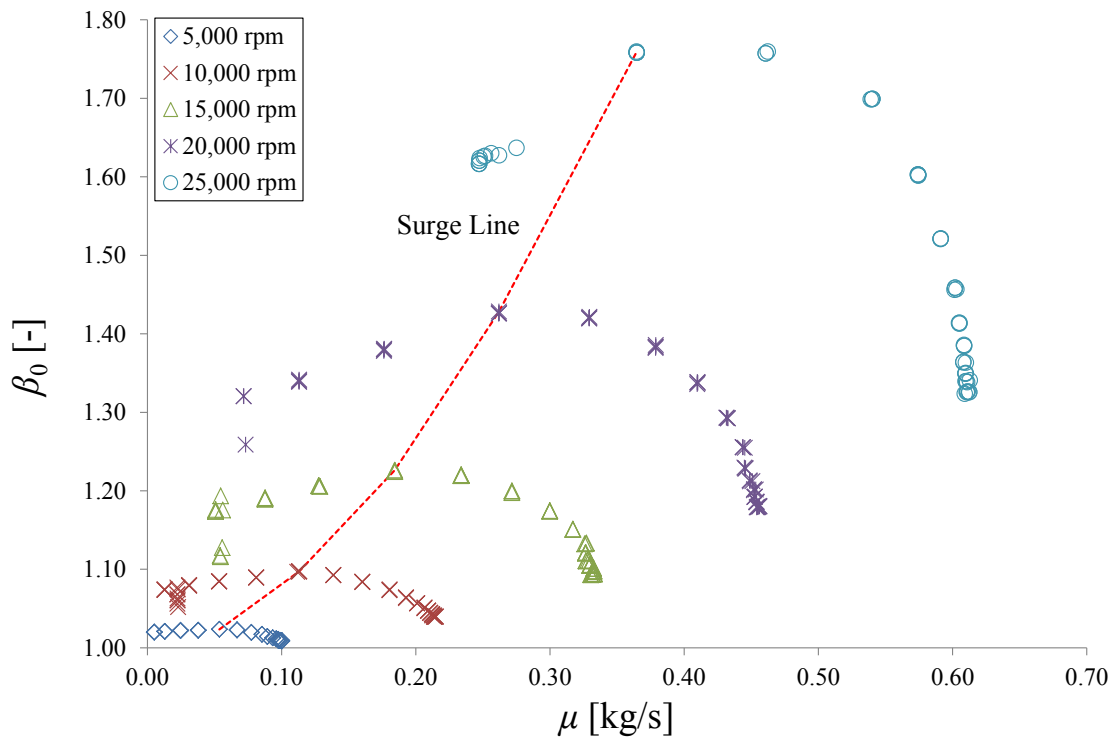


Fig. 3.15 - Steady state performance map: pressure ratio

In Fig. 3.15, at 20,000 rpm and 25,000 rpm, the overall characteristic presented a choking area at high mass flow rate. This testified that the increasing performance of the axial stages contributed more to the overall compressor characteristics. Due to the lack of manufacturer data, the surge line shown in Fig. 3.15 was simply estimated by using the peak values of the characteristic curves at each performed rotational speed.

Fig. 3.17 shows a wide scatter between values belonging to low mass flow rates. In this region, instability was prevalent so the operating point experienced a continuous and alternated repositioning between the characteristic curve and the stalled curve. Moreover, as already mentioned, the bleed valve was removed and the bleed chamber was plugged to install the temperature and pressure sensors. Due to the characteristic shape of the bleed valve section, the air at the fifth stage, accumulated in a circumferential volute which directly connects the air to the bleed valve chamber. This volute circumferentially increases its internal volume towards the bleed valve chamber.

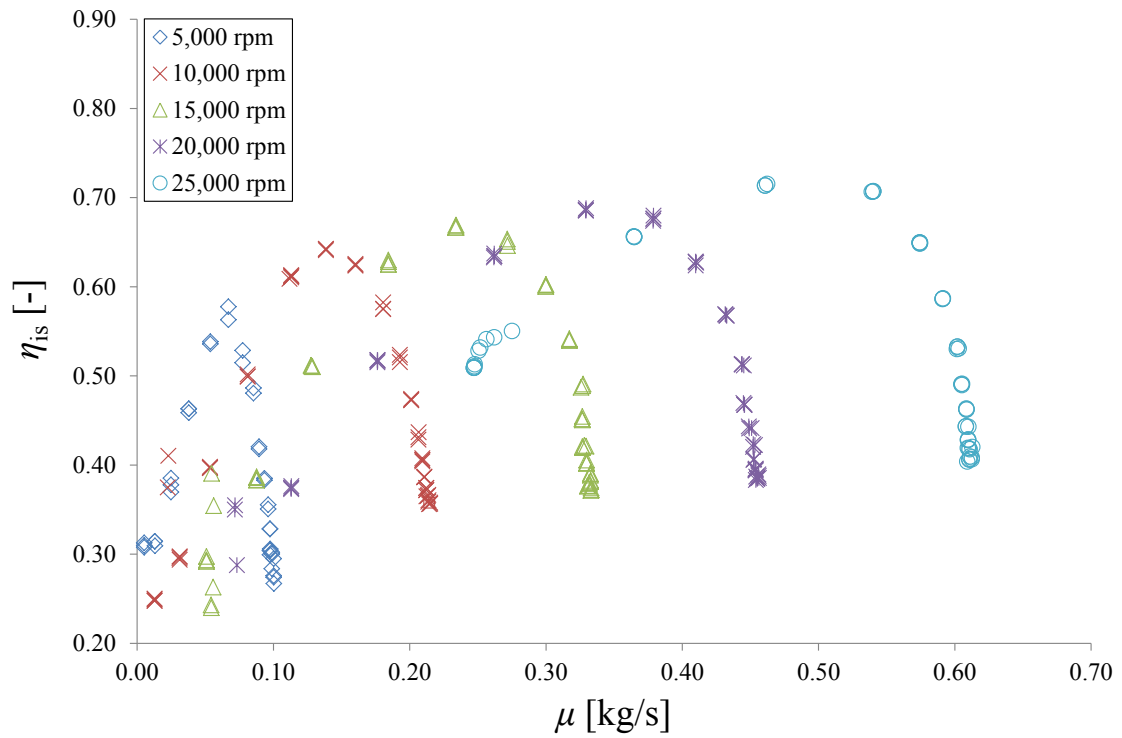


Fig. 3.16 - Steady state performance maps: isentropic efficiency

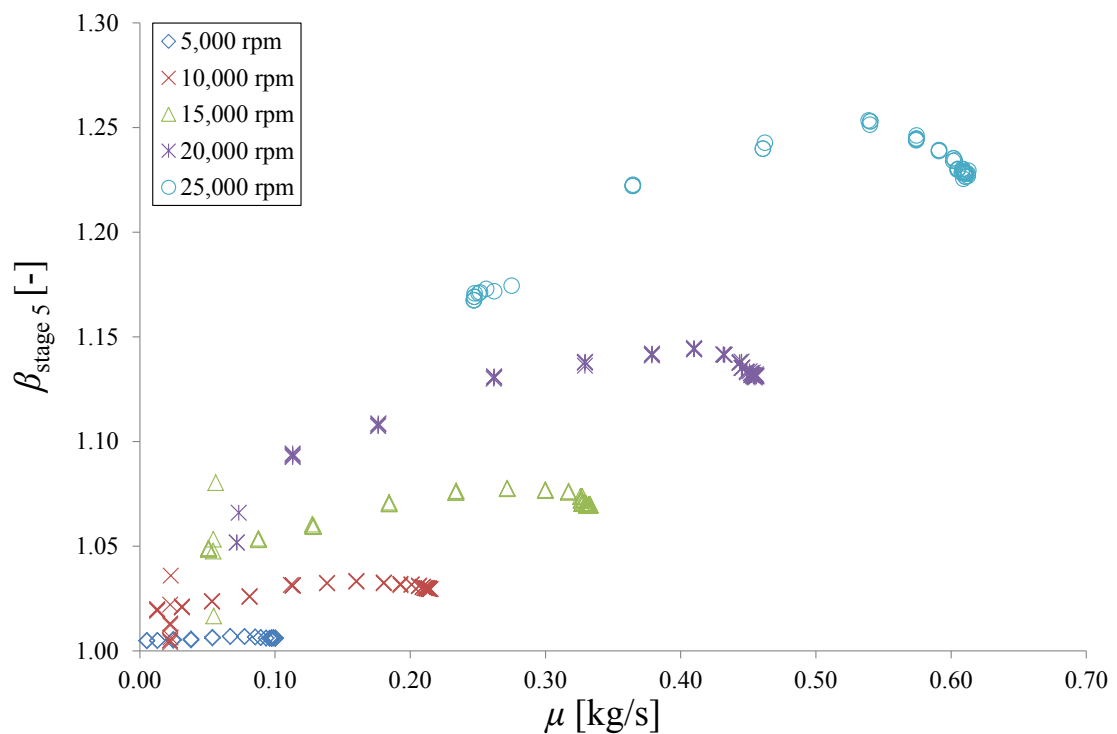


Fig. 3.17 - Steady state performance maps: static pressure ratio at stage five (bleed valve position)

The accumulation of mass flow inside this volute produced a sort of hysteresis effect, which sometimes amplified the compression ratio slightly over the peak of the

curve. Therefore, the operating point did not immediately change position between the characteristic curve and the stalled curve, but went through a path that is difficult to reconstruct through instantaneous measurements. The combination of these conditions led to the scattered trend reported in Fig. 3.17 for very low mass flow. The scatter, and thus the path, increased with the rotational speed because the perturbation had higher amplitudes. In the curve at 20,000 and higher, this phenomenon was not present because Valve 1 was not completely closed.

After the occurrence of stall, it is evident that the compressor no longer reached a stable condition, generating a continuous shift between the characteristic and stalled curve. A longer waiting time for stabilization would generally allow this phenomenon to be reduced but so as not to compromise the integrity of the system; the test methodology (closing of the valve and data logging) was applied with a reduced waiting time for the stabilization of the parameters. In fact, the aim of this analysis was only to determine the characteristic curve and identify the point where instability occurred.

Fig. 3.16 illustrates the isentropic efficiency curves, corresponding to the same data of Fig. 3.15, and Fig. 3.17. The static instability was evident, by the deviation (scattering) between the last two-three points of the curve (especially at 10,000, 15,000 and 20,000 rpm) on its positive slope part. This behavior was consistent with stall because overall mass flow was almost constant and the operating point suddenly dropped (see Fig. 3.15 and Fig. 3.17), which means that stall was achieved through a sudden pressure ratio drop.

The static instability was only found for curves at 5,000, 10,000, 15,000 and 20,000 rpm while it was not found at 25,000 rpm because Valve 1 was not completely closed in this test.

An important note to mention is that the mass flow rate values, m_1 , utilized for determining the curves of Fig. 3.15, Fig. 3.16, and Fig. 3.17 were those of the hot wire sensor, since the measurements were more reliable than those of the orifice plate at low flow regimes. The mass flow rate data did not achieve a zero value even when the valve was totally closed, which is only due to the type of mass flow rate sensor (hot wire type) which has difficulty showing zero mass flow due to its proximity to the compressor inlet (which implies the presence of vortices and stalled cell perturbations) and the lack of stabilization of the operating point in the stalled curve.

3.5.3 Dynamic Behavior

The dynamic tests were carried out configuring the piping system in Layout #2. These tests were performed following some specific steps. After an initial linear increase, until the desired rotational speed v , stabilization of the parameters was achieved and a stall ramp (i.e. the characteristic curve toward stall and/or surge) was initiated by closing Valve 2 at constant velocity (see Compressor Dynamic Tests and surge inception paragraph).

When surge occurred, the valve was stopped for a sufficient amount of time for the development of instability to be completed and then it was opened again. Fig. 3.18 shows the trend of the most important measurements monitored during the test at $v = 10,000$ rpm. It is evident, by looking at the mass flow recorded downstream of the plenum (by using the hot wire sensor) and upstream of the compressor (using the orifice plate), that surge started when $\alpha = 25^\circ$.

A particular note needs to be made regarding these two measurements: during surge, the value downstream of the plenum was subjected to very low amplitude oscillations because the flow was more stable. In fact, the Δp_{p-amb} was always positive during the test and the plenum attenuated the fluctuation amplitude downstream thereof.

By looking at Fig. 3.18 an important point to highlight is that the surge cycle was shown to be well captured, not only by the static pressure transducers but also by the electric motor mechanical power (calculated through the torque meter data referred to M_{mot}), and by the thermocouple which measures the compressor inlet stagnation temperature. Also T_{02} and T_{stage5} (not illustrated) showed a significant and progressive increment during surge, but the characteristic oscillations of surge were less evident. This means that classic thermocouples are sufficient to detect surge, especially when positioned to measure stagnation temperature at the inlet of the compressor.

Fig. 3.19 confirms what is stated above by presenting the recorded values of the outlet pressure, p_2 , alongside the two mass flow rates, m_1 and m_3 , and the normalized power. The pressure fluctuations demonstrated excellent correspondence, not only with m_1 but also with p_p (not shown in the plot) and $P_{mec,norm}$. Their oscillation amplitudes were compatible and their trend clearly followed the rapid change in the flow field. The frequency of the surge oscillation was around 0.7 Hz and the maximum compressor outlet pressure deviation between p_{2max} and p_{2min} , with respect to the mean of p_2 during surge,

was 0.04 bar. A very close result was found for p_p as well. It can be noted that m_3 showed limited oscillation amplitudes but of the same frequency as those which characterized m_1 .

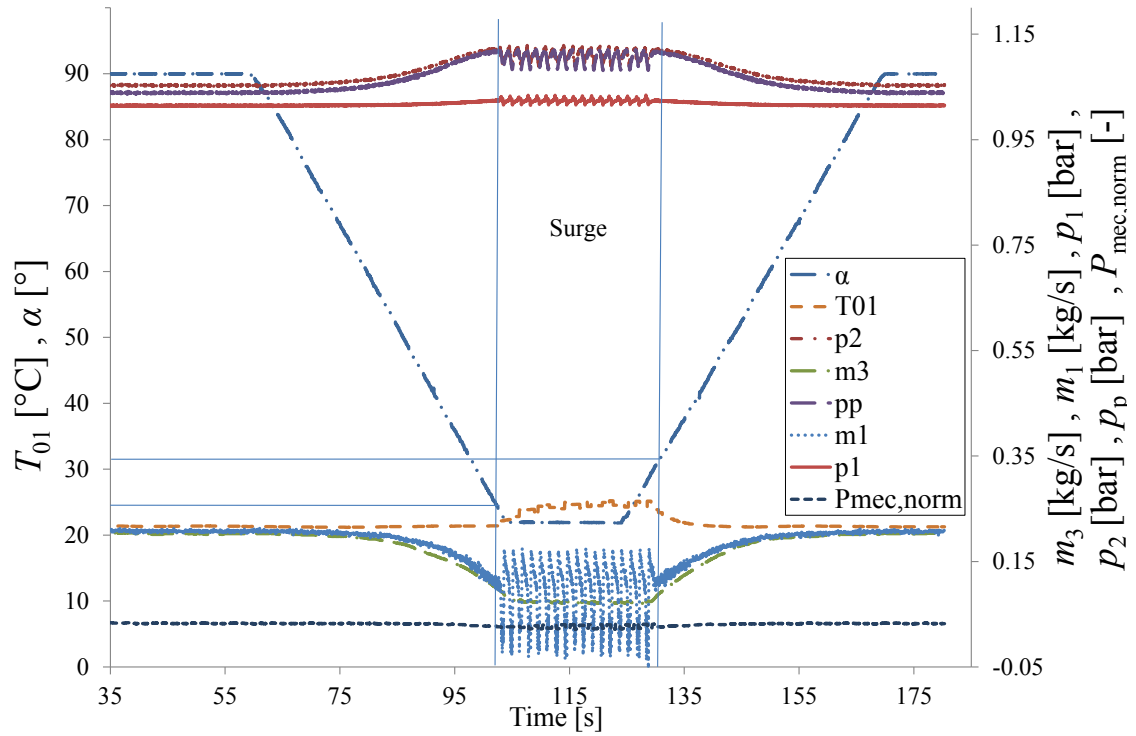


Fig. 3.18 - Dynamic Test @ $v = 10,000$ rpm

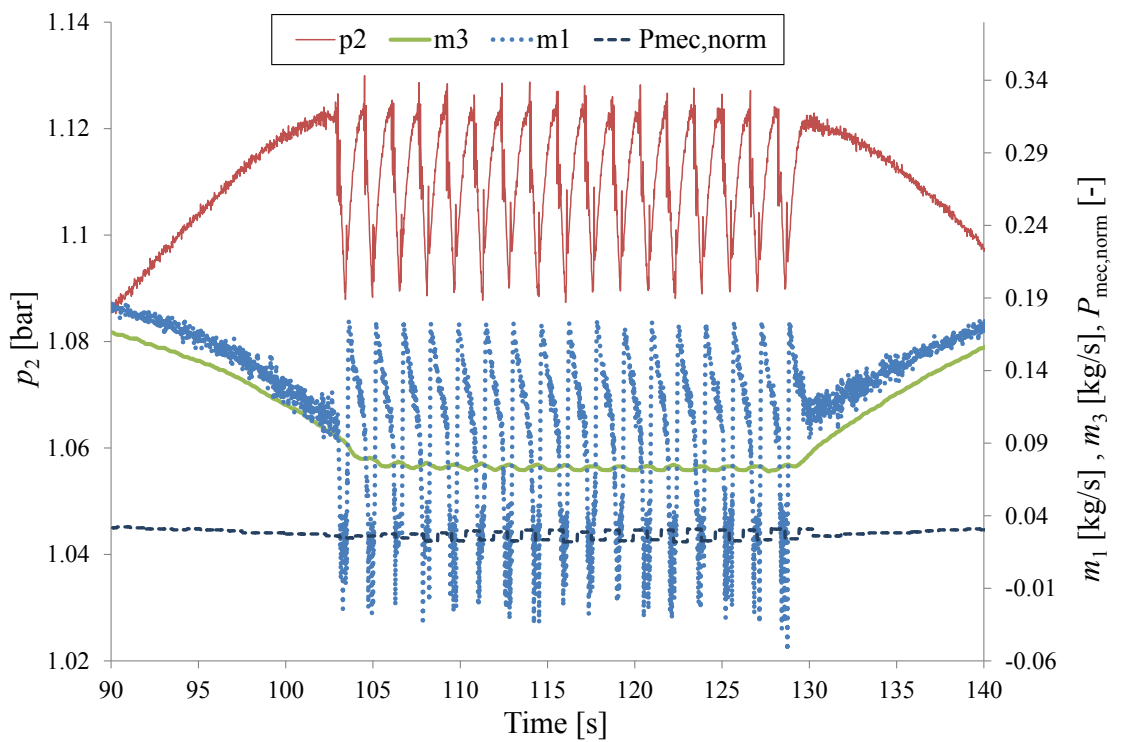


Fig. 3.19 - Dynamic test @ $v = 10,000$ rpm. Typical surge oscillations encountered on p_2 , m_1 , m_3 and $P_{mec, norm}$

The characteristic curve and the path of the compressor operating point during the dynamic test are presented in Fig. 3.20.

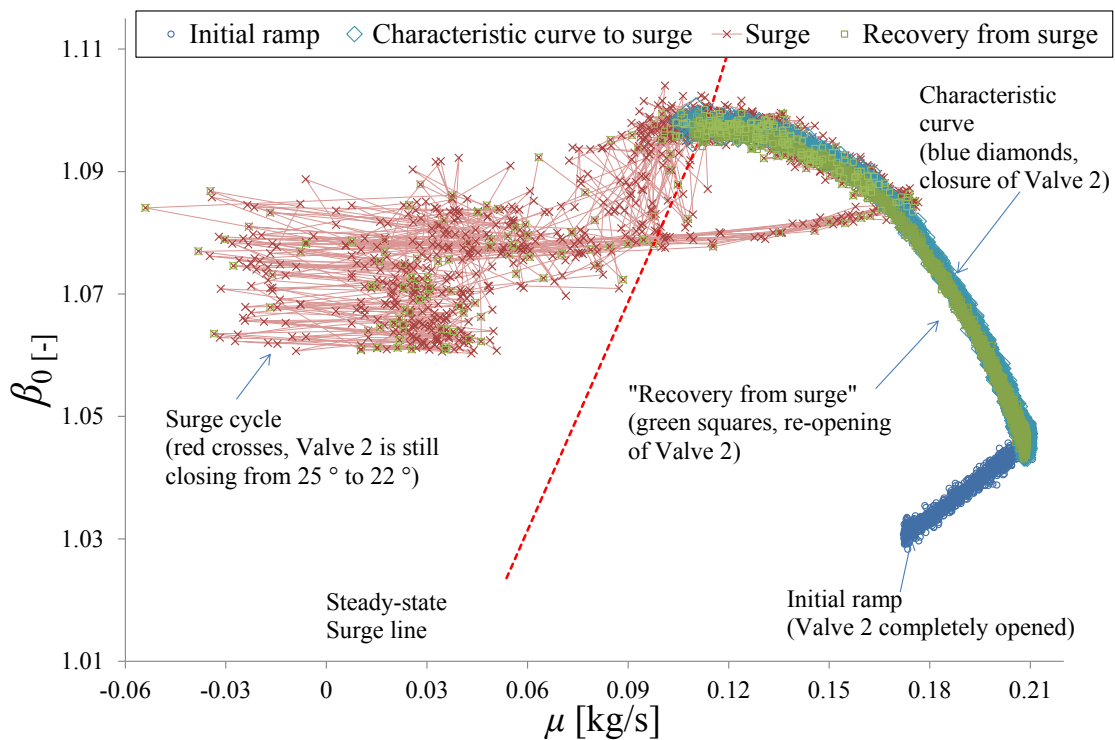


Fig. 3.20 - Dynamic Test @ $\nu = 10,000$ rpm. Characteristic curve towards to surge and recover from surge

As can be seen, this plot was composed by the initial ramp (blue circles) in order to achieve the rotational speed of 10,000 rpm, the stall ramp (blue diamonds), obtained by a linear closure of Valve 2, the surge cycle with the reversal flow (red crosses, at this point of the test Valve 2 was at 25° but was still closing), and a final curve (green circles) obtained by opening the valve in order to recover from surge.

Dynamic instability was achieved a few instants after the operating point approached the surge line (calculated by using the peaks of steady-state characteristic maps). Successively, instability could totally develop describing several times the surge cycle. Similar behavior occurred during the dynamic tests at $\nu = 5,000$ and $\nu = 15,000$ rpm. This is an important result because it ensures that steady-state surge line, as simply calculated here, is a reliable, and even preventive, surge-approaching indicator even during transients of the compressor.

Fig. 3.20 also shows that the compressor experienced rotating stall before deep surge, which occurred at each surge cycle. In fact, once the surge phenomenon started, the

operating point demonstrated (i) movement from the peak of the characteristic curve to the stalled curve, then (ii) high oscillations at very low mass flow regimes, and finally, (iii) movement along the stalled curve towards the characteristic curve before the cycle was repeated again. This behavior appeared to be the same even at $\nu = 5,000$ and $\nu = 15,000$ rpm. During the opening of Valve 2, a hysteresis phenomenon was noted, which delayed the return of stable compressor conditions.

This fact is also observable in Fig. 3.18 where it is evident that surge started at a closing angle $\alpha = 25^\circ$, whereas the recovery from instability occurred at about $\alpha = 33^\circ$. Very similar results to those illustrated were obtained at $\nu = 15,000$ rpm (in Fig. 3.21 the typical p_2 , m_1 , m_3 and $P_{\text{mec,norm}}$ oscillations during surge are presented) and at $\nu = 5,000$ rpm. At 15,000 rpm, surge pulsations (see Fig. 3.21) occurred with a frequency of 0.5 Hz with approximately doubled amplitudes compared to $\nu = 10,000$ rpm. At 5,000 rpm the oscillation presented a frequency of 1 Hz with significantly reduced amplitudes compared to those at higher rotational speeds.

The dynamic tests were also used to study the mechanisms of surge inception in an attempt to detect the local perturbations which lead to this phenomenon.

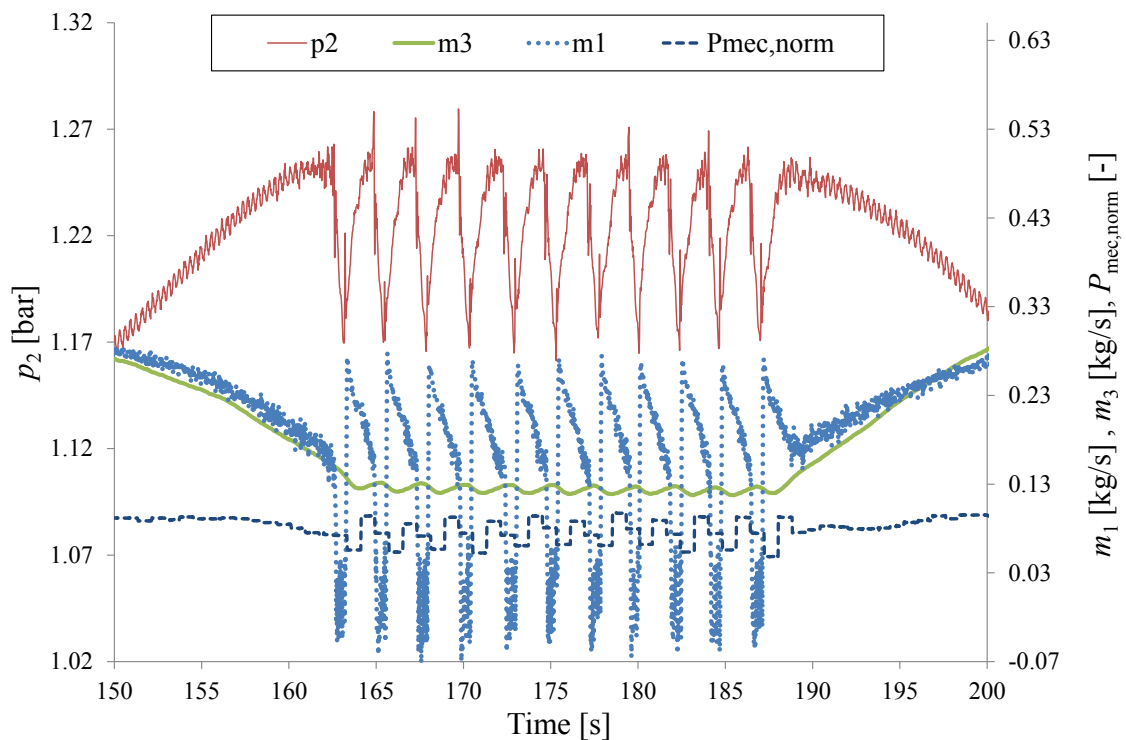


Fig. 3.21 - Dynamic Test @ $\nu = 15,000$ rpm. Surge pulsations of p_2 , m_1 , m_3 and $P_{\text{mec,norm}}$

This study was done by investigating the results obtained by the two fast response piezoresistive pressure transducers (Kulite XQ-093 series), located circumferentially (at a relative angular distance of 180° to each other) immediately before the compressor inlet (see Tab. 3.3). The study was initially focused on the instants before surge in order to identify its inception phenomena. Fig. 3.22 reports the trend of dynamic pressure value amplitudes at the compressor inlet. The scattered trend, which precedes surge, was clear evidence of rotating stall conditions. Moreover, from this figure it is evident that after surge inception, surge and stall are alternatively present; in other words, each surge cycle is originated by a short period of rotating stall. This behavior agrees with the typical behavior of axial machines (Day, 1994) and with the operating point path of Fig. 3.20.

A frequency domain analysis was then conducted on the signals of these two transducers and the result of Kulite #1 is shown in Fig. 3.23 (similar results were obtained from Kulite #2).

This figure represents the waterfall diagram (referred to the dynamic test at 10,000 rpm) of the fast Fourier transform, in terms of frequency normalized to the rotor revolution frequency, at time intervals of 2 s throughout the experiment.

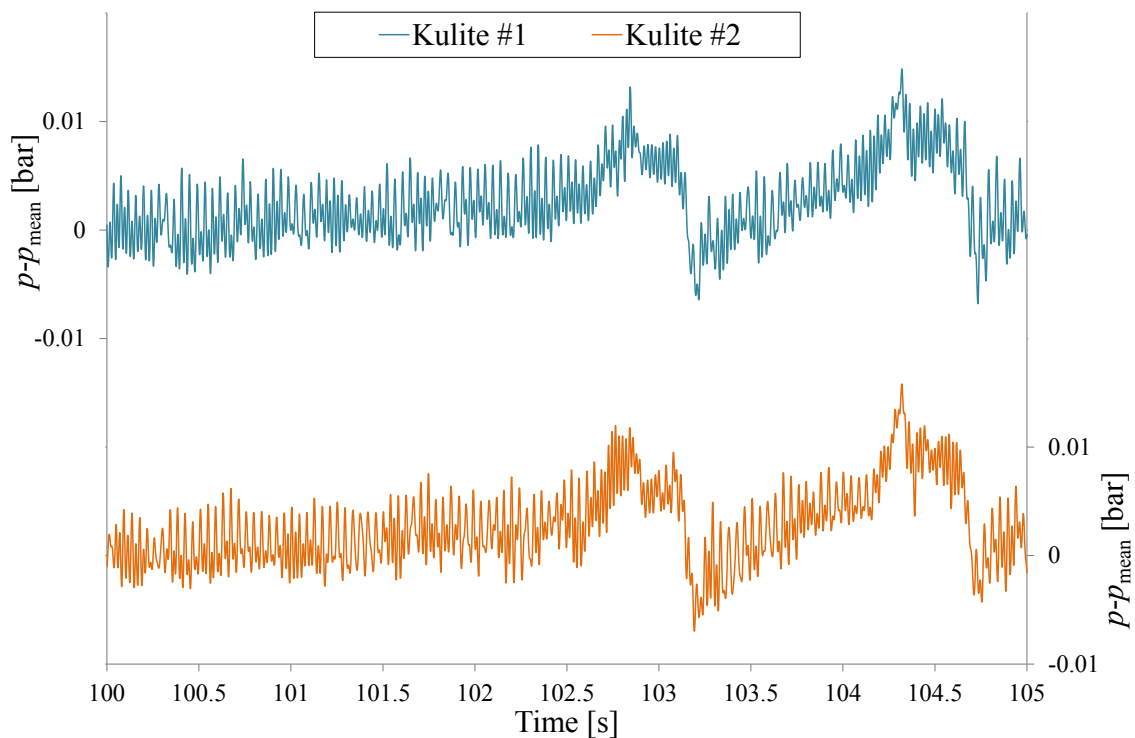


Fig. 3.22 - Dynamic Test @ $v = 10,000$ rpm. Fast response transducers signals at compressor a few instants before surge

It should be noted that a fluid dynamic perturbation (and the relative second harmonic) was present during the dynamic test. Its characteristic frequency, initially at 13 % of the rotor speed, increased until 15 % during the closure of Valve 2. During the surge cycle, the dominant frequency was that of surge pulsations, i.e. 0.7 Hz while the fluid dynamic perturbation seemed to be less marked and with minor amplitude. When Valve 2 started to be re-opened and the compressor recovered from surge, the frequency of the perturbation recovered its original characteristics.

This phenomenon is compatible with a stall cell which is rotating at about 13 % of the rotor speed. The stalled cell grew as the compressor was going towards surge; the increase in its frequency was valid evidence of this because, as the boundary interface was growing, the sensors were detecting this rotating cell more frequently.

It should be emphasized that, as the test was conducted at a rotational speed of 10,000 rpm the compressor was far from its nominal operating conditions (and the bleed chamber was closed). This is evident by observing in Fig. 3.17 the destabilizing effect of the axial part of the compressor. Therefore, even with Valve 2 completely open, the presence of stalled cells was expected, as the frequency analysis confirmed.

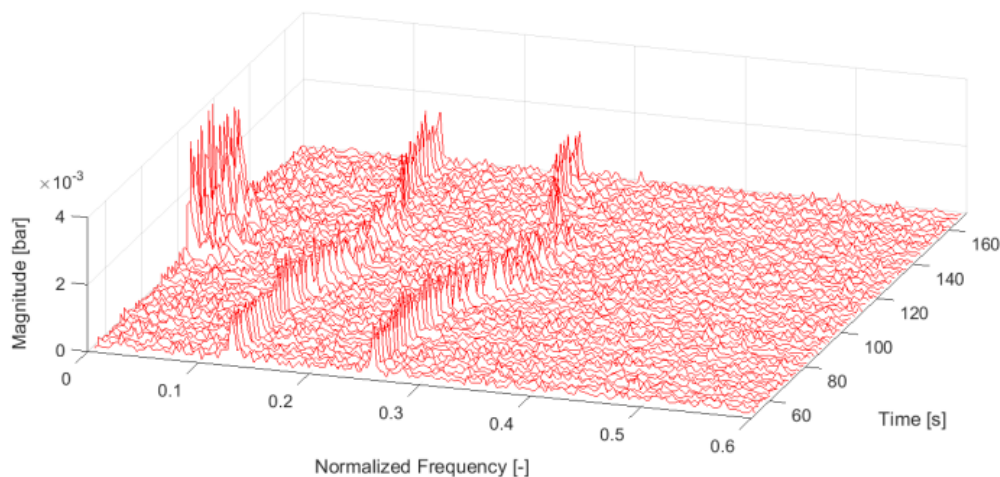


Fig. 3.23 - Dynamic Test @ $v = 10,000$ rpm. Stall analysis at compressor inlet. Frequency domain analysis

Fig. 3.24 shows the oscillations recorded by the two fast response transducers at $v = 10,000$ rpm with Valve 2 completely open. In this figure, the rotating perturbations induced by the stalled cell are easily recognizable. The two signals are highly comparable to each other and their frequency is exactly the same (13 % of the rotor speed). Moreover, their phase shift, in temporal values, is around 0.024 s (consistent with their rotational speed).

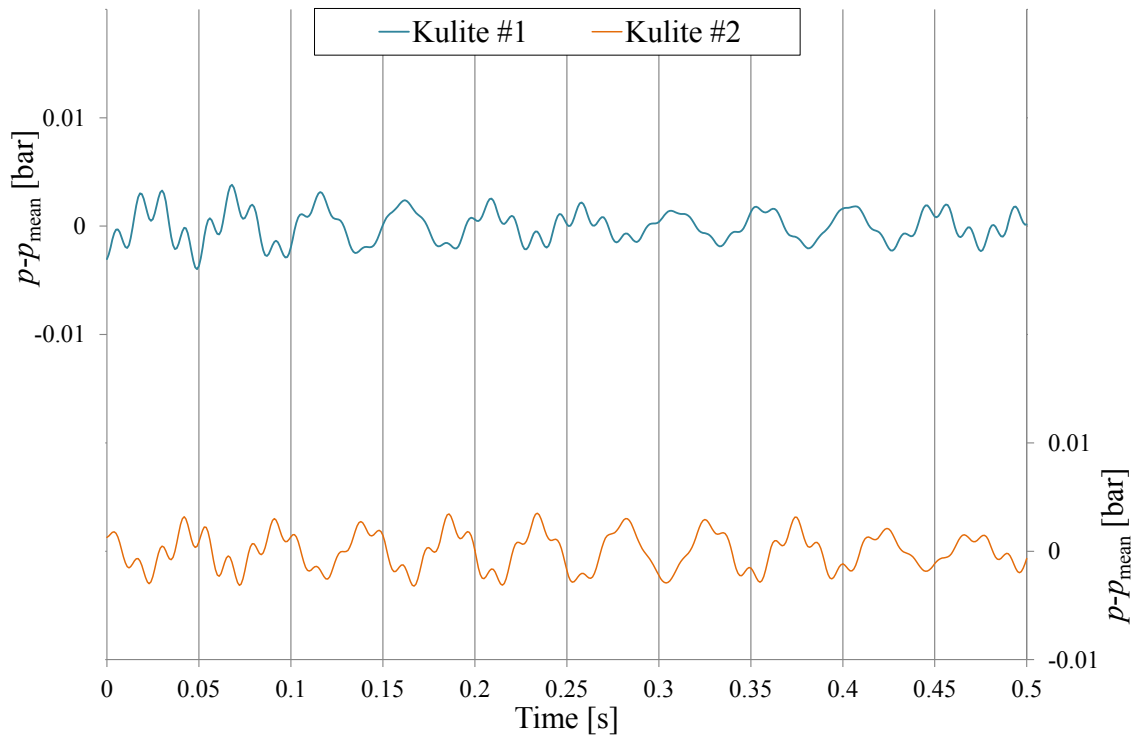


Fig. 3.24 - Dynamic Test @ $v = 10,000$ rpm. Stall analysis at compressor inlet. Complete development of rotating perturbations.

3.6 Conclusions

This chapter describes an experimental campaign to analyze the performance of an axial-centrifugal compressor. The aim was to investigate the steady state and the dynamic behavior of the compressor, through the determination of the characteristic maps, the analysis of surge instability and its inception mechanism.

A detailed description of the test rig, the acquisition system and the methodology used for the tests was reported. The test rig proved to be effective in the characterization of the stable and unstable behavior of an axial-centrifugal compressor. It could be configured in Layout #1 and Layout #2, the former used for the steady-state performance evaluation and the latter for the dynamic tests.

The first series of tests demonstrated that:

As expected, the high speed compressor at low velocity did not receive an important contribution to the pressure rise from its axial stages which had a clear destabilizing effect, but as the velocity increased, the characteristic curve of these stages achieved a more stabilized and typical trend.

Static instability was reached and identified by the abrupt drop in β_0 when stall occurred.

The dynamic tests performed showed that:

- The surge line, which was simply estimated by using the peak values of the steady-state characteristic maps, showed to be reliable for transient as well. It demonstrated to be a precautionary parameter for preventing the dynamic instability during the dynamic test at the performed rotational speeds.
- Deep surge occurred at very low mass flow values generating backflow. The operating point, at each surge cycle, moved from the characteristic curve to the stalled curve, then experienced high oscillations and moved along the stalled curve towards the characteristic curve
- Deep surge pulsations were detected satisfactorily by all the static pressure sensors and mass flow measurement at the compressor inlet and downstream of the plenum (the latter presented strongly reduced oscillation amplitudes). Moreover, the stagnation temperature, measured through a classic thermocouple at the compressor inlet, proved to be an optimum parameter for surge detection, as did the mechanical power developed by the electric motor of the test rig (and thus the torque, as the rotational velocity demonstrated to be a highly stable parameter). Therefore, by observing the time series of these two parameters it is possible to clearly distinguish surge inception even with simple instrumentation (fast response thermocouples are not necessary).
- The surge pulsation frequency showed a slight decrease when the test was carried out at higher rotational speeds but presented higher amplitudes. This is connected with the size of the surge cycle; the larger the surge cycle is, the higher the amplitudes are, and the more the frequency decreases. This implies that deep surge pulsation has characteristics which depend not only on the type of compressor, and the piping system, but also on the compressor operating conditions. This also suggests that different degrees of deep surge could be classified depending on the pulsation characteristics, which could determine the extent of hysteresis needed in order to recover a stable condition.

By comparing the results from steady-state and dynamic tests it is clear how the piping system could affect not only the operating range, but also the type of instabilities occurring on the compressor. This agrees with many works in literature on radial and axial compressors, therefore, this study offers a valid experimental validation also for multistage centrifugal-axial compressors.

Finally, an analysis of the signals recorded from two fast response miniature pressure transducers positioned circumferentially at the compressor inlet showed that:

- A stall cell rotating at 13 % of the rotor speed was present due to the destabilizing action of the axial compressor. This cell appeared to grow in proximity to surge, while reducing its amplitude during surge.
- After surge occurrence, the alternation of stall and surge was observed.

4 Experimental Activity -

Part II

The importance of predicting and preventing these dangerous phenomena is vital since they lead to a loss of performance and severe damage to the compression system and the compressor components. The identification of the typical precursors of these two types of compressor unstable behaviors can imply many advantages, in both stationary and aeronautic applications, such as i) avoiding the loss of production (in industry) and efficiency of systems and ii) reducing the cost of maintenance and repairing. Many approaches can be adopted to achieve this target, but one of the most fascinating is the vibro-acoustic analysis of the compressor response during operation.

A set of triaxle accelerometers and microphones, suitable for capturing broad-band vibration and acoustic phenomena, were installed in strategic positions along the compressor and the test rig. Tests were carried out at different rotational speeds, and with two different piping system layouts, by varying the discharge volume and the position of the electric control valve.

Moreover, two different methodologies were adopted to lead the compressor towards instability. This experimental campaign allowed the inception of compressor stall and surge phenomena and the acquisition of a great amount of vibro-acoustic data which were firstly processed through an innovative data analysis technique (cyclostationary domain analysis), and then correlated to the thermodynamic data recorded. Subsequently, the precursor signals of stall and surge were detected and identified demonstrating the reliability of the methodology used for the study of compressor instability. The results provide a significant contribution to the knowledge of the inception mechanisms of these instabilities. In particular, the experimental data can offer a valid support to the improvement of surge and stall avoidance (or control) techniques since it presents an alternative way of analyzing and detecting unstable compressor behavior characteristics by means of non-intrusive measurements.

The development and description of the test rig, the methodology of the tests and the results are presented.

4.1 Introduction

Nowadays, unstable compressor behavior is not yet fully understood and is still an attractive topic for many researchers since it strongly affects the operability and functionality of these turbomachines and thus the systems, such as gas turbines, of which they are fundamental components. In particular, unstable operation can arise in process industries due to startups or unpredictable and rapid transients during operation. These types of events can lead the compressor to rotating stall or surge.

These two phenomena are related to each other since stall very often precedes surge (Marshall & Sorokes, 2000) (Tryfonidis, et al., 1994). The degree of danger of these two phenomena is not only due to the severe loss of aerodynamic nominal conditions, which bring about decreases in power and efficiency, but also to the mechanical damage that they can produce inside the compressor and mechanical system components. These effects can, in some cases, lead to the destruction of the compressor or some component of the piping system.

The vibrations and noise can contribute to the deterioration of the compressor components. Vibrations, intended as casing vibrations and blade vibration, are important since the first instantaneously modifies the tolerance of the compressor while the second, if hard, can lead to the partial or total breaking off of the blades (Cumpsty, 1989) (Meher-Homji & Gabriles, 1998). Noise is a less complex and dangerous threat than vibrations but recently the study of aeroelasticity is becoming more popular in order to examine some aerodynamic and aeroacoustic aspects (Petry, et al., 2010), and to design acoustic treatments. Interesting examples, with application to stall and surge conditions, are provided by the work of Vahdati et al. (Vahdati, et al., 2008) and that of Schoenenborn and Breuer (Schoenenborn & Breuer, 2012). It is clear that in unsteady processes these quantities represent a serious complication and can often be related since both of them can reveal important clues regarding the operating condition of the compressor.

Stall and especially surge are often preceded by typical audible pulsating sounds and vibrations which help to understand that the operating limit of the compressor is about to be reached (Boyce, 2003). In fact, surge and near surge conditions are accompanied not only by outlet temperature excursion and fluctuating differential pressure (and mass flow rate), but also by the resulting pulsating noise and the increasing of vibrations (especially in the low frequency range). However, these precursors are not always detected, so the

threat of failure cannot always be recognized. On the other hand, stall can also be dangerous even without degenerating into surge. Stall cells can, in fact, introduce disturbances which can excite some blade passing frequency (or their harmonics), as well as the natural frequencies of the blades, impeller shroud or casing.

Some compressors (typically small scale) can operate for a long time in mild surge conditions, resisting pressure and mass flow oscillations without registering mechanical harm; and even recovering by themselves from the instability (if the instability is light and depending on the operating conditions and layout of the system). However, the dangerous effects of stall and surge should be avoided and somehow predicted or detected in their inception phase. This is the context in which this work is focused.

In this work an experimental campaign on a multistage axial-centrifugal compressor is carried out. The facility is the same as that described in chapter 3 but, in this case, additional sensors (accelerometers and microphones) were installed along with their specific high frequency data acquisition system (see section “Experimental Test Rig”). The aim of the chapter is to compare the dynamic vibro-acoustic response to the thermodynamic data recorded during tests, demonstrating the evidence of stall and surge by using the aforementioned new instrumentation and obtaining supplementary information about these two phenomena - stall and surge were proven to have cyclostationary features which can be detected well by a cyclostationary domain analysis (which will be described below). The following paragraph of this chapter of present a literature review of the main works regarding stall and surge (especially those carried out by means of non-intrusive techniques), the basics of cyclostationary analysis, and the description of the test rig and methodology used for this study. Finally the results of this experimental campaign are shown in detail, followed by the main conclusion drawn.

4.2 Literature Review

The relevance of compressor stall and surge has led to many experimental campaigns, or theoretical studies, in order to increase the knowledge of these two phenomena and their inception process (McDougall, 1990), (Day, 1993) (Escuret & Garnier, 1995) (Vo, et al., 2005). The research advancements on stall and surge knowledge were reported by Day (Day, 2016), who wrote an exhaustive review of the main works regarding this topic. In the literature, many experimental studies on compressors are present and all of them use different instrumentation, methodologies and signal analyses.

A recent work (Li, et al., 2015) was conducted by Li et al. They have analyzed test rig data, by means of the short-time-Fourier-Transform, from a seven-stage compressor by using both casing static pressure and outlet total pressure signals. Their analysis revealed that their methodology was capable of identifying stall precursors - identified as intermittent components (with energy close to the energy of the rotor frequency component) at stall frequency generated before the onset of stall.

An interesting paper was also presented by Gallus and Hoenen (Gallus & Hoenen, 1986), who have studied the airfoil and endwall boundary layers in a subsonic compressor stator. By analyzing hot-wire probe results, they demonstrated that when the compressor was approaching stall, the separated region of the blade boundary layers was evident. In that analysis the periodic signal of the blade could not be identified in the separated region, and therefore, the blade passing signal deteriorated towards stall. A few years later, the same authors carried out a further investigation presenting a method for monitoring aerodynamic load (Hoenen & Gallus, 1993). Based on the experimental results, the spectra analysis showed a different pattern with respect to nominal conditions when the compressor was approaching the surge line. They measured the unsteady pressure distribution in 8 stages of the multistage axial compressor of a LM5000 gas turbine and found a reduced pressure rise in the 13th stage, where periodic fluctuations (blade passing frequency) disappeared. They correlated this event to the rotating stall phenomenon occurring on that stage. Bright et al. (Bright, et al., 1997) explored various techniques for identifying the stall precursors in several configurations of a high speed compressor stage, exposing the potential advantages of the correlation integral method, which borrows ideas from chaos theory to identify changes in the underlying nonlinear dynamics of fluid flow.

Dhingra, et al. (Dhingra, et al., 2003) carried out an analysis of compressor aerodynamic instability precursors was carried out by installing pressure sensors on the compressor casing located over the rotor of three different compressors. The authors used a modified form of the auto-correlation based approach to quantify the repetitiveness of the blade signature, finding that the correlation parameter reduced when the compressor was operating close to the stability range limit. This phenomenon was interpreted as a stall and surge precursor. This phenomenon was interpreted as a stall and surge precursor. The same phenomenon and the same conclusions were also reported by Inoue, et al (Inoue, et al., 1991) where the deterioration of the blade passing periodicity signal was encountered and recognized as a stall precursor.

A similar work was also conducted by Young et al. (Young, et al., 2013), who focused their study on the relationship between the blade passing non-repetitiveness near stall, rotor eccentricity and tip-clearance. This work demonstrated that i) when approaching stall, the blade passing irregularity changes with the tip-clearance geometry and ii) eccentricity also affects the signal which always achieved its maximum non-repetitiveness value in the proximity of the maximum clearance. They concluded that the use of the blade passing signature analysis would not be a reliable stall warning method by itself, but at least another parameter between tip clearance size or eccentricity should be measured (obviously taking into consideration other sources of irregularity). Their result is partially in contrast with the work of Christensen et al. (Christensen, et al., 2008) who developed a real-time algorithm based control software for stall management. They used over-the-rotor dynamic pressure sensors and adopted a correlation method, similar to that of Dhingra et al. (Dhingra, et al., 2003), suggesting that this system can potentially be used in routine engine testing, but also for military and commercial engines.

Nowadays, other novel methods and instruments are being proposed in order to monitor the condition of gas turbines online, for identifying compressor stall and surge inception, but also regarding the status of the gas turbine components (in particular the blades). One of these methods is vibro-acoustic analysis. This approach could also potentially give important information only by measuring the casing vibrations (Forbes & Randall, 2009) (Forbes & Randall, 2008) and therefore using a non-intrusive technique; which represents a relevant aid to the maintenance and continued operation of these machines. In fact, the vibration and acoustic measurements could enable a deeper comprehension of unsteady phenomena effects (Simmons, et al., 2006).

An experimental campaign conducted by Lawless and Fleeter (Lawless & Fleeter, 1995) (Lawless & Fleeter, 1993) was based on the Fourier analysis of simultaneously sampled data regarding sensitive electret microphones. The microphones were uniformly located around the inlet and three different diffuser geometries of a compressor. The authors also demonstrated the reliability of their methodology in the detection of stall precursor by finding different typologies of stall pattern depending on the diffuser mounted. Morini, et al (Morini, et al., 2007) performed a preliminary analysis of the incoming flow instabilities near surge which, based on vibro-acoustic measurements, allowed the identification of the unstable behavior precursors. In (Aretakis, et al., 2004) a similar investigation was also made by Aretakis et al. who continued the research of their previous works (Aretakis & Mathioudakis, 1996) (Aretakis & Mathioudakis, 1998). They

found that an acoustic signature, exhibiting a good correlation with the operating point of the compressor curve, can be obtained. They also found that the most suitable parameter for the determination of the compressor condition (unstalled, stalled or in surge) is the acoustic pressure level RMS value corresponding to a sub harmonic frequency range (which is the range of frequency below the compressor speed component).

All these examples testify the relevance and the potential of the various approaches for studying stall and surge in a compressor. In particular, the vibro-acoustic analysis has demonstrated great potential which should be explored by the further research.

Rotating machine vibro-acoustic signals can be naturally divided into periodic and random components (D'Elia, et al., 2016). Excitation forces induced by machinery rotating mechanisms result in the periodic counterpart of the vibro-acoustic signal. On the other hand, random contribution is mainly related to the non-periodic mechanisms such as: turbulence around fan blades, admission and exhaust of fluids in pumps, and so on.

By studying the energy flow inside the random contribution, pivotal information on the operating condition of the machine can be obtained. Signals which exhibit hidden periodicity of their energy flow are said to be cyclostationary. To the knowledge of the authors, there are no previous applications of the cyclostationary analysis of vibro-acoustic signals for the detection of both stall and surge phenomena in compressors.

This chapter explains and uses an innovative methodology - the methodology is not new but it is the first time it is applied to stall and surge analysis - underlining the capability and usefulness of accelerometers and microphones for detecting stall and surge

4.3 Cyclostationary Analysis

The rationale of cyclostationarity was firstly formalized by Gardner (Gardner, 1986). However, an approach based on the concept of the “energy conveyed by the signal” was introduced by Antoni in (Antoni, 2009). This approach details a new definition and framework for the analysis of such signals. Several orders of cyclostationarity can be defined. Generally speaking, any cyclostationary behavior that can be detected by a non-linear transformation of degree n is referred to as n th order cyclostationarity. As stated in the work of Antoni (Antoni, 2009), when a non-linear transformation of second degree highlights hidden periodicity inside the signal (second order cyclostationarity), the energy

is conveyed in a periodic fashion. The central idea consists of decomposing the energy flow not only into a constant trend, but also into periodic components which depict how the energy is travelling with time. De facto, the simplest non-linear transformation that can be applied in order to study the energy flow inside the signal is the squaring operator.

This decomposition is performed by the mean instantaneous power (MIP), which reads as the Fourier series of the energy flow per unit of time at each instant t (Antoni, 2009):

$$P_x(t) = \sum_{\alpha \in A} P_x^\alpha e^{j2\pi\alpha t} \quad (4.1)$$

Where

$$P_x^\alpha = \lim_{T \rightarrow \infty} \frac{1}{T} \int_T |x|^2 e^{-j2\pi\alpha t} dt \quad (4.2)$$

is the cyclic power of the signal at cyclic frequency α and A is the set of all the cyclic frequencies associated with non-zero periodic components. The MIP provides a global vision as to how the signal energy is slowing over time.

Among all the descriptors used for analyzing cyclostationary signals, the Cyclic Modulation Spectrum (CMS) has the ability to display the cyclic frequency α along with the spectral frequency f , and is defined as (Antoni, 2009):

$$P_x^\alpha(f; \Delta f) = \lim_{T \rightarrow \infty} \frac{1}{T} \int_T |x_{\Delta f}(t; f)|^2 e^{-j2\pi\alpha t} dt \quad (4.3)$$

Where $x_{\Delta f}(t; f)$ is the filtered version of the signal through a frequency band of width Δf centered at frequency f . Therefore, the CMS is simply the Fourier Transform of the well-known Spectrogram. The spectral and cyclic frequencies can be interpreted as the carrier frequency of the wave that transports the energy and its modulation frequency. In fact, the signal envelope represents the energy fluctuation as a function of time, which is completely reminiscent of the MIP definition. Consequently, the CMS represents the envelope frequencies α as a function of the carrier frequency f , computed in the frequency band of width Δf .

4.4 Test rig

The experimental test rig is located at the Engineering Department of the University of Ferrara. The entire facility as well as the data acquisition system of thermodynamic sensors has been exhaustively described in the previous chapter, thus in this section only a brief summary is reported.

The object of this study is a multistage axial-centrifugal compressor, see Fig. 4.1, that has six axial stages and one centrifugal. The number of blades for each stage of the compressor are illustrated in Tab. 4.1 together with the blade passing frequencies (BPFs) and the vane passing frequencies (VPFs) at $N=10,000$ rpm (only these values are shown as the results of this work are focused on that velocity). The BPFs and VPFs are calculated as:

$$\text{BPF} = \frac{N z_r}{60} \quad (4.4)$$

$$\text{VPF} = \frac{N z_s}{60} \quad (4.5)$$

The piping system (a scheme is proposed in Fig. 4.2) is thought to be modular so that two layouts can be obtained: Layout #1, which is equipped with a small discharge volume and Layout #2, which instead consists of a large discharge volume and is dedicated to surge analysis. The mass flow rate is regulated by controlling Valve 1 in Layout #1, and Valve 2 in Layout #2 (in future, these valves will be replaced in order to precisely control the percentage changes of area, or mass flow during tests). The inlet configuration is the same for both layouts and consists of an inlet duct where an orifice plate is installed. The compressor is driven by an electric motor which is remotely regulated by a control system software developed in LAbVIEW. In addition to the thermodynamic sensors already installed, see Fig. 4.2 (a), the compressor was equipped with additional instrumentation with its specific high frequency data acquisition system.

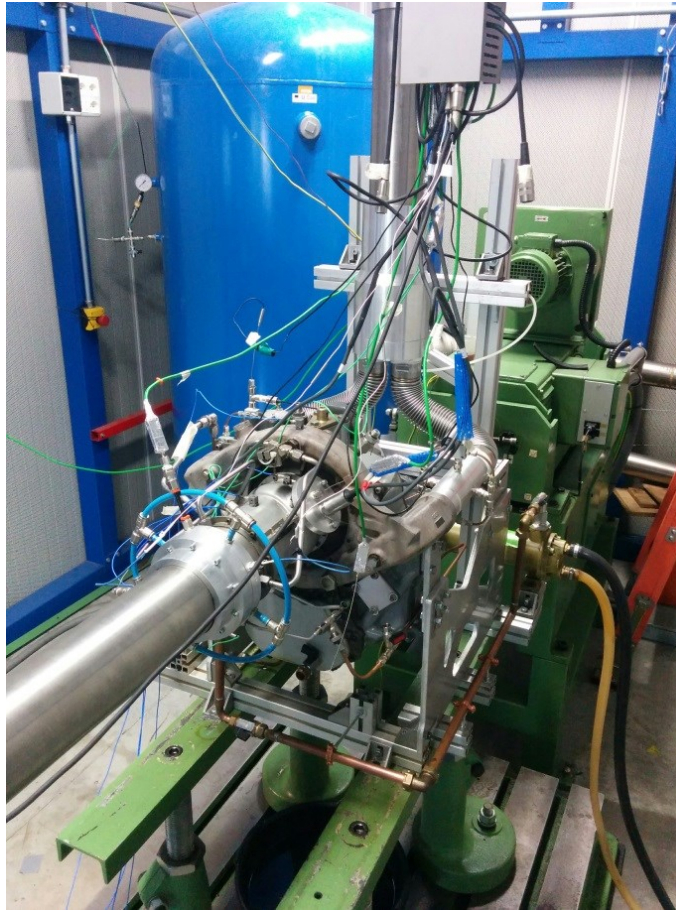


Fig. 4.1 - The tested compressor

In particular, a set of triaxial accelerometers and microphones were adopted to record vibrational and acoustic signals during compressor operation. The installed accelerometers have a linear frequency range of 1 Hz to 10 kHz. Vibro-acoustic signals were acquired by means of LMS Scadas III front-end allowing a maximum sample frequency of 204,800 Hz. The accelerometers and microphones, Fig. 4.2 (b), like the sensors for thermodynamic parameters, Fig. 4.2 (a), were installed in strategic locations along the compressor, the piping system and the test rig zone.

In particular, three accelerometers were installed on the axial part of the compressor casing and another on the centrifugal stage casing as shown in Fig. 4.3. The locations of the accelerometers were decided so that they were equally spaced along the compressor casing. The exact positioning is not relevant in such a small space since the vibration path between sources and response points is basically the same in such a small area. Obviously, the axial casing and the centrifugal casing are treated as different structures. In the axial compressor the accelerometers, Fig. 4.3 (a), were placed in the vicinity of the stator/rotor boundary of the first and the sixth stages, and on the rotor of the third stage. In the radial

compressor, an accelerometer (Fig. 4.3 (b)) was positioned on the centrifugal stage casing. The images of the microphones are not shown in this Thesis.

An important note should be made regarding the compressor bleed valve: also in this case (see also chapter 3) this valve was removed and replaced by an aluminum tap, in order to install some measurement sensors. This implies that compressor blow off is completely suppressed during the operation.

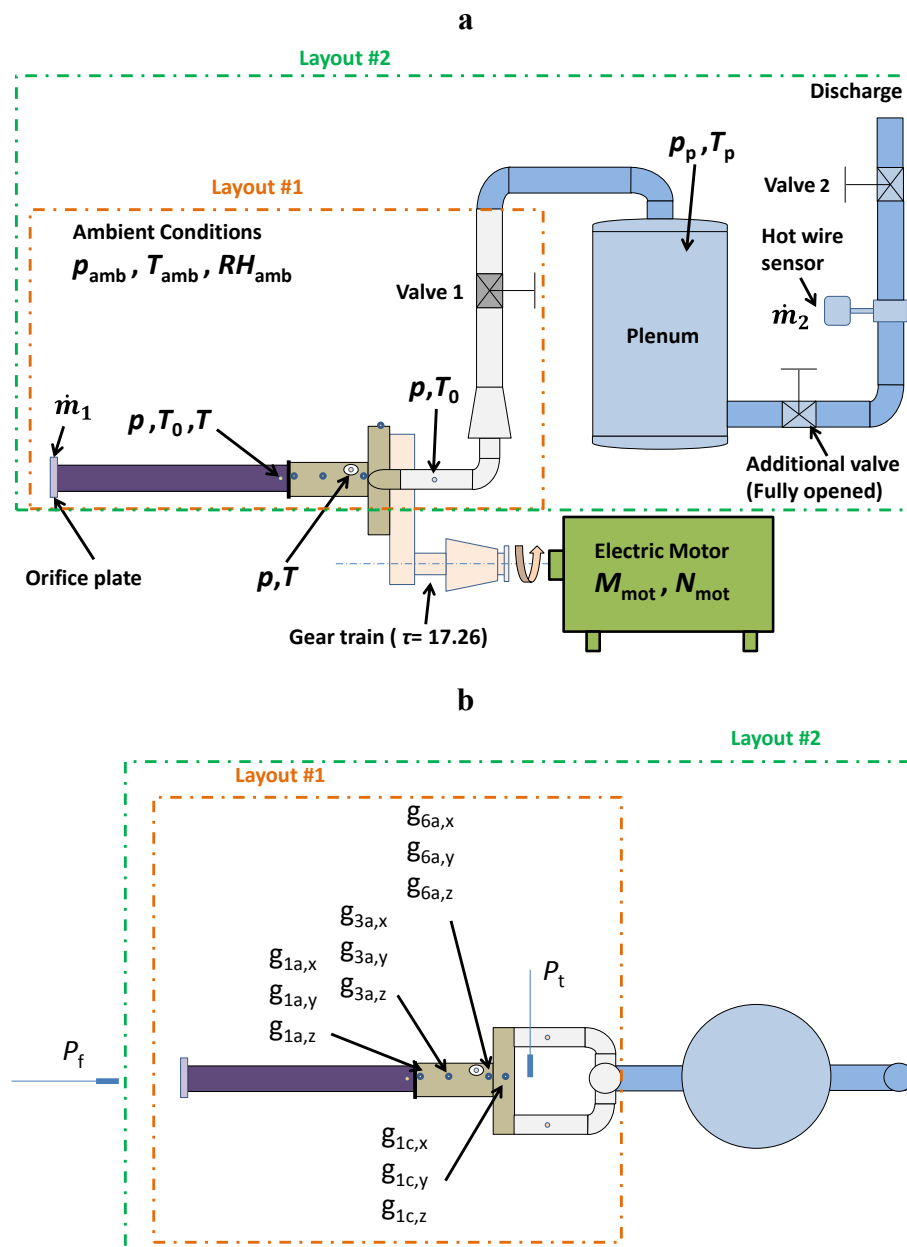


Fig. 4.2 - Piping system configuration. Layout #1 and Layout #2 with the (a) thermodynamic and (b) vibro-acoustic sensors

Tab. 4.1 - Number of stator and rotor blades of each stage

Stage	Type	Rotor (z_r)	Stator (z_s)	@ 10,000 rpm	
				BPF [Hz]	VPF [Hz]
1st	Axial	16	14	2666	2333
2nd		20	26	3333	4333
3rd		16	28	2666	4666
4th		25	32	4166	5333
5th		28	36	4666	6000
6th		25	30	4166	5000
7th	Centrifugal	28	12	4666	2000

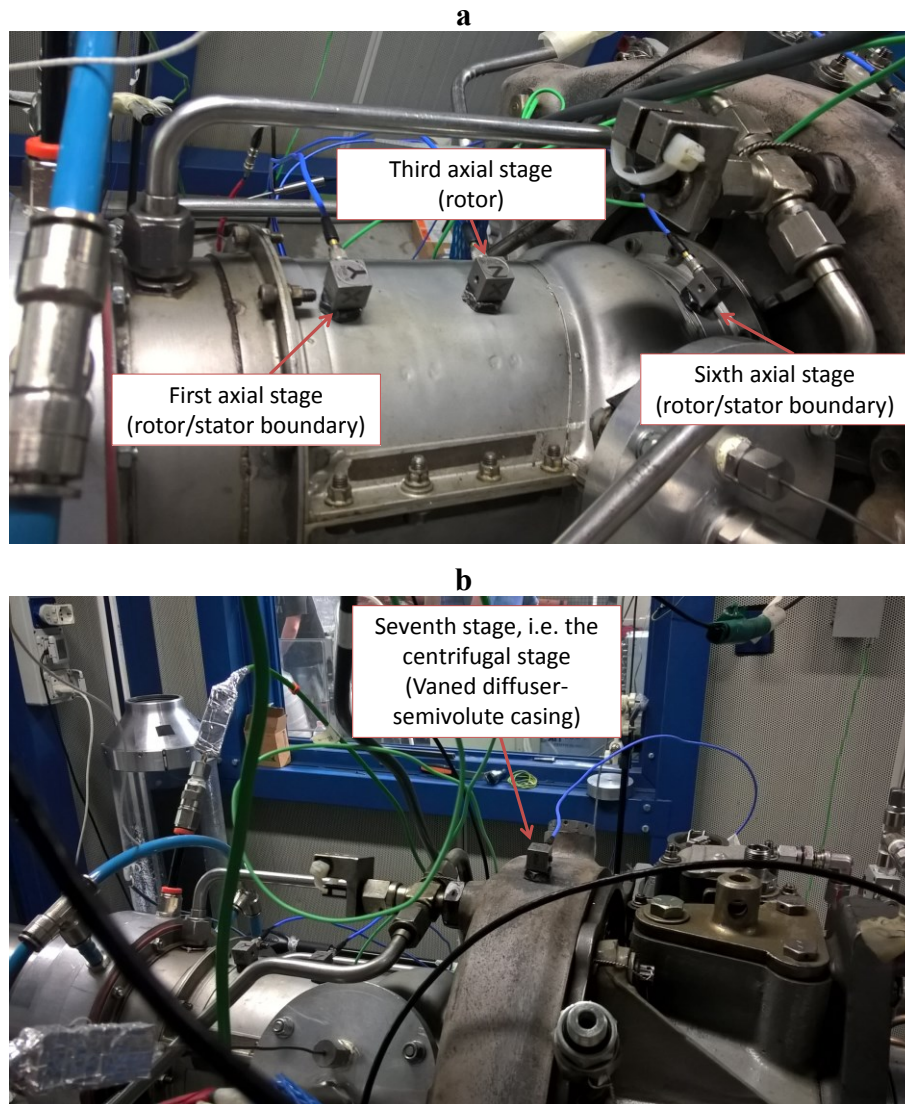


Fig. 4.3 - Installation of the accelerometer on the axial part (a) and the radial part (b) of the compressor

4.5 Methodology and Data Acquisition

The test methodology is close to that of the previous chapter so the compressor is tested in both Layout #1 and Layout #2, and it is driven to the instable regime by closing the control valve (Valve 1 or Valve 2). The first configuration is suitable for stall analysis, since the limited compressor downstream volume, also facilitates the stability of the operating points beyond the characteristic curve peak of the compressor. On the other hand, the second configuration is suitable for surge analysis since the accumulating mass in the plenum generates the compressor surge, once Valve 2 has achieved a certain degree of closure.

The compressor was tested at different rotational speeds: 5000, 10,000, 15,000 20,000 rpm. However, in this work only the results at 10,000 rpm are shown since they are representative of the phenomena which were also detected at the other velocities. Both the continuous and the step-by-step closure (with steps of 5-10 degrees, depending on the proximity to the surge line) of the valves were carried out, in Layout #1 and Layout #2. Concerning the step-to-step closing valve mode test, each measurement was made after waiting a certain time which allowed the complete stabilization of the compressor regime. The amount of time was variable, depending on the operating point achieved by the compressor (subsequent to the valve closure) and the degree of closure applied (5 or 10 degrees). Generally the stabilization of parameters was found after a range of 20-40 s. Thus, in this work, this test will be called steady-state. On the other hand, transient tests are conducted by closing the control valve, with a closing velocity of 1.5 °/s, until surge occurs while the data are recorded throughout the experiment. Tab. 4.2 briefly illustrates the type of tests performed, specifying the layout, the control valve used and the closing mode of the valve.

The vibro-acoustic sensors were recorded simultaneously with a sample frequency of 51,200 Hz for an extent of 60 s in the case of steady-state measurement, while during transient tests, signals were acquired for a long enough time to encompass all the valve closure. (the valve takes about 60 s to go from fully open to fully closed, but the signal recording continued for an additional 30-60 s to capture the fully-developed instability features).

The aim is the identification of the fluid-dynamic compressor instabilities, i.e. stall and surge, through the analysis of the vibro-acoustic compressor signature.

Tab. 4.2 - Type of tests carried out

Piping system	Controlled valve	Closing mode of the valve	Type of test
Layout #1	Valve 1	Step-by-step	Steady-state
		Continuous	Transient
Layout #2	Valve 2	Step-by-step	Steady-state
		Continuous	Transient

4.6 Uncertainty

The uncertainty in the recorded vibro-acoustic values is mainly related to the quantization process. The LMS Scadas III front-end used in this work has an A/D converter with 24 bits per channel, which can be distributed in selected amplitude ranges, therefore the quantization error is negligible. The uncertainty in the results is related to the estimation of equations (2) and (3). As reported in the work of Antoni (Antoni, 2009), the estimator variance is linked to the time signal length (equation (2) and (3)), and window length (equation (3)). De facto, the CMS (equation (3)) is obtained by the Fourier Transform of the Spectrogram, which suffers from the uncertainty principle, i.e. the product of time (Δt) and frequency (Δf) resolution is lower bounded by the Heisenberg inequality ($\Delta t \Delta f \leq 1/4\pi$). Therefore, the length of the window function must be chosen accordingly in order to reach a good compromise between resolution and estimation accuracy (the frequency resolution is reported in each figure presented in this chapter).

4.7 Test Results and Discussion

The experimental data were recorded by using all the sensors shown in Fig. 4.2. In this paragraph only the most significant results are depicted. In particular, they concern the accelerometers positioned at the third stage as well as the intake duct microphone.

4.7.1 *Frequency Analysis*

Firstly, a standard frequency analysis is carried out on the aforementioned signals. In particular, the signal spectra are obtained using the FFT algorithm with a Hanning windows function of 5.12 s length and overlapping factor of 2/3. The Hanning window is chosen due to its capability of reducing the spectrum leakage for random signals, while its

length/overlapping factor is selected in order to obtain a good compromise between frequency resolution (0.1953 Hz) and noise reduction (33 averages).

Fig. 4.4 plots the spectra of the intake duct microphone in the case of Layout #1 in a steady-state test for two valve positions, i.e. completely open and completely closed. It is possible to note that for the completely open valve position (Fig. 4.4 (a)), the signal spectrum is mainly characterized by the VPF/BPF frequency as well as the rotation frequency (171.7 Hz). These components disappear completely when the valve is fully closed (Fig. 4.4 (b)), on the other hand, there is a clear amplitude increase in the low frequency region (17.97 Hz). This component dominates the signal spectrum for the completely closed valve position and therefore may be related to the characteristic frequency of surge phenomena.

The same analysis was carried out on the $g_{3a,x}$ accelerometer signal. Fig. 4.5 depicts the spectrum comparison of the accelerometer signals in the case of Layout #1 in a steady-state test for two valve positions, i.e. completely open and completely closed.

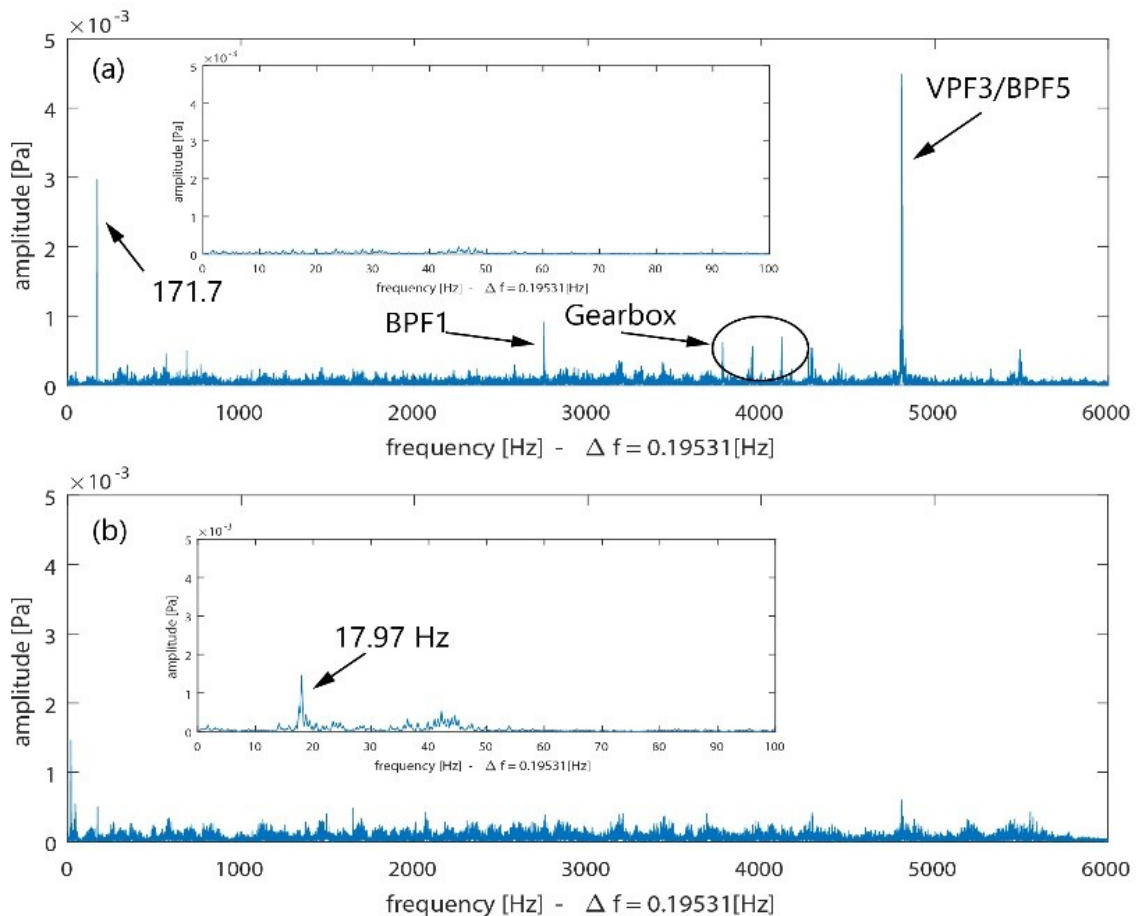


Fig. 4.4 - Layout #1 steady-state test microphone P_f spectrum: valve completely opened (a), valve completely closed (b).

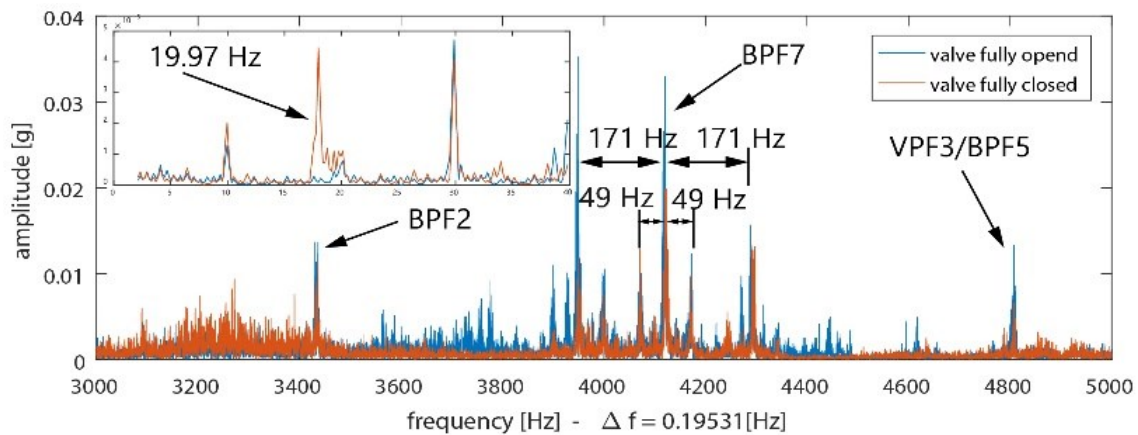


Fig. 4.5 - Layout #1 steady-state test; comparison of $g_{3a,x}$ accelerometer signal

The high frequency content is dominated by the VPF/BPF components. These components decrease in amplitude from the completely open valve position to the completely closed one. This phenomenon can be related to the effect of compressor instability (Hoenen & Gallus, 1993). Moreover, the BPF7 (7th stage BPF), is strongly modulated by two distinct families of sidebands, i.e. 49 Hz modulation frequency and 171 Hz modulation frequency. The modulation frequency of 171 Hz is the modulation at the compressor rotation frequency which may be related to a small speed fluctuation during the test. On the other hand, the modulation frequency of 49 Hz is not related to any mechanical phenomena, so may be connected with fluid-dynamic ones. However, no visible changes in the sideband amplitude can be seen when going from the completely open to the completely closed valve position. By comparing the results related to the two valve positions in the low frequency region, it is possible to see the rise of the component at 19.97 Hz. This component may be related to the surge phenomenon even if its frequency is not the same as the one found by the analysis of the intake duct microphone. This slight change in frequency content is related to the average operation performed in the spectrum evaluation.

The surge phenomenon may be highlighted from the frequency analysis carried out below (Fig. 4.4 and Fig. 4.5), however no other significant information can be obtained with this type of analysis, i.e. no clear evidence of rotating stall cell signature. The only fluid-dynamic phenomenon which could be related to the presence of a rotating stall cell is the modulation of the BPF frequency at 49 Hz. Therefore, this non-intrusive sensor spectrum analysis does not provide complete information on the fluid-dynamic phenomena arising during the operation of the compressor.

4.7.2 *Cyclostationary Analysis*

In order to characterize the instability phenomena more precisely, a cyclostationary analysis was carried out on the aforementioned sensors. As before, the surge phenomenon may be outlined by the analysis of the microphone P_f signals. Due to its type and location, this sensor is responsive to the air stream coming out of the compressor. Fig. 4.6 highlights the microphone P_f time signal with its MIP in the case of Layout #1 in a steady-state test for two valve positions, i.e. completely open and completely closed. The randomness of the time signal is noticeable for the completely opened valve (Fig. 4.6 (a)), while as the valve closes (Fig. 4.6 (b)), a periodic component dominates the signal. Moreover, the periodicity of the MIP highlights that the signal energy is flowing in a periodic fashion. This is related to the air stream hitting the sensor during the instability of the compressor operating condition, i.e. the surge. The cyclic power of such a signal can then be evaluated in order to extract the cyclic frequencies of the energy flow.

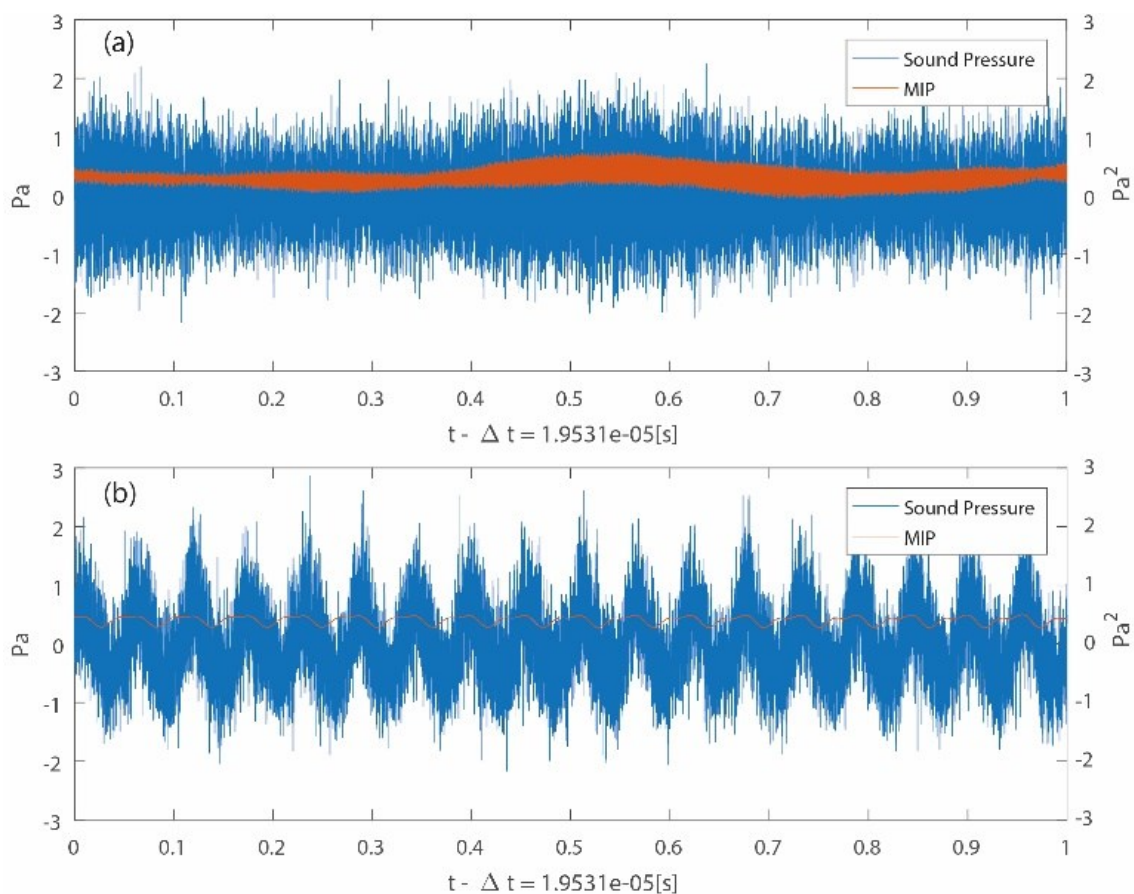


Fig. 4.6 - Layout #1 steady-state test microphone P_f time signal (left) with its MIP (right): (a) valve completely opened, (b) valve completely closed

The evolution of the surge phenomenon can be highlighted by the transient test in which the valve is continuously closed until surge occurs. In order to extract the signal cyclic power during the compressor dynamic operating condition, a Hanning window function of a two second width (Antoni, 2009) is slid over the time signal and the cyclic power of the windowed signal is evaluated. The Hanning window is chosen due to its ability to reduce spectral leakage. The window length is chosen in order to reach a good compromise between frequency resolution and low estimator variance (Antoni, 2009). Fig. 4.7 depicts the result of this analysis. In particular, as the time increases (the valve is completely opened @ $t=0$ and then it starts to be closed), the cyclic frequency at 18 Hz arises with its main harmonics (35.5 Hz and 53.5 Hz). De facto, this cyclic frequency is related to the energy flow during the surge phenomenon. This sensor does not perceive the modulation due to the stall cells during dynamic operation, but it only registers the characteristics of the deepest instability, i.e. the surge.

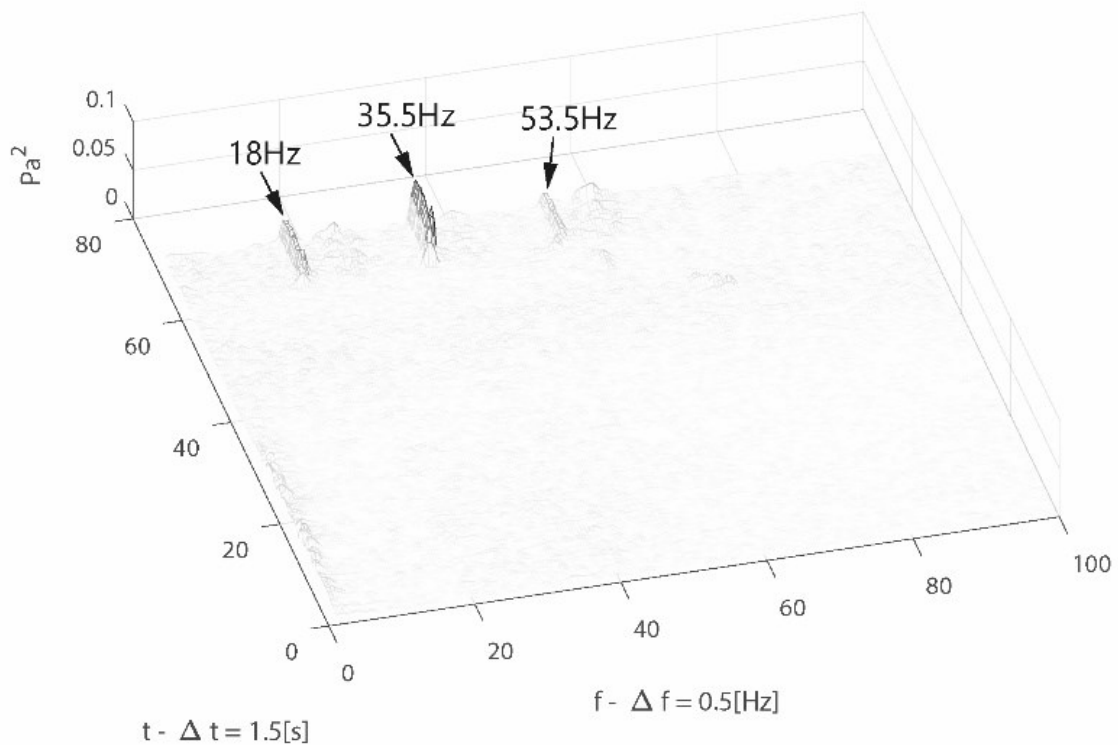


Fig. 4.7 - Layout #1 transient test: cyclic power of microphone P_f

Pivotal information concerning the compressor stall phenomenon can be obtained by the analysis of the acceleration signals. The CMS of the vibration signals is evaluated during the steady-state test in Layout #1. This technique can emphasize the modulation frequencies related to the signal energy flow with respect to its carrier frequencies. Figure 6 depicts the results of this analysis. It is possible to see that strong modulation phenomena are visible around 4000 Hz, where the main BPFs of the system are located (see Tab. 4.1).

The main modulation frequencies involved are at 20.17 Hz and 49.08 Hz in the case of the completely opened valve (Fig. 4.8 (a)). This result changes slightly when the valve is completely closed, Fig. 4.8 (b). Firstly, the modulating component at 20.17 Hz decreases its frequency to 20.03 Hz, and the component at 49.08 Hz decreases its amplitude. Moreover, it is possible to see the emergence of a new cyclic frequency at 17.94 Hz which involves a greater range of spectral frequencies. As explained before, the spectral and cyclic frequencies are respectively the carrier and the modulating frequency of the energy flow inside the signal. Through analysis of the P_f microphone signals, it is possible to relate the component at 17.94 Hz to the surge phenomenon, while the other modulating frequencies have to be related to other fluid-dynamic phenomena, such as stall cells. Therefore, in order to depict this behavior, an analysis of the acceleration signals during the transient test in Layout #1 is carried out. A Hanning window function is slid over the acceleration time signal and the cyclic power for each windowed portion is evaluated and depicted in Fig. 4.9. Two main cyclic frequencies are visible at the beginning of the test, i.e. 20 Hz and 49 Hz, when the valve is completely opened. As explained above, this phenomenon is related to fluid-dynamic perturbations which modulate the energy flow carried by the main system BPFs. Therefore, they can be easily related to stall cells.

This is in agreement with what was found in the previous chapter, in which two high frequency dynamic pressure sensors installed at the inlet annulus of the compressor registered a stall cell rotating with a frequency around 20 ± 0.5 Hz. The analysis of the acceleration signals confirms the presence of a stall cell located in the first axial stages of the compressor (the exact position and size is difficult to define due to the absence of inside pressure measurements). Moreover, as mentioned above, at least another stall cell is present in the successive stages, and this cell/s rotates with a frequency of 49 Hz. Unfortunately, it is not possible to establish the number of stall cells without using other types of intrusive sensors.

This phenomenon is due to the operating conditions. De facto, the compressor is operating at a very low rotational speed, compared to its nominal speed; which is the reason why the stall cells generate at the first stages.

The generation of these stall cells could be prevented by a proper bleed valve, but in this case the component is not present, thus rotating stall is expected to be generated at the first axial stages - this does not mean that the overall compressor is operating unstably,

but only that the axial compressor has a destabilizing effect which affects the overall performance, i.e. the compressor as a whole is operating off-design.

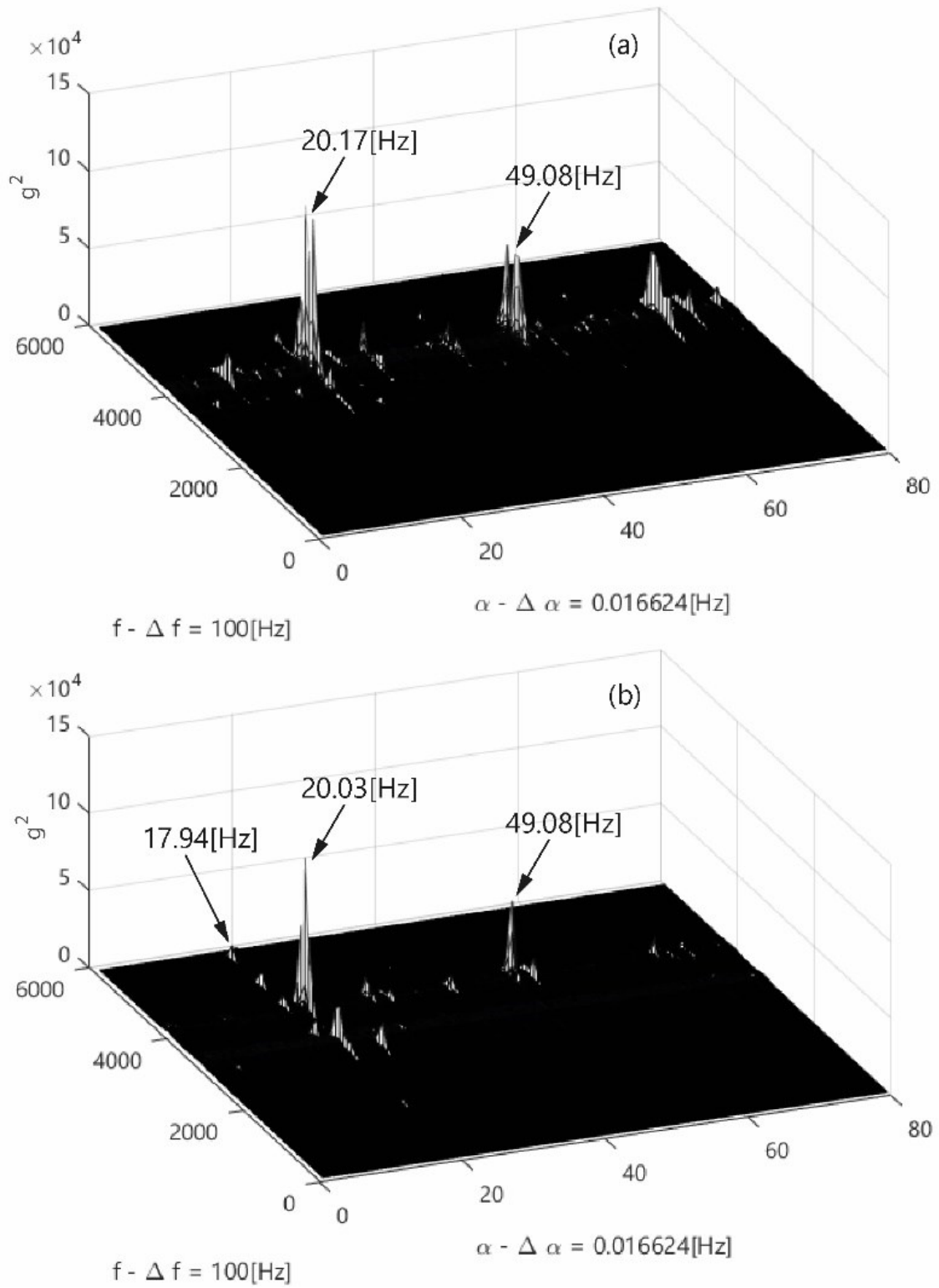


Fig. 4.8 - Layout #1 steady-state test CMS of the g_{3ax} accelerometer: (a) valve completely open, (b) valve completely closed

An interesting phenomenon successively occurs by further closing the valve. Fig. 4.9 shows that at a certain closing angle of Valve 1 (approximately 25-30 °, around $t=60$ s - obviously the data logging began before to the valve was closed), a new cyclic frequency of about 60 Hz generates. Immediately before, the stall cell rotating at 49 Hz disappears.

This highlights the evolution of the compressor stall along with the changing size of the existing stall cell/s, or its interaction with potential new stall cell/s generated. The new modulating frequency, which represents the new stall cell/s, is obviously a surge precursor and decreases with the closure of the valve.

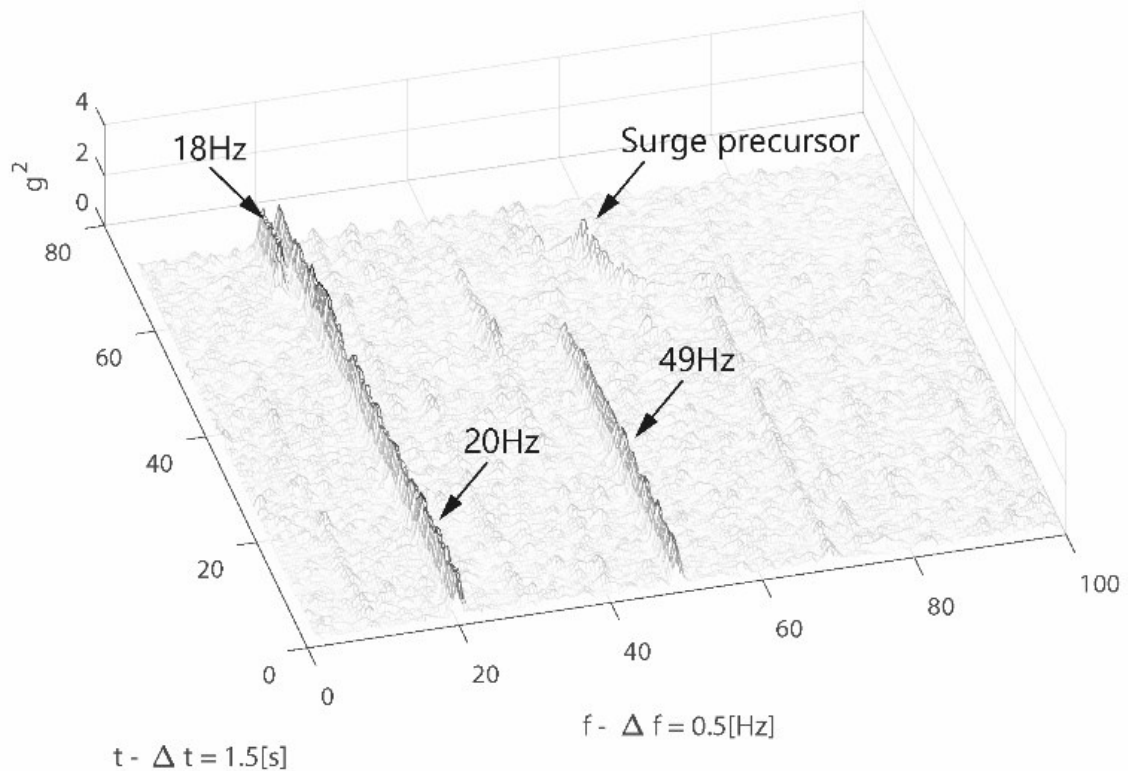


Fig. 4.9 - Layout #1 transient test: cyclic power of accelerometer $g_{3a,x}$

Successively, when the valve is completely closed, surge occurs with a frequency of 18 Hz. This type of surge can be described as an instability which evidently develops because of the total absence of mass flow rate. Therefore, its high frequency is due to the small downstream volume, and thus to the small accumulation of energy that this volume allows. Another important fact is that, in surge, the original cyclic frequencies are still present, although with a lower amplitude. This confirms that in this condition, the compressor alternates surge and rotating stall of the first stages depending on the direction of the flow.

The same analysis has been carried out for the Layout #2 (with the plenum circuit). Fig. 4.10 depicts the cyclic power of the acceleration signal evaluated in the same way as for Layout #1 (Fig. 4.9).

The main cyclic frequencies (20 Hz and 49 Hz) related to stall phenomenon are still visible in Layout #2. As expected, the cyclic frequency related to the surge event (1 Hz) has a lower value compared to Layout #1, due to the bigger compressor downstream volume. This consideration is supported by what has been shown in the previous chapter. However, in the case of Layout #2 it not possible to see the surge precursor (see Fig. 4.10 compared to Fig. 4.9); only the presence of a harmonic of 20 Hz arises a few seconds before surge, which is not sufficient to state that it is a surge precursor (however, according to what was found in chapter 3 this harmonic may be the result of stall cell growth - further investigations are required). This behavior is mainly due to the influence of the piping system layout on the compressor dynamic characteristic behavior. In fact, in Layout #1 the fluid-dynamic instability occurs beyond the characteristic curve peak, while in Layout #2 the surge occurs in the vicinity of the peak, (see chapter 3). Therefore, the evolution of the surge precursor cannot be clearly identified due to the rapid change in condition from stall to surge.

The surge frequency in Layout #2 was also confirmed by using a dynamic model (the model is described in chapter 5). The model instead failed to estimate the surge frequency in layout #1, in which the model predicted stall rather than surge.

The results showed above highlight the possibility of detecting stall cell/s perturbation, surge precursors, as well as surge phenomena, with non-intrusive sensors such as accelerometers. It must be said that the cyclostationary analysis was also applied to the recorded data from the other accelerometers, and the results were very similar. All the outcomes indicate that cyclostationary analysis is a novel technique that can be used to detect stall (not often easily detected by simple frequency domain analysis such as FFT) and surge. Obviously, since this work is the first on this topic, further investigations are required to definitively prove the validity of this technique.

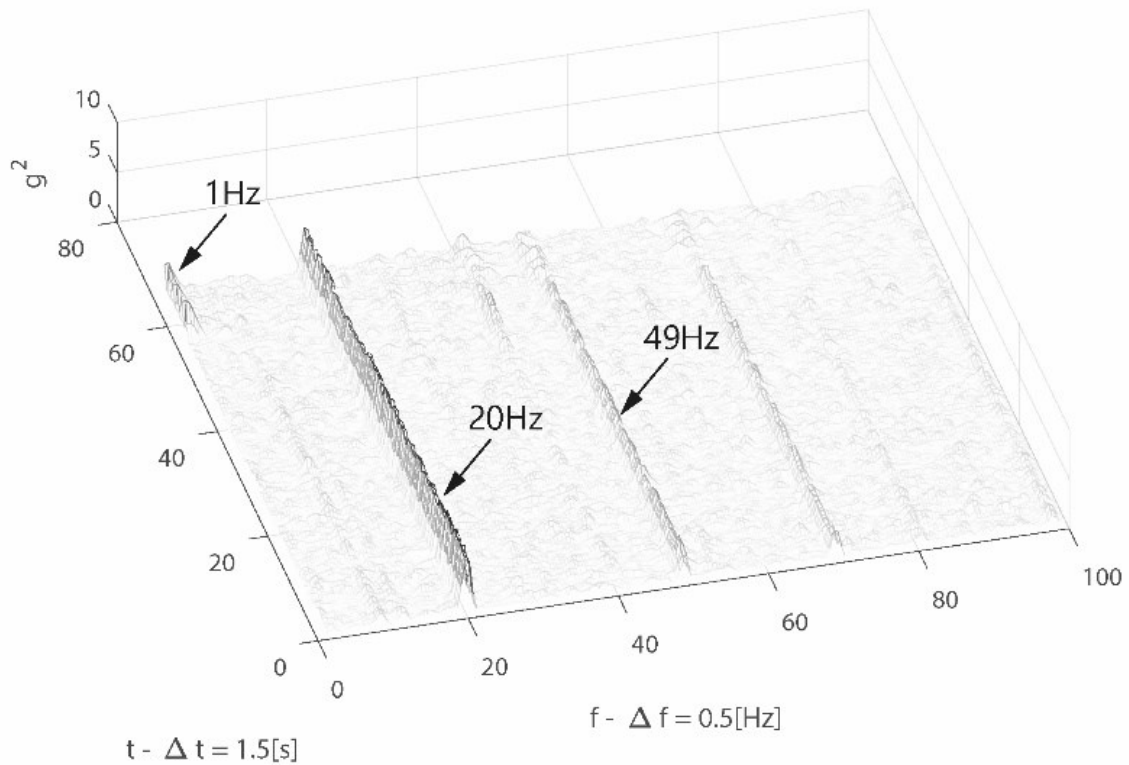


Fig. 4.10 - Layout #2 transient test: cyclic power of accelerometer $g_{3a,x}$

4.8 Conclusions

This chapter deals with a vibro-acoustic experimental study of the instability phenomena, such as stall and surge, occurring in a multi stage compressor.

Accelerometers were installed on the compressor casing in four different positions, and two microphones were positioned immediately above the compressor, and at a certain distance from the intake duct. Two types of test have been carried out with two different piping system layouts, namely Layout #1 and #2.

Cyclostationary analysis, which is a novel methodology for turbomachine data analysis, has been carried out on the vibro-acoustic signals in order to study energy flow related to fluid-dynamic instability phenomena. This analysis has shown capability in detecting stall cell/s perturbation, surge precursors, and surge phenomena. In particular, the cyclostationary analysis carried out on the acceleration signals showed the presence of two cyclic frequencies at 20 Hz and 49 Hz, which are related to rotating stall cell/s. Moreover, in Layout #1, the evolution of stall to surge is clearly visible as well as the surge frequency. Similar results have been obtained in Layout #2 in which the surge precursor was not clearly detected (only the occurrence of a harmonic frequency was found before

surge). This is mainly due to the influence of the piping system layout on the compressor dynamic characteristic behavior.

This work shows how an appropriate signal processing analysis of the vibro-acoustic signals could be used for the identification of compressor fluid-dynamic instabilities, i.e. stall and surge.

This type of data analysis seems to be more capable of detecting stall and surge and their precursor, compared to classical frequency analysis (FFT), but further investigations are required. This is the first work ever to use cyclostationary analysis applied to non-intrusive sensors, and to demonstrate the potential of this technique for the study of stall and surge. Future work will involve additional tests and comparison also with other compressors. Subsequently, the study will focus on the feasibility of cyclostationary analysis for real time application - from preliminary consideration, this may be possible.

5 Dynamic Modeling: Thermodynamics

Surge is recognized as the most significant flow instability of the compressor as it strongly influences performance causing pulsations of pressure that generate reverse flow. This phenomenon obviously has to be taken into consideration when designing the compression piping system, upstream and downstream of the compressor. Therefore, the prediction of the transient response of the compressor and the occurrence of surge, with its characteristic oscillations, is a crucial aspect which has acquired high consideration in literature. This chapter deals with the development and tuning of a nonlinear model for simulating the dynamic behavior of the compression system. The model is a first version of a more advanced model (see chapter 6). In fact it will be extended and improved in the next chapter with more accurate formulations and additional calculations in order to evaluate the axial surge forces. Therefore, this chapter presents the model which can be thought of as the preliminary version of the more complex model which will be described in the next chapter.

5.1 Introduction

Surge is a drastic phenomenon that can occur in the compressor and causes severe deterioration of performance (in terms of pressure ratio, and efficiency) with possible backflow generation and damage to the mechanical components belonging to the compressor block. Therefore, the modeling of the compressor transient behavior plays a fundamental role in predicting the amplitude and frequency of surge fluctuations during dynamic instability. The most important model was developed by Greitzer (Greitzer, 1976) and later his model was successfully implemented in (Moore & Greitzer, 1986). As also reported in (Longley, 1994) and (Day, 2016), many other authors have developed their own models, with specific additional and original features, for predicting compressor dynamic behavior and stability (Galindo, et al., 2008) (Jiang, et al., 2006) (Helvoirta & Jagera, 2007). The aim of this work is to continue the research activity started in (Morini, et al., 2006), by developing a new concept model and comparing the results with the experimental data obtained in chapter 3 in order to validate the model.

5.1.1 *System Modeling*

In order to create a valid dynamic lumped parameter model it is fundamental to create a modular structure. This means that the typical components of a general system (to be simulated) have to be independently modeled. In this case the system is a compression piping system, thus the typical components which can be identified are: valves, ducts, the plena and compressors. Therefore, each of these components needs to be univocally modeled so that it is possible to simulate every piping system configuration. This target is not always easy to achieve, not only because in-depth knowledge of the physical phenomena occurring on each component is required, but also because of the difficulty of taking these phenomena into account and at the same time creating a modular scheme without increasing the computational cost of the calculations. Fortunately, the bond graph approach, if combined with the use of a dedicated dynamic simulator or powerful software such as Matlab/Simulink, provides a good solution to this issue.

In fact, the Matlab/Simulink environment offers the possibility to easily create a modular construction of the model thanks to the use of the subsystem modules which can, by nature, represent multi-port elements (with the possibility of many inputs and many outputs). Bond graphs are a well-known technique, useful for modeling the individual components of a system. This approach has been used in many engineering fields but only in a few works has been adopted for modeling the dynamic behavior of compression piping systems. The following sub-paragraph gives a general description of the main feature of this technique.

5.2 Bond Graph Approach

The bond graph is a schematic representation that can be applied to the system and allows the simple construction of the differential equations needed to describe the dynamic behavior of the system (Brown, 2007). The bond graph is a robust modeling technique which can be used in many types of engineering systems (in particular by mechanical and electrical engineers) thanks to i) its ability to consider many energy domains and ii) the easy description of the components through constitutive relations. This work does not describe in detail the bond graph theory since extensive literature regarding this topic is presented in (Brown, 2007) (Karnopp, et al., 1990). However, since basic knowledge of the topic is required to clearly understand the subsequent description of the model, the following part of this paragraph gives a brief picture of the basics of bond graph theory.

This method allows graphic representation of the system through one-port or multi-port elements using edges, called “bonds”, which transport the power from one element of the system to another. The physical components of a real system can be represented in a bond graph by means of some basic elements, the most important being: sources (effort or flow source), sinks (effort or flow), resistances, energy storages, gyrators and transformers. The basic bond graphs are shown in Tab. 5.1 along with the relations which rule them. The two conjugated variables that define the energy quantities are the effort, e , and the flow, \dot{f} , so that the power is (Borutzky, 2010):


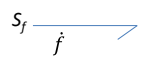

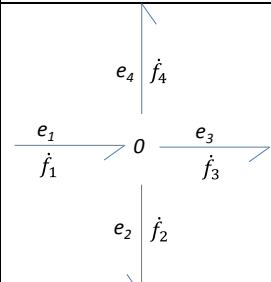
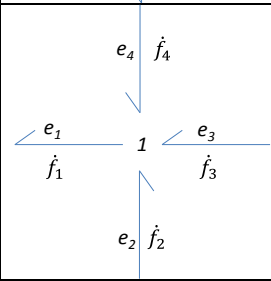
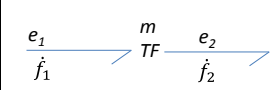
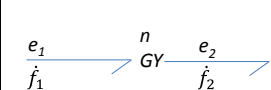
$$P(t) = e(t) \dot{f}(t) \quad (5.1)$$

Thus, the effort and flow variables assume various physical quantities depending on the type of system that is analyzed. Generally, in a fluid system like the one treated in this work, the effort is the pressure whereas the flow is the volumetric flow rate. The direction of the energy flow is determined by half arrows while the causality, which is the order of calculation of the effort and flow, can be chosen by evaluating the direction of the energy flow and the inputs (effort or flow) established for each component. One bond is linked to another bond through some basic elements which do not introduce either energy storage or energy dissipation; these elements are called “junctions”. In a bond graph two types of “junctions” can be found: the “0-junctions”, where the flow is the same in each bond, and the “1-junction” where the effort is the same in each bond (see Tab. 5.1) (Karnopp, et al., 1990) (Borutzky, 2009). Another important feature of the bond graph is the causality which basically defines the computation order of the efforts and flows. This is fundamental in order to clearly describe a physical system; for this reason, the bond graph can be implemented with the causality assignment.

The causality is graphically indicated by a stroke on one side of the bond and it is necessary to instruct the model to follow the causal assignment. Basically the stroke indicates where the effort (or the flow) is calculated. Therefore, the causality defines the flux direction of the effort and the flow so that the corresponding causality rule and equation is completely defined. Of particular interest is the causality of the energy storages (showed in Tab. 5.2). This causality of the energy storages can be a differential causality or an integral causality. The graphic difference between these two different assignments and their equations is shown in Tab. 5.2. It is clear that they are crucial for determining the differential equations which govern the system. Regarding the junctions, the strokes can be set depending on the causality of the linked bonds but as a rule, in a “0-junction” only one

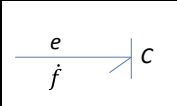
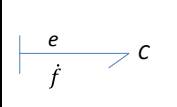
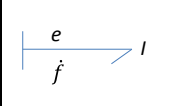
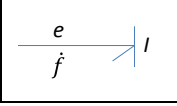
bond transports the effort towards the junction while the others transport the flow. Similarly, in a “1-junction”, only one bond transports the flow towards the junction whereas the other bonds transport the effort. Therefore, the junctions, with their linked bonds, are built by arrows with strokes that help to formulate the equations.

Tab. 5.1 - Bond graph basic elements

Effort source		-
Flow source		-
Resistance		$e=R\dot{f}$
“0 Junction”		$e_1=e_2=e_3=e_4$ $\dot{f}_1=\dot{f}_2+\dot{f}_3+\dot{f}_4$
“1 Junction”		$e_1=e_2+e_3+e_4$ $\dot{f}_1=\dot{f}_2=\dot{f}_3=\dot{f}_4$
Transformer Or modulated transformer		$e_1=m e_2$ $\dot{f}_2=m \dot{f}_1$
Gyrator or modulated gyrator		$e_2=n \dot{f}_1$ $e_1=n \dot{f}_2$

Now that a brief description of the basics of bond graph has been provided, it is clear that this technique is useful even when modeling complex systems because it provides the graphic representation of the energy flux. For all these reasons, the bond graph approach guarantees many advantages in terms of modularity and permits the easy formulation and implementation of the differential equations governing the system.

Tab. 5.2 - Causality of energy storage elements

Derivative causality Energy storage compliance		$\dot{f} = C \frac{d e}{d t}$
Integral causality Energy storage compliance		$e = \frac{1}{C} \int \dot{f} d t$
Derivative causality Energy storage inertance		$\dot{f} = I \frac{d e}{d t}$
Integral causality Energy storage inertance		$e = \frac{1}{I} \int \dot{f} d t$

5.3 Literature Review

The importance of modeling the dynamic behavior of a compressor or, more generally, of a compression system is due to the model's ability to predict, during operation, the occurrence of off-design conditions, instabilities and thus dangerous events. The reliability of these predictions assumes a fundamental role in i) the design of the compressor (or system components) and ii) the improvement of the control systems, in particular those associated with compressor instabilities such as stall and surge.

Many authors have developed dynamic models for predicting performance during compressor instability. All of these models have different features but many of them are based on a common root, which is the Greitzer model (Greitzer, 1976). An important example of these surge models is that developed by Morini et al. (Morini, et al., 2006), not only for the model concept description, but also for its exhaustive literature review, approximately up to the early 2000s.

Subsequently, many other authors implemented new models. An example is the work of Galindo et al. (Galindo, et al., 2008) who carried out a campaign on a centrifugal compressor for automotive engines by modeling its behavior during surge and trying to predict how the compressor downstream volume affects the results. They developed a reliable compressor model (according to the Greitzer's Model) which was implemented in a pre-existing 1D gas-dynamic model of the piping system. In the work of Vepa (Vepa, 2010), an unsteady nonlinear model was presented. That model was an extension of Moore and Greitzer's (Moore & Greitzer, 1986) and aimed to control surge and rotating stall by actively stabilizing the compressor. The results showed that the controller was

efficaciously able to inhibit surge and stall. A robust modeling technique, which is still used (as also reported by Day (Day, 2016)), is the parallel compressors approach. This theory was proposed for the first time by Pearson and McKenzie (Pearson & McKenzie, 1959) and allows the study of the inlet distortions by treating the compression system as two compressors, operating in parallel, which discharge the same static pressure (Cousins & Davis Jr., 2011). This approach has been used in the past by many authors, for example in Mazzawy's work (Mazzawy, 1977). Nowadays, it is still a powerful solution, since it is a potential additional implementation to some classic surge models, to take into account also the effect of the inlet distortions (Floyd & Davis, 2015).

It is clear that in any dynamic model, a significant role is played by implemented compressor characteristic curves. A comparison between different ways of modeling the compressor characteristics was presented by Grong (Grong, 2009). In that work, dedicated to the control of surge, the close coupled valve and the drive torque actuation control methods were compared. Their potential advantages/limitations were highlighted, identifying the possible measurements time delay as a negative factor which made the controllers unable to react in a suitable amount of time to rapid transients. Another study, focused on the modeling of compressor performance during surge, is that presented by Belardini, et al. (Belardini, et al., 2016), in which the authors highlighted the importance of knowing the reverse flow. They developed and compared a 1D model and a Computational Fluid Dynamic (CFD) based method to predict the second quadrant compressor curves (i.e. the compressor performance in reverse flow conditions), emphasizing the fast execution of the first (more suitable to the standard production sector) against CFD, which was instead shown to be more powerful, allowing a deeper insight into the fluid structures. (in particular, blockage and secondary flows) at very low flow rates - the range in which the 1D model did not show good agreement with experimental data.

In the work of Leufvén and Eriksson (Leufvén & Eriksson, 2013) a compressor flow model was developed for simulating the behavior in choke, normal and surge operating conditions of an automotive compressor. This model was validated against a large automotive compressor map. The authors used the ellipse model structure to extrapolate data to small turbo speeds, which are not usually provided on the manufacturer datasheet. Recently, two interesting works on surge modeling (Kilchyk, et al., 2013) and active surge control (Yoon, et al., 2010) were carried out. In the work of Kilchyk, et al. (Kilchyk, et al., 2013) a lumped parameter model was applied to a radial compressor, including the effects of heat transfer, whereas Yoon et al (Yoon, et al., 2010) developed

and validated a control algorithm based on the actuation on the impeller tip clearance using magnetic bearings.

Based on this review, it is clear that that the modeling of surge has achieved a certain degree of robustness, even if the experimental results cannot always be exactly replicated. The progress in this sector can be represented by the improvement of the detection, avoidance and control systems.

5.4 Physical Model and System Components

The model implementation was based on the physical configuration corresponding to Layout #2. Very few examples of bond graph modeling of turbomachines and compression systems can be found in literature (Uddin & Gravdahl, 2015) (Movaghar & Novinzadeh, 2011) (Krikelis & Papadakis, 1988). The following subparagraphs describe the basic system components, their inputs, their mathematical modeling, and their bond graph with the causality assignment. In this model, the variable considered as effort is the pressure whereas the variable considered as flow is the mass flow rate, therefore the model uses the “pseudo” bond graphs. By using a simple scheme for each element and by exploiting the bond graph theory, the elements of a system can be mathematically defined. In this work, the modeled elements are: the valve, the duct, the plenum and the compressor. Their graphic representation and bond graphs are illustrated in Fig. 5.1.

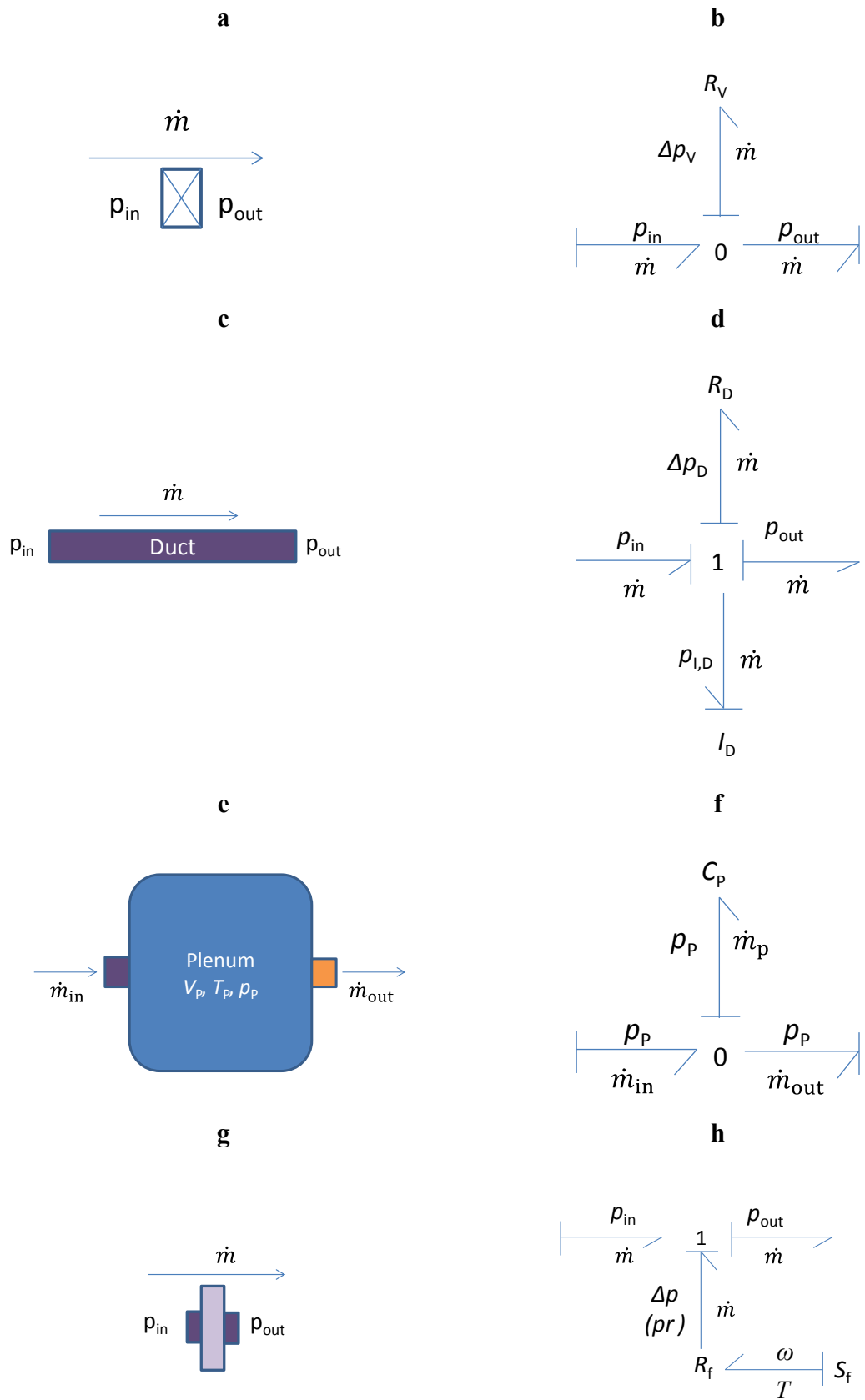


Fig. 5.1 - Scheme and bond graph of the basic elements of the model

5.4.1 The Valve Element

The valve, Fig. 5.1 (a), is a dissipative element and its characteristic parameter is fluid resistance, R . The bond graph of this element consists of a “1-junction” (Fig. 5.1 (b)), linked to three bonds: one bond represents the resistance effect, and the other two represent the inlet and the outlet energy flux. In this element the outlet temperature is assumed equal to the temperature at the inlet (and vice versa in case of reverse flow) therefore, the increase of fluid entropy and also the heat exchange to the atmosphere are neglected. This element determines the pressure drop Δp_v , given the mass flow and the pressure at the inlet (outlet), by calculating the pressure at the outlet (inlet) as shown in (5.2) and (5.3). In order to evaluate the valve coefficient K_V , the modeling of this component behavior, in particular the quantification of the valve resistance R_v , requires the use of algebraic correlations or, alternatively, constitutive relations of the valve (i.e. the characteristic curve of the valve, which can be implemented and read by the model).

$$\Delta p_V = e(f_{in=out}, e_{in}, R_V) = e(\dot{m}_{in=out}, p_{in}, K_V) = \frac{\dot{m}^2}{K_V^2 \bar{\rho}} \quad (5.2)$$

$$\Delta p_V = e(f_{in=out}, e_{out}, R_V) = e(\dot{m}_{in=out}, p_{out}, K_V) \quad (5.3)$$

After the calculation of the pressure drop, the valve pressure outlet (inlet) is:

$$p_{out} = p_{in} - \Delta p_V \quad (5.4)$$

$$p_{in} = p_{out} + \Delta p_V \quad (5.5)$$

Obviously, the implemented correlations are also able to evaluate the backflow conditions by properly managing the term signs. In addition, a second type of valve was modeled, in order to increase the modularity, as an element which uses the same physical principle and equation but determines the mass flow rate, given the pressure drop, as shown in (5.6).

$$\dot{m} = K_V \times (\pm \sqrt{|\bar{\rho} \Delta p_V|}) \quad (5.6)$$

5.4.2 The Duct Element

The duct, sketched in Fig. 5.1 (c), is an inertance energy storage element which also has a dissipative effect. Therefore, the characteristic parameters of this element are the

fluid resistance, R_D , and the inertia, I_D , which can be generated on the fluid flow. The typical bond graph of a duct is generally represented as a 1-junction which is connected to a resistance R and to an inertance I (see Fig. 5.1(d)). Similarly to the valve, the outlet flow is assumed to have the same temperature as the entering flow. The dynamic model for the pipe element is based on the lumped parameter approach, hence perturbation propagation time from one end of the pipe is not accounted for. This is a major assumption, particularly in dealing with compressor surge where wave propagation time is crucial. The present approach neglects this effect. The duct was then modeled as an element which, given the pressure at the inlet, p_{in} , and at the outlet, p_{out} , calculates the mass flow as a function of the efforts entering and exiting the junction, and determines Δp_D , that is the pressure drop due to the fluid resistance R_D . These dependencies between the characteristic parameters are shown in (5.7) and (5.8).

$$\dot{m}=f_{in=out} \left(\sum e_{in, out}, I_D \right)=f_{in=out} \left(\sum p_{in, out}, I_D \right) \quad (5.7)$$

$$\Delta p_D=e \left(R_D, f_{in=out} \right)=e \left(R_D, \dot{m}_{in=out} \right) \quad (5.8)$$

The bond graph equations of this element are then:

$$\begin{cases} p_{I,D}=p_{in}-\Delta p_D-p_{out} \\ \frac{d \dot{m}}{d t}=\left(\frac{p_I}{I}\right) \end{cases} \quad (5.9)$$

The derivative mass flow rate and the pressure drop are calculated as:

$$\frac{d \dot{m}}{d t}=\frac{A}{L}\left(p_{in}-\Delta p_D-p_{out}\right) \quad (5.10)$$

$$\Delta p_D=f \frac{L}{D} \rho \frac{V^2}{2} \quad (5.11)$$

5.4.3 The Plenum Element

The plenum element, in Fig. 5.1 (e), was considered as an accumulator, i.e. a capacitive component with a characteristic compliance C_p . In an actual fluid system, it also causes pressure drop, but in this work, only the capacitive action was taken into account since the resistance effect is negligible, compared to the energy accumulation process. Therefore, the dissipative effect generated at the inlet and at the outlet can be considered negligible since the main effect of this component is to store energy. This element

calculates the plenum pressure, p_p , given the mass flow rate at the inlet, \dot{m}_{in} , and at the outlet, \dot{m}_{out} , by exploiting the dependency written in (5.12).

$$p_p = e_{in=out} \left(\sum f_{in,out}, C_p \right) = e_{in=out} \left(\sum \dot{m}_{in,out}, C_p \right) \quad (5.12)$$

The equations used for this element are then:

$$\frac{d p_p}{d t} = \frac{\gamma R_g T_p}{V_p} (\dot{m}_{in} - \dot{m}_{out}) \quad (5.13)$$

$$\frac{d T_p}{d t} = \frac{1}{m_p C_p} \left[\sum_{L_{in,out,P}} \dot{m}_{in,out} C_{p, in,out} T_{in,out} + T_p \alpha_p V_p \frac{d p_p}{d t} \right] \quad (5.14)$$

As can be seen, the temperature is derived from the conservation of energy. The bond graph of the plenum (Fig. 5.1 (f)) consists of a “0-junction” connected to a capacitance and to the inlet and outlet energy flux. The plenum, like the other elements of the model, is assumed to be adiabatic - this assumption is justified by the fact that the dynamics of fluid heat exchange is much faster than that of the piping system mass heat exchange.

5.4.4 The Compression Stage Element

The compression module was thought to represent a single stage of the compressor thus if a multistage compressor is simulated, then this module needs to be implemented n_{stage} times, in series. If only the overall maps of a multistage compressor are known this element represents the overall compressor. This element was treated as a resistance field which acts as a non-dimensional actuator disk with the rotational speed, ω , as input (the torque, M , is not considered since the balance equation of the rotating masses is not implemented). The general compressor representation used in this work is illustrated in Fig. 5.1 (g). The compressor calculates the pressure at the inlet, given the outlet pressure, the mass flow rate and the rotational speed. Moreover, it also determines the temperature at the outlet (or at the inlet when backflow occurs) by using the isentropic efficiency curves (or the first law of thermodynamics). The steady-state curves of the compressor, have to be experimentally obtained, as shown in chapter 3, at different corrected rotational speeds v . A parametric study is carried out in order to obtain the corresponding interpolated curves, up to the surge line of the pressure ratio, Fig. 5.2 (a), and the isentropic efficiency, Fig. 5.2 (b). These curves are approximately quadratic so they can be specified by three coefficients

which can be calculated. In fact, each of these quadratic curve (see Fig. 5.3 (a)), has three constant coefficients which can be expressed as a function of $\beta_{\mu=0}$, $\mu_{pr=0}$, $\mu_{\beta_{max}}$. A parametric procedure was then carried out to evaluate the fundamental parameters of the performance ($\beta_{\mu=0}$, $\mu_{pr=0}$, $\mu_{\beta_{max}}$, etc.) at the rotational speeds not performed during tests. Fig. 5.3 (b) illustrates the trend of these characteristic parameters as a function of the rotational speed of the compressor. The mass flow rate ideal maximum value (at zero pressure ratio), $\mu_{\beta=0}$, the value at the peak of the curve, i.e. $\mu_{\beta_{max}}$, together with other significant parameters are expressed as a function of the rotational speed by using quadratic or third degree polynomial curves. These correlations are implemented into the model so that at each rotational speed, the three coefficients of the quadratic characteristic curve of the compressor can be obtained.

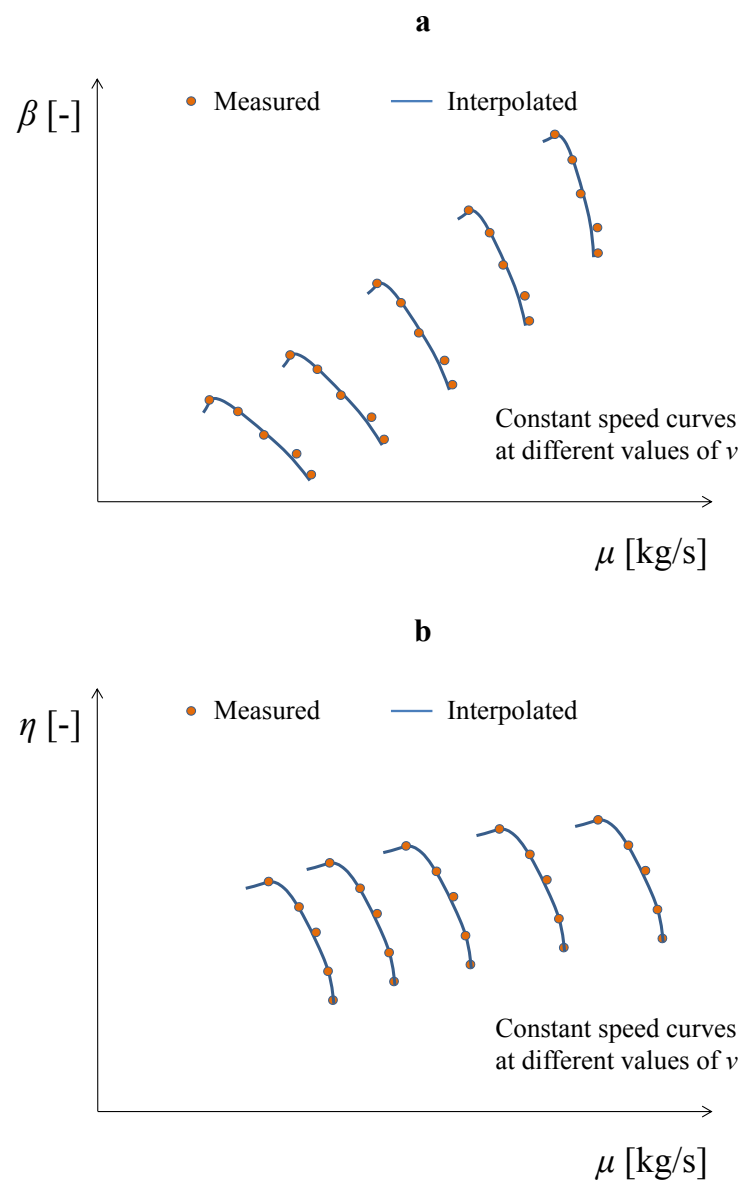


Fig. 5.2 - Steady-state measured and interpolated curve of performance maps: (a) pressure ratio; (b) isentropic efficiency

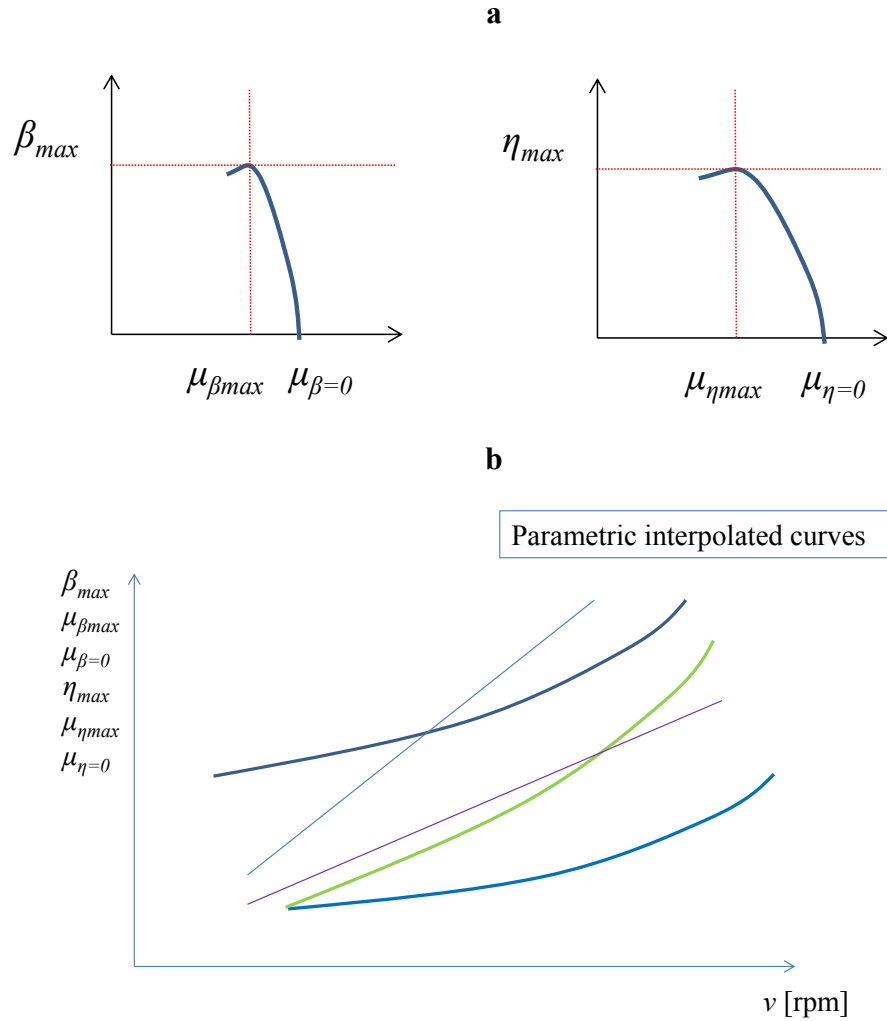


Fig. 5.3 - Parametric procedure: (a) the modelling of the performance curves; (b) the trend of characteristic parameters of the performance curves

The compression stage element essentially uses the parametric curves to calculate the inlet pressure, $p_{in,SS}$, in steady-state conditions, for a given mass flow rate, \dot{m} (the model will deal with the corrected mass flow μ) and an outlet pressure p_{out} , considered equal to the plenum pressure p_p . This dependency is written in (5.15). Moreover, as explained by (5.16) and (5.17), thanks to the isentropic efficiency curves and the impeller work, the outlet flow temperature can be determined. The temperature of the flow entering the plenum in direct flow is T_{out} while the temperature of the reversal flow leaving the compressor in backflow conditions is $T_{in, surge}$. The term $T_{out, surge}$ indicates the temperature entering the compressor during backflow.

$$p_{in, SS} = e_{in}(\omega, f_{in=out}, \beta_{SS}, e_{out}) = e_{in}(\omega, \dot{m}_{in=out}, \beta_{SS}, p_{out}) \quad (5.15)$$

$$T_{out} = e_{in}(\omega, f_{in=out}, \eta_{is}, T_{in}) = e_{in}(\omega, \dot{m}_{in=out}, \eta_{is}, T_{in}) \quad (5.16)$$

$$T_{in_surge} = e_{in}(\omega, f_{in=out}, gH_{in<0}, T_{out,surge}) = e_{in}(\omega, \dot{m}_{in=out}, gH_{in<0}, T_{out,surge}) \quad (5.17)$$

Regarding the pressure ratio, at the left of the characteristic curve, no stalled curve was implemented because this model aims to simulate surge, and in particular deep surge. Therefore, the operating point, once at the curve peak, bounces to the zero mass flow point, by means of a sudden drop in pressure, and then, at negative flow regimes, follows the Moore and Greitzer cubic law (Moore & Greitzer, 1986).

$$\beta_{in<0} = \beta_{in=0} + H \left[1 + \frac{3}{2} \left(\frac{\dot{m}}{W} - 1 \right) - \frac{1}{2} \left(\frac{\dot{m}}{W} - 1 \right)^3 \right] \quad (5.18)$$

where the main parameter to be calculated is the pressure ratio at zero mass flow rate. In this case this value was experimentally found at the tested rotational speeds. Then, similarly to the other parameters explained above, the parametric relation between $\beta_{m=0}$ and N was calculated. With regard to isentropic efficiency, the implemented method is analogous, however, for negative mass flow rates the efficiency is not considered while the first law of thermodynamics is applied. Also the temperature of the flow exiting from the compressor is calculated. In direct flow (and when the mass flow is zero) the temperature is calculated as

$$T_{out} = T_{in} (\beta)^{\frac{\gamma-1}{\gamma} \eta_p} \quad (5.19)$$

Where

$$\eta_p = \frac{\ln \left(\frac{p_{out}}{p_{in}} \right)^{\frac{\gamma-1}{\gamma}}}{\ln \left(\frac{\left(\frac{p_{out}}{p_{in}} \right)^{\gamma-1/\gamma} - 1}{\eta_{is}} + 1 \right)} \quad (5.20)$$

In reverse flow the compressor is treated as a generic machine and the first law of thermodynamics is applied (the concept of efficiency in this case can be confusing). This idea was shown to offer reliable results and the temperature leaving the compressor was found as:

$$T_{in,surge} = T_{out,surge} + \frac{gH_{in<0}}{C_p} \quad (5.21)$$

Where the work in reverse flow is calculated as:

$$gH_{in<0} = u_1^2 - u_2^2 \quad (5.22)$$

In this model, the calculation of the temperature at the exit of the compressor during surge, $T_{in,surge}$, is not relevant since the energy balance is not provided in the inlet duct module. This is a limitation of this model (and the advanced model described in the next chapter) which does not take into account the progressive heating of the compressor inlet flow rate during surge (this phenomenon is negligible for short-term surge events). In the next chapter the same approach, but also considering the expansion effect, is applied since the temperature of the flow exiting from a compressor stage plays a fundamental role in the axial force calculation.

5.5 Test Case Application

The model was applied to the experimental facility of the Engineering Department of University of Ferrara, previously described in this work. Therefore, for a comprehensive and more detailed description of the entire facility, the reader should consult chapter 3 and chapter 4. In particular, the model aims to simulate the test rig in Layout #2. The sketch of the configuration of the model elements and the system bond graph are depicted in Fig. 5.4. The model was implemented with the intention of simulating the pressure and mass flow fluctuations in the piping system during deep surge. Surge conditions were experimentally obtained by performing the compressor in Layout #2 (see chapter 3 and 4). Valve 2 was progressively closed until the pressure of the plenum was higher than the compressor outlet pressure, generating backflow.

The model, see Fig. 5.4 (a), simulates the piping system with an inlet valve (this valve is used to take into account the losses introduced by the orifice plate but also to give stability to the model) followed by an inlet duct and the compressor module. After the compressor a plenum is placed with its outlet duct which leads to the outlet valve. The bond graph, Fig. 5.4 (b), describes the causality of the calculations, the sources and the inputs/outputs of each components.

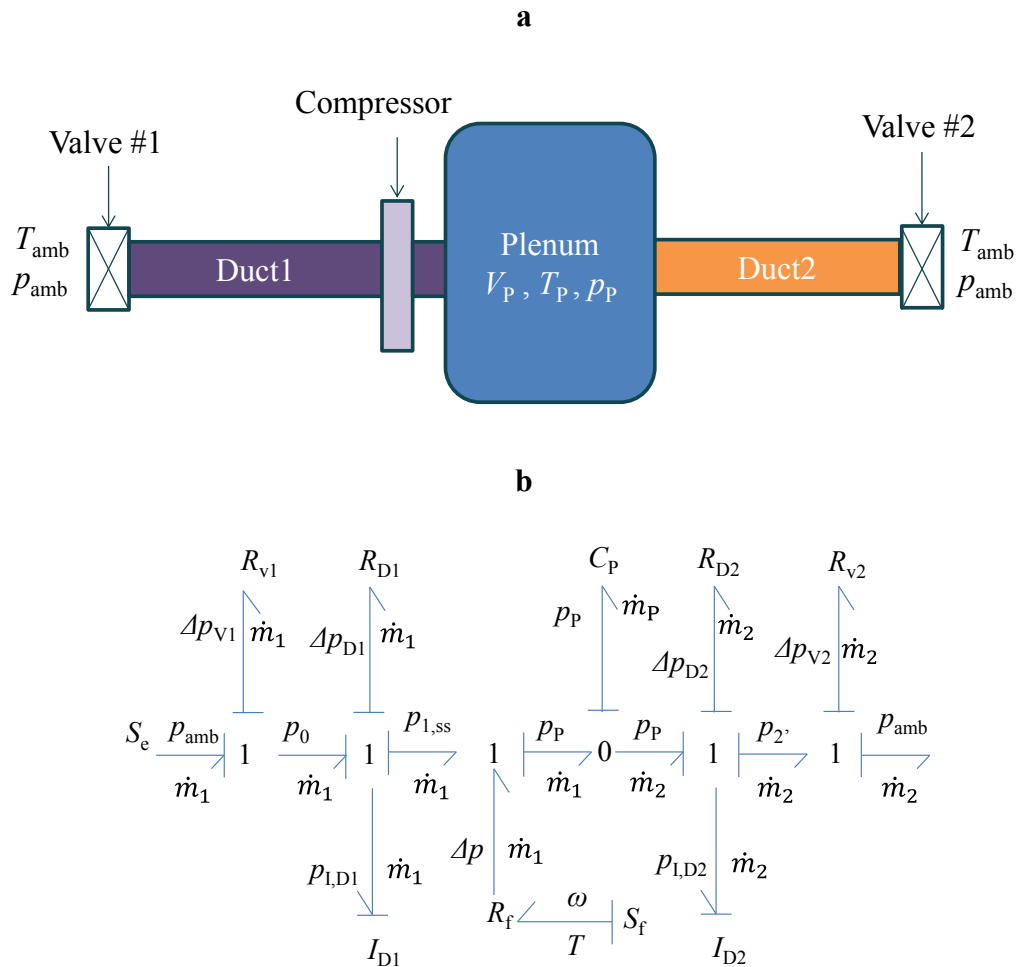


Fig. 5.4 - Diagram of the system: (a) graphic representation; (b) bond graph

The boundary conditions are the ambient temperature and pressure while the initial conditions are: the ambient conditions, the rotational speed of the compressor, fixed to 5000 rpm, and the mass flow rate, set equal to the choking mass flow at 5000 rpm. Obviously, if another initial value of rotational speed is used, it is suggested to set, as the initial condition, the choking mass flow rate corresponding to that speed. The compressor is the one described in chapter 3. Therefore, the steady-state performance curves, see Fig. 5.5, determined during the experimental activities were used to obtain the interpolated quadratic curves (as explained above). Successively the parametric procedure, described above, was applied to obtain the characteristic parameters useful for simulating the performance of the compressor at the various rotational speeds. In Fig. 5.6, these parameters are plotted as a function of the corrected rotational speed.

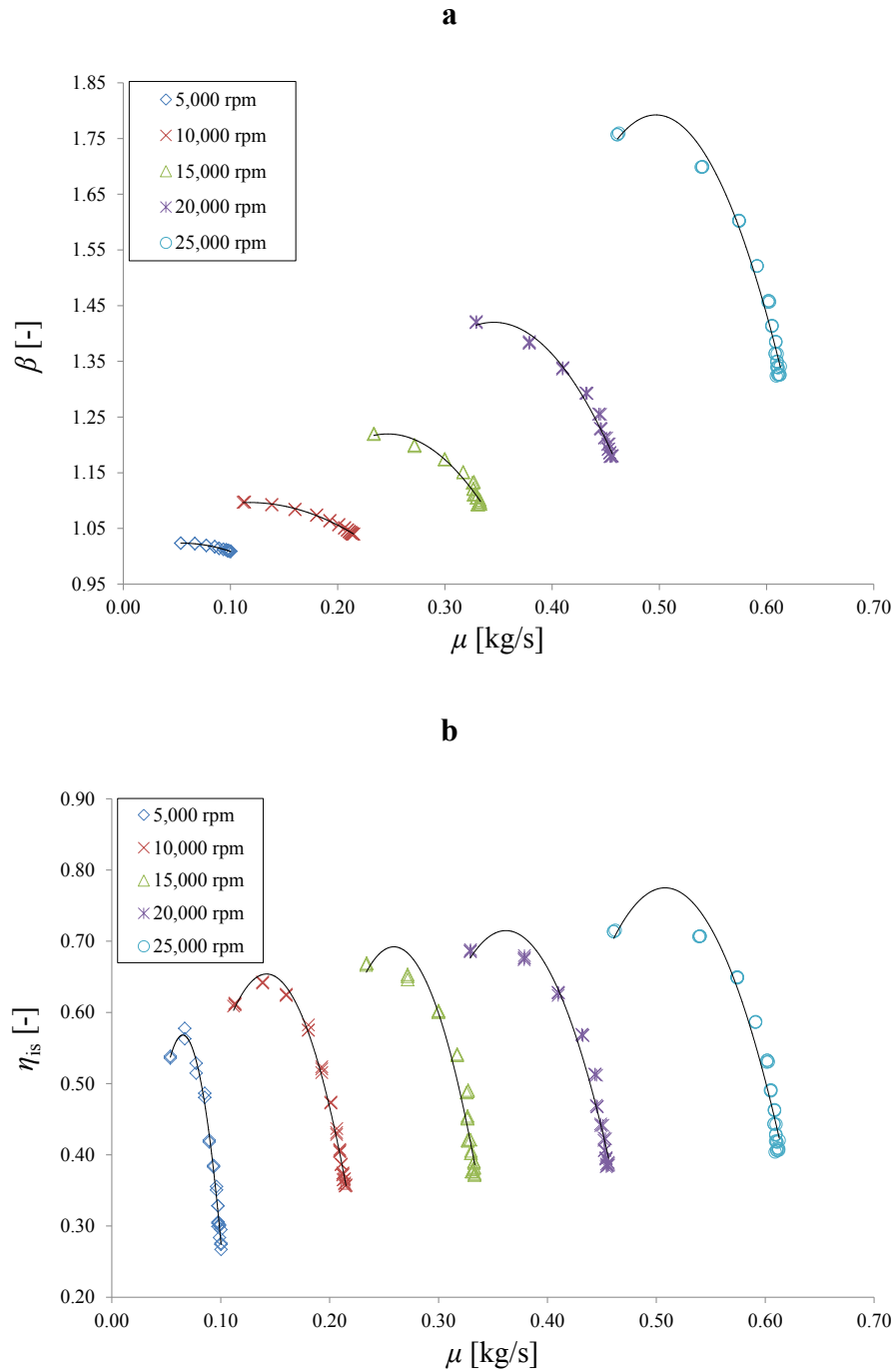


Fig. 5.5 - Steady-state interpolated curves of performance maps: (a) pressure ratio; (b) isentropic efficiency

As mentioned above, the Simulink environment allows a modular structure which fits well with the bond-graph approach. This is clear by looking at Fig. 5.7 where the modules, described above, can be clearly identified. Each module communicates with the others by means of connection lines which transmit the signal from one module to another.

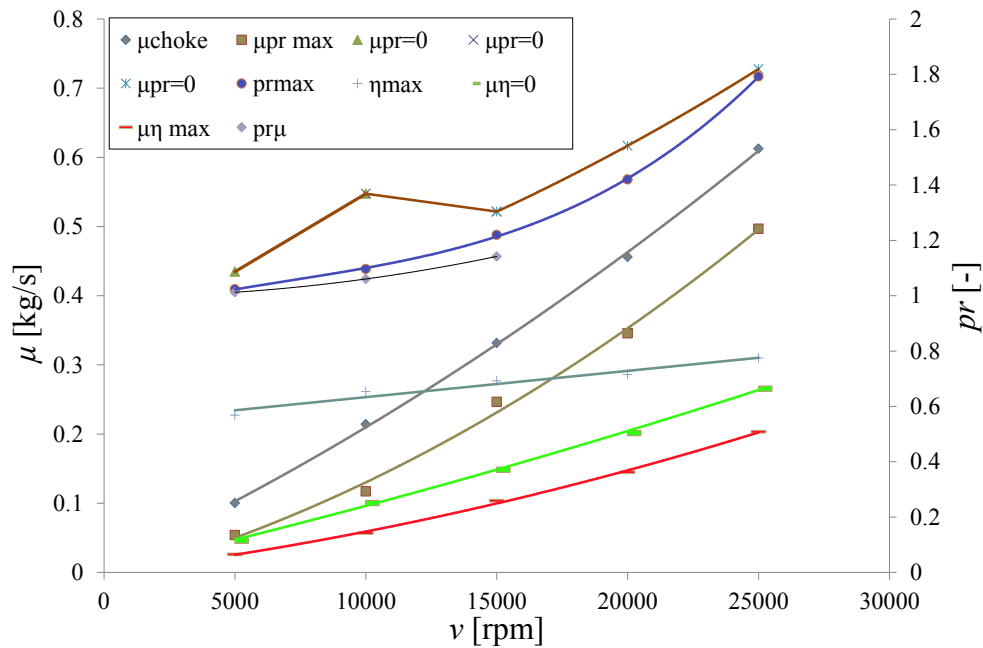


Fig. 5.6 - Parametric procedure: the trend of the characteristic parameters of performance curves

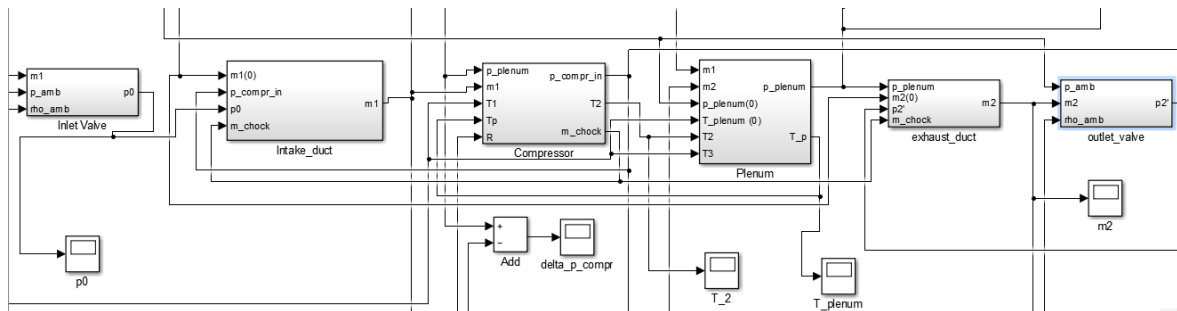


Fig. 5.7 - The model representation in the Simulink main screen; from left to right: inlet valve, inlet duct, compressor, plenum, outlet duct and outlet valve (the terms and names used in Simulink for certain parameters, or elements, may not be the same as those used in this chapter)

5.6 Validation and Results

The test and model results are reported in Fig. 5.8. The dynamic compressor characteristic (presented in terms of the pressure difference $p_P - p_{amb}$ as a function of μ , at $v=15,000$ rpm, Fig. 5.8 (a) obtained by the model was compared to the experimental recorded data. The actual data trend in surge condition, differs from the model one only in terms of variation of mass flow rate, around the zero mass flow point. This phenomenon occurred at each surge cycle and was probably due to the specific shape of the compressor stalled curve (which is not taken into account in this work) or to some sort of flow accumulation in small capacitance volumes (which cannot be easily modeled in detail)

along the circuit. The model shows high correlation with the actual data, evaluating both the pressure drop and the mass flow. The values of p_p , as a function of time (see Fig. 5.8 (b)), recorded during tests are plotted and compared with the predicted values of the model. It can be clearly seen that the absolute values of amplitude and frequency during surge are highly comparable.

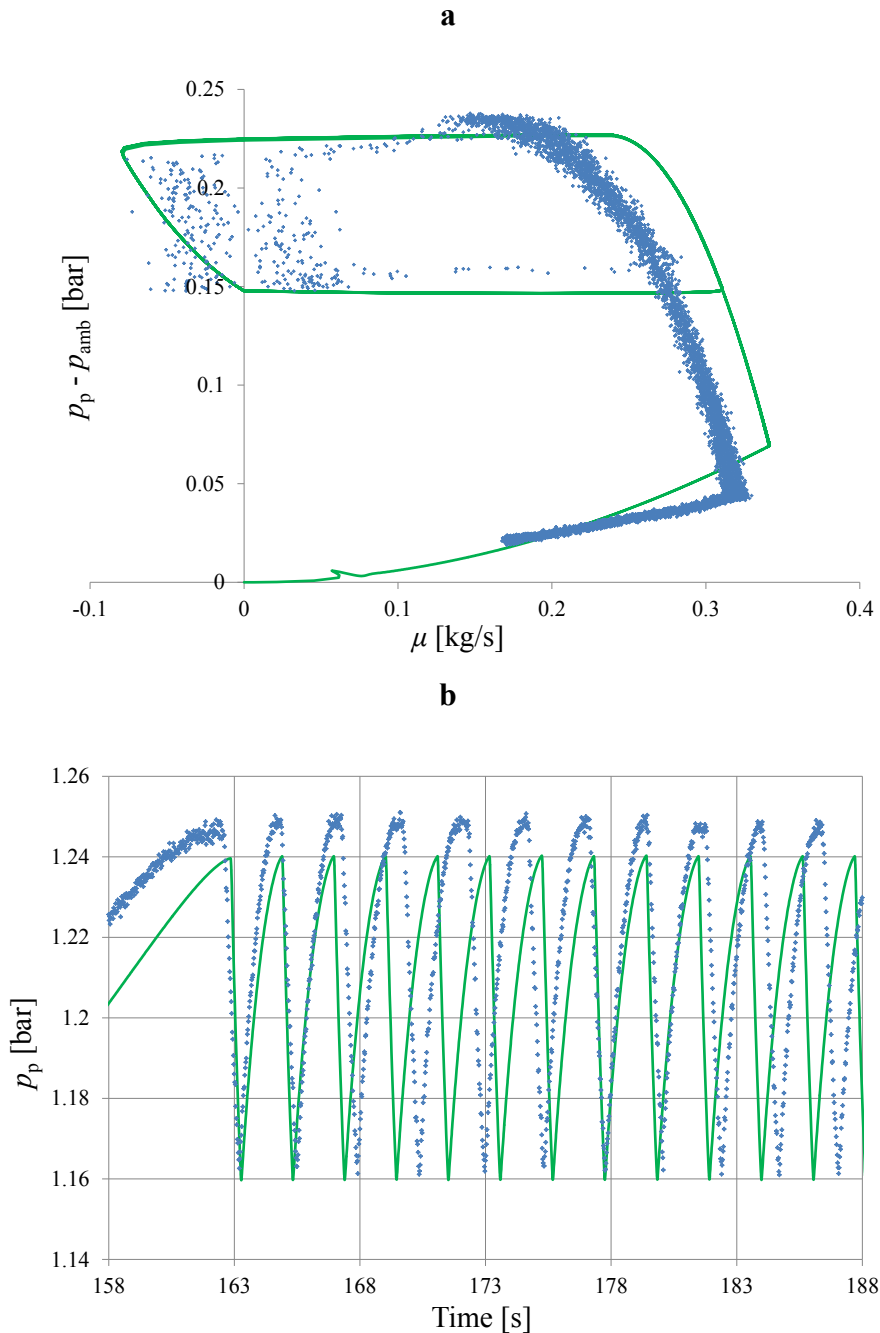


Fig. 5.8 - Comparison between experimental and model results: (a) dynamic characteristic curve; (b) pressure fluctuation in the plenum.

The model slightly underestimates the amplitudes of the surge pulsations, which is due to the inevitable uncertainty introduced by the parametric procedure. The experimental maximum value of the plenum pressure (during surge) was equal to 1.249 bar whereas the

model calculated a value of 1.240 bar. The actual surge frequency was 0.45 Hz while the model predicted a frequency of 0.49 Hz; this is probably due to the fact that the oscillations of the real system did not perfectly resemble each other. These minimal differences between the model and the test data are acceptable since a simple model, with a very low computational cost, cannot perfectly fit the values of an experimental test rig. The precision of this model is significantly improved in its advanced version (see next chapter) by implementing more experimental curves, thus obtaining more accurate parameterization, and more rigorous formulations in the compressor module.

Other interesting results are shown in Fig. 5.9 which depicts the trend of the mass flow rate at the compressor inlet (in blue) and at the plenum outlet (in green). From this figure, it is possible to confirm that the model is able to predict the unstable behavior of the system. Moreover, the stabilizing effect of the plenum, downstream thereof, is confirmed by the reduced flow oscillations.

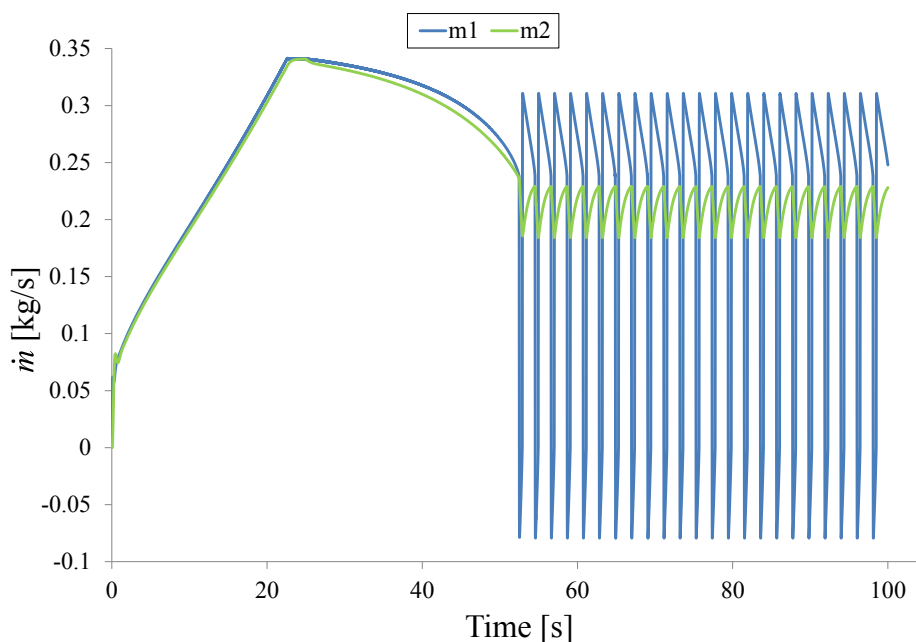


Fig. 5.9 - Mass flow rate at the compressor inlet, m_1 , and at the plenum outlet, m_2

As described in the previous section of this chapter, the model is able to simulate the plenum temperature variation during a transient event, and thus during surge. In Fig. 5.10 the plenum temperature obtained from the simulation is plotted, showing typical surge fluctuations. However, the resulting trend cannot be considered completely reliable since, downstream of the compressor, the temperature can become high and this implies that the thermal inertia of the ducts and plenum can highly affect the final temperature pattern. In particular, the oscillations can be expected to be less marked and the mean averaged value

to increase during surge. Moreover, during surge, a progressive increase in the temperature at the compressor inlet, and thus at the compressor outlet takes place due to the continuous backflow of higher temperature flux (coming from the plenum). Although these considerations are relevant, it can be said that lack of these additional calculations does not significantly affect the results, if the surge occurs only for a few seconds.

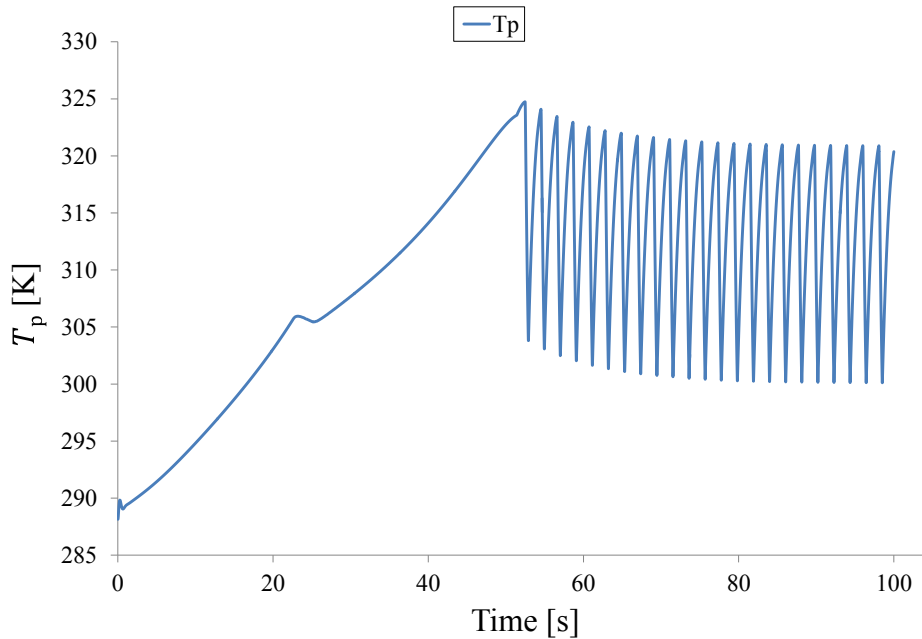


Fig. 5.10 - Simulation results: plenum temperature

5.7 Conclusions

This chapter presents a bond graph modeling approach applied to a general fluid system and is dedicated to the study and prediction of the dynamic behavior of a compression piping system during surge. Four basic elements were identified: the valve, the duct, the plenum and the compression module. Therefore, this model can be applied to any fluid system made of these components. A parameterization of the steady-state characteristic curves experimentally obtained in the test rig of the Engineering Department of the University of Ferrara was carried out. The model proved to be highly effective, after being properly tuned, in the prediction of the pressure and mass flow rate amplitudes and frequencies, demonstrating high correlation with the experimental data despite its simplicity. These considerations are evidence of the usefulness of this model and its results in industrial applications.

The model extensions and advancements can be found in the next chapter.

6 Dynamic Modeling: Thermodynamics and Axial Forces

The unsteady force acting on centrifugal compressors is an important parameter to be considered throughout the operating life of these turbomachines. When the compressor is operating in surge conditions, these forces can become highly dangerous for the mechanical and aerodynamic structures. This instability is usually avoided in industrial applications but the anti-surge systems could not react in time when emergency shutdowns or power failures take place. During these rapid transients, surge can thus develop, generating unsteady forces which can harm the close clearance components of the compressor. Therefore, the ability to predict the characteristics and dynamics of these surge forces would allow the estimation of the off-design fatigue cycles produced on these components by the surge aerodynamic pulsations. Currently, no validated method exists to predict the frequency and amplitude of the surge forces and determine the potential damage of these components.

The lumped parameter model, presented in the previous chapter, is improved with some different thermodynamic calculations and is provided with a supplementary tool to estimate the characteristics of the axial force applied to the thrust bearing. The model is validated using the experimental data recorded at the Southwest Research Institute facility. The possibility to validate the model also with a different compressor type and test rig was a great opportunity to test the robustness of the simulator, its validity and potential application to any generic test rig.

The high correspondence of the simulator results with the test data implies that this model can offer significant information about the severity of a surge event and the quantification of the machine performance losses together with possible damage to the close clearance components. This study, which is also developed in partnership with Solar Turbines Inc., is a first important step that can lead to the schedule optimization of maintenance and repair operations.

6.1 Introduction

Compressors are frequently used, especially in oil and gas applications, to allow the completion of certain processes (Rasmussen & Kurz, 2009) (Kurz & Brun, 2005) (Kurz, 2005). Among the many types of compressors, a significant role is certainly played by centrifugal compressors that are often used in the process pipeline industry, offshore industry and chemical process industry as well. This is mainly due to their compact size, efficiency, and large tolerance to process fluctuations (from the large lower pressure processes to the high-pressure ones), high reliability and generally limited maintenance costs (Boyce, 2003).

When analyzing the functionality of a centrifugal compressor, it is not sufficient to focus on aerodynamic performance, as the trustworthiness of the mechanical system components also needs to be evaluated. In fact, the close clearance components of a centrifugal compressor are essential for the integrity of the system, so their wear grade and predicted operational life have to be monitored. It is clear that the components which define the fluid-dynamic path of the compressor can also influence these parameters. Interactions between the fluid, rotor and stator can vary significantly with the compressor's working conditions, since they mainly depend on the operating pressure. These interactions are the main factors responsible for the generation of forces which can damage some compressor components (Moore, et al., 2011). Therefore, the prediction of these forces is indisputably convenient in order to schedule repairs or maintenance, thus allowing significant savings in terms of costs and preventing unpredicted production losses.

The bearing system, which constrains the rotor movement, is subject to the generated aerodynamic and mechanical force. It follows that the thrust bearing is one of the most critical elements, since its design and possible damage are evaluated by considering the thrust acting on it (Lüddecke, et al., 2016). The evaluation of these loads plays a fundamental role, especially for centrifugal compressors, and can provide an accurate prediction of the bearing life. As mentioned above, centrifugal compressors are frequently chosen in oil and gas applications. These industrial processes usually require a low pressure ratio, since the operating range needs to be as large as possible, thus from very high flows (stonewall) to low flows (near surge) (Kurz, et al., 2011). Choke conditions, in some circumstances, cause drop in efficiency but usually do not usually represent a risk for the reliability of the mechanical

components of the unit. Surge is instead recognized as a drastic event which negatively affects the performance of a compressor (Cumpsty, 1989) generating cyclic mass flow and pressure pulsations, and thus impeding the turbomachinery from carrying out its work and guaranteeing the designed thermodynamic parameters of the process. Although surge is now effectively prevented in industry, thanks to special dedicated control systems (surge avoidance systems controlling recycle circuits - in the case of compressed gases - or blow off valves - in the case of compressed air), some unpredictable transitory events or power failures can generate this phenomenon before the surge avoidance systems can react. When surge occurs, the aerodynamic features of the compressor completely change as does the axial thrust which can then severely damage the structures belonging to the compressor, and subsequently cause its destruction.

It is clear that, to correctly predict the axial thrust discharged on the thrust bearing, especially during surge, it is necessary to estimate the thermodynamic performance of the compressor during this instability. This chapter presents a dynamic model for predicting the performance of a compressor installed in a piping system. This work represents the further development of the model presented in the preceding chapter and it is carried out in partnership with the Southwest Research Institute (SwRI) and Solar Turbines Inc. The model is able to estimate the frequency and the amplitude of mass flow rate and pressure oscillations, upstream and downstream of the compressor, during surge. The model is developed in the Matlab/Simulink® environment and its main characteristic is its modularity, given by the approach on which it is based. The model also has a specific additional tool dedicated to the calculation of the axial aerodynamic force and the resultant thrust acting on the bearing.

In the following sections of the Thesis a brief literature review of the main works related to these topics, a description of the model, also showing the main results utilized for its validation (based on the experimental results obtained at the SwRI test facility), and a sensitivity analysis are presented.

6.2 Literature Review

Whereas literature offers accurate methods for evaluating radial thrust, it is less precise and complete regarding the estimation of the axial thrust, due to the high

number of factors which influence this prediction. This implies that the evaluation of axial thrust still cannot count on a universal and completely reliable method. This section of the Thesis lists the experimental, modeling and even purely theoretical works dealing with axial thrust evaluation.

The study of axial thrust on turbomachinery began approximately around the 1960s, and one of the first and most representative works, although focusing on centrifugal pumps, was presented by Domm and Zilling (Domm & Zilling, 1966). Later, since the works of Kurokawa and Toyokura (Kurokawa & Toyokura, 1972), the effect of radial inward leakage flow on axial thrust in turbomachines also began to be analyzed. They theoretically and experimentally examined the flow between the impeller and the casing of a radial turbomachine finding the influence of some parameters such as angular momentum and axial spacing between the rotor and the casing.

After the study of Mazzawy (Mazzawy, 1980) who introduced the problem of structural loads in gas turbines during surge, the evaluation of the forces generated in a turbomachines acquired more interest. In fact, he was one of the firsts to offer a simple model for estimating the impact of surge force on engine structures. Some other authors (Bondarenko, et al., 1992) developed a set of equations considering the flow between the casing and the impeller; the results showed good agreement with the experimental data. Lately, some researchers (Baldassarre, et al., 2015) have developed a 1D software to estimate radial pressure distribution along impeller surfaces, and subsequently, the total axial thrust acting on the rotor; they validate the model using the experimental data from two high –pressure centrifugal compressors tested at full load. In that work they used the correlation of (Da Soghe, et al., 2009).

More recently, some authors have tried to approach this topic by means of computational fluid dynamics (Moore, et al., 2011). They applied for the first time CFD methods to study the rotordynamic forces on a centrifugal compressor. They used a particular meshing technique which allowed (i) a significant time saving and (ii) adequate correlation to the recorded data. This study revealed that most of the destabilizing force occurred in the shroud gap. In the work of Han and Cizmas (Han & Cizmas, 2003) a numerical method, not validated with experimental data, for the calculation of the axial thrust of a centrifugal compressor was presented. In that investigation both the flow through the impeller and the leakage flow on the back side

of the wheel were simulated for a single operating point. Relevant work has been carried out, in recent years, by Bidaut and Dessibourg (Bidaut & Dessibourg, 2014). They reported remarkable thrust measurements on different types of compressors. They also described the main concepts and key points that need to be considered for the correct evaluation of axial thrust. They conducted the study focusing on the parameters which affect this calculation most. They also reported a set of equations, based on literature, for achieving an accurate estimation of the axial loads. Based on their history review, the experimental evaluation of thrust is quite a recent activity. Some measurements were carried out in the 1990s (Baumann, 1999) when a study on rotordynamic stability was performed, focusing on the influence of thrust brakes. Later, Bidaut and Baumann performed other measurements (Bidaut, et al., 2009) in a 655 bar compressor, recording data by means of a thrust collar in the gear and also taking the rotor damping.

For high pressure applications, the thrust calculation should carefully take into consideration the phenomena occurring along the side cavities, as shown in the work of Petry, et al. (Petry, et al., 2013) and Roy, et al. (Roy, et al., 1999). Many authors have carried out studies, even without the specific aim of calculating axial thrust, to analyze the flow in the side chambers (Li, 2013) (Will, 2011). These examples may be very useful for developing a mathematical algorithm to evaluate in detail the pressure distribution along the gaps for a high pressure compressor. One of the main references with extensive dissertation of rotating flows in the cavities is the book published by Childs (Childs, 2011). Finally, the last important study to mention is that of Lüddecke, et al. (Lüddecke, et al., 2016) in which the rotor motion of a turbocharger was analyzed. In that paper the thrust bearing reaction forces were also measured under various engine operating conditions and a model was proposed. The results were compared with the recorded data, and the approach used has proved to be successful for a single-stage waste gate turbocharger.

This section highlights that, currently, the methodology used to calculate centrifugal compressor axial thrust, especially for high-pressure applications, is still a field of research which needs to be explored, advanced and expanded. For this reason, this work aims to provide a significant contribution by offering the description and results of a brand new dynamic model with an additional tool for calculating the net axial thrust during surge.

6.3 Improvement of the Thermodynamics of the Model

This section reports the modifications and additional implementations applied to the model described in chapter 5.

6.3.1 *General Improvements*

The model is based on the hypothesis of ideal gas, however, since the future target of this advanced version of the model is the oil & gas applications field, the simulator code was intended to be able to handle different types of gases and mixtures. For this reason, this improved version allows the assessment of the specific heat coefficients, the gas constants and the specific heat ratios (Rohsenow, et al., 1998), thus it is currently suitable for low-to-medium pressure applications. The constant coefficients which are useful for calculating the specific heat as a function of temperature, were found. By using the molecular weight of the gas as input, R_{gas} , and γ were determined. This procedure was applied to several gases used in industry. Moreover, if a mixture is used in the model and the correct percentage fraction of gases is set, the characteristic gas constant of the mixture can be calculated.

To make the model suitable for the Industry sector (this project was carried out within the framework of the Gas Machinery Research Council activity), all these inputs, together with the geometrical inputs of the systems and steady-state curves of the compressor (or single-stages, see subsection “The compressor”) are automatically uploaded in the Matlab workspace. This is done by means of a specific script which communicates with an Excel® file.

For the same reason, despite the complexity of the model, the computational cost was carefully taken into account.

6.3.2 *The Valve Element*

The valve element was not modified but a new type of valve is implemented in the model. This new valve was modeled, in order to increase the modularity of the model, as an element which uses the same physical principle and equation but determines the mass flow rate, given the pressure drop, as shown in (6.1):

$$\dot{m} = K_V \times (\pm \sqrt{|\bar{\rho} \Delta p_V|}) \quad (6.1)$$

6.3.3 The Duct and the Plenum Elements

The duct and the plenum elements were not modified, so they maintain the same features described in Chapter 5.

6.3.4 The Compression Stage Element

In the previous version of the model, only one compressor module was created, which was able to simulate a single stage (if the single stage maps were provided) or the overall compressor (if the single stage maps were provided). That module is a reliable modeling solution but it is quite simple and inherently limited. In this new version of the model, two types of compressor modules were implemented, so one or the other can be used depending on the performance data provided. If only the overall compressor maps of a multistage compressor are known, the compressor is modeled by the “Overall Compressor” module, otherwise, if the maps of each specific stage are known, the compressor can be modeled using the “Single Stage” module (by placing in series as many modules as the number of stages). Both of these modules read the performance curves of the compressor, i.e. the static to static pressure ratio and the isentropic efficiency, in terms of corrected rotational speed coefficient, N_{corr} , and corrected mass flow rate coefficient, \dot{m}_{corr} , expressed as

$$N_{\text{corr}} = \frac{N}{\sqrt{\gamma R T_{\text{in}}}} \quad (6.2)$$

$$\dot{m}_{\text{corr}} = \frac{\dot{m} \sqrt{R T_{\text{in}}}}{p_{\text{in}} \sqrt{\gamma}} \quad (6.3)$$

This choice allows the assessment of the variation in compressor performance with the type of gas and changes to ambient conditions, except for humidity (Dixon & Hall, 2013) (Berdanier, et al., 2015) (Kurz, 2005). Taking the single stage representation and nomenclature of Fig. 6.1 as reference, three different cases can occur during the simulation:

1. The compressor works in the stable range
2. The compressor works in the unstable range (but with $m > 0$)
3. The compressor works in the reverse flow range

Case 1

In this case the operating point is in the negative slope part of the characteristic curve, as highlighted in Fig. 6.2. The module reads the corrected characteristic curves developed through the parametric study (these curves, as examined in the previous chapter, are derived from the experimental data). In this case, no implementation is applied with respect to the first version of the model, thus the formulations are the same as those reported in Chapter 5.

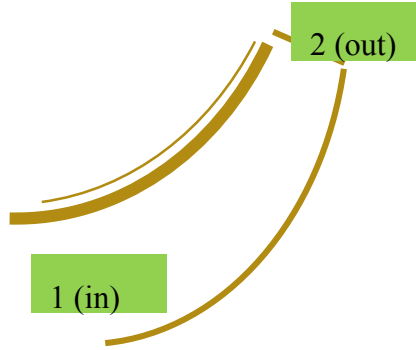


Fig. 6.1 - Sketch of the “single stage” module and nomenclature of the inlet and outlet sections; this nomenclature is also valid for reverse flow conditions (case 3)

Case 2

In this case, the operating point calculated by the model goes at the left of the characteristic curve peak. The model can adopt two different curves, as shown in Fig. 6.2: (a) the Moore and Greitzer cubic law, as also implemented in (Belardini, et al., 2015); or (b) the sudden pressure drop/rise (this is the only option present in the first model version). The first or the second alternative may be chosen depending on the type of effect the surge is expected to have generated, and depending on the type of characteristic curve the compressor is expected to have beyond the peak. The cubic law, which is also valid for reverse flow, allows the calculation of the pressure ratio as:

$$\beta_{\dot{m}<0} = \beta_{\dot{m}=0} + H \left[1 + \frac{3}{2} \left(\frac{\dot{m}}{W} - 1 \right) - \frac{1}{2} \left(\frac{\dot{m}}{W} - 1 \right)^3 \right] \quad (6.4)$$

where the main parameter to be calculated is $\beta_{\dot{m}=0}$, i.e. the pressure ratio at zero mass flow rate:

$$\beta_{\dot{m}=0} = \left(1 + \frac{\eta_{is\dot{m}=0} g H_{id\dot{m}=0}}{C_p T_{in\dot{m}=0}} \right)^{\frac{\gamma}{\gamma-1}} = \left(1 + \frac{\eta_{is\dot{m}=0} \pi^2 \left(\frac{N}{60} \right)^2 (D_2^2 - D_1^2)}{C_{p(T1\dot{m}=0)} T_{1\dot{m}=0}} \right)^{\frac{\gamma}{\gamma-1}} \quad (6.5)$$

The outlet temperature (or T at section 2, in Fig. 6.1) is calculated as

$$T_{\text{out}} = T_{\text{in}} (\beta)^{\frac{\gamma-1}{\eta_p}} \quad (6.6)$$

The polytropic efficiency, η_p , is calculated from the isentropic efficiency, η_{is} as shown in Chapter 5.

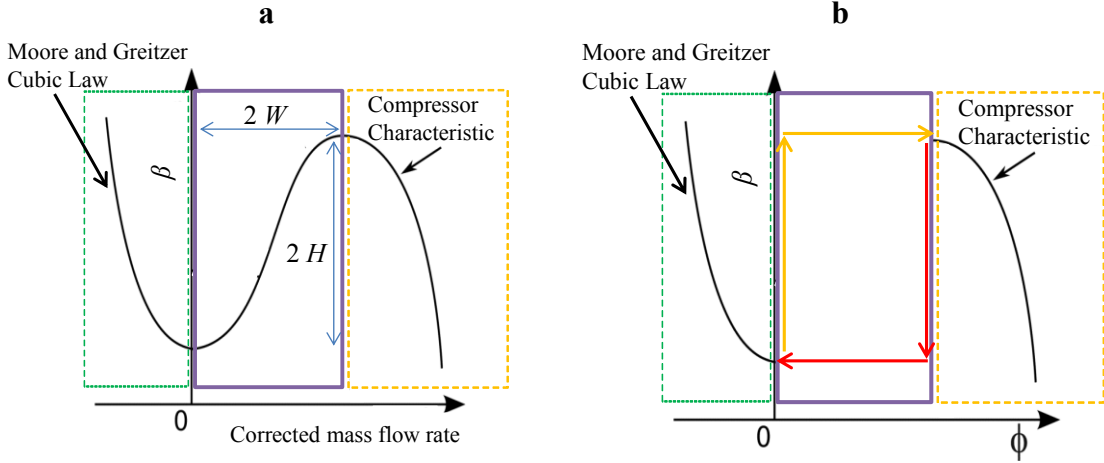


Fig. 6.2 - Compressor curves in surge conditions: (a) Moore and Greitzer Cubic Law; (b) sudden pressure rise/drop

In direct flow conditions, the isentropic efficiency derives from the maps experimentally obtained (as in the previous version of the model), whereas at zero mass flow it is calculated by following a procedure that considers the losses due to incidence and frictions, as reported in (Gravdahl & Egeland, 2012) and also utilized by Jiang, et al (Jiang, et al., 2006):

$$\eta_{\text{is}_{\dot{m}=0}} = \frac{gH_{\text{id}_{\dot{m}=0}}}{gH_{\text{id}_{\dot{m}=0}} + \Delta h_{\text{loss}_{\dot{m}=0}}} - \Delta\eta_{\text{bf}_{\dot{m}=0}} - \Delta\eta_{\text{c}_{\dot{m}=0}} - \Delta\eta_{\text{v}_{\dot{m}=0}} - \Delta\eta_{\text{d}_{\dot{m}=0}} \quad (6.7)$$

With:

$$\Delta\eta_{\text{bf}_{\dot{m}=0}} \approx 0.03 \quad (6.8)$$

$$\Delta\eta_{\text{c}_{\dot{m}=0}} = 0.3 \frac{l_{\text{cl}}}{b} \quad (6.9)$$

$$0.02 \leq \Delta\eta_{\text{v}_{\dot{m}=0}} \leq 0.05 \quad (6.10)$$

And with

$$\Delta h_{\text{loss}_{\dot{m}=0}} = \Delta h_{\text{if}_{\dot{m}=0}} + \Delta h_{\text{ii}_{\dot{m}=0}} + \Delta h_{\text{df}_{\dot{m}=0}} + \Delta h_{\text{di}_{\dot{m}=0}} \quad (6.11)$$

where

$$\Delta h_{\text{ii}_{\dot{m}=0}} = \frac{u_1^2}{2} \quad (6.12)$$

$$\Delta h_{\text{ii}_{\dot{m}=0}} = \frac{1}{2} \left(\frac{D_2 u_1}{D_1} \right)^2 \quad (6.13)$$

$$\Delta \eta_{\text{d}_{\dot{m}=0}}, \Delta h_{\text{df}_{\dot{m}=0}}, \Delta h_{\text{if}_{\dot{m}=0}} \approx 0 \quad (6.14)$$

Case 3

In this case reverse flow occurs and the pressure ratio is found, as in the first version of the model, by means of the cubic law. When surge occurs, the concept of efficiency can be misleading, so in this Thesis a different strategy was used to evaluate the temperature. In fact, the first law of thermodynamics was applied to the compressor, also considering the expansion effect that the gas experiences in reverse flow, along the compressor. The expansion work is calculated as:

$$W_{\text{exp,C}} = p_{\text{out}} v_{\text{out}} - p_{\text{in}} v_{\text{in}} \cong \frac{p_{\text{out}} - p_{\text{in}}}{\rho_{\text{out}}} = \frac{p_{\text{out}}}{\rho_{\text{out}}} \left(1 - \frac{p_{\text{in}}}{p_{\text{out}}} \right) = R_g T_{\text{out}} \left(1 - \frac{1}{\beta_{\dot{m}<0}} \right) \quad (6.15)$$

The temperature of the flow leaving the compressor is then:

$$T_{\text{in}} = T_{\text{out}} + \frac{gH_{\text{id}_{\dot{m}<0}} - W_{\text{exp,C}}}{C_p} \quad (6.16)$$

where that T_{out} is the temperature entering the compressor. The impeller work, gH_{id} , is calculated by using the Euler equation. Therefore, this module can simulate both vaneless and vaned diffuser compressors. The difference between these two cases (vaneless and vaned diffusers) is the calculation method of the impeller work in reverse flow since the impeller entering flow incidence is substantially different. In a vaneless diffuser (Ferrara, 2013) the flow is considered entering with a perfect radial direction at the impeller tip whereas in a vaned diffuser the incidence depends on the vane angles. Therefore, the following can be assumed:

$$gH_{\text{id}_{\dot{m}<0}} = |u_1 c_{\theta 1} - u_2 c_{\theta 2}| \approx \sigma u_1^2 \quad (6.17)$$

$$gH_{id_{m<0}} = |u_1 c_{\theta 1} - u_2 c_{\theta 2}| \approx |\sigma u_1^2 - u_2^2| \quad (6.18)$$

where the slip factor (which can be tuned by the user) is expressed as:

$$\sigma = \frac{c_{\theta 1}}{u_1} \quad (6.19)$$

6.3.4.1 Single stage maps predictions

The concept and methodologies explained above are applied to both the “Overall Compressor” and the “Single Stage” module. However, in the overall compressor module only the overall maps of the compressor are given as inputs. In that module a procedure is then applied to estimate the inter-stage values of pressure and temperature, a problem which other authors have faced in different ways (Tibboel, 2003) (Casey & Robinson, 2013). This additional calculation is not required when analyzing the compression system dynamics, but was implemented because the estimation of the pressure and temperature at the inlet and outlet of each impeller becomes fundamental when calculating the axial fluid-dynamic thrust.

In direct flow and zero flow conditions, the layout of the “overall compressor” module is that shown in Fig. 6.3. The known values of pressure and temperature are shown in green, whereas the values to be calculated are shown in orange.

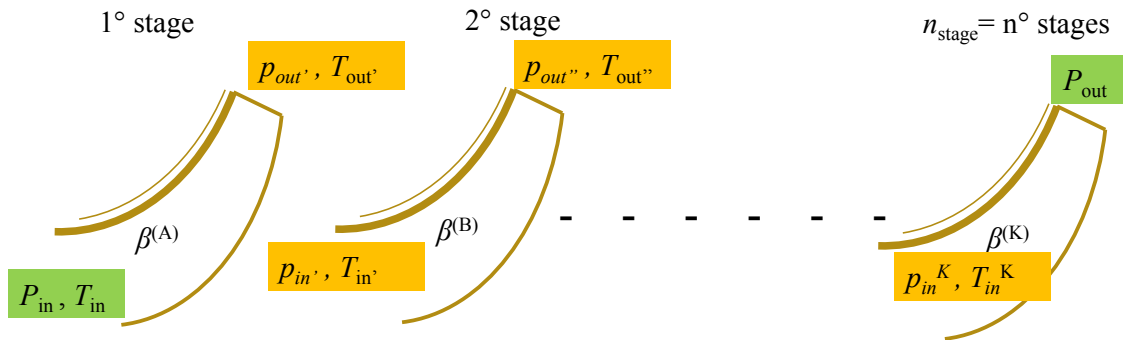


Fig. 6.3 - Sketch of the impellers of a multistage compressor and the physical quantities (pressure and temperature) in direct flow

It is assumed that:

$$P_{out'} = P_{in'} \quad (6.20)$$

$$P_{out''} = P_{in''} \quad (6.21)$$

....

$$P_{out^{(K-1)}} = P_{in^K} \quad (6.22)$$

and that:

$$T_{out'} = T_{in'} \quad (6.23)$$

$$T_{out''} = T_{in''} \quad (6.24)$$

....

$$T_{out^{(K-1)}} = T_{in^K} \quad (6.25)$$

Therefore, the presence, and thus the effect, of the diffuser are neglected. It is then assumed that the pressure ratio and thermodynamic transformation of each stage is carried out by the related impeller. The isentropic efficiency of each stage, is obtained from the maps, in the stable operating range, while at zero mass flow rate, it is calculated as previously shown in (6.7). The outlet temperature of each stage is calculated by using the same formulations explained in (6.6) and (6.16). The pressure ratio of each stage cannot be easily estimated without any specific information. For this reason, an assumption has to be applied as a calculation rule. The following relation is assumed:

$$\frac{\beta^{(B)}}{\beta^{(A)}} = \text{const}_{(1)} = \frac{\beta_{\dot{m}=0}^{(B)}}{\beta_{\dot{m}=0}^{(A)}} \quad (6.26)$$

$$\frac{\beta^{(C)}}{\beta^{(A)}} = \text{const}_{(2)} = \frac{\beta_{\dot{m}=0}^{(C)}}{\beta_{\dot{m}=0}^{(A)}} \quad (6.27)$$

....

$$\frac{\beta^{(K)}}{\beta^{(A)}} = \text{const}_{(n_{stage}-1)} = \frac{\beta_{\dot{m}=0}^{(K)}}{\beta_{\dot{m}=0}^{(A)}} \quad (6.28)$$

Where β is the pressure ratio. Therefore the ratio between the pressure ratio of each stage and the pressure ratio of the first stage remains constant; this constant value depends on the values of the pressure ratio of each stage at zero mass flow rate.

Consequently, the overall pressure ratio $\beta^{(AK)}$, which is obtained by using the same methodology explained in the “Single stage” module, can be expressed as:

$$\beta^{(AK)} = \beta^{(A)} \beta^{(B)} \beta^{(C)} \dots \beta^{(K)} = \beta^{(A) n_{\text{stage}}} \text{COST} \quad (6.29)$$

where $\text{COST} = \text{cost}_{(1)} \text{cost}_{(2)} \dots \text{cost}_{(n_{\text{stage}}-1)}$

Therefore, by knowing the overall pressure ratio, it is possible to calculate the pressure ratio and the outlet pressure of each stage through the following equations:

$$\beta^{(A)} = \sqrt[n_{\text{stage}}]{\frac{\beta^{(AK)}}{\text{COST}}} \quad (6.30)$$

$$P_{\text{out}'} = P_{\text{in}} \beta^{(A)} \quad (6.31)$$

$$\beta^{(B)} = \beta^{(A)} \text{cost}_{(1)} \quad (6.32)$$

$$P_{\text{out}''} = P_{\text{in}'} \beta^{(B)} \quad (6.33)$$

...

$$\beta^{(K)} = \beta^{(A)} \text{cost}_{(n_{\text{stage}}-1)} \quad (6.34)$$

In reverse flow conditions, the layout used in the model is illustrated in Fig. 6.4:

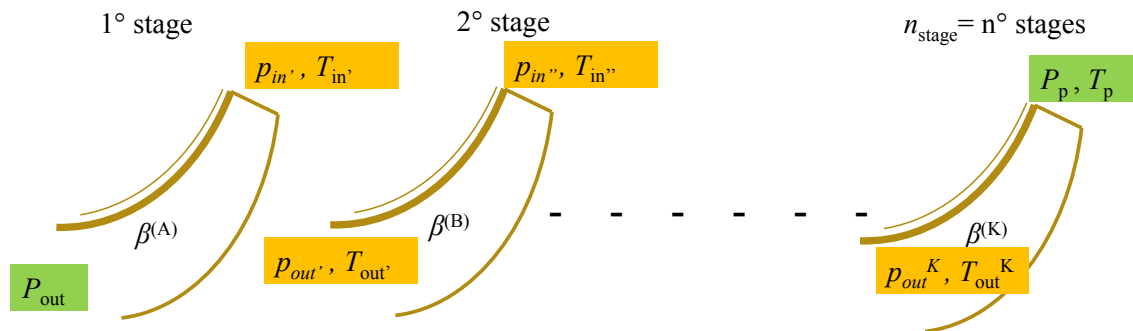


Fig. 6.4 - Sketch of the impellers of a multistage compressor and the physical quantities (pressure and temperature) in reverse flow

The procedure for the inter-stage pressure values calculation (explained above) remains valid, whereas the estimation of the inter-stage temperature values passes through the same calculation steps previously shown in the “compressor overall” module (obviously in this case the formulations are carried out at each stage).

6.4 Axial Force Calculation

When evaluating the force which acts on the thrust bearing, it is important to evaluate the aerodynamic thrust generated in the impeller, but also the characteristics of the of the mechanical systems.

6.4.1 Aerodynamic Thrust

The axial load in a compressor is generated by the accumulation of the thrust of the impeller (or impellers) belonging to the compressor. When calculating the forces, a fundamental role is played by the geometrical dimension of the rotor diameters and the seal clearances in addition to the balance piston geometry and the operating conditions. As already mentioned above, the evaluation of the resultant force strongly depends on the pressure, mass flow rate and temperature at the inlet and at the outlet of each impeller. Therefore, before applying the calculation it is important to count on a reliable compression system model. Fig. 6.9 shows the typical layout of single “in-line” impeller and the pressure contributors. The axial thrust calculation is implemented in the model as a separate tool and is carried out at each impeller (if the subject is a multistage compressor), since the thermodynamic conditions at the compressor inlet and outlet are not sufficient to obtain a good estimation. The resultant fluid-dynamic axial force, $F_{ax,fluid}$, is calculated considering the main contributions (Japikse, 1996) (Lüdtke, 2004) (Gülich, 2008) (see Fig. 6.9), which are basically the inlet and outlet static pressure, the pressure along the disc cavities, the axial momentum variation between the inlet and the outlet, and finally, the pressure distribution on the balance piston. Based on the layout of Fig. 6.9 the resultant equation for each perfectly radial impeller is:

$$F_{ax,fluid} = F_{st,in} + F_{sh} + F_{mom} - F_h - F_{pis} \quad (6.35)$$

The most difficult contributions to be estimated are F_{sh} and F_h , which derive from the flow fluid-dynamics in the hub and shroud cavities. These two forces are the result of a static force, constant along the disks, and a kinetic force which varies with the radius. By applying the radial equilibrium in a control volume of a cavity, it is possible to obtain the derivative equation of the pressure with respect to the radius:

$$\frac{dp}{dr} = \rho r C_{fc}^2 \omega^2 \quad (6.36)$$

By integrating this equation, the pressure value at a specific radius of the shroud or hub cavity is:

$$p_{sh,h}(r) = p_{disch} - \rho_{disch} \omega^2 r_{disch}^2 \frac{C_{fc}^2}{2} \left[1 - \left(\frac{r}{r_{disch}} \right)^2 \right] \quad (6.37)$$

This equation strongly depends on the core rotation factor, C_{fc} , which is very hard to estimate without weighing down the model with additional empirical formulations. To the knowledge of the author, there are no robust empirical ways as yet to determine this parameter with a reasonable computational cost. Moreover, to be very accurately calculated at each desired radius, the values of many other parameters, such as friction coefficients, roughness, etc., need to be known, which is very hard in industrial practice. The core rotation factor, in each position along the gap can be described as:

$$C_{fc} = \frac{\omega_{gas}}{\omega} \quad (6.38)$$

The study of the velocity triangles, in particular at the impeller tip, is necessary in direct flow as well as in reverse flow. Fig. 6.5 shows the velocity components of the meridian plane at the impeller suction and discharge, while Fig. 6.6 shows the velocity triangles in the front plane (the inlet triangles are also illustrated but they are not considered in the calculation of this model).

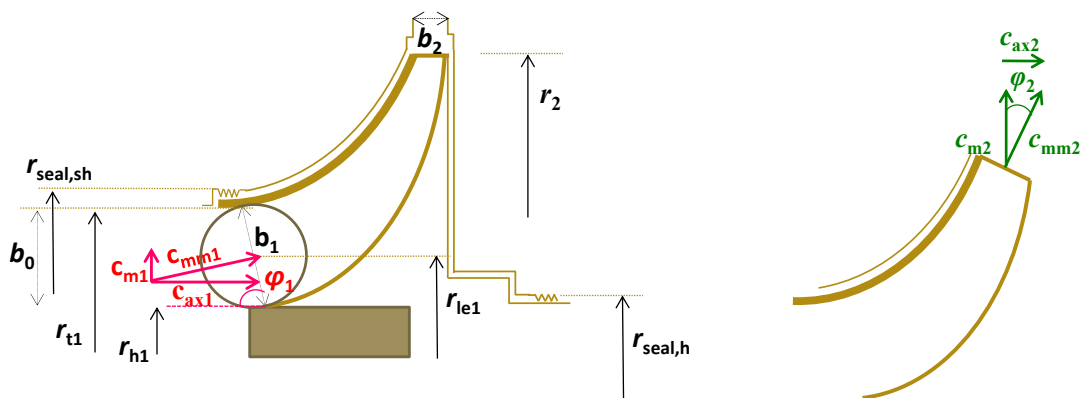


Fig. 6.5 - Sketch of the impeller velocity at the suction and at the discharge in the meridian plane (direct flow)

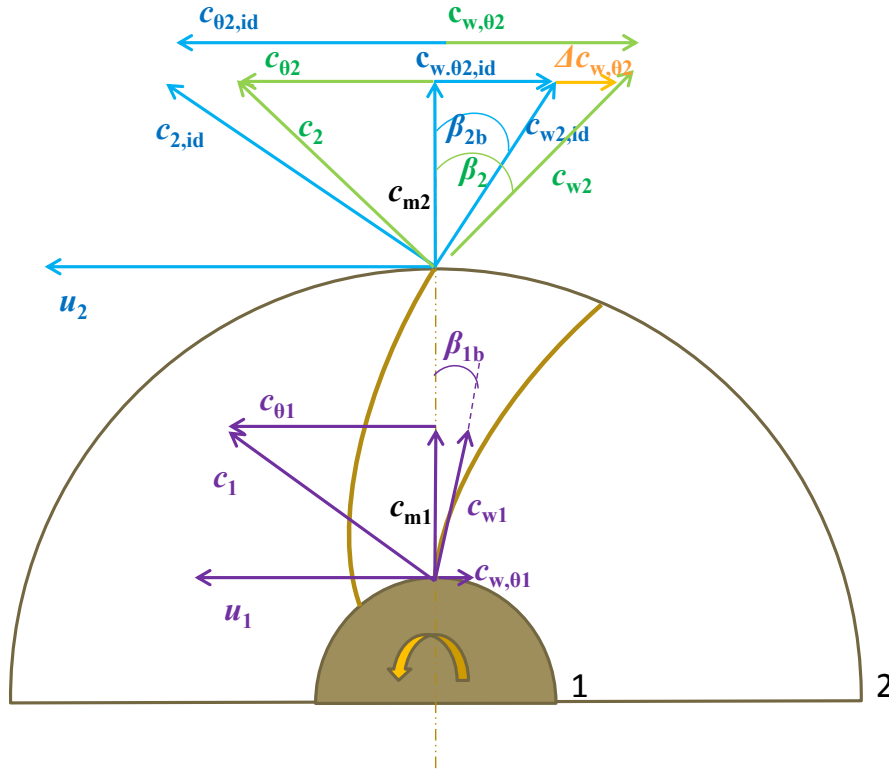


Fig. 6.6 - Sketch of the impeller velocity triangles at the inlet (section 1) and at the outlet (section 2) in the front plane (direct flow)

The following formulae is applied to calculate the passage area at the impeller suction (this area may not coincide with the passage area at the blade leading edge). The passage area is useful to calculate the velocity of the fluid which is necessary to estimate the momentum contribution to the axial force)

$$a_1 = \pi (r_{t1}^2 - r_{h1}^2) \quad (6.39)$$

In the case of an impeller with inducer, the passage area is

$$a_1 = \pi (r_{t1}^2 - r_{h1}^2) C_d \quad (6.40)$$

where C_d , which is tunable in the model, represents the penalty introduced by the blockage (or blockage coefficient). Then the velocity of the fluid when approaching the impeller suction is calculated as:

$$c_{mm1} = \frac{\dot{m}}{\rho_1 a_1} \quad (6.41)$$

where the density is:

$$\rho_1 = \frac{p_1}{R_g T_1} \quad (6.42)$$

Likewise, at the impeller discharge the passage area is also calculated, but in this case the geometry of the blades is considered:

$$a_{\text{geo}2} = 2 \pi r_2 b_2 - \frac{z b_2 t_2}{\cos(\beta_{2b})} \quad (6.43)$$

In this case the calculation of the area is useful to calculate the streamline velocity, which is convenient for estimating the momentum contribution to the axial forces, but also the tangential velocity of the fluid (needed to obtain the value of C_{fc} at the impeller tip). The absolute velocity is:

$$c_{\text{mm}2} = \frac{\dot{m}}{\rho_2 a_{\text{geo}2}} \quad (6.44)$$

where the density is:

$$\rho_2 = \frac{p_2}{R_g T_2} \quad (6.45)$$

Then, the radial component is found:

$$c_{m2} = c_{\text{mm}2} \cos(\varphi_2) \quad (6.46)$$

where the symbol φ_2 represents the angle (in the meridian view) between the radial direction and the stream line direction at the impeller tip.

Then two options can be chosen by the user: (i) the ideal case (no slip conditions are assumed) or real case (slip factor is taken into account).

The ideal tangential component is calculated as:

$$c_{\theta 2, \text{id}} = u_2 - c_{w, \theta 2, \text{id}} \quad (6.47)$$

where

$$c_{w, \theta 2, \text{id}} = c_{m2} \operatorname{tg}(\beta_{2b}) \quad (6.48)$$

In the real case, the slip conditions are evaluated by means of the Stodola correlations. Therefore, in this case the flow deviation is taken into consideration:

$$\Delta c_{w,02} = \frac{\omega \pi r_2 \cos(\beta_{2b})}{z} \quad (6.49)$$

Then:

$$c_{w,02} = c_{w,02,id} + \Delta c_{w,02} \quad (6.50)$$

And finally the tangential velocity is calculated as:

$$c_{\theta 2} = u_2 - c_{w,02} \quad (6.51)$$

In reverse flow conditions, the layout adopted by the model is shown in Fig. 6.7 and Fig. 6.8.

The geometric passage area is obviously the same calculated in direct flow:

$$a_{geo2} = 2 \pi r_2 b_2 - \frac{z b_2 t_2}{\cos(\beta_{2b})} \quad (6.52)$$

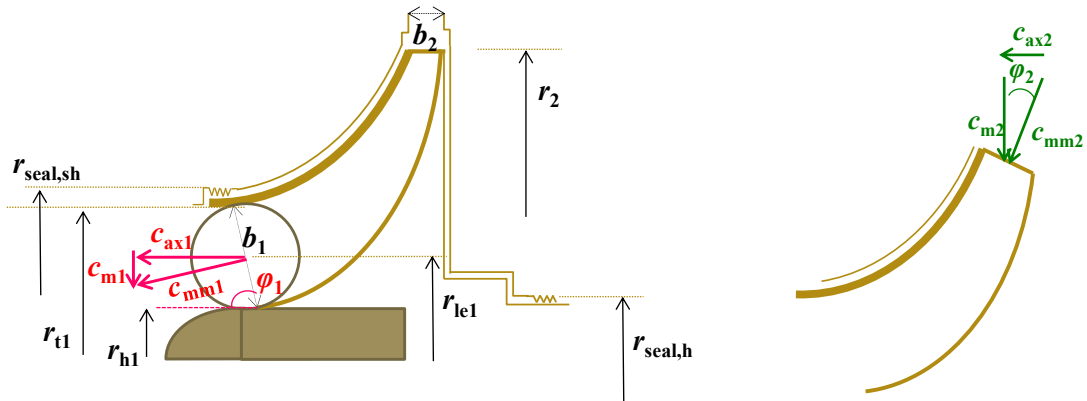


Fig. 6.7 - Sketch of the impeller velocity at the suction (left) and at the discharge (right) in the meridian plane (reverse flow)

The velocity of the fluid is:

$$c_{mm2} = \frac{\dot{m}}{\rho_2 a_{geo2} B} \quad (6.53)$$

Where B is the penalty due to blockage during reverse flow (this parameter is tunable by the user during the simulation). The blockage is generated by the high incidence angle of the relative velocity.

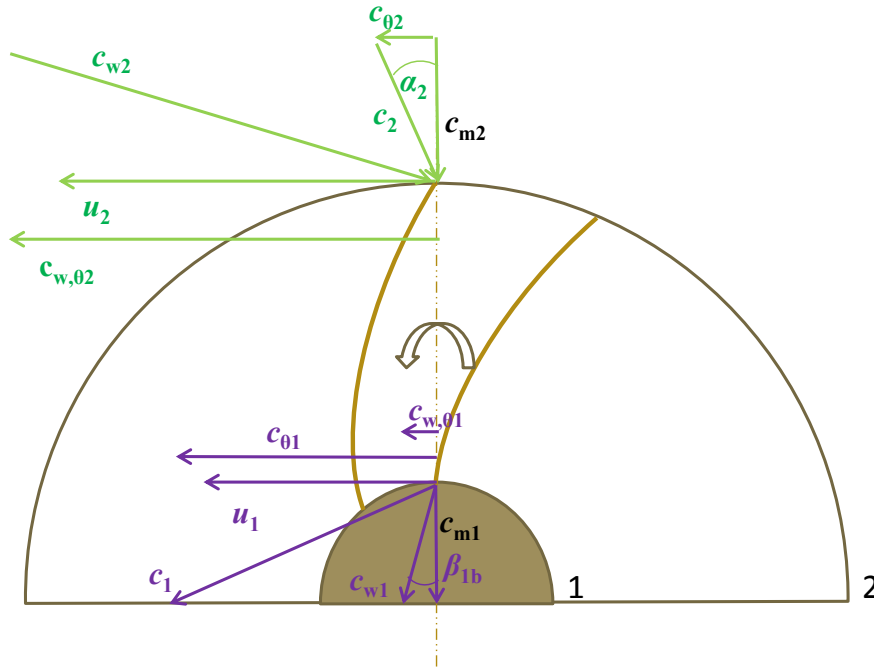


Fig. 6.8 - Sketch of the impeller velocity triangles at the inlet (section 2) and at the outlet (section 1) in the front plane (direct flow)

The density is calculated by means of the temperature of the plenum T_p (i.e. the temperature of the flow entering the compressor (the compressor experiences reverse flow, and thus $T_2 = T_{\text{out surge}} = T_p$):

$$\rho_2 = \frac{p_2}{R_g T_{\text{out,surge}}} \quad (6.54)$$

The radial component of the velocity is once again calculated as

$$c_{m2} = c_{m2} \cos(\varphi_2) \quad (6.55)$$

Then, for vaned diffusers the tangential velocity is:

$$c_{\theta 2} = c_{m2} \text{tg}(\alpha_{2b}) \quad (6.56)$$

Whereas for vaneless diffusers the tangential velocity is considered as zero:

$$c_{\theta 2} = 0 \quad (6.57)$$

During reverse flow, the fluid velocity (in the stream line direction), referred to the impeller suction, needs to be calculated:

$$c_{mm1} = \frac{\dot{m}}{\rho_1 a_1} \quad (6.58)$$

Where the density is found by means of the temperature of the flow exiting the compressor ($T_1 = T_{in,surge}$)

$$\rho_1 = \frac{p_1}{R_g T_{in\ surge}} \quad (6.59)$$

And the area a_1 is calculated as previously shown.

Since this model is dedicated to oil and gas applications with low-to-medium pressure values, and since the model was thought to provide a reliable indication in a reasonable simulation time, and with the requirement of knowing only the main geometric parameters, the core rotation factor is kept constant at each cavity. Based on literature, this method is very often used in industrial practice.

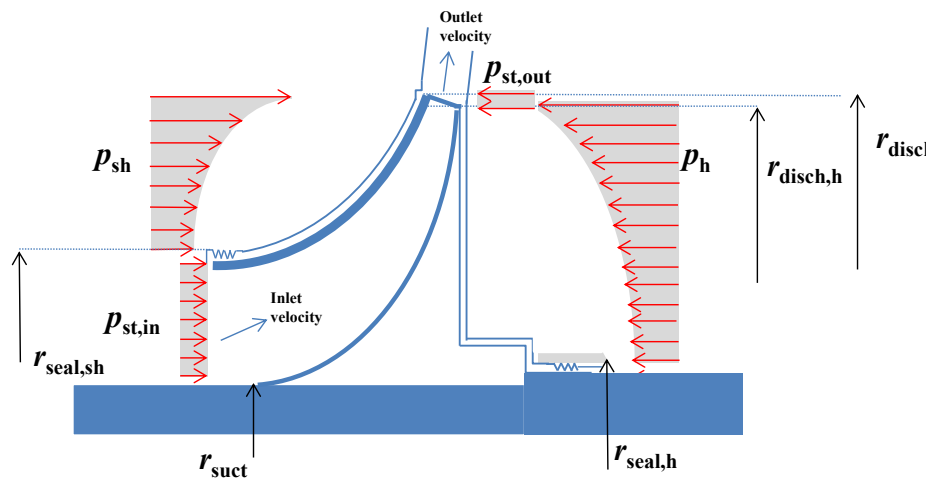


Fig. 6.9 - Force contributions in a single impeller

Once the pressure distribution is calculated with (6.37) at n discretization point along the gaps, the force contribution is given by:

$$F_{sh, h} = \sum_{i=1}^n p(r_i)_{sh, h} A(i)_{sh, h} \quad (6.60)$$

Where $A(i)$ is the area of the annulus between two consecutive discretization points (see Fig. 6.10).

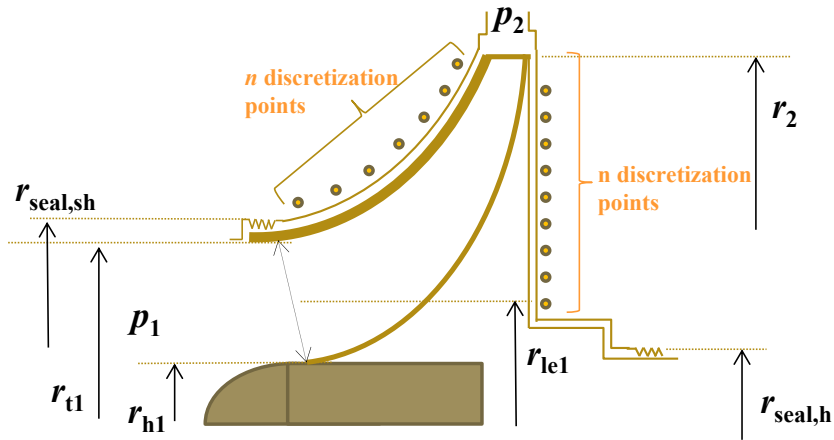


Fig. 6.10 - Qualitative illustration of the discretization points used to calculate the pressure along the gaps

In Fig. 6.11 a simple example of the calculation of the area and the force acting between two adjacent discretization points is presented. In this example only 5 discretization points are shown.

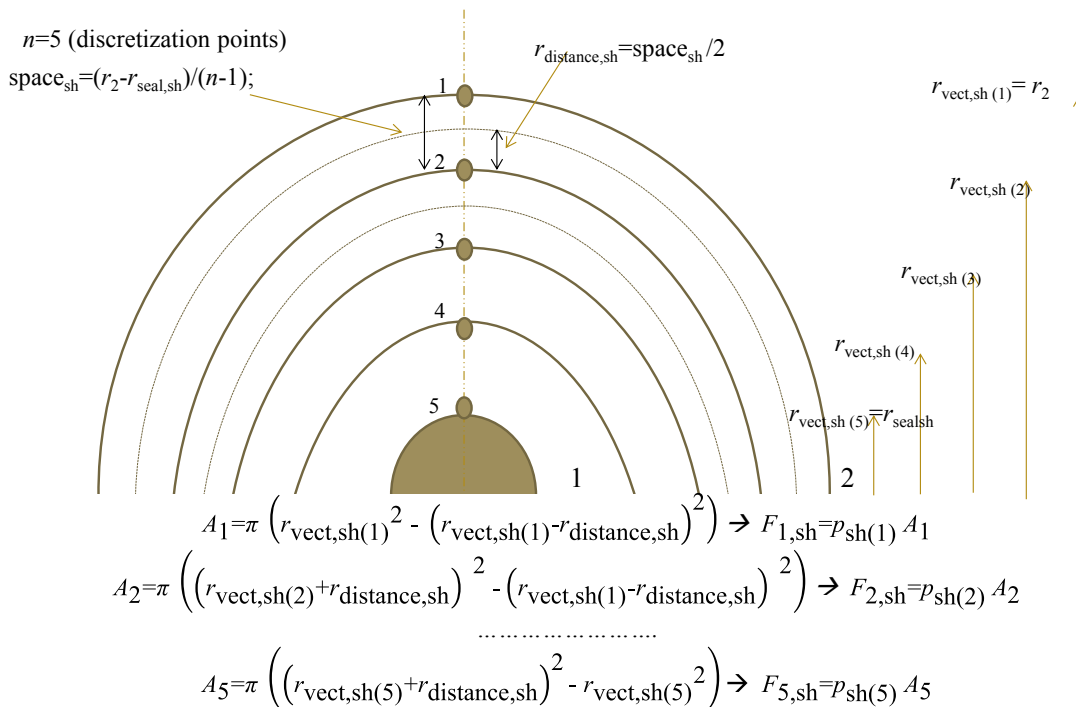


Fig. 6.11 - Example of calculation of the area at each discretization point (shroud cavity)

Another important contribution comes from the static force at the inlet which can be easily obtained as:

$$F_{st, in} = \pi (r_{seal, sh}^2 - r_{suct}^2) p_{suct} \quad (6.61)$$

where p_{suct} , which basically acts between the shroud seal radius and the impeller eye radius, is the static pressure at the impeller suction. A similar consideration can be made for the pressure at the impeller discharge. The variation in axial momentum is also important to evaluate. This contribution can be expressed as:

$$F_{mom} = c_{ax, suct} \dot{m} - c_{ax, disch} \dot{m} \quad (6.62)$$

Finally, the force acting on the balance piston surface needs to be considered. A simple assumption adopted is the uniformity of the pressure distribution on its faces, which are exposed to the discharge pressure and the suction pressure of the impeller. The equation used is:

$$F_{pis} = \frac{\pi}{4} (D_{pis}^2 - D_{seal, h}^2) p_{suct} \quad (6.63)$$

All these formulae allow the determination of the fluid-dynamic axial thrust which develops, in a single impeller, during operation. In case of multistage compressors, the same method needs to be applied to each stage and the overall thrust will be the sum of the axial force of each stage. In order to evaluate the severity of the surge forces, the characteristics of the bearing and the rotor also have to be taken into account.

6.4.2 Mechanical Thrust

The thrust bearing is the component which provides axial positioning for the rotating components and it also withstands axial forces not offset by the balance piston during compressor operation - these forces arise from the change in magnitude of the rotor axial velocity. Therefore, its characteristics have to be contemplated when computing its constraint force in order to evaluate the potential damage caused by a surge event. This force strongly depends on the stiffness, and damping characteristics of the bearing. The first value should be provided by manufacturers whereas the second one is quite hard to estimate (as, in general, for many mechanical systems). Therefore, a suitable modeling layout of a thrust bearing is a mass-spring-damper system on which an external force (i.e. the fluid-dynamic force) is applied, where the mass element is the rotor, i.e. the compressor shaft with the impellers. The system (see

Fig. 6.12 (a)) can be modeled by adopting the bond graphs, as shown in Fig. 6.12 (b). Therefore, the resultant force is given by:

$$F_{rot} = F_{ax,fluid} - F_{el} - F_{damp} \quad (6.64)$$

Where F_{el} and F_{damp} are, respectively, the elastic force and the damping force of the bearing whereas F_{rot} is the force generated by the rotor mass.

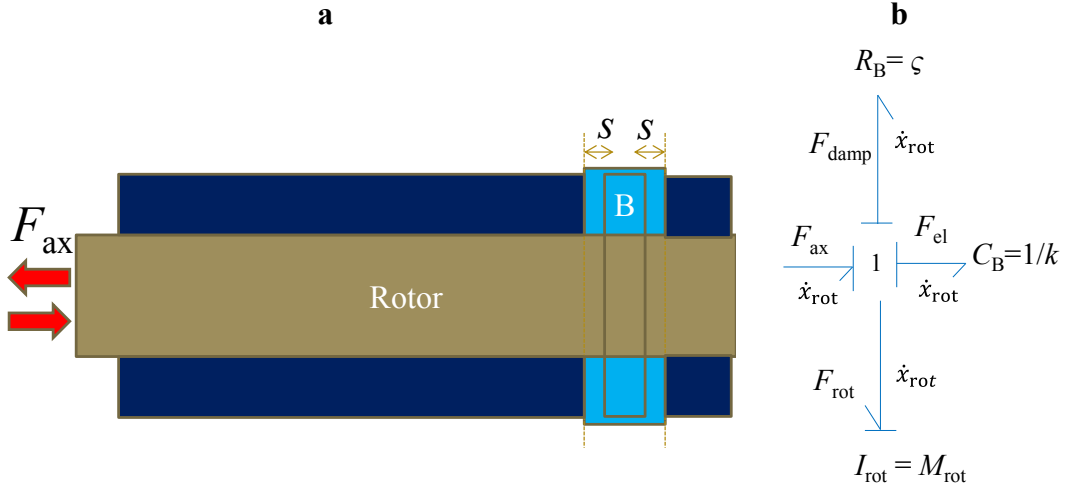


Fig. 6.12 - Bearing system: (a) diagram; (b) bond graph

The acceleration of the rotor can then be found as:

$$\ddot{x}_{rot,ax} = \frac{F_{ax,fluid} - F_{el} - F_{damp}}{M_{rot}} = \frac{F_{ax,fluid} - kx - \zeta\dot{x}}{M_{rot}} \quad (6.65)$$

The above equation provides a fairly good approximation of the net axial thrust acting on the thrust bearing, which is its reaction force, calculated as:

$$F_{ax,B} = -F_{el} - F_{damp} \quad (6.66)$$

6.5 Test Case Application: Two-stage Centrifugal Compressor (SwRI)

The model described in this chapter, was applied to the test bench installed at the Southwest Research Institute. Therefore, also in this case the model reliability was proven by means of a validation with experimental data.

6.5.1 *The Choice of the Test Case*

As mentioned above, this part of the work was carried out in partnership with SwRI and Solar Turbine Inc. Since test facility built at the University of Ferrara (see Chapter 3 and Chapter 4) is not designed to measure the axial forces on the thrust bearing, the implementation of this type of measurements would have required significant changes to many parts of the existing test rig and the data acquisition software and hardware. Therefore, the test case used for tuning and validating this version of the model was a compression piping system test rig located at SwRI. The recorded data were provided by SwRI together with the other required input parameters, such as compressor geometry and maps, and layout of the system.

6.5.2 *The test Rig and the Layout of the Model*

The SwRI piping system layout is shown in Fig. 6.13. It consists of a complex system built to generate surge conditions and then to study the dynamic response of the compressor to rapid transients. The electric motor driven compressor processes the air at ambient conditions and the mass flow is regulated by means of the 6-inch control valve labeled CV001. Additionally a 1-inch manual valve can be opened when needed to allow for finer opening/closing steps of the control valve, thereby providing better control of the compressor's approach to surge.

The compressor is a multistage centrifugal compressor equipped with two radial impellers and two vaneless diffusers. The overall compressor maps are presented in Fig. 6.15, in terms of pressure ratio versus actual volumetric flow, at different rotational speeds (7000, 9000, 10,000, 11,000, 12,000 and 13,000 rpm). The isentropic efficiency curves are not provided but significant values of efficiency are known: the peak is equal to 65 % whereas, during surge, it ranges from 45 % to 50 %.

For this specific application, the model is implemented using the layout illustrated in Fig. 6.14 (a). The intake duct is preceded by an inlet valve, which is useful for providing stability to the model. Obviously, the pressure drops introduced by this element (which is not present in the experimental test loop) is set to infinitesimal by adjusting the valve coefficient.

The compressor downstream of the experimental test loop is evaluated as a plenum with a capacity equal to the volume of the ducts between the compressor and

the CV001 valve (the ducts up to the 1—inch manual valve were also taken into account). The remaining part of the test loop (downstream of the compressor) is basically considered as pressure drops by tuning the outlet valve coefficient.

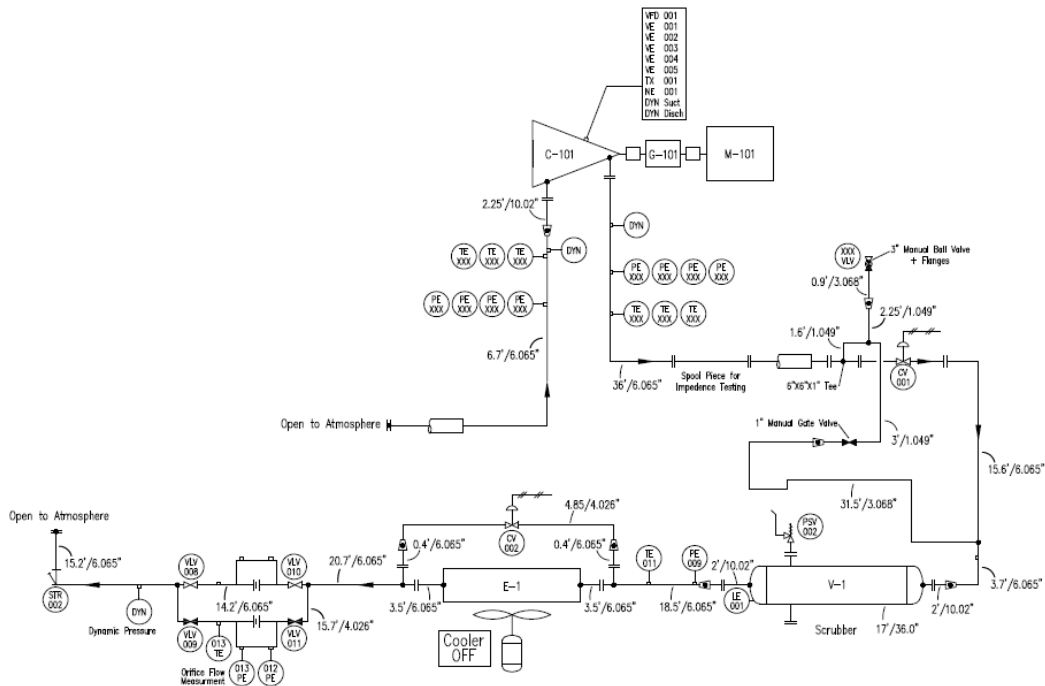


Fig. 6.13 - P&ID of the test rig

Fig. 6.14 (b) illustrates the bond graph of the entire piping system. The overall bond graph simply derives from the connection between the bond graphs of each element selected for the simulation. From this figure it is possible to understand the causal assignment adopted by the model more clearly in order to solve the differential equations and calculate the thermodynamic parameters.

The boundary conditions of the system are the ambient pressure and temperature (the values at which the test was conducted). The simulator was set with an ODE 45 solver with very small step size and tight tolerances in order to give maximum reliability to the results, although partially sacrificing the speed of the simulator. The parameterization of the performance curves was performed as explained in the previous chapter. Fig. 6.16 shows the parametric interpolation curves, as a function of the rotational speed, with reference to the maximum pressure ratio, β_{max} , and the mass flow rate at the peak of the curve, $\dot{m}_{corr, \beta_{max}}$, and at the ideal maximum mass flow rate, $\dot{m}_{corr, max}$. The term “ideal” is used to indicate that this point cannot be achieved by real systems but is only an ideal point which can be found mathematically, with the assumption of quadratic curves.

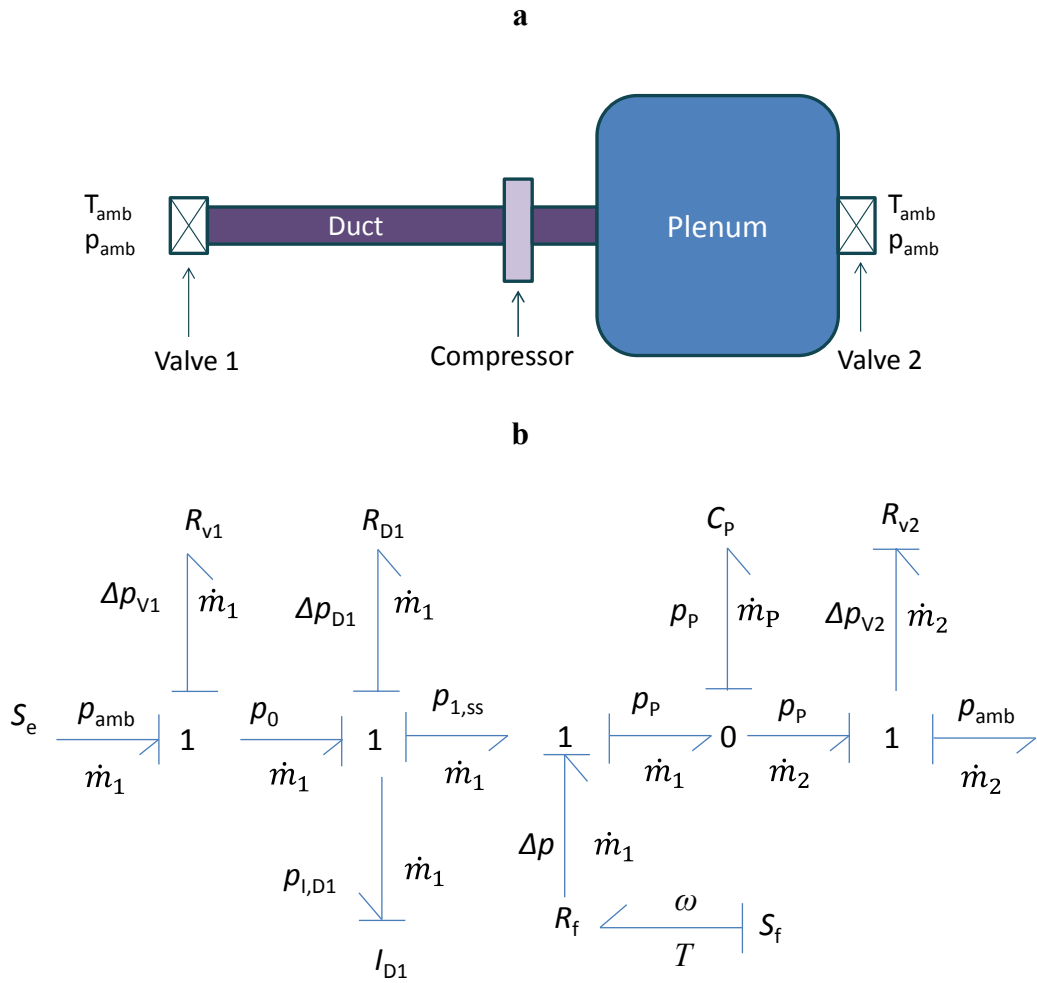


Fig. 6.14 - Layout of the system: (a) graphic representation; (b) bond graph

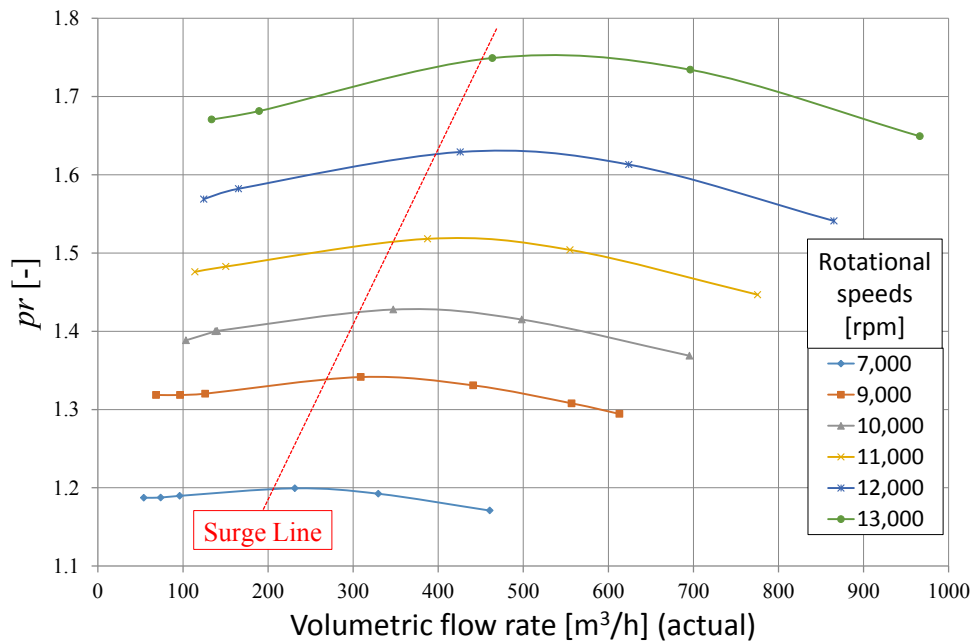


Fig. 6.15 - Steady-state interpolated curve of performance maps: pressure ratio

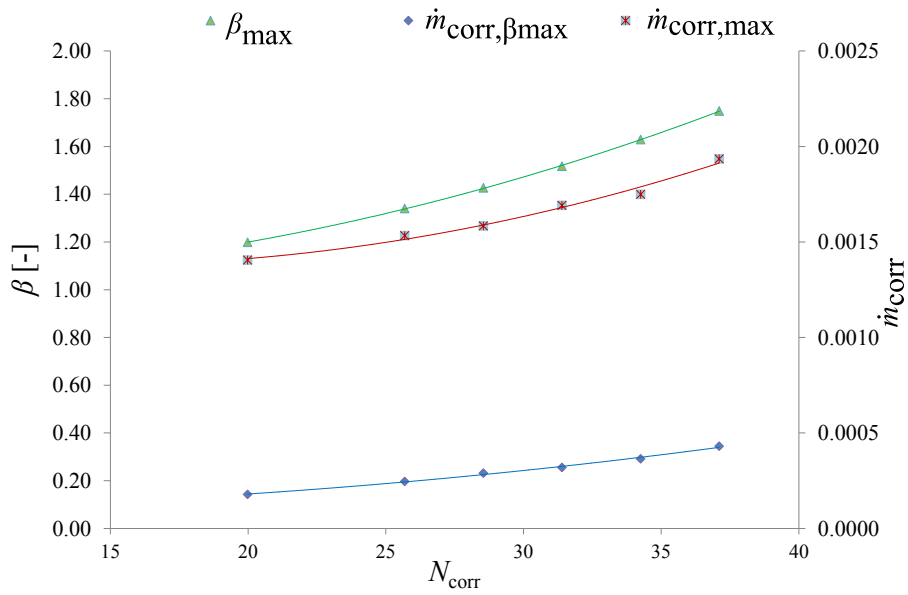


Fig. 6.16 - Parametric procedure: the trend of characteristic parameters of the performance curves

The isentropic efficiency experimental curves were assumed by the significant values provided by SwRI (as mentioned above the complete measurements were not recorded), and the same parametric procedure applied for the pressure ratio curves was carried out.

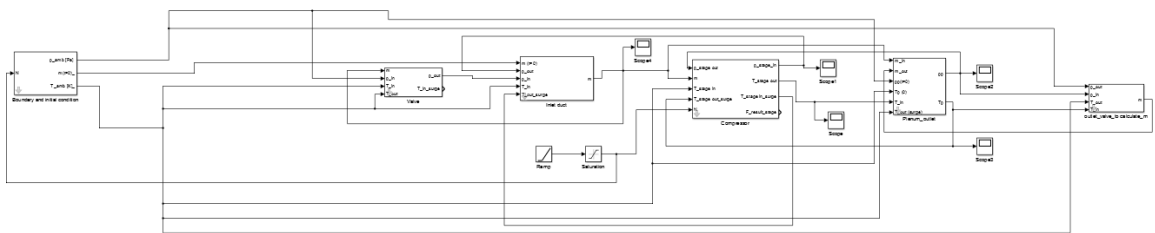


Fig. 6.17 - Simulink diagram of the model applied to the SwRI test case

In Fig. 6.17, the model representation in the Simulink main screen; from left to right: Inlet valve, Inlet duct, compressor, plenum and outlet valve (the terms and names used in Simulink for certain parameters, or elements, may not be the same used in this Thesis).

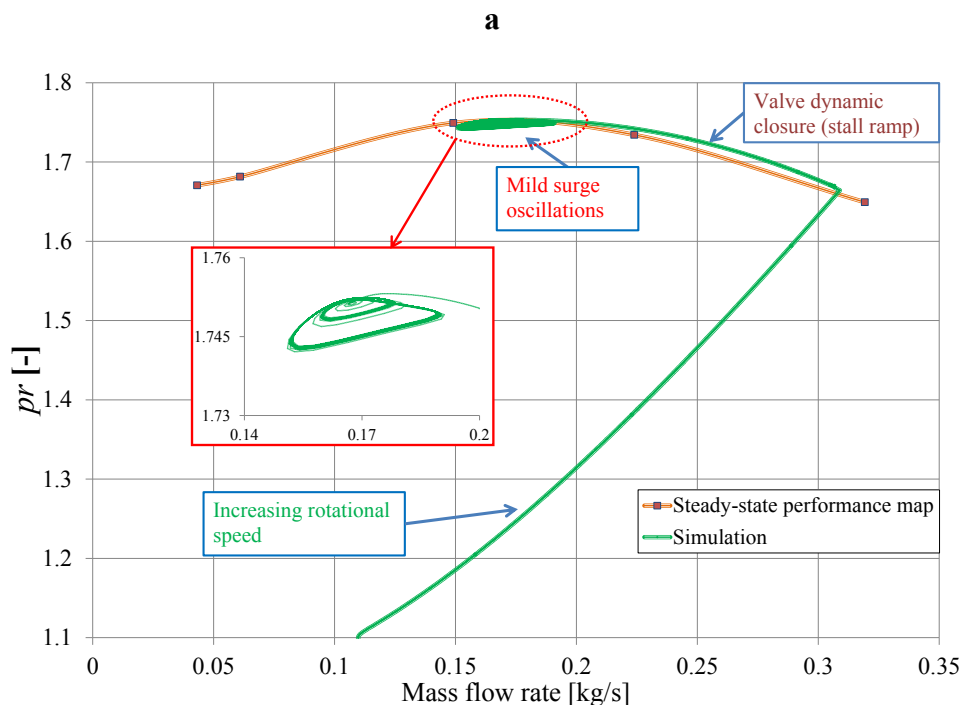
6.6 Validation and Results

The model allows the compressor performance to be simulated at any rotational speed. The validation of the results was carried out by comparing the thermodynamic and force data results, at 13,000 rpm, obtained in the experimental facility and resulting from the model. Some additional relevant plots are also shown in order to demonstrate the reliability and accuracy of the thermodynamic and axial force calculation of the model.

In the model, the compressor achieves the desired speed, through a linear accelerating ramp from an initial value (usually fixed at 5000 rpm). The outlet valve starts to close after a certain amount of time (usually fixed equal to 20 s) by linearly reducing the valve coefficient up to a suitable value to generate mild surge. The results of a typical model simulation, in terms of compressor operating point path and discharge pressure of each impeller, are presented in Fig. 6.18 (a) and Fig. 6.18 (b) respectively.

The characteristic curve resulting from simulation is expressed, in Fig. 6.18 (a), as the pressure ratio versus the mass flow rate. After the initial ramp, from 5000 rpm to 13,000 rpm, the stall ramp obtained by closing the outlet valve can be identified. This curve very clearly resembles the experimental one, verifying the reliability of the model and parametric procedure applied - although the steady-state curve are used as inputs, the agreement with the model may not be obvious and strongly depends on the procedure; in this case the parametric procedure was successful at all rotational speeds. Finally, surge is obtained, with the characteristic mild oscillations of the operating point around the characteristic mild oscillations of the operating point around the characteristic curve peak. The simulation lasts 100 s and the trends of the discharge pressure of the two impellers, in Fig. 6.18 (b), show the typical increase due to the velocity increase in the first 15 s, and due to the closure of the valve between the range 20-29 s. Subsequently, mild surge fluctuations occur during the remaining time of the simulation. Simulations were also carried out at other compressor speeds. The model and thermodynamic results are shown in Tab. 6.1 in which a comparison between model and experimental results of the pressure ratio values at surge onset at the different rotational speeds tested. The consistency of the model is clear from the error column of this table, in which the maximum error is 0.8%. The axial thrust acting in the thrust bearing is calculated by a separate module as a function of the mass of the rotor, the stiffness and the damping effect of the bearing

system. The resultant axial force generated by the compressor at 13,000 rpm, and supported by the bearing, is shown in Fig. 6.19. As can be seen, this simulation lasts only 50 s since this time range is considered enough for the complete development of surge and its dynamic phenomena. The trend of Fig. 6.19 represents the elastic-viscous constrain force of the bearing, $F_{ax,B}$, at 13,000 rpm, in response to the fluid-dynamic thrust and to the rotor mass dynamic force. The first ramp is the result of the increasing of compressor velocity (from 5000 rpm to 13,000 rpm). After about 15 s the desired rotational speed (13,000 rpm) is achieved. Then the valve starts to close, generating the increase in axial force, as expected, and leading the compressor towards surge. In surge the axial force achieves an approximate mean value of 1100 N, showing the typical oscillations which reflect the pressure and mass flow pulsations. Tab. 6.2 reports the main results of the simulator in terms of axial force absolute values, in mild surge conditions at 13,000 rpm. Tab. 6.3 shows a comparison between experimental data and simulation results in terms of averaged and peak-to-peak values and frequency. The percentage error, regarding the average value of force, and peak-to-peak error is around 14 % and 5 %, respectively. Regarding the frequency the percentage error is higher, but the absolute values are very close and can be considered consistent with each other. Moreover, taking into account the complex phenomena under investigation - the difficulty of simulating the same degree of surge generated during tests is very high, especially for mild surge - the simulation results can be considered in good agreement with experimental results.



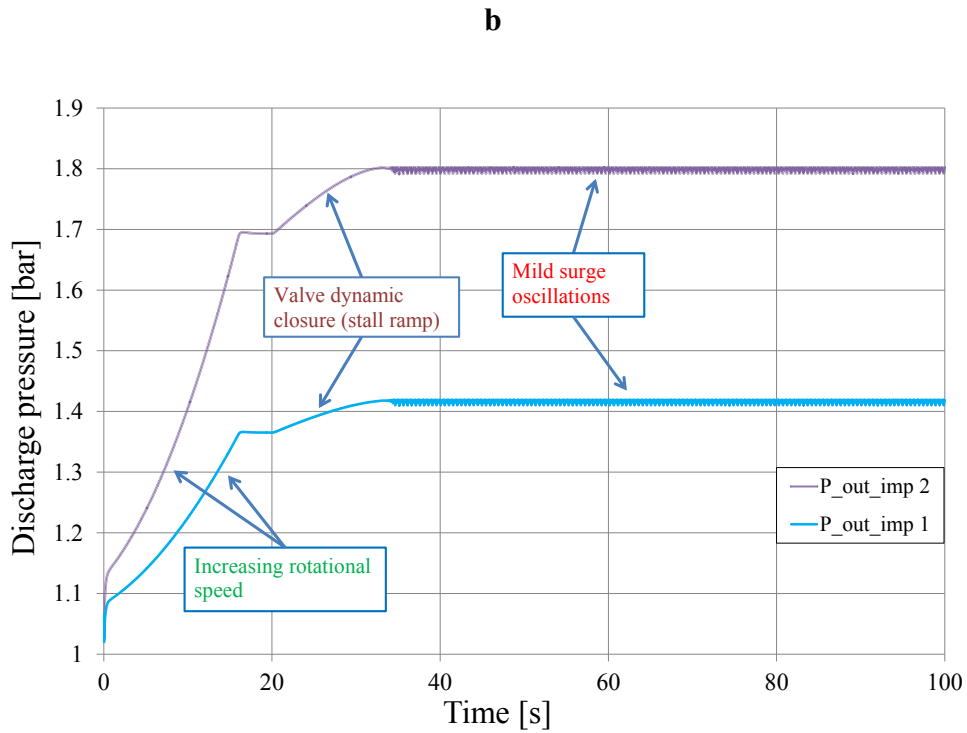


Fig. 6.18 - Model results: (a) operating point path (comparison with steady state experimental curve); (b) discharge pressure of the impellers

Tab. 6.1 - Comparison between experimental and model results: pressure ratio at surge conditions

Rotational speed [rpm]	Pressure ratio @ surge condition (peak of the curve)		
	Model	Test data	Error [%]
7000	1.21	1.2	-0.8 %
9000	1.33	1.34	-0.7 %
10,000	1.42	1.42	-
11,000	1.52	1.51	-0.7 %
12,000	1.63	1.62	-0.6 %
13,000	1.75	1.74	-0.6 %

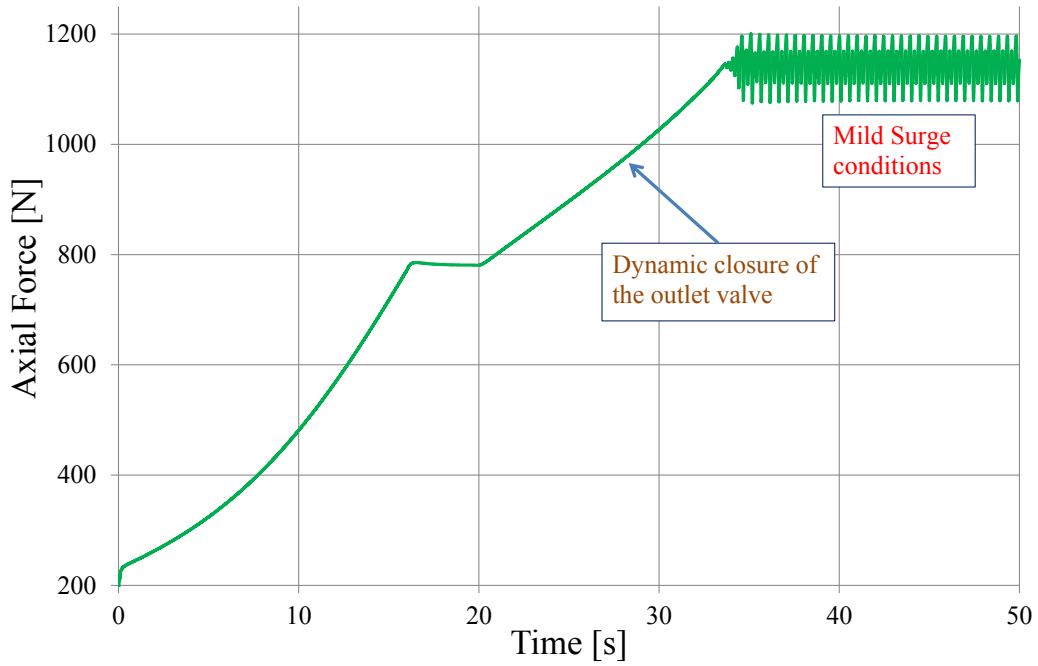


Fig. 6.19 - Model results of the net axial force acting on the bearing at 13,000 rpm

Tab. 6.2 - Simulation results at surge condition

		Axial force peaks [N]	
Mild Surge	max	1197	
	min	1080	

Tab. 6.3 - Comparison between simulations results and test data

		Average axial thrust [N]	Peak-to-peak axial thrust [N]	Frequency[Hz]
Surge @13,00	Simulator	1120	117	4
	Test Data	980	111	2.5
Percentage Error		~14 %	~5 %	~60 %

Fig. 6.20 presents an additional exhaustive comparison of the axial force at 13,000 rpm. It is clear how the model is capable of predicting not only the average magnitude of the axial forces with considerable accuracy, but also the axial force oscillations. This fact is evident in surge and in no-surge conditions too. In this latter case the recorded data showed tiny fluctuations which could also be due to an unstable measurement signal. Obviously, the model cannot predict these small oscillations since the implemented code does not consider any unstable phenomena until the compressor operating point goes beyond the characteristic curve peak. However, the average value of the force is close to the experimental measurements. Hence, the validation demonstrates the reliability of the model for centrifugal compressors dynamic modeling working in any given piping system.

Since a validation at only one rotational speed is not sufficient to decide on the reliability of the model, the values of the axial force at the other rotational speeds were also analyzed. The evidence of the reliability of the model can be found in Fig. 6.21. Fig. 6.21 (a) shows the results, in terms of peak-to-peak forces during surge, $F_{\text{peak-to-peak}}$, obtained by the experimental tests and by the model, at different rotational speeds. It is clear that the magnitude of the results obtained by the model is highly consistent with that of the recorded data.

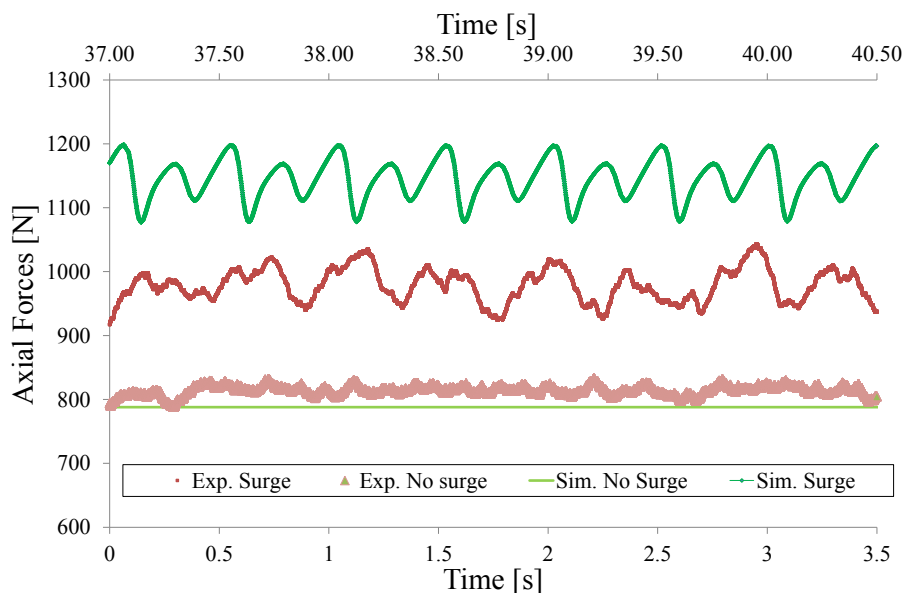
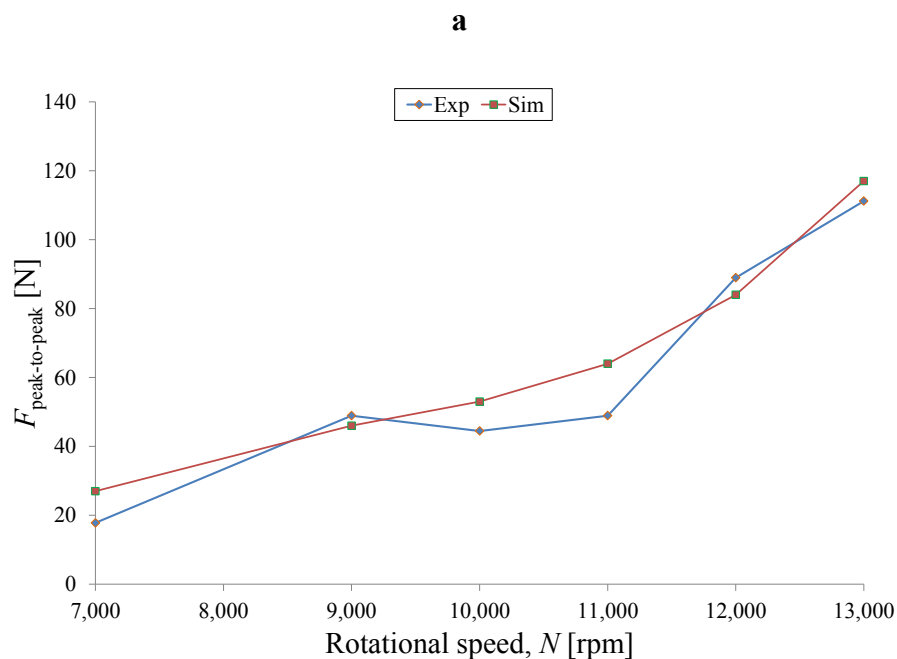


Fig. 6.20 - Validation of the model: comparison of the axial force results at 13,000 rpm in surge and non surge conditions

The model is less precise at a specific range of rotational speeds, 10,000-11,000 rpm, where the comparison shows a divergence of the results, although the absolute

value of this difference is not significant (the dissimilarity is tiny, thus it is not dangerous when evaluating the load on a thrust bearing). This slight disagreement is due to a particular phenomenon, observed during the experimental tests, related to the measured axial force fluctuations. In fact, similar results were experimentally recorded at 9,000, 10,000 and 11,000 rpm, contrary to what could theoretically be expected (a rising axial force peak-to-peak was expected, by increasing the rotational speed). These experimental results can be explained by the non-homogeneous degree of surge obtained at the different rotational speeds, due to the degree of closure of the valve. A proportional closure of the valve should be applied, at the different rotational speeds, in order to obtain the same degree of surge. Since, in this case the same valve closure was applied at 9,000, 10,000 and 11,000 it is difficult to exactly obtain the same values of the model.

Similarly, Fig. 6.21 (b) shows the surge frequency of the axial force recorded during tests and simulations, at the different rotational speeds. It is clear that the qualitative nature of the simulation results agrees with the experimental one. However, the absolute frequency values calculated by the model are always higher than those recorded in the test case. This can be justified by several factors: (i) the small volume of the test rig piping system, (ii) the model sketch chosen by the authors; and (iii) the high unpredictability of mild surge; and (iv) the difficulty of the axial force frequency experimental evaluation.



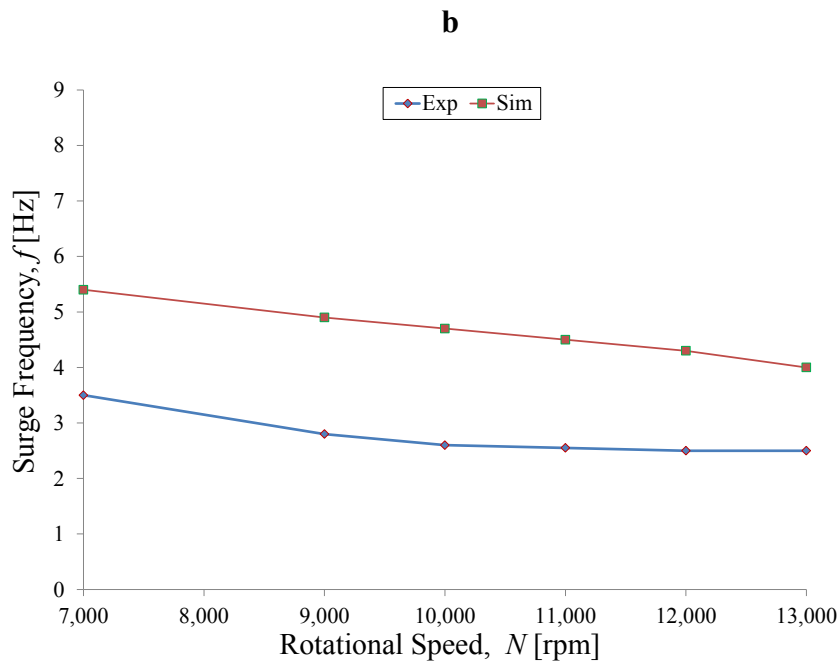


Fig. 6.21 – Validation of the model: peak-to-peak forces (a); surge frequency (b)

In fact, the model struggles to identify the correct frequency when the imposed downstream volume is small, whereas it is quite precise if the size of the downstream piping system is larger; which is clear from looking at the validation shown in the previous chapter ($V_p = 1.5 \text{ m}^3$). Moreover, the sketch used for this piping system, does not consider the effect of the duct inertia at the compressor downstream but only the capacitance effect (the chosen layout provides a plenum immediately after the compressor, and after the plenum a downstream valve). This implies that the simulator tends to calculate a frequency higher than that recorded, especially with small imposed downstream volumes. In addition, the experimental measurement of axial force vibration frequency may be subject to a certain level of uncertainty due to the electrical noise, the filtration of data, and the correct positioning of the load cells (incorrect positioning could result in misinterpretation of the carrier frequency).

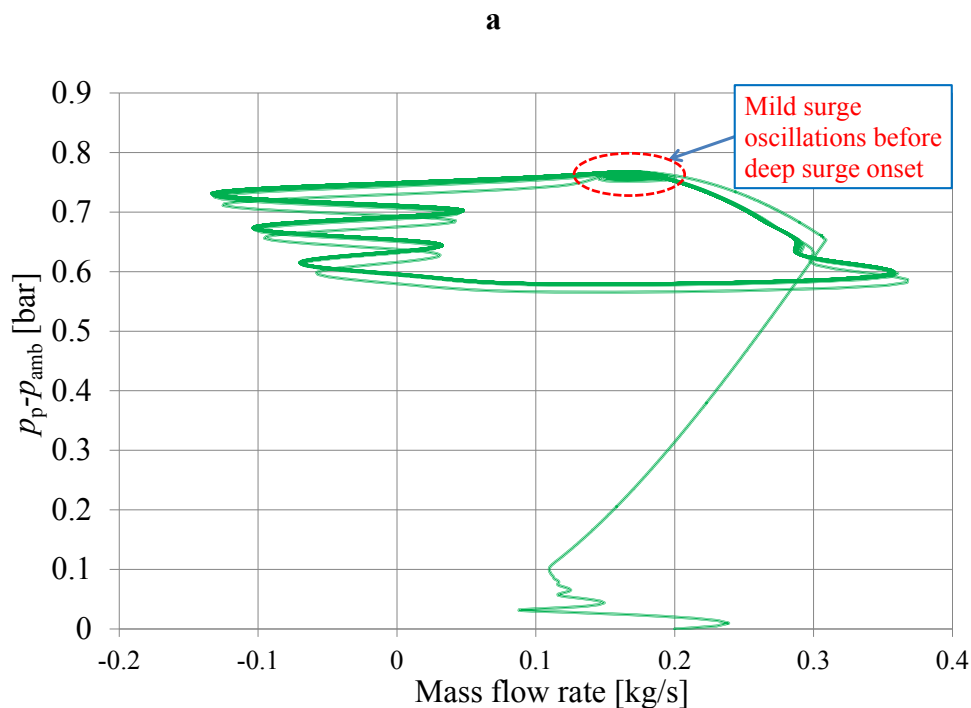
6.6.1 Deep Surge

This paragraph shows interesting model results regarding deep surge conditions. This instability is obtained by further reducing the mass flow rate in the model. Fig. 6.22 (a) shows the dynamic compressor characteristic curve in terms of differential pressure $p_{\text{amb}} - p_p$ (since it provides the clearest representation of the deep surge cycle) during the deep surge process, whereas in Fig. 6.22 (b) the axial force oscillations are shown. It is evident that mild surge arises as a first instability and then

a transition to deep surge occurs. These results cannot be compared to recorded data since such test might severely damage the compressor, however the thermodynamic results (Fig. 6.22 (a)) are quite reliable since a validation of the preliminary and simplified version of this model was carried out in the previous chapter of this Thesis. The force results generated in deep surge cannot be validated, but they seem highly consistent with what is expected to occur - in deep surge the amplitudes of the forces increase while the frequency decreases - see Fig. 6.22 (b) (future work will focus on this theme).

6.6.2 Sensitivity Analysis

In order to understand more clearly which parameters affect surge severity the most, in terms of axial forces acting on the thrust bearing, a sensitivity analysis was carried out. The analysis focuses on the bearing stiffness k , the rotor mass M_{rot} , and the compressor downstream volume V_p . The aim is to evaluate the potential effect of these quantities on $F_{peak,max}$, $F_{peak,min}$ and $F_{peak-to-peak}$, respectively the maximum, minimum and peak-to-peak values of the force. Obviously, also the rotational speed N of the compressor (not presented in this analysis) during operation plays a very important role due to the pressure ratio and impeller work that characterize the compressor when the peak of the curve is achieved, i.e. before surge.



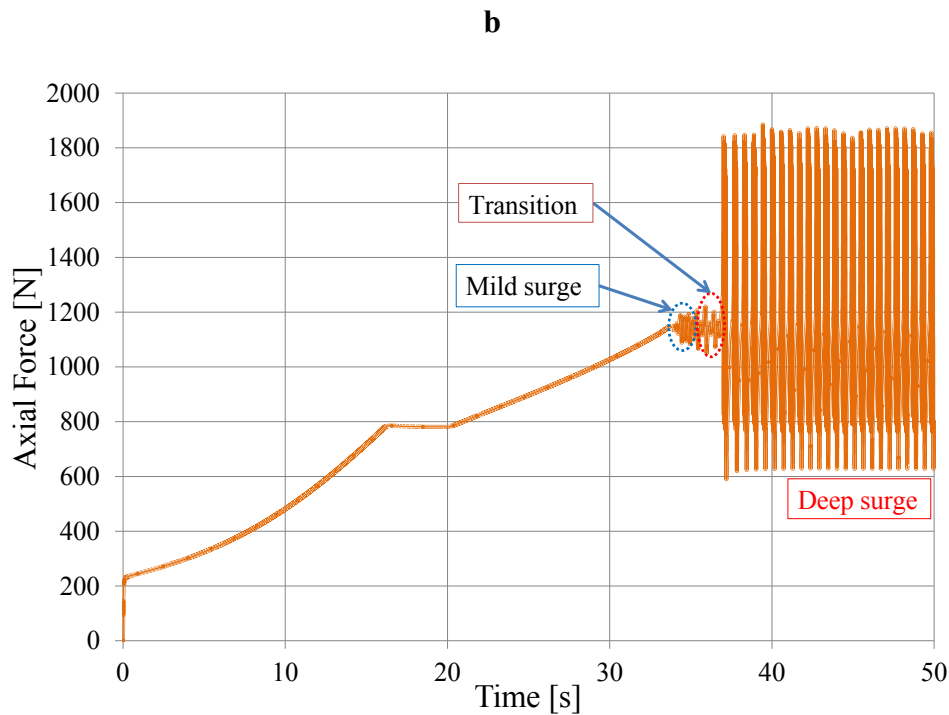


Fig. 6.22 - Deep surge simulation @13,000 rpm: compressor characteristic curve (a) and net axial force $F_{ax,B}$ (b)

Another very significant parameter which affects the calculation of the forces, is the radius of the impellers r_{disch} . Regarding this parameter, it is difficult to analyze its effect only by varying it in the model as an independent parameter, since it would affect the compressor performance curve, thus the values of pressure ratio and work. In Fig. 6.23 the peak-to-peak values of the net axial force are plotted, alongside the maximum and minimum peaks, against the volume between the compressor and the control valve. It is clear that the increase in volume affects the magnitude of the force since it changes the degree of the surge (this consideration is simplistic since in a certain range of volumes, the type of surge, and thus the forces generated, strongly depends on the throttling area of the valve). This is testified by the increase in the maximum peak and peak-to-peak values with the volume, and the decrease in the minimum peak values. This trend continues until a certain volume, which is the dimension that generates the maximum surge cycle, after which the force values remain similar.

Fig. 6.24 shows the influence of the stiffness, k , of the bearing by keeping the clearance constant. The results refer to a 1 m^3 downstream volume so that deep surge is achieved. It can be stated that the higher the stiffness, the less dangerous the surge, for the thrust bearing. The decrease in k results in an approximately constant trend of $F_{peak,max}$ and $F_{peak-to-peak}$ until about $30 \cdot 10^6 \text{ N/m}$. However, by further diminishing k ,

these values decrease; which would mean that in that region, i.e. for lower values of k , the stresses are minimized. This fact can be misleading because, by reducing k , the maximum elastic force, $F_{el,max}$, of the bearing also goes down, and this increases the danger of plastic deformation, and subsequent destruction of the bearing. On the other hand, a bearing with a high level of stiffness could generate and transmit vibrations to the mechanical and aerodynamic components; which is not desirable in any application. Fig. 6.25 illustrates the effect of the rotor mass on the axial force oscillations acting on the bearing. Also in this case the results refer to a 1 m^3 downstream volume. The mass of the rotor was seen to have an important influence in surge conditions. In fact, the increase in mass leads to an increase in force amplitudes. This phenomenon was not observed when analyzing smaller oscillations (mild surge) since those fluctuations are more rapid, in terms of frequency, and less strong in terms of amplitudes. Therefore, in mild surge conditions, the mass of the rotor did not exhibit any substantial influence the loads acting on the bearing. In fact, the higher the amplitude of the fluid-dynamic force, the more significant the acceleration of the mass. Considering that (i) a general force is given by mass multiplied by acceleration, (ii) usually, a higher mass is subject to lower acceleration (especially in this particular case), and (iii) the influence of the acceleration on the resultant force is generally lower than that of the mass; it is feasible to state that the higher the mass, the more this mass affects the force produced by the rotor movement (in the axial direction).

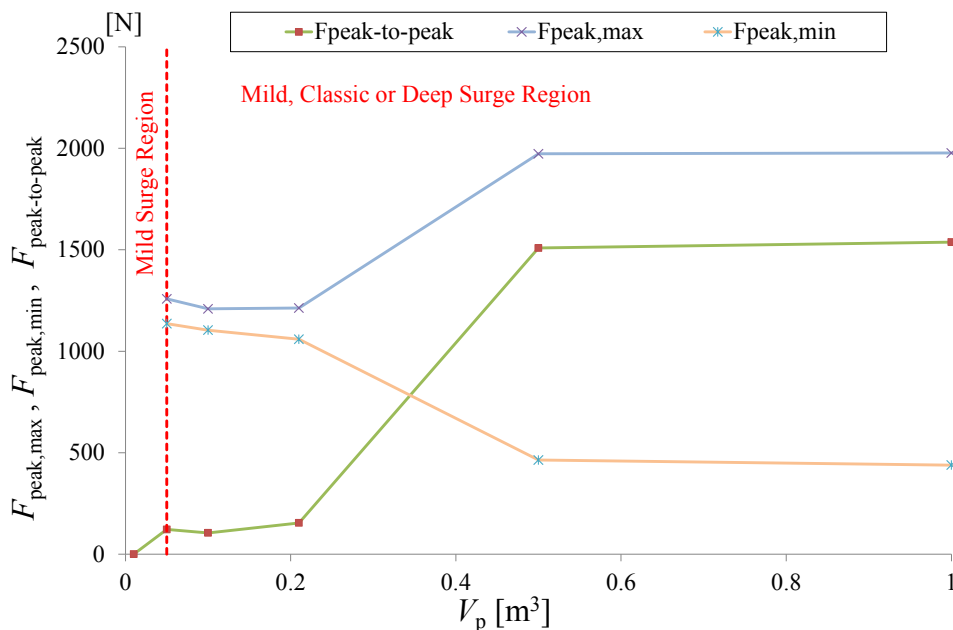


Fig. 6.23 - Influence of the compressor downstream volume on the axial force

This fact implies that if the rotor is moved by the fluid-dynamic thrust generated on the impellers, the higher the rotor mass, the higher the maximum peak and the peak-to-peak values. On the other hand it could signify a high moment of inertia and thus an advantage in case of emergency shutdown, since the rotor would slow down very gently, limiting the inception of surge.

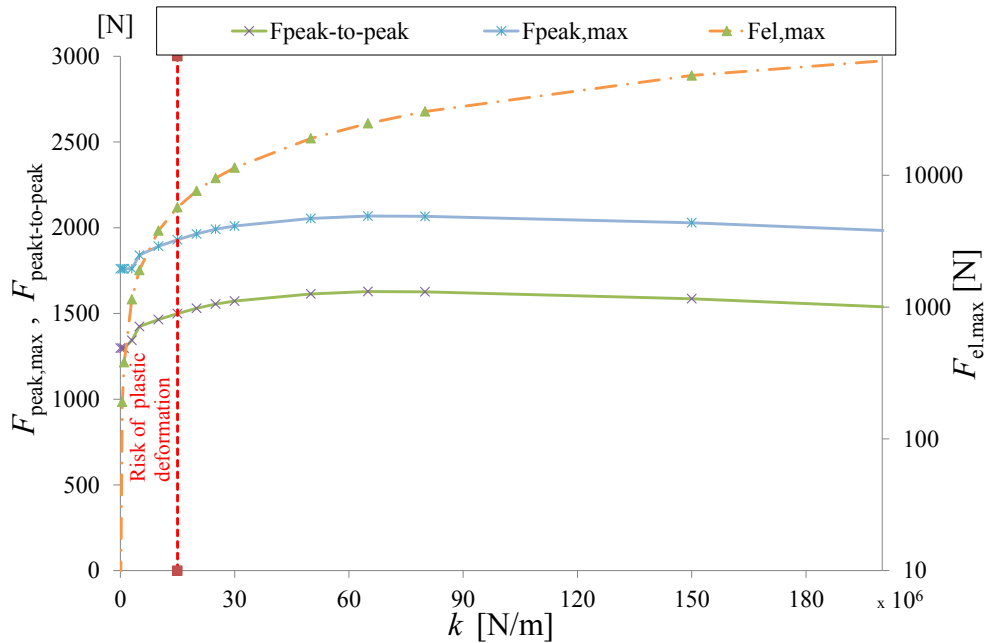


Fig. 6.24 - Influence of the bearing stiffness on the axial force

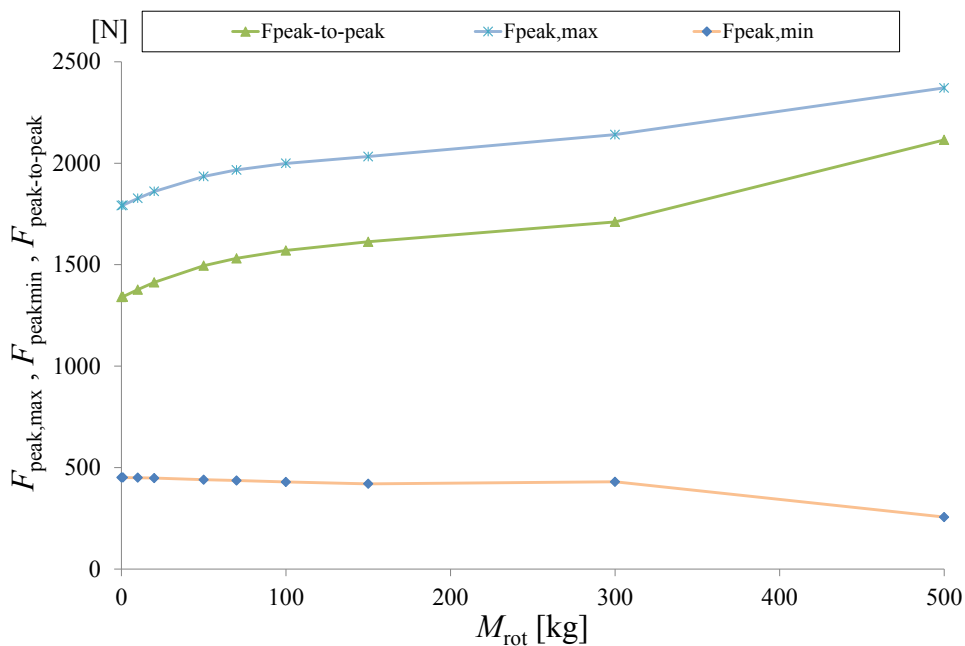


Fig. 6.25 - Influence of the rotor mass on the axial forces

6.7 Conclusions

In this chapter a model for the prediction of the dynamic behavior of a compressor, in particular during surge is proposed. This model is based on the bond graph approach which allows a modular structure and can be applied to many engineering systems.

The study of the axial force focuses on the main contributions given in a single impeller so that the model can also be applied to multistage compressors. The simulator can manage several types of gas and mixture making it suitable for oil and gas applications.

The model was applied to the SwRI test case by implementing the compressor curves and the geometric dimensions alongside the layout of the piping system. A comparison between the experimental data and the simulator response, at a rotational speed of 13000 rpm, was carried out, demonstrating the high accuracy of the model (and its modular structure), which has proved to be strongly successful in simulating surge. In fact, the dynamic characteristic curve obtained by the model successfully resembles the real steady-state curve of the compressor and the surge, in this case mild surge, appears immediately after the characteristic curve peak. Moreover, the simulated trend of the axial force on the thrust bearing was shown to be highly compatible with the experimental data acquired in surge conditions. Additional comparisons with experimental data were carried out at the other rotational speeds tested. The validation showed that the model succeeds in determining values of surge frequency and axial thrust values, very close to the ones recorded during testing.

A deep surge condition scenario predicted by the model is also reported. The simulation showed the high increase of the surge cycle, which generates a significant increase in axial thrust oscillations. This analysis of the deep surge condition could not be validated since running the compressor in deep surge would likely damage the compressor itself and its components. However, the preliminary version of this model (developed in the previous chapter) was shown to be highly reliable in simulating the thermodynamic of deep surge.

A sensitivity analysis demonstrated that the increase in downstream volume led to an increase in axial stresses on the bearing during surge. This effect is valid up to a

definite value of the volume, which can be identified as the volume that causes the maximum surge cycle.

Moreover, the value of the bearing stiffness was confirmed to be a fundamental factor to be taken into account. The surge severity was shown to decrease with the increase in stiffness despite the consequent rise in vibrations.

As a general rule it can also be stated that, the higher the rotor mass, the higher the axial force peaks are. This effect was clear in deep surge conditions, due to higher pressure fluctuations and their frequency, which allowed greater movement in the axial direction of the mass, thus generating a higher bearing reaction force.

Further discussion is required on the subject of fatigue, which is not covered in this work.

This model can be then considered a powerful instrument for simulating the thermodynamic behavior of the compressor and predicting the axial thrust which acts on the thrust bearing in stonewall, surge, but also in generic transients. This is a precious contribution, especially to industry since it increases the understanding of the fatigue forces acting on the bearing, in order to predict and prevent maintenance, or repairs, but also for providing additional guidelines for the correct selection, or design, of the thrust bearing.

Despite the great strength of the model presented in this Thesis, some improvements are still needed to overcome its current limits. The next step of the research will be the accurate calculation of the core rotation factor along the gaps, in order to make the model suitable also for high pressure compressors too.

7 Final Remarks and Recommendations

This Thesis had the aim of studying unstable compressor behavior under stall and surge conditions. The investigation was done by experimentally testing (i) a turboshaft axial-centrifugal compressor, at the Engineering Department of the University of Ferrara, in order to evaluate its thermodynamic performance, and (ii) a two-stage centrifugal compressor, at the SwRI test facility, to identify the axial force acting on the thrust bearing, in particular during surge cycles. By using the test data, a model was developed in two different steps. A first version, dedicated to simple thermodynamics, was realized to simulate the typical surge pressure, temperature and mass flow rate oscillation, whereas a second more advanced version (thermodynamic equations were added and more accuracy was given to the model) was done to calculate the axial net thrust of the bearing, based on the experimental results.

7.1 Summary of the Results

Experimental study of stall and surge

An intense activity was performed in order to design and build the new test-rig. Many new components were designed and added to achieve a suitable system structure and configuration. A new transmission line was created by modifying the original epicyclic gearbox of the turboshaft engine; the resulting overall gear ratio was 17.26. An in-house developed lubricating system was created to ensure the correct functionality of the compressor and its gearbox. Moreover, the piping system was thought to be modular so that two different configurations could be obtained, depending on the type of tests to be done. Basically a small downstream volume allowed the study of steady-state, static instability and stall characteristics, whereas a large downstream volume allowed the study of surge, its inception process and characteristics.

In order to collect the data and control the system during test, an efficient data acquisition and control system was developed and implemented in LabVIEW; which

allowed them to regulate the sampling frequency and adopt two hardware modules, one dedicated to the high-frequency data, and another to the low-frequency data.

One of the themes that emerged from the experimental analysis on the axial-centrifugal compressor was the possibility of correctly detecting both steady-state characteristics and stall and surge phenomena. Firstly, steady-state tests were carried out to determine the characteristic curve of the compressor and the point of static instability at different rotational speeds (5000, 10,000, 15,000, 20,000 and 25,000 rpm). Afterwards, stall and surge were analyzed. The following list summarizes the main results (of this work):

- According to many works of literature, the piping system configuration affects the type of instability which arises and the point at which instability is achieved, in radial and axial compressors. Thus, this can be considered valid also for axial-centrifugal compressors.
- Static instability was detected by the sudden drop in β_0 when flow breakdown occurred.
- Deep surge was achieved once the operating point passed the surge line (obtained by connecting the peak points of the curves at the different rotational speeds). At each surge cycle, the compressor has experienced stall and surge alternatively. This phenomenon was noticed by analyzing the operating point path during surge process.
- The surge frequency decreased by increasing the compressor rotational speed; but the amplitude of the surge oscillations increased. This demonstrates that surge process has characteristics which depend on the type of compressor and its operating point. Therefore, different degrees of surge can arise and they can be determined by the magnitude of the fluctuation (amplitude and frequency).
- A hysteresis effect was highlighted during surge recovery; which delayed the compressor in reaching stable conditions. The extension of the hysteresis could be determined by the degree of surge generated.
- A stall cell was identified at the first stages of the compressor, even with the valve completely open. This was due to the destabilizing effect of the axial

compressor (the bleed valve was removed to position temperature and pressure sensors throughout the tests). The compressor operated with a stall cell rotating at 13 % of the rotor speed (at 10,000 rpm). This cell appeared to grow when the compressor was approaching surge. During the surge process the cell was still present but with reduced amplitude, which testified once again the alternate presence of stall and surge during surge process.

In a second round of investigations, four accelerometers and two microphones were used to acquire and analyze vibro-acoustic measurements. In this case, more combinations of tests were carried out but with the same two configuration layouts of the systems. An additional and dedicated acquisition system was used for these vibrational and acoustic measurements. A novel methodology, namely cyclostationary analysis, was introduced and used for analyzing stall and surge experimental data obtained from accelerometers and microphones. The analysis of cyclic frequencies was carried out at the different rotational speeds (showing analogous results). Considering the main results at 10,000 rpm as representative, it was found that:

- Surge could easily be identified in both configurations (in Layout #1 surge was more similar to static instability due to its high frequency). This was not surprising since a macroscopic phenomenon such as deep surge is expected to be well detected even with accelerometers and microphones.
- The presence of two stall cells (one rotating at 20 Hz and another at 49 Hz) was found. The stall cell at 20 Hz (around 13 % of rotor speed), is compatible with the stall cells identified by thermodynamic measurements at the first stages of the compressor. The stall cell at 49 Hz is located in the successive stages of the compressor.
- The surge precursor (i.e. the evolution of the stall cells) could be detected as well. The acceleration signals, by means of the cyclostationary analysis, proved to perceive the growth of the stall cells and their mutation into a bigger cell before surge, as in Layout #1. In layout #2 this evolution was less evident due to the influence of the piping system geometry, which affected the dynamic behavior of the compressor and its point of instability.

It was then demonstrated that even with non-intrusive sensors, coupled with the cyclostationary analysis (which is a very novel technique in this context), complex fluid-

dynamic instability phenomena such as, stall and surge can be studied, which is highly relevant in order to avoid any fluid-dynamic disturbance.

Modeling of surge and axial forces during surge process

A lumped parameter model was developed in Matlab/Simulink environment by adopting the bond graph approach. This is a novel technique in the context of compressor surge analysis since only a few authors have used it and proved its reliability in the past. The model took into consideration the fundamental components of a compression piping system (valves, ducts, plenums and compressors) and the aim was to simulate the dynamic behavior of the compressor, especially during surge.

The model was thought to be as modular as possible and able to simulate any simple piping system. For this reason, each abovementioned element is modeled as an independent module. The compressor maps, experimentally obtained at the engineering department (the compressor was the abovementioned axial-centrifugal compressor) were implemented into the compressor module by means of a parametric procedure. The model was accurately tuned and simulations, at various rotational speeds, were executed. Taking the model results at 15,000 rpm as representative, the outcome showed that:

- The model offered a realistic simulation of what actually occurred during a deep surge. This was noticed by comparing the surge cycle described by the operating point.
- The prediction of the pressure and mass flow rate oscillations was consistent with the recorded data: a maximum error of 0.009 bar was found regarding the pressure oscillation amplitude, whereas a negligible difference in frequency was found (0.004 Hz).

Therefore, despite its simplicity and low computational cost, the model showed that it was highly useful and robust (in terms of accuracy); which is relevant due to its potential use in industrial applications.

The model was successively improved in order to simulate a two-stage centrifugal compressor installed at the experimental test facility of SwRI. This second and improved version of the model was developed with the aim of predicting the axial surge forces on the thrust bearing. The previous version the model was improved by enhancing the parametric implementation of the compressor curves (the compressor steady-state curves were

provided by SwRI), adopting more accurate calculations for the unstable operation range of the compressor, and a more modular model structure (an additional downstream valve module was created). Moreover, in order to make the model user-friendly, a specific Excel file was created in which all the system and compressor inputs are inserted. These inputs can be easily modified in Simulink environment as well by means of a specific mask, generated for each module. As in the previous version of the model, the compressor module represented a single stage of a multistage compressor or the overall compressor. The compressor module was also extensively modified to include two different compressor behaviors after approaching the surge line: a sudden drop/rise or the cubic law.

The simulator outcomes were compared with the experimental data provided by SwRI. The simulations reflected the actual behavior of the compressor during surge and the axial force prediction methodology showed to be highly reliable, once the model was properly tuned. Validation was carried out at the different experimentally tested rotational speeds (7000, 9000, 10,000, 11,000, 12,000 and 13,000 rpm) demonstrating that:

- The simulated compressor characteristic curve well resembled the actual experimental one at the different rotational speeds. This was demonstrated by analyzing the operating path at 13,000 rpm and by means of the pressure ratio values at the different curve peaks (a maximum error of 0.8 % was registered).
- Mild surge was simulated and the results of the axial forces in terms of amplitude and frequency were very consistent with the experimental ones. The axial force peak-to-peak values resulted close to the recorded data; especially for higher rotational speeds (a maximum error of 6 N was found). At a specific range of rotational speeds the difference is greater than at the other regimes (the maximum error is 15 N at 11,000 rpm). This is probably due to the different generated degree of surge (which strongly depends, especially in mild surge conditions, on the degree of closure of the valve).
- The predicted frequency showed higher values than those recorded. This could be due to the inherently difficulty of the model has in computing the results with very small volumes, or to the model scheme used for this piping system (only a plenum, without a downstream duct, was considered after the compressor) and to the difficulty of experimentally evaluating this parameter with good accuracy. However the trend of the measured and

predicted frequency at the different rotational speed are qualitative consistent. Moreover, since the surge is a low-frequency phenomenon which is expected to last only a few seconds before the anti-surge control intervenes, an extremely correct evaluation of the frequency is not crucial.

- Axial force and compressor thermodynamics in deep surge conditions were simulated. The results showed highly credible trends and values; in particular, the surge cycle became higher resulting in cyclic reverse flow and higher axial thrust on the bearing.

A sensitivity analysis was carried out by varying a significant piping system factor (plenum volume) and mechanical parameters (the rotor mass, the stiffness and the axial clearance of the bearing). It was found that:

- The axial forces increase with the increase in plenum volume. This was verified up to a maximum limit, i.e. the volume which generated the maximum deep surge cycle.
- The severity of the surge event decreased by increasing the bearing axial stiffness.
- In deep surge conditions, higher axial forces were generated by higher values of rotor mass.

The final version of the model exhibited a significant reliability in predicting complex parameters such as the surge axial forces, in addition to the thermodynamic parameters of the compressor during surge. Therefore, its reliability and its potential contribute to the oil and gas industry was demonstrated, offering a solid base for future efforts regarding the evaluation of thrust bearing damage during surge.

7.2 Future Directions

The comprehension of compressor instability phenomena is still a challenge in the turbomachinery sector. An improvement of this knowledge could offer a better insight into the effect that these phenomena can cause, in terms of performance and damage. Unfortunately, the research did not yet establish a unique way to analyze this problem and, as a consequence, the results offered by many researchers were sometimes conflicted.

Since experimental analyses are fundamental and the accuracy of the used methodology is crucial, a universal and recognized instrumentation and technique would surely reduce this potential non-homogeneity. For this reason, the choice of the proper instrumentation, data acquisition and data analysis technique play a fundamental role.

The present work offers a solid basis for future investigation on stall and surge thanks to the demonstrated reliability of the test rig, the measurements and the coherence of the results. However, the fact that relevant results were obtained by testing only one compressor it is not sufficient to undoubtedly declare the universal effectiveness of the adopted methodology. This is the motivation for undertaking further investigations on new and different types of compressors (single stage, multistage, axial and centrifugal type). Moreover, another field in which research is becoming important is the study of stall and surge under wet compression conditions to evaluate the performance benefit or disadvantages of these operational conditions. The future efforts of this project aim in this direction.

The experimental investigations are fundamental because, nowadays, it is still impossible to predict how the compressor will stall (stalling mechanism) and exactly what its behavior in surge will be (in terms of operating point path) before these phenomena occur. For example: will the compressor intermittently go into stall during the surge process? Currently, the answer is known only after having observed the compressor in stall, and in surge. For this reason, many researchers are trying to develop and improve the existing models with the aim of getting closer to a universal method for evaluating the instability of compressors. Also in this context, the perspective work of this project aims to (i) implement a code in the model for simulating rotating stall, (ii) improve the calculation and prediction of the axial forces, and subsequently (iii) evaluate a strategy to establish if a compressor require inspection and/or maintenance after an instability phenomenon has occurred.

List of Symbols

Normal letters

A	area, flow-through area
a	speed of sound
B	dimensionless number described in eq (1), blockage
b	impeller suction and discharge width
C	compliance
C_d	blockage coefficient
C_{fc}	core rotation factor
C_p	specific heat (constant pressure)
C_v	specific heat (constant volume)
c	number of acquisition channels
D	diameter
E	energy
e	effort variable, energy per unit mass
F	force
f	frequency, spectral frequency, skin friction coefficient, flow variable
g	acceleration, gravitational acceleration, staggered gap
gH	impeller work
H	head
h	specific enthalpy
I	inertance
K	valve coefficient, generic non-dimensional coefficient
k	stiffness
L	length, effective length, camber line
M	torque, mass
Ma	Mach number
m, \dot{m}	mass flow rate
N	rotational speed, number of stages
n	generic non-dimensional number
P	power
$P_x(t)$	mean instantaneous power
P_x^α	cyclic power at cyclic frequency α
$P_x^\alpha(f; \Delta f)$	cyclic modulation spectrum
p	pressure
pr	pressure ratio
Q	thermodynamic heat
R	resistance

r	radius
R_g	gas constant
RH	relative humidity
S	source, entropy
s	bearing clearance, entropy per unit mass
T	temperature
t	time, blade thickness
U	mean rotor velocity
V	volume
v	specific volume
W	generic thermodynamic work
\dot{W}	generic thermodynamic work rate
w	velocity
x	spring deformation
$x(t)$	time signal
$x_{\Delta f}(t;f)$	filtered version of the time signal through a frequency band of with Δf centered at frequency f
z	number of blades/vanes, Cartesian coordinate direction

Greek Letters

α	throttling valve position, cyclic frequency, expansion coefficient, generic angle
β	pressure ratio, flow angle
ΔE	energy variation
Δc	velocity difference
Δf	frequency band
Δh	Specific enthalpy change
Δp	relative pressure, pressure difference
γ	$\frac{p_0}{p_{0,\text{ref}}}$ non-dimensional pressure parameter
γ	specific heats ratio
ζ	damping coefficient
η	efficiency
ϑ	$\frac{T_0}{T_{0,\text{ref}}}$ non-dimensional temperature parameter
μ	$\frac{\dot{m} \sqrt{\theta}}{\gamma}$ non-dimensional corrected mass flow rate
ρ	density
ϱ	dynamic viscosity
τ	gear ratio, transmission ratio
ν	$\frac{N_c}{\sqrt{g}}$ corrected rotational speed
φ	flow coefficient, angle between the stream line and the radial, or axial, direction
Ψ	stage loading
ψ	pressure rise coefficient
ω	angular velocity

Subscript and Superscript

0	stagnation physical quantity
1,2,3	test rig sections and segments, modeling component generic sections
1a, 3a, 6a	first, third and sixth axial stage
1c	radial stage
ax	axial
amb	ambient conditions
B	bearing
b	blade
bf	back-flow
C	compressor
c	Compressor, clearance
cDAQ	NI Compact DAQ
cl	axial clearance
corr	corrected
D	duct
d	diffusion
damp	damping
disch	discharge
df	friction at the diffuser
di	incidence at the diffuser
e	effort
el	elastic, electric quantity
exp	expansion
f	frontal, flow
fluid	fluid-dynamic
geo	geometric
h	hub cavity
I	inertance
id	ideal
if	friction at the impeller
ii	incidence at the impeller
in	inlet section
is	isentropic
m	radial component of velocity
max	maximum
min	minimum
mm	velocity component in the streamline direction
mod1	module 1
mod2	module 2
mom	momentum
mot	electric motor
norm	normalized
out	outlet section

P	plenum
PTFE	polytetrafluoroethylene
p	plenum, polytropic
pis	balance piston
r, rot	rotor
ref	reference conditions
SS	steady-state
s	stator
sh	shroud cavity
st	static
stage	compressor stage
stage5	section at fifth axial stage
suct	suction
T	turbine
TS	total-to-static
t	top, impeller inlet (or outlet) tip section
V	valve
v	volute
w	relative component of velocity
x	axial direction
y	lateral direction
z	vertical direction
ϑ	tangential component of velocity

Acronyms

BPF	blade passing frequency
CFD	computational fluid-dynamic
CMS	cyclic modulation spectrum
DF	diffusion factor
ESD	emergency shutdown
FFT	Fast Fourier Transform
GMRC	Gas Machinery Research Council
IC	internal combustion (engine)
MIP	mean instantaneous power
PIV	particle image velocimetry
SM	surge margin
SD	standard deviation
SwRI	Southwest Research Institutes
VPF	vane passing frequency

Bibliography

- Abdelhamid, A., 1980. *Analysis of rotating stall in vaneless diffusers of centrifugal compressors..* s.l., s.n.
- Abdelhamid, A., 1987. A new technique for stabilizing the flow and improving the performance of vaneless radial diffusers. *Journal of turbomachinery*, 109(1), pp. 36-40.
- Abdelhamid, A. & Bertrand, J., 1980. Distinctions Between Two Types of Self Excited Gas Oscillations in Vaneless Radial Diffusers. *Canadian Aeronautics and Space Journal*, 26(2), pp. 105-117.
- Abdelhamid, A., Colwill, W. & Barrows, J., 1979. Experimental Investigation of Unsteady Phenomena in Vaneless Radial Diffusers. *Transaction of ASME*, Volume 101, pp. 52-59.
- Adomaitis, R. & Abed, E., 1993. *Local Nonlinear Control of Stall Inception in Axial Flow Compressors*, s.l.: s.n.
- Amann, C. & Nordenson, G., 1961. The Role of the Compressor in Limiting Automotive Gas Turbine Acceleration. *Centrifugal Compressors, SAE Technical Progress series*, Volume 3.
- Antoni, J., 2009. Cyclostationarity by examples. *Mechanical Systems and Signal Processing*, Volume 23, pp. 987-1036.
- Aretakis, N. & Mathioudakis, K., 1996. *Radial Compressor Fault Identification Using Dynamic Measurement Data*. s.l., s.n.
- Aretakis, N. & Mathioudakis, K., 1998. Classification of Radial Compressor Faults Using Pattern-Recognition Techniques. *Control Engineering Practice*, 6(10), pp. 1217-1223.
- Aretakis, N., Mathioudakis, K., Kefalakis, M. & Papailiou, K., 2004. Turbocharger Unstable Operation Diagnosis Using Vibroacoustic Measurements. *Journal of Engineering for Gas Turbines and Power*, 126(4), pp. 840-847. DOI: 10.1115/1.1771686.
- Ariga, I., Masuda, S. & Ookita, A., 1987. Inducer stall in a centrifugal compressor with inlet distortion. *Journal of turbomachinery*, 109(1), pp. 27-35.
- Arnulfi, G. et al., 1999. (1999). Multistage centrifugal compressor surge analysis: Part II—Numerical simulation and dynamic control parameters evaluation.. *Journal of turbomachinery*, 121(2), pp. 312-320.
- Arnulfi, G. et al., 1999. Multistage centrifugal compressor surge analysis: Part I—Experimental investigation. *Journal of turbomachinery*, 121(2), pp. 305-311.
- Balchen, J. & Mummé, K., 1988. *Process Control: Structures and Applications*. New York: Van Nostrand Reinhold Company.
- Baldassarre, L. et al., 2015. *Axial Thrust in High Pressure Centrifugal Compressors: Description of a Calculation Model Validated by Experimental Data from Full Load Test*. s.l., s.n.
- Barrand, J., Caignaert, G. & Guiton, P., 1984. *Experimental determination of the reverse flow onset in a centrifugal impeller*. Texas A&M University, s.n.
- Baumann, U., 1999. *Rotordynamic Stability Tests on High-Pressure Radial Compressors*. s.l., s.n.
- Belardini, E. et al., 2016. *2nd Quadrant Centrifugal Compressor Performance: Part II*. s.l., s.n.
- Belardini, E., Rubino, D., Tapinassi, L. & Pelella, M., 2015. *Modeling of Pressure Dynamics During Surge and ESD*. Doha, Qatar, s.n.
- Benser, W., 1953. *Analysis of Part-Speed Operation for high-Pressure-ratio Multistage Axial-Flow Compressors*, Washington: NACA.
- Berdanier, R., Smith, N., Fabian, J. & Key, N., 2015. Humidity Effects on Experimental Compressor Performance-Corrected Conditions for Real Gases. *Journal of Turbomachinery*, 137(3), p. art. no. 031011. DOI: 10.1115/1.4028356.
- Bettocchi, R. et al., 2011. Setup of an Experimental Facility for the Investigation of Wet Compression on a Multistage Compressor. *Journal of Engineering for Gas Turbines and Power*, 133(102001), p. 10.
- Bettocchi, R., Pinelli, M. & Spina, P., 2005. A Multistage Compressor Test Facility: Uncertainty Analysis and Preliminary Test Results. *Journal of Engineering for Gas Turbines and Power*, 127(1), pp. 170-177.

- Bidaut, Y., Baumann, U. & Al-Harthy, S., 2009. *Rotordynamic Stability of a 9500 psi Reinjection Centrifugal Compressor Equipped with a Hole Pattern Seal—Measurement versus Prediction Taking into Account the Operational Boundary Conditions*. s.l., s.n.
- Bidaut, Y. & Dessibourg, D., 2014. *The Challenge for the Accurate Determination of the Axial Rotor Thrust in Centrifugal Compressors*. Houston, TX, s.n.
- Biliotti, D., 2013. *Characterization of vaneless diffuser rotating stall on centrifugal compressors for industrial applications*. s.l.:PhD Thesis, Energy Engineering and Innovative Industrial and Environmental, università degli Studi di Firenze.
- Bondarenko, G., Ganelin, B. & Marufenko, T., 1992. Method of Calculating Axial Forces in a Centrifugal Compressor Based on a Refined Model of Flow. *Chemical and Petroleum Engineering*, 28(2), pp. pp. 81-85. DOI: 10.1007/BF01148826.
- Bonnaure, L., 1991. *Modelling High Speed Multistage Compressor Stability*. Boston: Master of Science, Massachusetts Institute of Technology.
- Borutzky, W., 2009. Bond Graph Modeling and Simulation of Multidisciplinary Systems - An Introduction. *J. Simulation Modeling Practice and Theory*, 17(1), pp. 3-21.
- Borutzky, W., 2010. *Bond Graph Methodology Development and Analysis of Multidisciplinary Dynamics System Models*. London: Springer-Verlag.
- Boyce, M. P., 2003. *Centrifugal compressors: a basic guide*. s.l.:PennWell Books.
- Bright, M., Qammar, H., Weigl, H. & Paduano, J., 1997. Stall Precursor Identification in High-Speed Compressor Stages Using Chaotic Time Series Analysis Methods. *Journal of Turbomachinery*, 119(3), pp. 491-500.
- Brooke, G., 1932. *Surging in Centrifugal Superchargers*. s.l., s.n.
- Brown, F., 2007. *Engineering System Dynamics, a Unified Graph-Centered Approach- 2nd Edition*. Boca Raton: CRC Press.
- Brown, R. N. & Lewis, R. A., 1986. Centrifugal Compressor Application Sizing, Selection and Modelling. *Proceedings of the 23rd Turbomachinery Symposium*), pp. 195-201.
- Bullock, R. & Finger, H., 1951. Compressor Surge Investigated by NACA. *SAE J.*, Volume 59, p. 42-45..
- Bulot, N., Ottavy, X. & Trebinjac, I., 2010. Unsteady Pressure Measurements in a High-Speed Centrifugal Compressor. *Journal of Thermal Science*, 19(1), pp. 34-41.
- Cameron, J., 2007. *Stall inception in a high-speed axial compressor*. s.l.:PhD Dissertation, Aerospace and Mechanical Engineering, Notre Dame, Indiana.
- Campbell, K. & Talbert, J., 1945. Some advantages and limitations of centrifugal and axial aircraft compressors. *SAE Technical Paper*, Issue 450224.
- Camp, T. & Day, I., 1998. A Study of Spike and Modal Stall Phenomena in a Low Speed Axial Compressor. *ASME J. Turbomach.*, 120(3), pp. 393-401.
- Camp, T. & Day, I., 1998. A Study of Spike and Modal Stall Phenomena in a Low-Speed Axial Compressor. *Journal of Turbomachinery*, 120(3), pp. 393-401.
- Cargill, A. & Freeman, C., 1991. High-Speed Compressor Surge With Application to Active Control. *Journal of Turbomachinery*, 113(2), pp. 303-311.
- Casey, M. & Robinson, C., 2013. A Method to Estimate the Performance Map of a Centrifugal Compressor Stage. *Journal of turbomachinery*, 135(2), p. 021034.
- Chen, Y. et al., 1994. *Experimental investigation of the flow field of deep rotating stall in a centrifugal compressor*. s.l., s.n.
- Childs, P., 2011. *Rotating Flow*. s.l.:Butterworth-Heinemann, Oxford.
- Choi, M., Smith, N. & Vahdati, M., 2013. Validation of Numerical Simulation for Rotating Stall in a Transonic Fan. *Journal of turbomachinery*, 135(2), p. 021004.
- Christensen, D. et al., 2008. Development and Demonstration of a Stability Management System for Gas Turbine Engines. *Journal of Turbomachinery*, 130(3), p. 03101.

- Cornelius, C., Biesinger, T., Galpin, P. & Braune, A., 2013. Experimental and Computational Analysis of a Multistage Axial Compressor Including Stall Prediction by Steady and Transient CFD Methods. *J. Turbomach*, 136(6), p. 061013 .
- Courtiade, N. & Ottavy, X., 2013. Experimental Study of Surge Precursors in a High-Speed Multistage Compressor. *Journal of Turbomachinery*, 135(6), p. 061018.
- Cousins, W. & Davis Jr., M., 2011. *Evaluating Complex Inlet Distortion with a Parallel Compressor Model: Part 1 - Concepts, Theory, Extensions, and Limitations*. s.l., s.n.
- Cousins, W., Ph.D. thesis, 1996. *The dynamics of Stall and Surge Behavior in Axial-Centrifugal Compressors*. Virginia Polytechnic Institute and State University, Blacksburg, Virginia, USA.: s.n.
- Cumpsty, N., 1989. *Compressor Aerodynamics*. s.l.:Longman, C..
- D'Elia, G., Cocconcelli, M., Mucchi, E. & Dalpiaz, G., 2016. Combining blind separation and cyclostationary techniques for monitoring distributed wear in gearbox rolling bearings. *Journal of Mechanical Engineering Science*, p. DOI: 10.1177/0954406216636165..
- Da Soghe, R., Facchini, B., Innocenti, L. & Miccio, M., 2009. *Analysis of Gas Turbine Rotating Cavities by an One-Dimensional Model*. s.l., s.n.
- Das, D. & Jiang, H., 1984. An Experimental Study of Rotating Stall in a Multistage Axial-Flow Compressor. *J. Eng. Gas Turbines Power*, 106(3), pp. 542-551.
- Day, I., 1993. Stall Inception in Axial Flow Compressors. *ASME J. Turbomach.*, 115(1), p. 1–9.
- Day, I., 1994. Axial Compressor Performance During Surge. *Journal of Propulsion and Power*, 10(3), p. 329–336.
- Day, I., 2016. Stall, Surge, and 75 Years of Research. *J. Turbomach*, 138(1), p. 011001.
- Day, I., 2016. Stall, Surge, and 75 Years of Research. *J. Turbomach*, 138(1), p. 011001.
- Day, I. et al., 1999. Stall Inception and the Prospects for Active Control in Four High Speed Compressors. *ASME J. Turbomach.*, 121(1), p. 18–27..
- Day, I. & Cumpsty, N., 1978. The Measurement and Interpretation of Flow Within Rotating Stall Cells in Axial Compressors,. " *J. Mech. Eng. Sci.*, 20(2), pp. 101-115.
- Day, I. & Freeman, C., 1994. The Unstable Behavior of Low and High Speed Compressors. *Journal of Turbomachinery*, 116(2), pp. 194-201.
- Day, I., Greitzer, E. & Cumpsty, N., 1978. Prediction of Compressor Performance in Rotating Stall. *ASME J. Eng. Gas Turbines Power*, 100(1), pp. 1-12.
- Dazin, A. et al., 2008. Rotating instability in the vaneless diffuser of a radial flow pump. *Journal of Thermal Science*, 17(4), pp. 368-374.
- Dean, R., 1974. *The Fluid Dynamic Design of Advanced Centrifugal Compressors*. Brussels: Creare TN-85, Creare Inc, Hanover New Hampshire, presented as lectures at Von karman Institute.
- Dean, R. J. & Young, L., 1977. The Time Domain of Centrifugal Compressor and Pump Stability and Surge. *Journal of Fluids Engineering, Trans. ASME*, pp. 53-63..
- Dean, R. & Senoo, Y., 1960. Rotating wakes in vaneless diffusers. *Journal of Basic Engineering*, 82(3), pp. 563-570.
- Dhingra, M., Neumeier, Y. & Prasad, J., 2003. *Stall and Surge Precursors in Axial Compressors*. s.l., s.n.
- Dixon, S. & Hall, C., 2013. *Fluid mechanics and Thermodynamics of Turbomachinery*. s.l.:Butterworth-Heinemann..
- Dodds, J. & Vahdati, M., (2015). Rotating Stall Observations in a High Speed Compressor—Part II: Numerical Study. *Journal of Turbomachinery*, 137(5), p. 051003.
- Dodds, J. & Vahdati, M., 2015. Rotating Stall Observations in a High Speed Compressor—Part I: Experimental Study. *Journal of Turbomachinery*, 137(5), p. 051002.
- Domm, U. & Zilling, H., 1966. *Axial Thrust in Centrifugal Pumps*. Braunschweig, s.n.
- Dunham, J., 1965. Non-Axisymmetric Flows in Axial Compressors. *Mechanical Engineering Science, Monograph*, , Institution of Mechanical Engineers, Volume 3.

- Eckardt, D., 1976. Detailed Flow Investigations Within a High Speed Centrifugal Compressor Impeller. *Trans AME Journal of Fluids ENgineering*, Volume 98, pp. 390-402.
- El-Sayed, A., 2008. *Aircraft Propulsion and gas turbine engines*. s.l.:CrRC Press.
- Emmons, H., Pearson, C. & Grant, H., 1955. *Compressor Surge and Stall Propagation*. s.l., s.n.
- Escuret, J. & Garnier, V., 1995. *Stall Inception Measurements in a High-Speed Multi-Stage Compressor*. s.l., s.n.
- Everitt, J. & Spakovszky, Z., 2013. An Investigation of Stall Inception in Centrifugal Compressor Vaned Diffuser. *Journal of Turbomachinery*, Volume 135, p. 011025.
- Farokhi, S., 2014. *Aircraft propulsion*. s.l.:John Wiley & Sons..
- Ferrara, E., 2013. *Characterization of Vaneless Diffuser Rotating Stall on Centrifugal Compressors for Industrial Applications*. s.l.:PhD Thesis, University of Florence, Florence..
- Finger, H., Essig, R. & Conrad, E., 1952. *Effect of Rotor and Stator Blade Modifications on Surge Performance of an 11-Stage Axial-Flow Compressor.*, s.l.: I- Original Production Compressor of XJ40-WE-6 Engine.
- Fink, D., Cumpsty, N. & Greitzer, E., 1992. Surge Dynamics in a Free-Spool Centrifugal Compressor System. *Journal of Turbomachinery*, 114(2), pp. 321-332.
- Floyd, R. J. & Davis, M. J., 2015. *Validation of a Modified Parallel Compressor Model for Prediction of the Effects of Inlet Swirl on Compressor Performance and Operability*. s.l., s.n.
- Foley, J., 1951. Compressor Surge Topic at SAE Round Table. *SAE J.*, , 59(1), pp. 46-50.
- Forbes, G. & Randall, R., 2008. *Separation of Excitation Forces from Simulated Gas Turbine Casing Response Measurements*. s.l., s.n.
- Forbes, G. & Randall, R., 2009. *Gas Turbine Casing Vibrations Under Blade Pressure Excitation*. s.l., s.n.
- Frigne, P. & Van Den Braembussche, R., 1984. Distinction between different types of impeller and diffuser rotating stall in a centrifugal compressor with vaneless diffuser. *Journal of Engineering for Gas Turbines and Power*, 106(2), pp. 468-474.
- Galindo, J., Serrano, J., Climent, H. & Tiseira, A., 2008. Experiments and modelling of surge in small centrifugal compressor for automotive engines. *Experimental Thermal and Fluid Science*, 32(3), p. 818–826.
- Galindo, J., Serrano, J., Guardiola, C. & Cervelló, C., 2006. Surge Limit Definition in a Specific Test Bench for the Characterization of Automotive Turbochargers. *Experimental Thermal and Fluid Science*, 30(5), pp. 449-462.
- Galindo, J., Tiseira, A., Arnau, F. & Lang, R., 2013. On-Engine Measurement of Turbocharger Surge Limit. *Experimental Techniques*, 37(1), pp. 47-54.
- Gallus, H. & Hoenen, H., 1986. *Experimental Investigation of Airfoil and Endwall Boundary Layers in a Subsonic Compressor Stage*. s.l., s.n.
- Gardner, W., 1986. The spectral correlation theory of cyclostationary time-series. *Signal Processing*, 11(3), pp. 13-36.
- Girsberger, R. & Rohne, K., 1990. *investigation of te flow phenomena in the inlet of an unshrouded centrifugal compressor impeller operating at part load*. s.l.:Institution of Mechanical Engineers.
- Gravdahl, J. & Egeland, O., 1997. *A Moore-Greitzer Axial Compressor Model with Spool Dynamics*. s.l., s.n.
- Gravdahl, J. & Egeland, O., 2012. *Compressor surge and rotating stall: modeling and control*. s.l.:Springer Science & Business Media.
- Gravdahl, J., Egeland, O. & Vatland, S., 2002. Drive Torque Actuation in Active Surge Control of Centrifugal Compressor. *Automatica*, 38(11), p. 1881–1893.
- Greitzer, 1976. Surge and Rotating Stall in Axial Flow Compressors—Part I: Theoretical Compression System Model. *Journal of Engineering for Power*, 98(2), pp. 190-198.
- Greitzer, E., 1976b. Surge and Rotating Stall in Axial Flow Compressors—Part II: Experimental Results and Comparison with Theory. *Journal of EGINEERING for Power*, 98(2), pp. 199-211.
- Greitzer, E. & Moore, F., 1986. A Theory of Post-Stall Transients in Axial Compression Systems: Part II—Application. *Journal of Engineering for Gas Turbines and Power*, 108(2), pp. 231-239.

- Greitzer, E. M. T. C. S. & G. M. B., 2007. *Internal flow: concepts and applications*. s.l.:Cambridge University Press.
- Greitzer, E., Tan, C.S. & Graf, M., 2007. *Internal flow: concepts and applications*. s.l.:Cambridge University Press.
- Grong, T. S., 2009. *Modeling of Compressor Characteristics and Active Surge Control*. s.l.:Student Thesis, Norwegian University of Science and Technology.
- Gülich, J., 2008. *Centrifugal Pumps*. Berlin: Springer.
- Hansen, K., Jorgensen, P. & Larsen, P., 1981. Experimental and theoretical study of surge in a small centrifugal compressor. *Journal of Fluids Engineering*, 103(3), pp. 391-395.
- Han, Z.-X. & Cizmas, P., 2003. A CFD Method for Axial Thrust Load Prediction of Centrifugal Compressors. *International Journal of Turbo and Jet Engines*, 20(1), pp. 1-16.
- Helvoirta, J. & Jagera, B., 2007. Dynamic model including piping acoustics of a centrifugal compression system. *Journal of Sound and Vibration*, 302(1-2), p. 361-378.
- Hendricks, G. et al., 1993. *Analysis of Rotating Stall Onset in High Speed Axial Flow Compressors*. Monterey, CA., s.n.
- Hendricks, G., Sabnis, J. & Feulner, M., 1997. Analysis of Instability Inception in High-Speed Multistage Axial-Flow Compressors. *ASME J. Turbomach*, 119(4), p. 714-722.
- Hoenen, H. & Gallus, H., 1993. *Monitoring of Aerodynamic Load and Detection of Stall in Multi Stage Axial Compressors*. s.l.:American Society of Mechanical Engineers, pp. 1-8.
- Hoying, D., Tan, C., Vo, H. & Greitzer, E., 1988. *Role of blade passage flow structures in axial compressor rotating stall inception*. s.l., s.n.
- Huang, P. & Yin, J., 2014. *Transient Surge Dynamics: A Shock Tube Theory and Experimental Comparison*. s.l., s.n.
- Huppert, M. & Benser, W., 1953. Some Stall and Surge Phenomena in Axial-Flow Compressors. *J. Aeronaut. Sci.*, 20(12), p. 835-845.
- Hynes, T. & Greitzer, E., 1987. Method for Assessing Effects of Circumferential Flow Distortion on Compressor Stability. *J. Turbomach*, 109(3), pp. 371-379.
- Inoue, M., Kuroamaru, M., Iwamoto, T. & Ando, Y., 1991. Detection of a Rotating Stall Precursor in Isolated Axial Flow Compressor Rotors. *Journal of Turbomachinery*, 113(2), p. 281-287.
- Inoue, M. et al., 2001. Comparative studies on short and long length-scale stall cell propagating in an axial compressor rotor. *Journal of turbomachinery*, 123(1), pp. 24-30.
- Iura, T. & Rannie, W., 1953. *Observations of Propagating Stall in Axial-Flow Compressors*. s.l.:s.n.
- Jansen, W., 1964. Rotating stall in a radial vaneless diffuser. *Journal of Basic Engineering*, 86(4), pp. 750-758.
- Japikse, D., 1980. *The influence of diffuser inlet pressure fields on the range and durability of centrifugal compressor stages*. s.l., s.n.
- Japikse, D., 1981. *Stall, Stage Stall, and Surge*. s.l., s.n.
- Japikse, D., 1982. *Advanced Diffusion Levels in Turbocharger and Related Centrifugal Compressors*. s.l., s.n.
- Japikse, D., 1996. *Centrifugal Compressor Design and Performance*. s.l.:Wilder, VT: Concepts ETI, Inc..
- Jiang, W., Khan, J. & Dougal, R., 2006. Dynamic centrifugal compressor model for system simulation. *Journal of Power Sources*, 158(2), p. 1333-1343.
- Kabalyk, K. et al., 2016. Experimental Investigation of the Influence of the Inlet Duct Configuration on the Unstable Operation of a Single-Stage Centrifugal Blower. *Proceeding of the institution of Mechanical Engineers, Part A: Journal of Power and Energy*, p. Doi: 10.1177/0957650915624817.
- Kammer, N. & Rautenberg, M., 1986. A distinction between different types of stall in a centrifugal compressor stage. *Journal of Engineering for Gas Turbines and Power*, 108(1), pp. 83-92.
- Karnopp, D., Margolis, D. & Rosemberg, R., 1990. *System Dynamics A Unified approach -2nd Edition*. New York: John Wiley.

- Kilchyk, V., Abdelwahab, A. & Rosinski, A., 2013. *Application of the Surge Model to Radial Compressor System Cycle Optimization*. s.l., s.n.
- Kobayashi, H., Nishida, H., Takagi, T. & Fukushima, Y., 1990. A study on the rotating stall of centrifugal compressors. II-Effect of vaneless diffuser inlet shape on rotating stall. *JSME Transactions*, Volume JSME Transactions, 56, 2646-2651., pp. JSME Transactions, 56, 2646-2651..
- Koch, C., 1981. Stalling pressure rise capability of axial flow compressor stages. *Trans ASME Journal of Engineering for Power*, 98(1), pp. 411-424.
- Koff, S. & Greitzer, E., 1986. Axisymmetrically stalled flow performance for multistage axial compressors. *Journal of Turbomachinery*, 108(2), pp. 216-223.
- Kosuge, H., Ito, T. & Nakanishi, K., 1982. A Consideration Concerning Stall and Surge Limitations Within Centrifugal Compressors. *Journal of Engineering for Power*, 104(4), pp. 782-787.
- Krikelis, N. & Papadakis, F., 1988. Gas turbine modelling using pseudo-bond graphs. *International Journal of Systems Science*, 19(4), pp. 537-550.
- Kurokawa, J. & Toyokura, T., 1972. *Study on the Axial Thrust of the Radial Flow Turbomachinery*. Tokio, s.n.
- Kurz, K., Marechale, R., Fowler, E. & Min Ji, C. M., 2011. *Operation Of Centrifugal Compressors In Choke Conditions*. Houston, Texas., s.n.
- Kurz, R., 2005. *Gas turbine performance*. Houston, TX., s.n.
- Kurz, R. & Brun, K., 2005. *Site Performance Test Evaluation for Gas Turbine and Electric Motor Driven Compressors*. s.l., s.n., pp. 53-62.
- Kurz, R. & White, R., 2004. Surge Avoidance in Gas Compression Systems. *Journal of Turbomachinery*, 126(4), pp. 501-506.
- Lawless, P. & Fleeter, S., 1993. *Rotating Stall Acoustic Signature in a Low Speed Centrifugal Compressor: Part 2 - Vaned Diffuser*. s.l., s.n.
- Lawless, P. & Fleeter, S., 1995. Rotating Stall Acoustic Signature in a Low-Speed Centrifugal Compressor: Part 1 - Vaneless Diffuser. *Journal of Turbomachinery*, 117(1), pp. 87-96.
- Lennemann, E. & Howard, J., 1969. *Unsteady Flow Phenomena in Rotating Centrifugal Impeller Passages*. Cleveland, Ohio, s.n.
- Leufvén, O. & Eriksson, L., 2013. A Surge and Choke Capable Compressor Flow Model-Validation and Extrapolation Capability. *Control Engineering Practice*, 21(12), pp. 1871-1883.
- Li, C., Xu, S. & Hu, Z., 2015. Experimental Study of Surge and Rotating Stall Occurring in High-speed Multistage Axial Compressor. *Procedia Engineering*, 99(DOI: 10.1016/j.proeng.2014.12.707), pp. 1548-1560.
- Liu, A. & Zheng, X., 2013. Methods of Surge Point Judgment for Compressor Experiments. *Experimental Thermal and Fluid Science*, Volume 51, pp. 204-213.
- Li, W., 2013. Model of Flow in the Side Chambers of an Industrial Centrifugal Pump for Delivering Viscous Oil. *Journal of Fluids Engineering, Transactions of the ASME*, 135(5), p. art. no. 051201. DOI: 10.1115/1.4023664.
- Longley, J., 1988. *Inlet Distortion and compressor stability*. s.l.:PhD Thesis Dissertation, University of Cambridge.
- Longley, J., 1994. Review of non-steady flow model for compressor stability.. *J. Turbomach*, 116(2), pp. 202-215.
- Longley, J. & Hynes, T., 1990. Stability of Flow Through Multistage Axial Compressors. *J. Turbomach.*, 112(1), pp. 126-132.
- Loss, I., 1949. *Surge preventing device for centrifugal compressors*. U.S. Patent, Brevetto n. 2,470,565,.
- Lüddecke, B. et al., 2016. Unsteady thrust force loading of a turbocharger rotor during engine operation. *Journal of Engineering for Gas Turbines and Power.*, 138(1), p. art. no. 012301. DOI: 10.1115/1.4031142.
- Ludtke, K., 1983. Aerodynamic Tests on Centrifugal Process Compressors—the Influence of the Vaneless Diffuser Shape. *J. Eng. Power*, 105(4), pp. 902-909.
- Lüdtko, K., 2004. *Process Centrifugal Compressors*. Berlin: Springer.

- Marelli, S. et al., 2014. Experimental Analysis on the Performance of a Turbocharger Compressor in the Unstable Operating Region and Close to the Surge Limit. *Experimental thermal and Fluid Science*, Volume 53, pp. 154-160.
- Marshall, D. & Sorokes, J., 2000. *A review of aerodynamically induced forces acting on centrifugal compressors, and resulting vibration characteristics of rotors*. Houston, TX, Sept, pp. 18-21., s.n.
- Mattingly, J., 1996. *Elements of Gas Turbine Propulsion*. s.l.:Mc Graw-Hill series in aeronautical and aerospace engineering. Mc Graw-Hill.
- Mazzawy, R., 1977. Multiple Segment Parallel Compressor Model for Circumferential Flow Distortion. *J Eng Power, Trans ASME*, Volume 99 Ser A (2), pp. 288-296.
- Mazzawy, R., 1980. Surge-induced structural loads in gas turbines. *Journal of engineering for power*, 102(1), pp. 162-168.
- McAulay, J., 1951. *Investigation of Surge characteristics of a XJ34-WE_32 TurboJet Engine*, s.l.: NACA Research Memorandum.
- McDougall, N. C. N. H. T., 1990. Stall Inception in Axial Compressors. *ASME J. Turbomach.*, 112(1), p. 116-123.
- Meher-Homji, C. & Gabriles, G., 1998. *Gas Turbine Blade Failures—Causes, Avoidance, and Troubleshooting*. Houston, TX, s.n.
- Mizuki, S., Kawashima, Y. & Ariga, I., 1978. *Investigation concerning rotating stall and surge phenomena within centrifugal compressor channels..* s.l., s.n.
- Moore, F., 1984. A Theory of Rotating Stall of Multistage Axial Compressors: Part I—Small Disturbances. *ASME J. Eng. Gas Turbines Power*, ., 106(2), pp. 313-320.
- Moore, F., 1984b. A Theory of Rotating Stall of Multistage Axial Compressors: Part II—Finite Disturbances. *ASME J. Eng. Gas Turbines Power*, 106(2), pp. 321-326.
- Moore, F., 1984c. A Theory of Rotating Stall of Multistage Axial Compressors: Part III—Limit Cycles. *ASME J. Eng. Gas Turbines Power*, 106(2), pp. 327-334.
- Moore, F. & Greitzer, E., 1986. A Theory of Post-Stall Transients in Axial Compression Systems: Part I—Development of Equations. *J. Eng. Gas Turbines Power*, 108(1), pp. 68-76.
- Moore, J., Ransom, D. & Viana, F., 2011. Rotordynamic force prediction of centrifugal compressor impellers using computational fluid dynamics. *Journal of Engineering for Gas Turbines and Power*, 133 (4), p. art. no. 042504. DOI:10.1115/1.2900958.
- Morini, M., Pinelli, M. & Venturini, M., 2006. Development of a One-Dimensional Modular Dynamic Model for the Simulation of Surge in Compression Systems. *Journal of Turbomachinery*, 129(3), pp. 437-447.
- Morini, M., Pinelli, M. & Venturini, M., 2007. *Acoustic and Vibrational Analyses on a Multi-Stage Compressor for Unstable Behavior Precursor Identification*. s.l., s.n.
- Morini, M., Pinelli, M. & Venturini, M., 2007. *Application of a One-Dimensional Modular Dynamic Model for Compressor Surge Avoidance*. s.l., s.n.
- Movaghar, A. & Novinzadeh, A., 2011. *Ideal Turbo charger Modeling and Simulation using Bond Graph Approach*. s.l., s.n.
- Niazi, S., 2000. *Numerical Simulation of Rotating Stall and Surge Alleviation in Axial Compressors*. s.l.:PhD Dissertation, Aerospace Engineering, Georgia Institute of Technology.
- Pearson, H. & Bowmer, T., 1949. Surging in axial compressors. *Aeronaut. Q.*
- Pearson, H. & McKenzie, A., 1959. Wakes in Axial Compressors. *Journal of the Royal Aeronautical Society*, Volume 63, pp. 415-416.
- Petry, N., Benra, F. & Koenig, S., 2010. *Experimental Study of Acoustic Resonances in the Side Cavities of a High-Pressure Centrifugal Compressor Excited by Rotor/Stator Interaction*. s.l., s.n.
- Petry, N., König, S. & Benra, F., 2013. Influence of the Swirling Flow in the Side Cavities of a High-Pressure Centrifugal Compressor on the Characteristics of Excited Acoustic Modes. *Journal of Turbomachinery*, 135(3), p. art. no. 031024. DOI: 10.1115/1.40.
- Pullan, G. et al., 2015. Origins and structure of spike-type rotating stall. *Journal of Turbomachinery*, 137(5), p. 051007.

- Rasmussen, P. & Kurz, R., 2009. *Centrifugal compressor applications-upstream and midstream*. Houston, TX, s.n., pp. 14-17.
- Reneau, L., Johnston, J. & Kline, S., 1967. Performance and Design of Straight, Two-Dimensional Diffusers. *Journal of Basic Engineering, ASME Transactions*, 89(Series D), p. 141–150.
- Rohsenow, W., Hartnett, J. & Cho, Y., 1998. *Handbook of Heat Transfer*. s.l.: (Vol. 3), New York: McGraw-Hill.
- Roy, R. P., Devasenathipathy, S., Xu, G. & Zhao, Y., 1999. *A Study of the Flow Field in a Model Rotor-Stator Disk Cavity*. s.l., s.n.
- Saxer-Felici, H., Saxer, A., Inderbitzin, A. & Gyarmathy, G., 1998. *Prediction and measurement of rotating stall cells in an axial compressor*. s.l., s.n.
- Schoenenborn, H. & Breuer, T., 2012. Aeroelasticity at Reversed Flow Conditions—Part II: Application to Compressor Surge. *Journal of turbomachinery*, 134(6), p. 061031.
- Senoo, Y. & Kinoshita, Y., 1978. *Limits of rotating stall and stall in vaneless diffuser of centrifugal compressors*. s.l., s.n.
- Senoo, Y., Kinoshita, Y. & Ishida, M., 1977. Asymmetric Flow in Vaneless Diffusers of Centrifugal Blowers. *Journal of Fluids Engineering, Trans. ASME*, Volume March, pp. 104-114.
- Simmons, H., Brun, K. & Cheruvu, S., 2006. *Aerodynamic Instability Effects on Compressor Blade Failure: A Root Cause Failure Analysis*. s.l., s.n.
- Sovran, G. & Klomp, E., 1967. *Experimentally Determined Optimum Geometries for Rectilinear Diffusers with Rectangular Conical or Annular Cross Section*. Amsterdam, The Netherlands, s.n.
- Spakovszky, Z., 2004. Backwards Rotating Stall Waves in Centrifugal Compressors. *Journal of Turbomachinery*, 126(1), pp. 1-12.
- Spakovszky, Z. & Roduner, C., 2009. Spike and Modal Stall Inception in an Advanced Turbocharger Centrifugal Compressor. *Journal of Turbomachinery*, 131(3), p. doi:10.1115/1.2988166.
- Stoney, G., s.d. Scientific activities of the late Hon. Sir Charles Parson. *Engineering*, p. 144.
- Strazisar, A. et al., 2004. *Compressor Stall Control Through Endwall Recirculation*. s.l., s.n.
- Tibboel, G., 2003. *Modification of a One-Dimensional Dynamic Compression System Model to Calculate Stage Characteristics Internally*. s.l.: Student Thesis, University of Tennessee, Knoxville.
- Trébinjac, I., Benichou, E. & Buffaz, N., 2015. Full-Annulus Simulation of the Surge Inception in a Transonic Centrifugal Compressor. *Journal of Thermal Science*, 24(5), p. 442–451.
- Tryfonidis, M. et al., 1994. *Pre-stall Behavior of Several High-Speed Compressors*. s.l., s.n.
- Tryfonidis, M. et al., 1995. Pre-Stall Behaviour of Several High-Speed Compressors. *ASME J. Turbomach.*, 117(1), p. 62–80.
- Uddin, N. & Gravidahl, J., 2015. Bond Graph Modeling of Centrifugal Compressor System. *Simulation*, 91(11), pp. 998-1013.
- Vahdati, M., Simpson, G. & Imregun, M., 2008. Unsteady Flow and Aeroelasticity Behavior of Aeroengine Core Compressors During Rotating Stall and Surge. *Journal of Turbomachinery*, 130(3), p. art. no. 031017. DOI: 10.1115/1.2777188.
- Vepa, R., 2010. *Modelling and Quasilinear Control of Compressor Surge and Rotating Stall Vibrations*. s.l., s.n.
- Vo, H., Tan, C. & Greitzer, E., 2005. *Criteria for Spike Initiated Rotating Stall*. s.l., s.n.
- Wachter, J. & Lohle, M., 1984. Experimental investigation of the dynamic behavior of centrifugal compressors. In: *Stability, Stall and Surge in Compressors and Pumps*, D. Japikse, ed.. s.l.: ASME, New York, ASME FED, pp. 19, 23-30.
- Wang, H., Adomaitis, R. & Abed, E., 1994. *Nonlinear analysis and control of rotating stall in axial flow compressors*. s.l., s.n.
- Wang, H., Krstic, M. & Larsen, M., 1997. *Control of deep-hysteresis aeroengine compressors - Part I: A Moore-Greitzer type model*. s.l., s.n.
- Watanabe, H., Konomi, S. & Ariga, I., 1994. *Transient Process of Rotating Stall in Radial Vaneless Diffusers*. s.l., s.n.

- Will, B., 2011. *Theoretical, Numerical and Experimental Investigation of the Flow in Rotor-Stator Cavities With Application to a Centrifugal Pump*. s.l.:Doctoral Dissertation, Universität Duisburg-Essen, Fakultät für Ingenieurwissenschaften» Maschinenbau und Verfahrenstechnik» Institut für Energie- und Umweltverfahrenstechnik.
- Wlash, P. & Fletcher, P., 2004. *Gas Turbine Performance*. s.l.:John Wiley & Sons.
- Yoon, S. et al., 2010. Model Validation for an Active Magnetic Bearing Based Compressor Surge Control Test Rig. *Journal of Vibration and Acoustics, Transactions of the ASME*, 132(6), p. art. no. 061005.
- Yoshida, Y., Murakami, Y., Tsurusaki, H. & Tsujimoto, Y., 1990. *Rotating stalls in centrifugal impeller/vaned diffuser systems. 1st report, Experiment*. s.l., s.n.
- Young, A., Day, I. & Pullan, G., 2013. Stall Warning by Blade Pressure Signature Analysis. *Journal of Turbomachinery*, 135(1), p. art. no. 011033. DOI: 10.1115/1.4006426.
- Zaki, M., 2009. *Physics based modeling of axial compressor stall*. s.l.:Doctoral dissertation, Georgia Institute of Technology.
- Zheng, X. & Liu, A., 2015. Phenomenon and Mechanism of Two-Regime-Surge in a Centrifugal Compressor. *Journal of Turbomachinery*, 137(8), p. 081007.

Acknowledgments

I have never been good at showing my gratitude and appreciation but in this case it is worth to mention the person without whom this work would have not been possible.

I sincerely thank my advisor Professor Michele Pinelli for its constant supervision and for involving me in many interesting projects, some of which helped me to better develop my Ph.D. Thesis. These projects improved my knowledge and allowed me to study many useful arguments for my future career.

My heartfelt thanks goes to Professor Mirko Morini for its continuous guidance and for supporting me in developing and pushing forward ideas for my research and other related projects. His guidance was crucial for my Ph.D. achievements.

Part of this work is the product of the partnership with Southwest Research Institutes and Solar Turbines. For this reason I would like to thank Dr. Rainer Kurz and Dr. Klaus Brun for their availability, useful ideas and curiosity, which pushed me to enhance the quality of the analyses and the comprehension of the results.

I would like to express my acknowledgements to my advisor Professor Mauro Venturini, who was also my M.Sc. Thesis advisor, for introducing me to the Turbomachinery and Energy System Research Group of the Engineering Department of University of Ferrara, giving me the opportunity to take up the Ph.D. program.

It is also fair to say thank you to my colleagues of the “Fluid Machinery and Energy System and Research Group” for their precious suggestions and for being honest teammates in this experience at the University of Ferrara.

A strong thanks surely goes to my parents for incessantly helping me and my family during these years. They allowed me to focus on my research without being worried or distracted by the difficulties of life.

Finally, a special thanks goes to my wife Pilar and my daughter Nicole who gave me unconditional love and support. They gave me the strength to overtake challenging, stressful, and hard moments experienced along the journey of my Ph.D. They are my

Acknowledgments

inspiration and motivation for continuing to improve my knowledge and move my career forward.

Instability Phenomena in Multistage Compressors:
Experimental Analysis and Dynamic Modeling

Enrico Munari